Optical investigations on PTCDA on KCl(100)

Superradiant aggregates and single molecules

DISSERTATION

zur Erlangung des Doktorgrades (Dr. rer. nat.)
der Mathematisch-Naturwissenschaftlichen Fakultät
der Rheinischen Friedrich-Wilhelms-Universität Bonn

vorgelegt von
CHRISTIAN MARQUARDT
aus Siegburg

Bonn 2019

Angefertigt mit Genehmigung der Mathematisch-Naturwissenschaftlichen Fakultät
der Rheinischen Friedrich-Wilhelms-Universität Bonn

1. Gutachter:	Prof. Dr. Moritz Sokolowski
2. Gutachter:	Prof. Dr. Peter Zeppenfeld
Fachnaher Gutachter:	Prof. Dr. Arne Lützen
Fachfremder Gutachter:	Prof. Dr. Stefan Linden

Tag der Promotion: 31.05.2019
Erscheinungsjahr: 2019

Abstract

In the present work, condensed and diluted phases of 3,4,9,10-perylenetetracarboxylic dianhydride (PTCDA) were investigated on thin KCl(100) films on the Ag(100) surface. The samples were structurally characterized by spot profile analysis low energy electron diffraction (SPA-LEED), and bright field microscopy. The optical properties of the samples were investigated by fluorescence spectroscopy (FL), fluorescence excitation spectroscopy (FLE), and fluorescence microscopy. The work tackled three advanced questions of the so far already quite well understood sample system.

I The optical and structural properties of the condensed PTCDA/KCl(100) brickwall phase were reinvestigated for improved preparation conditions and an extended temperature range. Here a focus lied on the enhancement of the pure electronic transition with respect to the vibronic modes, called superradiance. The temperature dependence of the superradiance showed an atypical initial rise in the low temperature regime and could be explained by a theory based on finite size effects. It could be shown that the atypical low temperature behavior is the result of node planes in the wavefunctions of the excitonic ground states of brickwall-type aggregates. The node planes are induced by weak repulsive next-nearest-neighbor interactions and become dominant in the case of highly asymmetric aggregates. The experimental temperature dependence could be simulated by weighting the calculated temperature dependencies of individual aggregates with a domain size distribution extracted from a detailed SPA-LEED analysis.

II The homogeneous line profiles of single PTCDA molecules located at KCl-step edge sites were investigated by high resolution single molecule FLE spectroscopy. Here first a splitting of the inhomogeneous broadening into two main species could be observed. On top of the inhomogeneous broadening a statistical fine structure consisting of individual homogeneously broadened single molecule profiles was observed. Far off the center of the inhomogeneous profile, also spectrally isolated single molecule profiles were measured. The FLE measurements of these single molecules adsorbed on a surface revealed a molecular behavior qualitatively equivalent to that observed in earlier single molecule studies on molecules in solid hosts. This includes aspects as: the width and the form of the absorption profiles, the saturation behavior with the intensity of the excitation light, an observed broadening with temperature, and a tendency to undergo laser induced and independent spectral jumps.

III An UHV compatible light microscope for the brightfield and fluorescence application was developed and used to study the macroscopic surface morphology and the fluorescence signal from molecules on the sample surface. The microscope was developed for the investigation of samples under ultra high vacuum conditions and images the surface through a glass window.

Bright field images of the sample revealed a characteristic mesoscopic corrugation and a variety of local defects. In the fluorescence images, a mostly homogeneous coverage of the sample could be proven. However, also exceptions from this homogeneity were observed and could be correlated with the sample morphology. These included shading effects of mesoscopic surface protrusions related to an inclined angle of the molecular beam, occasional intensity variations presumably due to a local inhomogeneity of the KCl film thickness, and very local and bright fluorescence signals at some special surface defects.

Contents

1 Introduction

The optical properties of organic materials, i.e. the absorption and emission of light in the visible part of the electromagnetic spectrum, are important for many technological applications especially in the still growing fields of organic electronics and energy conversion [1, 2]. These properties are on the first sight mainly dependent on the chemical structure of the chromophores but are also largely affected by the interactions of them with the local environment. The detailed investigation of these interactions and the principles of how they modify the optical properties can thus help to provide important knowledge for the design of future materials and devices. The other way round, the optical properties and their variation can act as a sensitive probe for the detection of (smallest) environmental changes.

As a very impressive example for such environmental effects the color of many dye solutions can change dramatically by a variation of the solvent [3] or the dye concentration [4, 5]. This can be explained by molecule-solvent and molecule-molecule interactions, respectively. Similar environmental effects apply also for molecules embedded in solids [6, 7], molecules adsorbed on surfaces [8, 9], and molecules that are part of a molecular crystal [10, 11], or thin film [11, 12]. Apart from the pure energetic shift of the optical transition, numerous further variations of the optical properties, e.g., the appearance and vanishing of spectral features or their temperature dependence, can be related to interactions with the specific molecular environment.

In the present work, the optical properties of single and aggregated molecules were investigated following a surface science approach. The molecules were adsorbed on a dielectric surface and were experimentally investigated under clean ultra high vacuum (UHV) conditions. Due to the interactions between the molecules and the surface, the surface acts as a template. It stabilizes the molecules on distinct adsorption sites or mediates the assembly of the molecules in long range ordered structures. This structural control facilitates to relate the optical properties to the present structure. In the limit of low molecular coverages, this allows to study changes of the optical properties that are induced by the molecule-substrate interactions. For higher coverages and aggregated films especially molecule-molecule interactions play a role and become dominant for the optical properties. Here aspects like the influence of the packing and the size of aggregates can be studied.

A model system that has been studied over the last years by use of the above described approach is that of 3,4,9,10-perylenetetracarboxylic dianhydride (PTCDA) molecules adsorbed on a KCl(100) surface [8, 13–19]. The structural and optical properties of this system were extensively studied both for a condensed monolayer phase [8, 13, 14] and for diluted phases of isolated molecules on different adsorption sites [15–19]. The present work builds on these findings and uses the available

expertise with the sample system for establishing novel experimental techniques and answering so far inaccessible scientific questions.

The samples were investigated optically by fluorescence (FL) and high resolution fluorescence excitation (FLE) spectroscopy. Structural properties were obtained by spot profile analysis low energy electron diffraction (SPA-LEED) and in vacuo light microscopy. The PTCDA was deposited on thin epitaxial KCl films on a Ag(100) crystal surface.

In detail this thesis deals with three topics that will be briefly sketched in the following:

I The optical and structural properties of the condensed PTCDA/KCl(100) brickwall phase were reinvestigated for improved preparation conditions and an extended temperature range. Here a focus lied on the enhancement of the pure electronic transition with respect to the vibronic modes, called superradiance. This was studied as an effect of the temperature, the aggregate size and the aggregate shape. The results are explained in a simple theoretical model based on the symmetry of the wavefunctions of the excitonic states. The results are supported by a detailed SPA-LEED analysis.

II The homogeneous line profiles of single PTCDA molecules located at KCl-step edge sites were investigated by high resolution single molecule fluorescence excitation spectroscopy. The inhomogeneous broadening was overcome by spatial and spectral dilution so that the single molecule absorption lines became accessible. Additionally single molecule related photophysically processes like spectral jumps and a saturation behavior were studied.

III An UHV compatible light microscope for the brightfield and fluorescence application was developed and used to study the macroscopic surface morphology and the fluorescence signal from molecules on the sample surface. The development of the microscope and the observed surface structures are described.

The present thesis is organized as follows: Chapter 2 provides an overview on the related literature. An introduction in the theoretical background of the experimental techniques and the studied phenomena is given in Chapter 3. The used experimental setup and the preparative details are presented in Chapter 4. The Chapters 5, 6, and 7 discuss the individual results of the superradiant PTCDA brickwall phase, the singe molecule spectroscopy, and the in vacuo optical microscopy. Finally, Chapter 8 summarizes the different topics and gives an outlook on further open questions and strategies for their solution.

2 Literature review

This chapter presents an overview on the scientific fields that are related to the present thesis. The preparative and structural part of this thesis is nested in surface sciences, in particular in the section of surface sciences that deals with large organic molecules adsorbed on dielectric surfaces. Important concepts and related works of this field are briefly reviewed in Chapter 2.1. The spectroscopic experiments of this work are strongly connected to the concepts of superradiance in molecular aggregates and spectral resolved single molecule detection in solid hosts. An overview on these topics is given in Chapter 2.2 and Chapter 2.3, respectively. Finally, Chapter 2.4 gives a short review on preceding works on the optical spectroscopy of PTCDA on alkali halides.

2.1 Organic molecules on dielectric surfaces

The properties of (sub-)monolayer coverages of organic molecules on surfaces have been extensively studied for various sample systems. These studies can be roughly classified by the substrates used for the molecular deposition. Metallic [20–22], semiconductive [23, 24], and dielectric substrates [25, 26] can be distinguished. For the present work particularly the dielectric substrates are of interest.

Dielectric substrates that have been used for the deposition of molecules are various alkali halides [8, 13–15, 27–29] and metal oxides [30–33], boron nitride [34–36] and more complex minerals like silicates [37, 38] and carbonates [39, 40]. Experiments have been carried out either on bulk crystals [13, 32, 39] or on thin dielectric films that were grown on (semi-) conductive substrates [8, 14, 15, 27, 30, 34]. The use of thin dielectric films is motivated by the possibility to use the standard electron based surface science techniques like scanning tunneling microscopy (STM) [41], low energy electron diffraction (LEED) [42], and photo electron spectroscopy (PES) [43] for the structural and electronically characterization of the samples. This is not possible for dielectric bulk crystals due to an electric charging of the dielectric material. Structures on dielectric bulk crystals are thus investigated by non-electron based techniques, like atomic force microscopy (AFM) [28] and optical spectroscopy [13, 37].

In contrast to the binding of molecules to metal surfaces, which is often chemisorptive and results in covalent bond formation involving the molecular frontier orbitals and the valence and conduction bands of the metal [44], the binding to dielectric surfaces is usually physisorptive and driven by van der Waals and Coulombic interactions. Therefore, the intrinsic electronic properties of molecules on dielectric surfaces are less affected by the bonding to the substrate and can thus be studied in good approximation [27]. Often exactly this electronic ‘decoupling’ (with respect to the situation on metals) between the molecules and the substrate is the major motivation for the

use of dielectric substrates and thin films. A decoupling from a conductive surface is for example necessary for the detailed imaging of the intrinsic molecular orbitals by STM [27, 45] or to avoid fluorescence quenching in optical spectroscopy [8, 9]. Also for the technical application of molecular structures in electronic devices, an insulating substrate is mandatory [29]. In the case of thin insulating films, not only the choice of the material but also the thickness of the films needs to be considered for the formation of a sufficient band-gap and thus for a satisfactory decoupling [35, 46].

The molecules that have been investigated on dielectric substrates can be classified in two groups. The first group contains the aromatic (hydro-) carbons without additional functional groups. These are molecules like fullerenes [47], acenes [11, 33, 48, 49], diindenoperylene (DIP) [50, 51], DBP [6], and rubrene [52]. They are commonly weakly bound to dielectric surfaces by only van der Waals interactions. These interactions my be even weaker than the interactions with neighboring molecules. Therefore frequently dewetting of the molecules from the surface and the formation of crystallites is observed at elevated temperatures, leading to the so called Volmer-Weber growth scenario [29]. Condensed phases of this group of molecules tend to maximize attractive intermolecular interactions, which can lead for example to the upright standing by π-stacking of planar acenes [48, 53]. At low coverages and low temperatures, i.e., in the absence of neighboring molecules, these molecules adsorb however in a flat lying geometry on the surface [54].

The second group of molecules investigated on dielectric surfaces includes large aromatic hydrocarbons with functional groups like perylenederivatives [13, 55, 56], phthalocyanines [35, 57], and porphyrines [58, 59], but also smaller functional organic molecules, with e.g. functional acid groups [60]. Of course also the molecules of this group bind partially to the surface by van der Waals interactions. They, however, possess also an additional binding mechanism by Coulombic interactions between their polar functional groups and polar atoms of the surface. One special type of Coulombic interaction can be the hydrogen bonding of functional molecular groups to electron lone pairs of the surface [61]. These additional interactions can anchor the molecules on selective surface positions and can be used to tune the molecular assembly and hence the molecular properties [15, 61].

The investigated molecule of the present work (PTCDA) belongs to the second group of molecules. It exhibits partially negatively charged anhydride groups on both ends of the aromatic perylene core that can interact with positively charged cations of the surface (cf. Fig. 5.1). The adsorption of PTCDA has been investigated particularly on alkali halide surfaces. Experimental and theoretical studies have been reported for PTCDA on NaCl [62–66] KCl [13–15, 64–66], and KBr [55] surfaces. Both monolayer coverages [13, 14, 55, 62, 63] and diluted phases [15, 64–66] have been investigated. Theoretical investigations showed that the binding is dominated by strong Coulombic interactions between the anhydride groups and the alkali-ions of the surface. This interaction is strong enough to lead to a distortion of the molecule [64–66]. The extent of the distortion depends on the lattice match of the molecule an the substrate [64–66]. Despite the strong bonding, dewetting from dielectric KBr surfaces has been reported at elevated temperatures [55].

2.2 Molecular aggregates and exciton superradiance

The aggregation of dye molecules by self-assembly is commonly connected with drastic changes of their optical properties. This has first been discovered by Jelly [4] and Scheibe [5] in the 1930s for pseudoisocyanine chloride (PIC chloride) in ethanol solutions. It can be explained by an electronic coupling between the transition dipoles of the aggregated molecules and hence by a delocalization of the optical excitation over several coupled molecules.

On the basis of these first experiments the optical changes due to molecular aggregation have primarily been investigated for dyes in solutions. Here especially cyanines, but also merocyanines, squaraines, and perylenebisimides have been studied. A good overview on the different molecular classes, their aggregate shapes and optical properties in solution can be found in Ref. [67]. Concepts and mechanisms that are relevant for aggregates in solutions apply, however, also for any other inter-molecular arrangement. Therefore similar effects have also been investigated for molecular crystals [68, 69], molecular thin films [70–72], polymers [73, 74], small molecular clusters [75], or, like in the present work, for surface assembled monolayers [9, 13, 16, 36, 37].

Based on the optical changes due to aggregation, dye aggregates can be roughly divided into two classes: the J- and the H-aggregates. They differ structurally by the spatial arrangement of the optical transition dipoles inside the aggregate and thereby by the molecular packing. For J-aggregates (named after one of their discoverers, Jelly), the transition dipoles interact mainly attractively with each other. This leads to a red-shift with respect to the monomer spectrum. For a one dimensional aggregate, an attractive coupling of transition dipoles occurs for a head-to-tail arrangement of transition dipoles. In contrast, the transition dipoles in H-aggregates (H is for hypsochromic shift) interact mainly repulsively with each other, which results in a blue shifted absorption spectrum of the aggregate. Repulsive interactions of transition dipoles occur for parallel transition dipoles. For an illustrative example of the different coupling situations in H- and J-aggregates the reader is referred to Chapter 3.2.3.

Besides the optical shifts that occur during aggregation also various further effects that are mostly related to a redistribution of the oscillator strength in the absorption and emission spectra can be observed [76]. For the present work, especially the phenomenon called “superradiance” is of interest. This occurs almost exclusively in molecular J-aggregates and denotes the enhancement of the collective emission rate of an excitonic state with respect to the emission rate of an isolated monomer [77–79].

The extent of this enhancement is often taken as a measure for the coherence size of the excitation and is roughly proportional to the number of coherently coupled molecules N_{coh} [80]. The coherence size of the exciton is ultimately limited by the size of the molecular aggregate, but can additionally be reduced by static and dynamic (temperature induced) disorder in the molecular positions and optical transition energies [78, 81, 82]. This has been studied in numerous works, both experimentally [71, 81, 83] and theoretically [78, 82, 84].

By the enhancement of the collective emission rate of the excitonic state also its radiative lifetime is reduced. The measured radiative lifetime of the superradiant emission is then shorter than

the radiative lifetime of the monomer by a factor of N_{coh}. Therefore superradiance was mainly investigated by use of time dependent fluorescence spectroscopy [71, 72, 81, 85, 86].

A different method that allows the determination of N_{coh} from the time independent fluorescence spectrum was introduced by Spano [84]. It uses the ratio between the enhanced intensity of the pure electronic transition with respect to transitions into non-affected vibrational molecular modes of the same fluorescence spectrum. Although this is an indirect measure that is only valid under special conditions, it has been successfully applied to several systems [16, 87, 88].

Frequently especially the temperature dependence of the superradiant emission has been studied in order to investigate mechanisms that destroy the coherence and localize the excitation [16, 70, 86, 89]. Typically a monotonic decay of the superradiance with temperature was obtained [16, 86, 89]. At lowest temperatures often a saturation of the emission rate due to static disorder has been observed [70, 78, 81]. At present, the largest reported coherence sizes N_{coh} were obtained at cryogenic temperatures for PIC dyes in solutions: Values between 40 and 100 molecules were reported [70, 81]. Compared to this the reported values for molecular crystals or thin films, e.g., of anthracene, were significantly smaller, i.e., $N_{coh} < 10$ [71, 72].

A comparably novel approach to this field is the surface induced growth of J-aggregates, that was also used in the present work. So far, only the preceding work of M. Müller et al. that deals with PTCDA on KCl(100) has taken a closer look onto superradiance in two dimensional molecular aggregates on surfaces [16]. There a maximum value of $N_{coh} \approx 20$ was reported. Similar effects should, however, be observable in other surface induced structures, e.g., in the system MePTCDI on KBr [56] that also shows a J-aggregate like packing of transition dipoles.

A different but very impressive approach for the defined creation and studying of single aggregates on a surface was introduced by Zhang et al. [90]. Here, first small aggregates of ZnPc molecules were created on a NaCl film by manipulation with the STM tip. In a second step, the aggregate was electronically excited with the tip and showed the typically J-aggregate superradiance with a maximum value of $N_{coh} = 4$ for a linear chain of 4 ZnPc molecules.

Apart from studies on J-aggregates, exciton superradiance has also been considered for special situations in H-aggregates [85, 91] and hybrid aggregates that change the character of their coupling with temperature. Theoretically, a rise of the emission rate with temperature is derived. This has particularly been studied theoretically for polymers, but could not yet be verified experimentally [92, 93].

2.3 Spectrally resolved single molecule spectroscopy

The main motivation for the optical spectroscopy of single molecules is to obtain very local information on the molecules and their local environment. In usual optical spectroscopy this is only possible in a very limited way due to the typical averaging of the signal over an ensemble of molecules. By spatial and spectral isolation of the optical signal of a single emitter, this ensemble

averaging can however be circumvented so that the obtained signal becomes sensitive for local changes on the scale of the individual molecule.

Nowadays, this principle is mainly used in the life sciences, where single molecule techniques are applied for the detection and tracking of single particles in living cells at room temperature, e.g. in super-resolution microscopy [94, 95]. For the present work, however, rather the pioneer experiments on the detection of single molecules are important. These have been performed on diluted impurity molecules in solid hosts and were measured, in contrast to experiments in the life sciences, at cryogenic temperatures with high spectral resolution [96–101].

The first single molecule detection was accomplished by Moerner and Kador in 1989 [96], who used a frequency modulation technique to reduce the background signal and detect the absorption line of a single pentacene molecule in a *para*-terphenyl crystal. Only little later, in 1990, the same sample system was investigated by Orrit and Bernard [97], who introduced the background free and hence more straightforward fluorescence excitation technique in this field. Here a high resolution tunable laser was used to selectively excite single molecules.

Based on this second experiment the majority of the following experiments has been carried out using the fluorescence excitation technique. Typically highly emissive dye molecules like polyaromatic hydrocarbons (pentacene [96–98], terrylene [100, 102, 103]), or TDI dyes [104] have been studied. They were embedded in crystals of organic molecules [97, 98], Shpol'skii matrices [102], amorphous thin films [104], or polymers [105] in order to obtain very local information on the interactions with these host materials. It could be shown that especially the low temperature behavior of molecules in amorphous materials can be significantly different from that in a crystalline structure due to the presence of further degrees of freedom [100].

The spectral line width of single impurity molecules was found to approach the lifetime limited value typically at temperatures < 4 K [98]. For these temperatures, values between 8 MHz [98] and a few 100 MHz [103] have been reported depending on the investigated molecule, host material, and the specific defect site of the molecule. This width is several orders of magnitude smaller than the inhomogeneous width of the ensemble spectrum and hence sensitive for smallest changes of the molecular environment or the experimental conditions.

Especially the broadening of these profiles has frequently been studied for several individual molecules of a sample. It has been investigated as a function of the laser intensity in order to study the saturation behavior of the optical transition [106], or as a function of the sample temperature to probe interactions with phonons and vibrations of the local host [98]. The respective theoretical mechanisms for the broadening will be described in Chapter 3.2.2.

Apart from the broadening, spectral diffusion of the transition energy of a molecule, the phenomenon called blinking , and the optical switching of a molecule between two optical transition energies have been investigated [97, 98, 100, 102]. The high energetic sensitivity facilitated even the detection of the influence of an external electric field (Stark effect) [105] or an applied external pressure [107] on the spectral positions. By temporally correlated spectroscopy also quantum mechanical effects like photon bunching [108] and anti-bunching [109] could be observed.

Although there are many studies performing optical single molecule spectroscopy on molecules in solids or solutions, so far only little is known on the optical behavior of single molecules on clean and well-defined surfaces. Some experiments were performed by the STM induced light emission technique (cf. Chapter 2.1) [90, 110, 111]. Experiments with optical excitation of single molecules on a surface were however only reported by Monti and co-workers [112, 113]. They described the detection of single perylenebisimide molecules on various substrates with a confocal UHV-microscope at room temperature. Depending on the substrate different blinking characteristics were observed. A spectral resolved measurement was however not performed.

2.4 Optical spectra of PTCDA on alkali halides

Besides the structural properties of PTCDA molecules on alkali halide (100) surfaces (cf. Chapter 2.1) also their optical properties have been investigated in very detail. The majority of these spectroscopic studies have been carried out on NaCl(100) and KCl(100) substrates for diluted [8, 9, 17–19] and condensed PTCDA phases [9, 13, 16]. They will be briefly reviewed in the following.

In Fig. 2.1 low temperature (20 K) fluorescence (FL) and fluorescence excitation (FLE) spectra of diluted PTCDA molecules adsorbed on NaCl and KCl surface sites are shown. The terrace site spectra (Fig. 2.1a and c) measured by M. Müller are dominated by strong 0-0 transitions at 19680 cm^{-1} for PTCDA on NaCl [9] and 20000 cm^{-1} for PTCDA on KCl [8]. These spectral positions are red-shifted with respect to the spectral position of PTCDA in He-nanodroplets [114] by 1300 cm^{-1} for PTCDA on NaCl and 960 cm^{-1} for PTCDA on KCl. These shifts were explained analogous to a solvation effect by a different stabilization of the electronic ground and excited states of the molecule by the interaction with the surface [8]. Quantum chemical calculations by M. Hochheim and T. Bredow showed that also the arch-like distortion of the molecules, due to the binding to the surface, is responsible for about 30 - 40% of the total red-shift of the transition energies [64].

The fluorescence spectra of isolated molecules show well resolved vibrational modes that are resolvable due to a comparably low inhomogeneous broadening of 20 cm^{-1} on the KCl(100) surface and 80 cm^{-1} on the NaCl(100) surface [115]. This was explained by the strong molecule substrate interaction and hence very defined adsorption sites. By polarization dependent fluorescence spectroscopy it could be shown that the molecules are highly oriented on the alkali halide substrate [8]. The obtained vibrational structure of the spectra is to a great extent similar to the spectrum in He-droplets and thus not affected by the surface bonding. However additional low energy vibrational modes < 200 cm^{-1} could be observed that occur due the breaking of the symmetry of the molecule on the surface (C_{2v}) with respect to that in the gas phase (D_{2h}) [8].

A. Paulheim et al. showed that a migration of PTCDA molecules to alkali halide step sites can be induced by annealing the sample to temperatures above $T = 70$ K or illumination of the sample with high laser intensities $P \approx 500$ W/cm^2 [17]. The respective spectra of PTCDA molecules at step sites of KCl and NaCl are depicted in Fig. 2.1b and c, respectively. They were found to be blue-shifted by ≈ 130 cm^{-1} with respect to spectra of molecules at terrace sites both for NaCl and

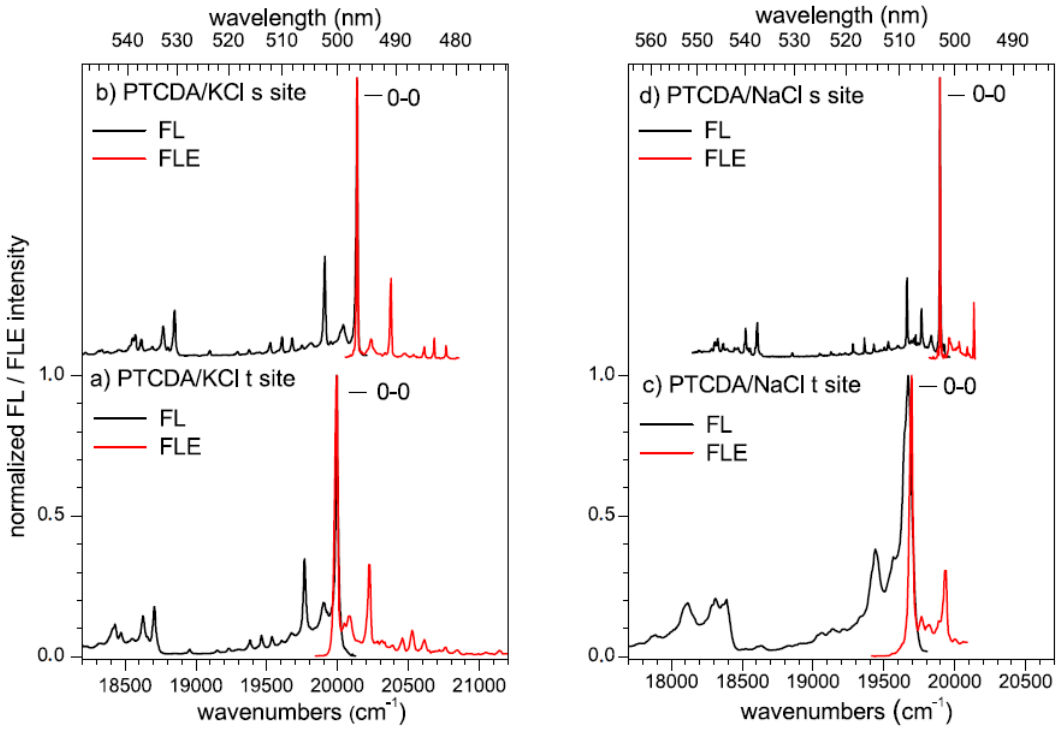

Figure 2.1: *Spectral overview of isolated monomers of PTCDA at KCl and NaCl surface sites. The spectra of molecules at terrace (t) sites are depicted in the lower panels (a,c). The spectra of molecules at step sites are shown in the top panels (b,d). The Figure was taken from [46]. For further details see text.*

KCl [19]. This blue shift could be explained by a lifting of one side of the molecule at the step edge and hence by a partially reduced arch-like distortion [46].

The spectra of molecules at step sites exhibit a inhomogeneous broadening of only 3 cm^{-1} (NaCl) and 5 cm^{-1} (KCl) [18]. This is significantly reduced with respect to the spectra of molecules at terrace sites due to a higher binding energy of the molecules and a thus even more defined adsorption sites [66]. In combination with an STM study [15] and theoretical calculations [65, 66] the respective adsorption sites at the step edges could be identified and related to the optical spectra. It was found that the molecules "dig" themselves into the step edge [46]. The high spectral resolution even facilitated a detailed investigation of the low energy surface induced vibrational modes, that were also detected for the molecules at step sites [19].

The optical properties of the monolayer phases of PTCDA were studied also for NaCl [9] and KCl [13, 16]. For PTCDA on NaCl a stable quadratic phase (19380 cm^{-1}) and a meta stable herring-bone phase 19120 cm^{-1} were found and investigated. Both structures showed a spectral red-shift and a pronounced spectral broadening with respect to the spectra of isolated molecules on terrace sites. The spectral shifts were explained to origin to a large extend from non-excitonic, solvation-like stabilization of the molecules. But the attractive excitonic stabilization contributes also to the red-shift. It was calculated to be ≈ -45 cm^{-1} for the quadratic phase and ≈ -105 cm^{-1} for the herring-bone phase so that both structures are formally J-aggregates. Nevertheless, no superradiance was observable for both of the PTCDA phases on NaCl [115].

The monolayer of PTCDA on KCl was found to form a brickwall structure with an optical transition energy of 19600 cm^{-1}. This transition is again red shifted (by 400 cm^{-1}) with respect to that of isolated molecules on KCl terrace sites. Here again, the major part of the shift was found to be due to solvation effects and only a contribution of 130 cm^{-1} was found to result from the excitonic interactions. The monolayer on KCl showed strong superradiance, with well resolved, but strongly suppressed vibrational modes in the FL spectrum [16]. In the FLE, an asymmetric broadening of the 0-0 transition was found that could be explained by finite size effects was found [16].

3 Theoretical background

This chapter provides an introduction in the theoretical background of the experimental techniques that were used and the physical phenomena that were investigated in this work. The techniques were low energy electron diffraction for the structural characterization of the sample, fluorescence- and fluorescence excitation spectroscopy for its optical characterization, and optical microscopy for imaging the sample. For a more detailed theoretical background it is referred to the cited textbooks and publications.

3.1 Low energy electron diffraction

Low energy electron diffraction (LEED) is a standard technique for the structural characterization of ordered surface structures. It can be used for the determination of the lattice parameters, i.e. the size and orientation of lattice vectors, with high precision [116]. Furthermore, it allows to study the form of the diffraction profiles to obtain information on the surface morphology, which includes the size, distribution, and correlation of defect structures like point defects, steps, and domain boundaries [117, 118]. Finally, by a quantitative analysis of the intensities of the diffraction pattern, in certain cases, also the atomic positions inside the unit cell of the lattice can be determined [119, 120].

LEED is based on the wave-like properties of electrons that were predicted by de Broglie [121] and experimentally confirmed for the first time in 1927 by Davisson and Germer [122]. The electron wavelength λ_e depends on the kinetic energy E_{kin} of the electrons and can be calculated according to the de Broglie relation:

$$\lambda_e = \frac{h}{p} = \frac{h}{\sqrt{2 m_e E_{kin}}}. \tag{3.1}$$

Typically electron energies in the range between 20 eV and 500 eV are used for LEED. These result in wavelengths λ_e between 3 $Å^{-1}$ and 0.5 $Å^{-1}$, which are on the order of inter-atomic distances and are hence suited for the structure analysis on this length scale. Different from X-rays, the interaction strength of electrons with matter is high so that the penetration depth of electrons into condensed matter is very limited. This penetration depth is energy dependent and has a minimum at about 100 eV for many materials [117]. Therefore, at typical LEED energies the electrons penetrate only few atomic layers and the method is highly surface sensitive.

A schematic drawing of a conventional LEED apparatus and the correspondent Ewald-sphere in the reciprocal space is depicted in Fig. 3.1. A collimated electron beam of defined energy hits the surface and the electrons are backscattered elastically and inelastically. Due to the periodicity of the surface and the wave character of the electrons, the elastically scattered electrons interfere

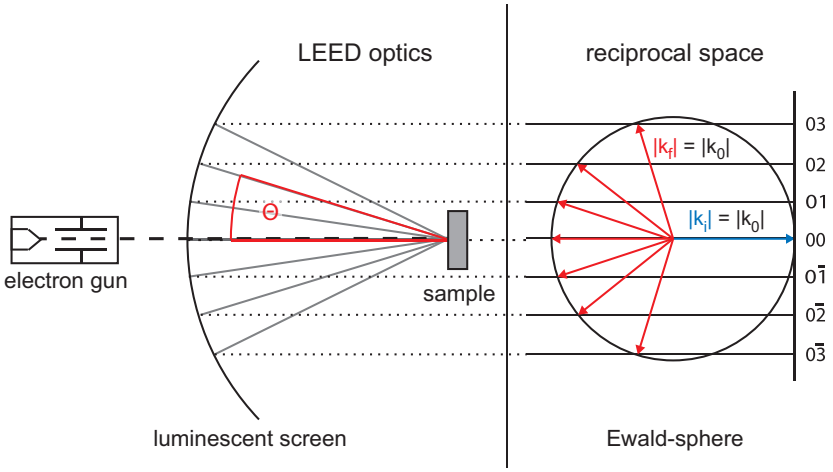

Figure 3.1: *Scheme of an optical LEED and the associated reciprocal space. The electron beam hits the sample surface under an angle of 90° and is elastically backscattered from there. The diffraction pattern can be observed on a luminescent screen. Each diffraction spot is defined by a diffraction angle Θ relative to the surface normal. The visible diffraction spots appear where the Ewald sphere cuts the diffraction rods normal to the surface. The radius of the Ewald sphere k_0 depends on the electron energy. The direction of the incident beam $\vec{k}_i$ remains constant while the directions of the diffracted $\vec{k}_f$ beams varies*

constructively or destructively leading to an angular intensity distribution with defined maxima of intensity, the diffraction pattern. This can be monitored on a spherical screen.

The conditions for constructive interference at a two dimensional surface lattice are as follows:

$$\vec{k}_{||}^{\mathrm{h,k}} = \mathrm{h} \cdot \vec{a}^* + \mathrm{k} \cdot \vec{b}^* \tag{3.2}$$

$$\left|\vec{k}_{||}^{\mathrm{h,k}}\right| = |k_0| \cdot \sin(\Theta) \tag{3.3}$$

$$|k_0| = 2\pi/\lambda_\mathrm{e} \tag{3.4}$$

Here $\vec{k}_{||}^{\mathrm{h,k}}$ is the wavevector that describes the diffraction spot with the indices h, k. The length of this vector depends on the diffraction angle Θ with respect to the surface normal and the radius of the Ewald sphere k_0. The latter is a function of the electron wavelength λ_e. While the direction of the incident wavevector $\vec{k}_i$ is usually normal to the surface, the direction of the diffracted beams $\vec{k}_f$ is variable.

Due to the limited penetration depth of the electrons there is only little diffraction in the direction perpendicular to the surface. Therefore also the interference in this direction is limited, and no periodic extinctions from the bulk appear, which is different from the situation in X-ray diffraction and results in "diffraction rods" perpendicular to the surface. The spots of the diffraction pattern appear where the Ewald sphere cuts these diffraction rods (see Fig. 3.1). The parameters of the surface lattice ($\vec{a}$, $\vec{b}$) can be determined from the geometrical arrangement of the diffraction rods ($\vec{a}^*$, $\vec{b}^*$); the surface symmetry can be determined from their periodic extinctions.

For the investigation of surface defects commonly a different type of LEED apparatus is used, the spot profile analysis low energy electron diffraction (SPA-LEED) apparatus. Here the LEED pattern is not detected on a screen, but electrostatically deflected and scanned over the small

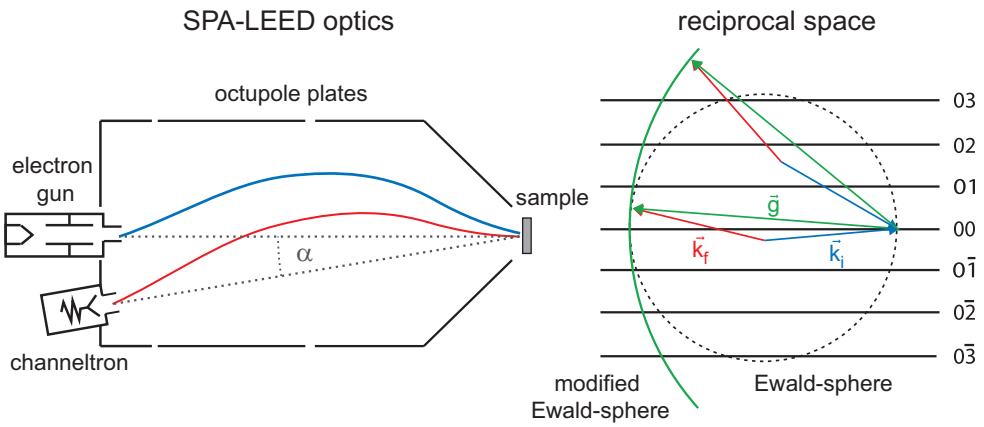

Figure 3.2: *Scheme of a SPA-LEED apparatus and its modified Ewald sphere construction. In a SPA-LEED apparatus the diffraction pattern is continuously deflected by an electrostatic octupole field and scanned over a stationary point detector (channeltron). Different from a conventional LEED the (small) angle α between the incident electron beam $\vec{k}_i$ and the deflected electron beam $\vec{k}_f$ remains always constant. In reciprocal space this results in a modified Ewald sphere almost twice as large as in the conventional case.*

aperture of a stationary point detector, the channeltron. This technique enables high resolution measurements with a high dynamic intensity range of up to 6 orders of magnitude. A sketch of the SPA-LEED apparatus and its modified Ewald sphere construction is shown in Fig. 3.2. Due to the fixed positions of the electron gun and the channeltron, the small angle α between the incident electron beam $\vec{k}_i$ and the detected diffracted beam $\vec{k}_f$ on the position of the sample remains always constant. This results in a large angle between $\vec{k}_i$ and $\vec{k}_f$ in reciprocal space and an Ewald-sphere almost twice as large as for a conventional LEED apparatus.

For an ideal single crystal surface without any defects, the sharpness and contrast of the diffraction pattern is determined by the quality of the LEED instrument. Deviations from an ideal surface like point defects, domain boundaries, or step edges result in a broadening of the spot profiles or an increase of diffuse background signal. Such defect structures are commonly analyzed within the kinematic approximation [117, 118]. This assumes that all scatterers at the surface exhibit the same scattering factor. Under this approximation the structure and morphology of the surface are given entirely by the position and profile form of the diffraction spots. For the analysis of the basis of the unit cell, additionally the absolute intensity of the spots needs to be considered as a function of the electron energy (LEED IV). This is described by the dynamical LEED theory [119, 120]. The present work however uses LEED primary for the detailed determination of the sizes of epitaxially grown two dimensional structures. For this purpose the LEED experiments are discussed within the kinematic approximation.

The size of two dimensional periodic surface structures can be limited either by step edges or domain boundaries. Depending on the correlation of these defect structures this results in a broadening (uncorrelated defects) or a splitting (correlated defects) of the involved spots [117]. In addition, it is possible to differentiate between effects that are caused by the presence of steps or domain boundaries from the energy dependence of the LEED pattern. While effects that are caused by

domain boundaries are independent of the electron energy, effects caused by step edges appear and vanish periodically with the electron energy and thus with the wavelength of the electrons.

Dependent on the wavelength of the electrons, beams that are scattered at the upper terrace of a step edge interfere constructively or destructively with beams that are scattered at its lower terrace. This depends on the phase shift between the scattered beams and is described by the scattering phase [118]

$$S = \frac{\vec{g} \cdot \vec{d}}{2\pi} = \frac{\left(g_x, \quad g_y, \quad g_z\right) \cdot \left(d_x, \quad d_y, \quad d_z\right)}{2\pi}. \tag{3.5}$$

Here $\vec{g}$ denotes the diffraction vector and $\vec{d}$ the step vector. The components of $\vec{d}$ are given by the respective crystal structure. The components g_x and g_y of the diffraction vector can directly be extracted from the spot position in reciprocal space $\vec{k_{||}}$. g_z equals the wavevector perpendicular to the surface $\vec{k_{\perp}}$. It can be calculated by

$$g_z = \left|\vec{k}_{\perp}\right| = \sqrt{\left(2 \cdot \cos\left(4^{\circ}\right) \left|\vec{k}_0\right|\right)^2 - \left|\vec{k}_{||}\right|^2} \quad \text{with} \quad \left|\vec{k}_0\right| = \frac{2\pi}{\lambda_{\mathrm{el}}}. \tag{3.6}$$

For integer values of the scattering phase $S = n$ the waves scattered at different terraces interfere constructively with each other and no spot broadening due to the presence of step edges occurs (in-phase condition). For half-integer values $S = n + \frac{1}{2}$ they interfere destructively, and the profile is maximally broadened by steps (anti-phase condition). The scattering phase needs always to be considered when analyzing the width of diffraction profiles and thus making statements on domain sizes and terrace widths in real space.

Domain or terrace sizes in real space can be determined from the widths of the spot profiles because these contain information on the sizes of periodic structures. The average size or the coherence length $\overline{\Gamma}$ can be roughly estimated from the full width at half maximum (FWHM) Δk of a spot profile via

$$\overline{\Gamma} = \frac{2\pi}{\Delta k}. \tag{3.7}$$

For a more precise determination of the terrace- and domain sizes it is possible to fit the profile with an adequate model that includes the correct auto-correlation function of scatterers on the surface. One commonly used example is a Lorentzian 3/2 profile form that results from an exponential decaying correlation function in 2D [123]. Alternatively it is also possible to simulate the spot profile in a bottom up approach. The diffraction pattern of a linear chain of scatterers can be described, e.g., by the Laue profile [124]:

$$I(k) = \frac{\sin^2\left(Nka/2\right)}{\sin^2\left(ka/2\right)}. \tag{3.8}$$

Here a denotes the periodical distance between the scatterers and N denotes the number of scatterers before chain termination. For a simulation of the spot profile of a real surface, now all possible correlation lengths and their probabilities P_N need to be considered

$$I(k) = \sum_N P_N \frac{\sin^2(Nka/2)}{\sin^2(ka/2)}. \tag{3.9}$$

This approach neglects any inter domain or inter terrace scattering, but can give a good approximation of the real situation. Independent of the chosen approach, it is necessary to take into account also the instrumental broadening that can be best determined by measuring the spot profile at the in-phase conditions of a perfect crystalline surface.

3.2 Fluorescence spectroscopy

3.2.1 Optical transitions in molecules

Optical spectroscopy probes the absorption and emission of light from the ultra violet and visible part of the electromagnetic spectrum (200 nm $\leq \lambda \leq$ 800 nm) [125]. By the absorption of photons, molecules are excited into energetically higher states. In the case of visible and ultra violet light the excitation energy corresponds usually to the transition of an electron from the highest occupied molecular orbital (HOMO) into the lowest unoccupied molecular orbital (LUMO) [126] without a spin flip. The molecule then is in the first electronic excited state S_1. By emission of a photon the excited state can decay radiatively back into the electronic ground state S_0. This process is called fluorescence.

The energy of the $S_0 \rightarrow S_1$ transition depends on the binding situation inside the molecule and especially on the energy spacing of the involved molecular orbitals. For example the energy gap in saturated hydrocarbons is relatively high, since the involved frontier orbitals have large contributions of localized strongly binding σ- and anti-binding σ^*-orbitals [126]. Here the electronic transition requires UV-light for excitation. In contrast, organic dye molecules usually exhibit widely delocalized π- and π^*-electron systems that are responsible for a smaller energy gap. There the electronic transitions can be excited by lower energetic light.

The transfer of an electron from a binding to an anti-binding molecular orbital by the optical excitation reduces the intra-molecular binding strength and thus slightly increases the intra-molecular distances. This is illustrated in a schematic potential energy diagram in Fig. 3.3a. Due to the change of the atomic potentials inside the molecule, molecular vibrations that share a direction with these displacements can couple to the optical transition. According to the Born-Oppenheimer approximation the positions of the nuclei remain constant during the absorption [127]. This results in “vertical” transitions with an intensity distribution given by the overlap of the nuclei wavefunctions between the inital and the final state (cf. Fig. 3.3b). This is called the Franck-Condon principle.

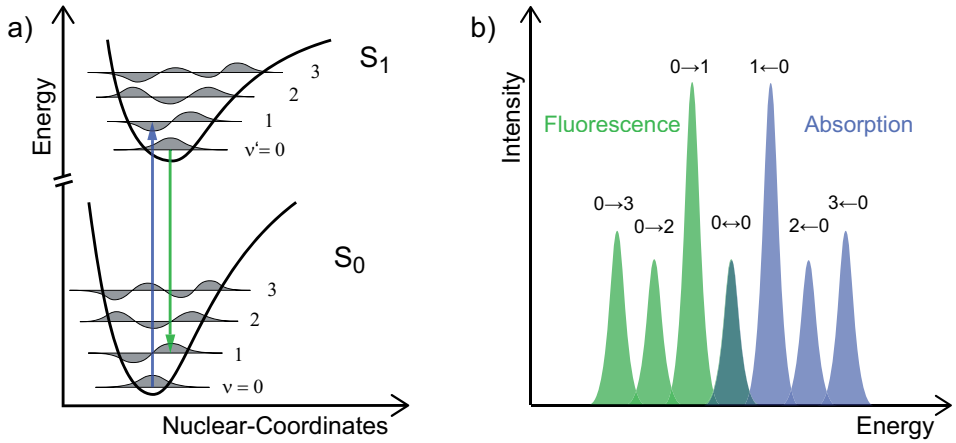

Figure 3.3: *Illustration of the Franck-Condon-Principle. a) Schematic drawing of the electronic ground state S_0 and the electronic excited state S_1 with their vibronic sublevels ν and ν' . The position of the binding potential of the S_1 state is shifted towards higher distances. Optical transitions occur vertically with a probability corresponding to the overlap of the wavefunctions between the sublevels. b) Schematic fluorescence and absorption spectrum with an intensity distribution according to a). The fluorescence and absorption spectra are mirror symmetric with respect to each other.*

After an electronic excitation, the vibrational energy of a molecule (in contact to a solid or liquid matrix) decays fast and non-radiatively, so that the molecule is in the vibrational ground state of the electronically excited state. From there it decays radiatively and again according to the Franck-Condon-principle, generating the fluorescence spectrum. For large organic dye molecules the difference in the positions of the atomic potentials between S_0 and S_1 is small so that the pure electronic 0-0 transition dominates the spectrum in absorption and emission. In addition, the vibronic peaks in absorption and emission have a comparable intensity and spectral position. Therefore the obtained absorption and emission spectra are often almost mirror symmetric with respect to the 0-0 transition.

3.2.2 Profile form and spectral linebroadening

The intensity of spectral features obtained in absorption and fluorescence spectra is always distributed over a (small) energy range, a phenomenon that is called spectral line broadening. It is possible to differentiate between broadening mechanisms that affect the spectral width of the individual molecular transitions, so called homogeneous broadening, and mechanisms that only affect the ensemble spectrum, so called inhomogeneous broadening. An example of both broadening types is given in Fig. 3.4. In the following, the broadening mechanisms that are relevant for the experiments of the present work are described.

Inhomogeneous broadening: The inhomogeneous broadening results from a distribution of the transition energies inside an ensemble of probed molecules [102, 128]. Thereby the individual molecular line profiles are each homogeneously broadened. For molecules on fixed positions, like in solid hosts or on a surface, the different transition energies are always due to locally different environments of the molecules that lead to different interactions and small energetic shifts. The width of

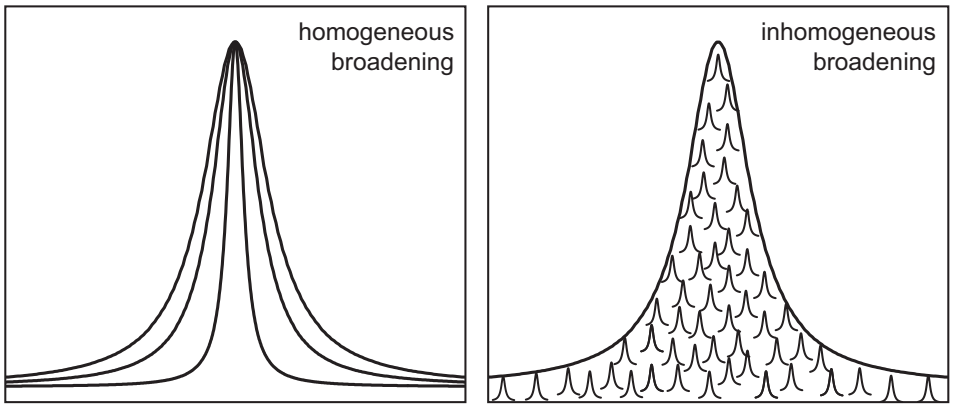

Figure 3.4: *Comparison of the homogeneous and the inhomogeneous broadening mechanism. The homogeneous broadening affects the individual molecular transition profile. The inhomogeneous broadening is given by the energetic distribution of the individual homogeneous profiles.*

the inhomogeneous broadening depends on the spread of the distribution of individual transition energies on the investigated sample. The inhomogeneous broadening dominates the ensemble spectrum at low temperatures, when the most homogeneous broadening effects are absent [129].

Natural broadening: The ultimate physical limit for the determination of the transition energy of a homogeneously broadened profile is given by Heisenberg's uncertainty principle and the lifetime of the excited state τ. In a classical picture the energy dissipation of the excited state by spontaneous emission can be described by an attenuated harmonic oscillator. The profile form of this process is then given as the Fourier transform of the exponential decaying oscillation and yields a Lorentzian profile with an intensity distribution dependent on the frequency ν:

$$I(\nu - \nu_0) = \frac{1}{2\pi} \cdot \frac{\Delta\nu}{(\nu - \nu_0)^2 + \left(\frac{\Delta\nu}{2}\right)^2}. \tag{3.10}$$

Here ν_0 denotes the central frequency of the profile and $\Delta\nu$ denotes its full width at half maximum (FWHM). In the absence of other broadening mechanisms the profile width is only limited by the finite lifetime of the excited state τ. In this case it is called natural linewidth $\Delta\nu_{\mathrm{nat}}$ and can be calculated according to the uncertainty principle by [130]:

$$\Delta\nu_{\mathrm{nat}} = \frac{1}{2\pi\tau}. \tag{3.11}$$

Temperature broadening: Additional to the natural broadening the profile of the optical transition can be broadened homogeneously by interactions of the molecule with its environment, e.g. phonons of the substrate [98, 101, 131, 132]. Hereby, the movement of the environment induces temporal fluctuations of the central frequency ν_0, which result again in a Lorentzian broadening of the profile. The resulting profile can then be described by a convolution of the natural lineprofile with the temperature broadened lineprofile. The width of the resulting profile is then given by the sum of the individual widths of the natural broadening $\Delta\nu_{\mathrm{nat}}$ and the temperature broadening $\Delta\nu_{\mathrm{T}}$

$$\Delta\nu(T) = \Delta\nu_{\mathrm{nat}} + \Delta\nu_{\mathrm{T}}(T). \tag{3.12}$$

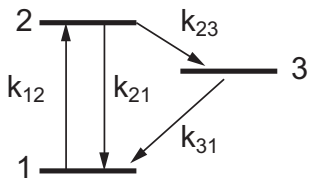

Figure 3.5: *Schematic drawing of the relevant transition rates in a molecular three level system. The transition rates between the different levels are denoted by k_{ij}.*

At very low temperatures $\Delta\nu_{\mathrm{T}}$ vanishes since the movements of the environment freezes out, then the profile form depends only on $\Delta\nu_{\mathrm{nat}}$ [133]. At higher temperatures however $\Delta\nu_{\mathrm{T}}$ becomes dominant for the profile width.

The exact temperature dependence of $\Delta\nu$ depends on the involved environmental processes. For molecules embedded in a solid environment usually two processes can be differentiated: An exponential growing thermal activation process that is related to the above mentioned substrate phonons or the coupling of the optical transition to frustrated molecular rotations [98], and a T^x-dependence that is related to thermal activated tunneling of environmental groups between two levels. The latter effect was primary observed for molecules embedded in amorphous hosts or polymers [100, 134].

Saturation broadening: The width of an optical transition can also be homogeneously broadened by the intensity of the excitation light I. This is connected to a saturation of the emission rate at high excitation intensities, which can be understood in the model of a molecular three level system as depicted in Fig. 3.5. The fluorescence emission rate of the 0-0 transition k_{21} depends on the population of the excited state. For low intensities this increases with increasing intensity due to a higher absorption k_{12}, however for higher intensities when the ground state gets more and more depopulated the absorption and hence also the emission saturates. The presence of an additional (long lived) triplet state ((3) in Fig. 3.5) further reduces the population of the ground state and thereby also the maximum emission rate. The fluorescence rate dependence $R(I)$ on the excitation intensity I follows the following equation [98]:

$$R(I) = R_\infty \frac{I/I_S}{1 + I/I_S}. \tag{3.13}$$

Here R_∞ denotes the emission rate at infinite excitation intensity and I_S is the saturation intensity. The latter is defined as the intensity where half of the maximum emission rate R_∞ is obtained.

$$R\left(I_S\right) = \frac{R_\infty}{2} \tag{3.14}$$

The saturation intensity I_S is also important for the saturation broadening [98]:

$$\Delta\nu_S = \Delta\nu_0 \sqrt{1 + I/I_S}, \tag{3.15}$$

where ν_0 denotes the linewidth at vanishing excitation intensity. The intensity broadening can be traced back to the increased probability for stimulated emission from the excited state that is

present at a high excitation intensity. The stimulated emission accelerates the radiative decay and thus reduces the excited state lifetime, which leads to a broadening.

By solving the differential equation system for the populations in the three level system for the stationary case [130], it can be shown that the parameters I_S and R_∞ can be described entirely by the photophysical constants of an investigated system [98].

3.2.3 Intermolecular coupling and collective excitations

Until now the optical properties of molecules have been considered for the isolated case without intermolecular interactions. However, for condensed molecular phases especially these interactions become decisive for the optical spectra. Mainly two effects need to be considered. Fig. 3.6 illustrates both effects for the simplest case of only two interacting molecules. The first effect is comparable to a solvation of the molecules and shifts the energy of the optical transition. Due to the neighboring molecules the molecular states involved in the electronic transition are unequally stabilized. The obtained shift depends to a great extend on the polarizability of the molecular surrounding and is commonly referred to as the D-term [135, 136].

The second effect is the resonant energetic coupling of excited molecules. Compared to the case of the isolated molecule, where the excitation is localized only on the excited molecule itself, the excitation in a condensed molecular phase can be exchanged between the molecules [135]. It can thus be delocalized and stabilized. For molecular aggregates both the excited electron and its corresponding 'hole' are located always on the same molecule (Frenkel-exciton [137, 138]).

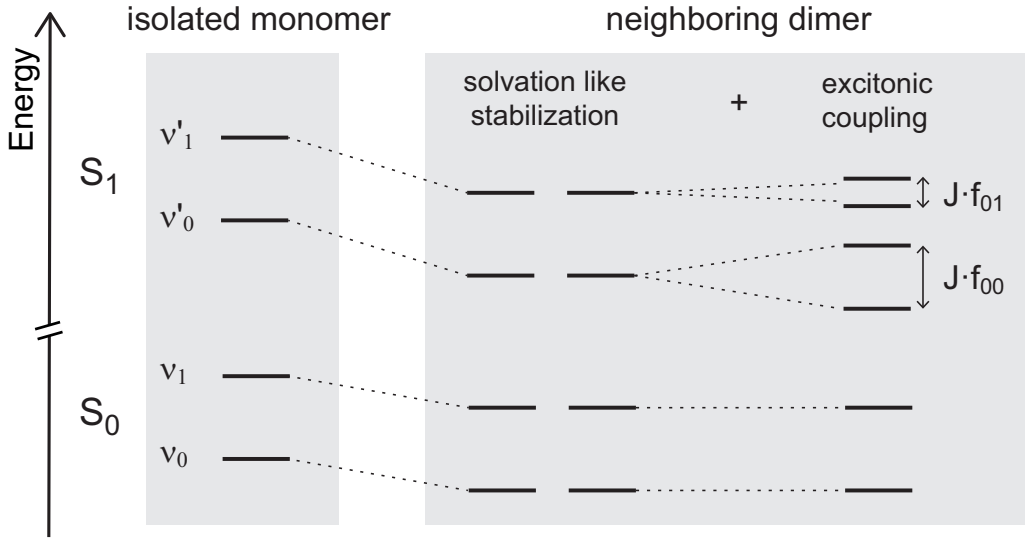

Figure 3.6: *Comparison of the electronic and vibronic states between an isolated molecule and two neighboring interacting molecules. Two types of intermolecular interactions can be distinguished. The first is a solvation like interaction that stabilizes both the electronic ground state S_0 and the electronic excited state S_1. Due to differences in the stabilization between the different states this induces an energetic shift of the optical $S_0 \rightarrow S_1$-transition. The second interaction is a resonant coupling of the transition dipoles that induces a splitting of the excited state levels. The amount of this splitting depends on the coupling strength J and the Franck-Condon factor $f_{0\nu}$ of the respective excited state. In the given example f_{00} is twice as large as f_{01}.*

The excitation is transfered between the different molecules by Coulombic interactions that are approximately described by interactions of the transition dipoles [127].

The excitonic coupling between the transition dipoles induces a splitting of each vibronic energy level of the excited state ν' into multiple new energy levels according to the number of coupled molecules. The maximum splitting depends on the coupling strength J between the molecules, which corresponds to the pure dipole interaction scaled by the Franck-Condon factor $f_{0\nu'}$ of the molecular excited state ν' [139].

The excitonic states of a multi molecule system (aggregate) can be calculated by solving the Schrödinger equation:

$$\hat{H}\phi^k = \epsilon^k \phi^k. \tag{3.16}$$

Here $\hat{H}$ denotes the Hamiltonian-operator, ϕ^k is the aggregate wavefunction of the excited state k, and ϵ^k is the corresponding eigenvalue.

ϕ^k can be expressed by a sum of single molecule wavefunctions $|n\rangle$ with the coefficients $c_{n,k}$:

$$|\phi^k\rangle = \sum_n^N c_{n,k}|n\rangle. \tag{3.17}$$

For the case of a single excitation in an N-molecule system, the single molecule wavefunctions $|n\rangle$ can be written as a product of one molecular wavefunction refering to the electronic excited state $|\phi_n^e\rangle$ and all $N-1$ other molecular wavefunctions refering to the electronic ground state $|\phi_m^g\rangle$

$$|n\rangle = |\phi_n^e\rangle \prod_{m\neq n} |\phi_m^g\rangle. \tag{3.18}$$

The wavefunction ϕ^k describes not only the the Coulombic interactions of all electrons and nuclei in one molecule, but also the interactions between the electrons and nuclei of all N molecules. Therefore the Hamiltonian $\hat{H}$ has to consider both the internal $\hat{H}_{\text{in}}$ and external interactions $\hat{H_{\text{ex}}}$ of all molecules. It can be written as:

$$\hat{H} = \hat{H}_{\text{in}} + \hat{H}_{\text{ex}}. \tag{3.19}$$

The internal interactions can be described by the transition energies of the single molecules E_0 and the above noted D-term. They enter into the diagonal elements of $\hat{H}$:

$$\hat{H}_{\text{in}} = \sum_n (E_0 + D)|n\rangle\langle n|. \tag{3.20}$$

The non-diagonal elements are related to the excitonic coupling J_{mn} between the molecules:

$$\hat{H}_{\text{ex}} = \sum_m \sum_{n\neq m} J_{mn}|m\rangle\langle n|. \tag{3.21}$$

In the simplest case, this coupling can be treated within the point dipole approximation, wherein the coupling J_{nm} between two molecules n and m can be calculated by:

$$J_{nm} = \frac{f_{0\nu\prime}}{4\pi\epsilon_0}\left(\frac{\vec{\mu}_n \cdot \vec{\mu}_m}{r^3} - 3\frac{(\vec{\mu}_n \cdot \vec{r})(\vec{\mu}_m \cdot \vec{r})}{r^5}\right). \tag{3.22}$$

Here $\vec{\mu}_n$ and $\vec{\mu}_m$ denote the transition dipole moments of the molecules m and n, and $\vec{r}$ denotes the vector between the centers of mass of the two molecules. The factor $f_{0\nu\prime}$ scales the pure dipole interaction by the Franck-Condon factor of the respective state of the uncoupled molecule.

By solving the eigenvalue problem for the complete Hamiltonian-matrix $\hat{H}$ one obtains the eigenvalues ϵ_k and the eigenvectors $\vec{c_k} = \begin{pmatrix} c_{1,k} & c_{2,k} & ... & c_{n,k} \end{pmatrix}$. While the eigenvalues represent the excitation energies of the excited states, the eigenvectors contain the contributions of the molecules to the aggregate wavefunctions.

The collective transition dipole moment of the excited states μ_k, and the respective collective oscillator strengths F_k, can be calculated as a sum of the individual transition dipole moments μ_n weighted by their coefficients $c_{n,k}$:

$$\mu_k = \sum_n^N c_{n,k}\mu_n, \tag{3.23}$$

$$F_k = |\mu_k|^2. \tag{3.24}$$

The collective oscillator strength F_k depends strongly on the signs and the symmetry of the coefficients $c_{n,k}$ of the wavefunction. For the case that all $c_{n,k}$ exhibit the same sign, i.e. for a wavefunction without node-planes, the transition dipole moment of such a state scales approximately with $\mu_k \propto \sqrt{N}$ [140]. The corresponding oscillator strength then scales with $F_k \propto N$, where N denotes the number of coupled molecules in the aggregate [140]. This increase of the collective oscillator strength with respect to the oscillator strength of a monomer is frequently called exciton superradiance. For alternating signs of the coefficients of the wavefunction $c_{n,k}$ or anti-symmetric wavefunctions ϕ^k, the coefficients cancel each other out and the respective states become subradiant or completely dark.

The position of the super- or subradiant states inside the manyfold of the k-states, i.e., the exciton band is determined by the packing and the interactions of the transition dipoles of the molecules inside the aggregate. Fig. 3.7 illustrates this dependence for two extreme cases of packed linear chains. For attractive coupling between the transition dipoles, like it is the case for J-aggregates, it is energetically favorable if the coefficients $c_{n,k}$ of the wavefunction have the same sign. Therefore states with high oscillator strength are located at the bottom of the exciton band. In the opposite case of repulsive coupling, which is typically the situation in H-aggregates, it is energetically unfavorable if the coefficients $c_{n,k}$ of the wavefunction have the same sign. States with high oscillator strength can therefore be found at the top of the exciton band [76].

With increasing number of molecules in an aggregate also the density of excitonic states in the aggregate increases. Thereby states with high oscillator strength get energetically closer, so that

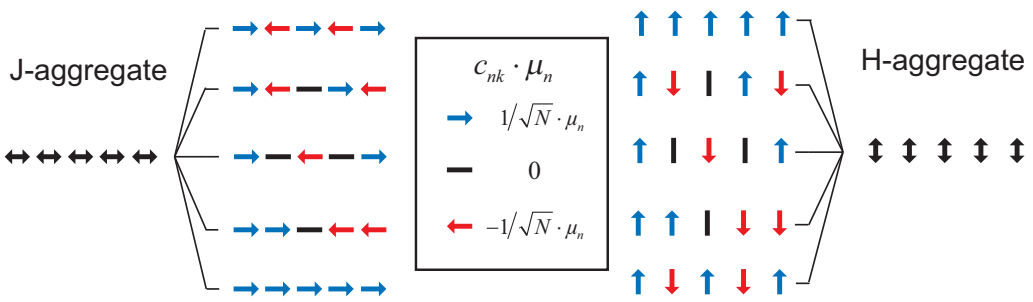

Figure 3.7: *Excitonic coupling in linear molecular aggregates. The packing of the molecular transition dipoles determines the coupling of the molecules. For the J-aggregate the transition dipoles couple attractively, therefore it is energetically favorable if all molecules have the same phase (sign of $c_{n,k}$). This is marked by all dipole vectors pointing in the same direction. For the H-aggregate the dipoles couple destructively, therefore it is energetically favorable if the molecules have an alternating phase. The states with high oscillator strength are located at the low energies for J-aggregates and at high energies for H-aggregates. For better visibility positive $c_{n,k}$ values are colored blue and negative values are colored red. Note that the $c_{n,k}$ are real numbers.*

in the limit of an infinite aggregate only a single bright state remains. The observation of multiple bright excitonic states, especially in absorption is related to finite size effects [16].

Experimentally, superradiance can be either measured by the reduction of the radiative lifetime τ_r of an excitonic state with respect to the monomer [71, 72, 81, 85, 86], or, as in the present work, by the enhancement of the pure electronic transition I_{00} with respect to transitions to the vibrational levels of the electronic ground state I_{01}. Here the superradiant enhancement factor η_{SR} can be directly determined from the aggregate emission spectrum since the decay rate of the transitions into vibrational levels of the ground state is not affected by the excitonic coupling [84]. η_{SR} can thus be directly extracted from the fluorescence spectrum by use of the following formula:

$$\eta_{SR} = I_{00} / \left(\frac{I_{01}}{f_{01}} \right). \tag{3.25}$$

Here I_{00} denotes the intensity of the pure electronic 0-0 transition, I_{01} denotes the intensity of a transition into a vibronic level of the electronic ground state, and f_{01} denotes the Franck-Condon-factor of the 0-1 transition. For details on the exact procedure it is referred to Appendix A.2.

For the experimental observation of superradiance in the fluorescence spectrum, the respective superradiant states have to be (thermally) populated after the optical excitation and the vibronic and excitonic relaxation. This is especially the case for J-aggregates since here the respective states are located at the bottom of the excitonic band and are thus thermally accessible.

The temperature dependence of the oscillator strength $F(T)$ of the aggregate can then be explained by the thermal population $p_k(T)$ of the superradiant and subradiant states k according to a Boltzmann distribution with the Boltzmann constant k_B:

$$p_k(T) = \frac{\exp(-E_k/k_B T)}{Z} \quad \text{with} \quad Z = \sum_k \exp(-E_k/k_B T) \tag{3.26}$$

$$F(T) = \sum_k p_k(T) F_k. \tag{3.27}$$

To obtain the theoretical superradiant enhancement factor $\eta_{\mathrm{SR}}^{\mathrm{theo}}$, the calculated oscillator strength of the aggregate F^{agg} (Eq. 3.24) again needs to be normalized with respect to the oscillator strength of the monomer F^{mono}

$$\eta_{\mathrm{SR}}^{\mathrm{theo}} = F^{\mathrm{agg}} / F^{\mathrm{mono}}. \tag{3.28}$$

The so obtained value of η_{SR} is equivalent to the frequently used coherence size of the exciton N_{coh} ($\eta_{\mathrm{SR}} = N_{\mathrm{coh}}$). The different name however accounts for the different physical picture that is connected with the described model. In the established picture [78, 140], the exciton is coherently delocalized over many molecules at low temperatures. With increasing temperature this coherence is disturbed and the exciton localizes. For that reason N_{coh} is typically reduced at elevated temperatures. In the present model the exciton is always delocalized over the complete aggregate. The temperature is then responsible for an increasing population of higher excited states that have a different oscillator strength dependent on the nodes of their excitonic state wavefunctions. Therefore dependent on the distribution of states with high and low oscillator strength across the exciton band, both a temperature dependent rise and drop of the superradiant enhancement can be explained.

3.2.4 Experimental techniques

In the present work fluorescence spectroscopy (FL) was used to measure the emission spectrum and fluorescence excitation spectroscopy (FLE) was used to measure the excitation spectrum. In the case of isolated molecules or a molecular monolayer, i.e. for a sample of infinitesimal thickness, the excitation spectrum equals the absorption spectrum [127]. A detailed description of the experimental setup used for the optical spectroscopy can be found in Chapter 4.1.2.

The FL spectrum can be measured by illuminating the sample by monochromatic light of a wavelength shorter than the one corresponding to the 0-0 transition, that means by light of a wavelength that can be absorbed by the vibronic modes of the excited state. This is typically done by a laser, since it is highly monochromatic and enables high illumination densities due to the available intensity and focusing capability. After vibrational relaxation the emitted photons are collected and monitored by a spectrometer. The obtained spectrum includes the pure electronic 0-0 transition and the resolved vibronic modes of the electronic ground state.

The largest advantage of FL is the absence of a background signal. This enables the detection of small amounts of emitters without problems due to the high signal to noise ratio. A drawback of the method is however its crucial dependence on the FL quantum yield ϕ_{FL} of the investigated sample

$$\phi_{\mathrm{FL}} = \frac{k_{\mathrm{r}}}{k_{\mathrm{nr}} + k_{\mathrm{r}}}. \tag{3.29}$$

If the decay rate of the non-radiative decay channels k_{nr} is significantly higher than the decay rate of the radiative decay channel k_{r}, no fluorescence occurs, and hence no FL spectra can be measured. This case applies for example for molecules adsorbed directly on metal surfaces, where fast fluorescence quenching takes place [141]. Also molecules with heavy atoms, which have a

high probability to undergo inter system crossing and to form long lived and spectrally shifted triplet states have a low FL quantum yield [126]. A second aspect that one should always be aware of is that only the emitting species are detected by FL measurements. These can also be defects or minority species, at which the excitation gets trapped before emission and which do not necessarily represent the majority species in the investigated sample [126].

For the measurement of the absorption spectrum fluorescence excitation spectroscopy is used. Here the sample is illuminated by a variable monochromatic light source and the integral fluorescence signal is measured as a function of the excitation wavelength λ_{exc}. Under the assumption that the quantum efficiency of the fluorescence ϕ_{FL} is independent from the excitation wavelength, the detected fluorescence signal is directly proportional to the absorption at this specific excitation wavelength. The experimental resolution of this method is independent from the spectrometer and defined entirely by the spectral width of the excitation light source. For this reason, usually tunable lasers with narrowed linewidths are used for excitation.

Of course also the FLE is a background free method and only applicable for fluorescent samples. However different from the FL spectrum, the measured FLE spectrum represents all absorbing species of the sample quantitatively. At least under the assumption of a quantum efficiency independent from the excitation wavelength.

By measuring the spectrally resolved fluorescence signal as a function of the excitation wavelength, spectrally different emitting species can be distinguished by a variation of the detection wavelength λ_{det}. This can be used to measure the absorption spectrum of different species independently from each other.

3.3 Optical microscopy

Light microscopy aims at the optical magnification of structures that are too small to be seen by the human eye. Besides the pure magnification of structures also the obtained contrast is important. For that reason in addition to simple bright field illumination, a variety of other methods exist that enhance the contrast and give access to additional information. Frequently used techniques are for example dark field-, phase contrast-, fluorescence-, and polarization microscopy.

In the present work bright field and fluorescence microscopy were used to image mesoscopic surface structures on a sample and the fluorescence of molecules that were adsorbed on that sample. For this purpose an incident light microscope was built that uses the same objective for both illumination and observation of the sample. A detailed description of the construction of this microscope and its specialties is given in Appendix A.4.

For the optical imaging, particularly the obtained imaging resolution is of interest. It depends partially on the quality of the optical components of the microscope, but is finally and inherently limited by the diffraction limit of the used light. According to the Abbe limit [142, 143], this means that the resolution depends on the collection angle α of the front lens of the microscope, the wavelength of the used light λ, and the refractive index n of the medium that is present between

the front lens of the microscope and the imaged object. The resolution or the smallest distance d of a periodic grating that can be optically resolved is then given by:

$$d = \frac{\lambda}{2 \cdot n \sin(\alpha)} = \frac{\lambda}{2 \cdot \mathrm{NA}} \quad \text{with} \quad \mathrm{NA} = n \sin(\alpha). \tag{3.30}$$

Here NA denotes the numerical aperture of the front lens of the microscope.

A peculiarity of the microscope that is used in the present work is that it images the sample through a glass window. This window acts like a cover slip or more generally like a parallel plate in the optical path and induces spherical aberration that reduce the maximum achievable resolution. This needs to be corrected especially for high NA microscope objectives. Detailed information on this issue can be found in Ref. [144].

4 Experimental

4.1 Experimental setup and procedures

The experiments of this work were carried out in an ultra high vacuum chamber. This was positioned next to an optical table and was equipped with a glass head for spectroscopic investigations of the samples prepared under UHV-conditions. The experimental setup is schematically shown in Fig. 4.1 with the UHV chamber on the right side and the optical table on the left side. Only the latest configuration of the optical setup that was used for the single molecule spectroscopy is shown. A drawing of the former optical setup that was used for the investigation of the condensed phase of PTCDA on KCl(100) can be found in Ref. [46].

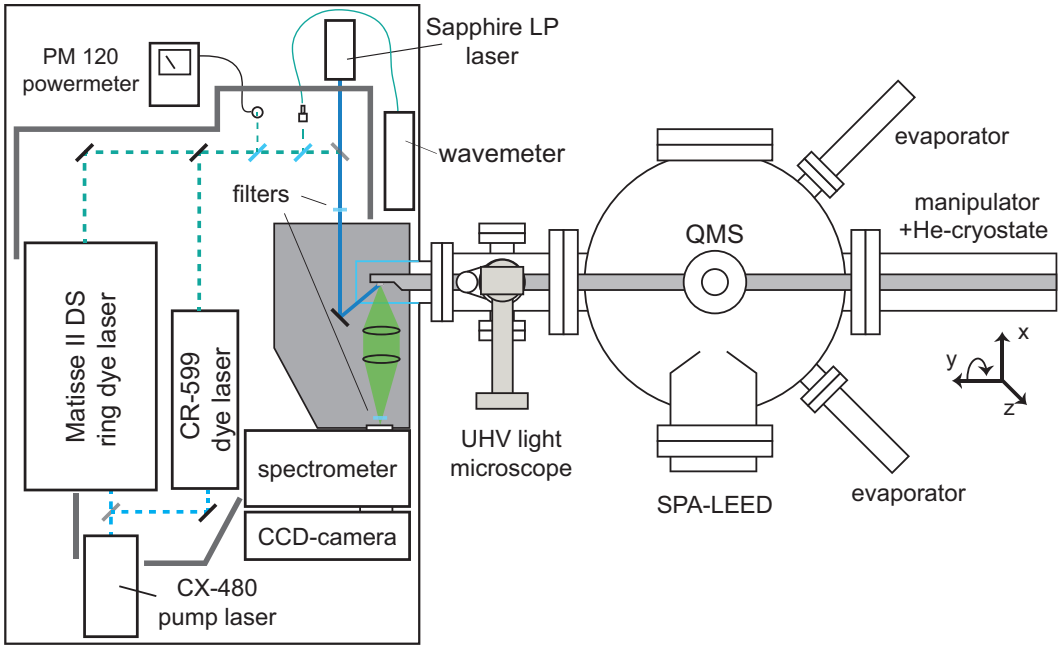

Figure 4.1: *Schematic drawing of the experimental setup. Only the latest optical setup that was used for the single molecule spectroscopy is shown. The drawing is not true to scale.*

4.1.1 UHV system

The stainless steel vacuum chamber was pumped by several pumps to reach ultra high vacuum conditions. Namely, a rotary pump, a turbo-molecular pump, an ion pump, a titanium sublimation pump, and an diffusion pump were used. In this configuration the chamber reached a base pressure of $1.5 \cdot 10^{-10}$ mbar after 48 h bake-out at 150 °C.

The experiments were carried out on a Ag(100) single crystal that was mounted to a long travel manipulator with a continuous-flow liquid helium cryostat. The sample mounting was optimized for low temperatures and good accessibility. A detailed description of the construction of the sample mounting can be found in Appendix A.4. The sample crystal was heated by thermal radiation from a filament and additional electron impact heating. Temperatures between 6 K and 1000 K were achieved. While the higher temperatures (> 70 K) were measured by a type-K thermocouple directly at the sample, the lower temperatures were measured by a Si-diode (DT-670B-SD, LakeShore Cryotronics) that was positioned 70 mm detached from the sample on the sample mounting. The low temperature measurement was experimentally confirmed by a second Si-diode mounted testwise directly on the backside of the sample. It was found that the temperatures measured on the sample mounting were only less than 0.5 K lower than the sample temperature, even at the lowest temperatures.

The UHV-chamber was equipped with a sputtergun (PU-IQE 11/35, Specs Nanotechnology) for the cleaning of the sample surface by Ar-ion bombardment. For the deposition of alkali-halides and organic molecules, home-built thermal evaporators with crucibles made of ceramic or glass were used. A quadrupole mass spectrometer (QMG 422, Pfeiffer Balzers) was used to monitor the molecular fluxes.

The structure and the quality of the prepared sample were controlled by a modified SPA-LEED apparatus (Omicron). Compared to the original apparatus here the diameter of the channeltron aperture was increased to 300 μm (originally: 100 μm) in order to increase the counting rate on the expense of the instrumental resolution. This is favorable for the investigation of organic structures due to the smaller necessary electron current on the sample and the thereby reduced radiation damage. SPA-LEED measurements were typically performed with a sample current of 1 nA. A second modification concerns the maximum deflection voltage of the SPA-LEED controller. This was decreased from former 150 V to 50 V in order increase the voltage stability at the more frequently used lower voltages.

A home-built incident light microscope was installed at the chamber in order to be able to image the sample under UHV conditions. The microscope could be operated in brightfield or fluorescence mode. For the imaging a thermoelectrically cooled 12-bit CCD camera (SensiCam 670 KS 3618, PCO) was used. All optical components of the microscope were placed outside the vacuum and the sample was imaged through a 1.75 mm thick glass window. For the highest magnification and resolution a 40$\times$ microscope objective with an ultra large working distance and a correction collar for the thickness of the glass window was used (Olympus CDPlan 40 PL, NA 0.5). In this configuration a maximum resolution of 0.7 μm was achieved. A very detailed description of the construction and the used optics of the microscope can be found in Appendix A.4.

4.1.2 Optical setup

For the spectroscopic measurements the sample was transferred into the glass head (quartz glass, VP63Q, Vacom) at the end of the vacuum chamber (cf. Fig. 4.1). There it was illuminated under an angle of $\approx 45\,^{\circ}$ with focused monochromatic laser light. The laser spot on the sample was

$\approx$ 0.2 mm in diameter. The fluorescence from the sample was collected and parallelized by an achromatic lens (glass: N-BAF10/SF10, $f = 100$ mm, $\varnothing = 50.8$ mm, NA $= 0.22$). Then it was focused by a second achromatic lens (glasses: N-BK7/SF2, $f = 200$ mm, $\varnothing = 50.8$ mm) onto the entrance slit of the spectrometer. In front of the entrance slit different optical long pass filters (e.g. $\lambda_{\mathrm{LP}} = 490$ nm, $\lambda_{\mathrm{LP}} = 520$ nm) were used in order to block scattered excitation light from the sample. For the exclusion of external background light the glass head, the lenses, and the entrance slit were placed inside a modular box made of black oxidized aluminum plates. The spectrometer (SpectraPro 2300i, $f = 0.3$ m, $f/\# = 4$, Acton) allowed the use of three blazed gratings with 300, 600 and 1200 grooves per millimeter. It was equipped with a liquid nitrogen cooled CCD-camera (Spec-10:100-BR(LN)) that was operated at -120 °C. Typically, the grating with 300 grooves per millimeter was used for the recording of overview spectra. For the accurate determination of spectral linewidths or the separation of different signals however the higher resolving grating with 1200 grooves per millimeter was used.

For the excitation of the sample different laser systems were used. For the measurements on the condensed PTCDA phase a combination of an Ar^+-laser (Innova Sabre R Ion Laser, DBW 15/3, Coherent) and a modified standing wave dye laser (CR-599, Coherent, modification by Radiant Dyes) was used. The Ar^+-laser had several laser lines in the blue and green range of the visible spectrum. For the FL spectroscopy in particular the lines at $\lambda = 476.5$ nm and $\lambda = 457.9$ nm were used. The tunable standing wave dye laser was used for the FLE measurements. It was operated with Coumarin 498 as a laser dye and was pumped by the 457.9 nm line of the Ar^+-laser. At a pumping power of 2 W the laser was continuously tunable between 495 nm and 545 nm at a minimum laser output of 30 mW. The dye-laser was equipped with a three-plate birefringent filter and had a linewidth of 1 cm^{-1}.

In order to suppress plasma lines from the Ar^+-laser, the excitation light of the fluorescence measurements was filtered by narrow single wavelength band-pass filters. The excitation light of the dye-laser was filtered by short-pass filters ($\lambda_{\mathrm{SP}} = 510$ nm, $\lambda_{\mathrm{SP}} = 530$ nm) in order to block fluorescence background signal from the dye jet in the detection range of the spectrometer. During the FLE measurement about 10% of the light of the dye-laser was reflected to a power meter (PM120, Thorlabs) for a later power normalization. For a reduction of the overall intensity on the sample and thus for a reduction of undesirable photo-induced processes the excitation power was reduced by neutral density filters. Typically, laser intensities between 15 $\mathrm{W/cm}^2$ and 150 $\mathrm{W/cm}^2$ were desirable on the sample.

For the single molecule experiments the previous laser setup was replaced. The new setup is depicted on the very left side of Fig. 4.1. The FL spectra of the sample were measured for control purpose with a low power optically pumped semiconductor laser (Sapphire LP USB CDRH, Coherent) that emits at 458.0 nm (50 mW). For the (single molecule) FLE measurements a tunable ring laser (Sirah Matisse II DS) was used. This ring laser is equipped with a reference cavity for frequency stabilization and can achieve a linewidth of < 250 kHz rms in frequency stabilized operation. Again Coumarin 498 was used as the laser dye. In this setup the laser dye was pumped by an optically pumped semiconductor laser (Genesis CX 480 4000, Coherent) at 480 nm and 4 W excitation power. Stable and tunable single mode operation with a laser output > 50 mW was

obtained between 495 nm and 525 nm, with a customized output coupler. The ring laser was operated non-frequency stabilized with a linewidth < 20 MHz rms, which was sufficiently narrow for the performed single molecule experiments in this work. The wavelength of the laser was monitored by a wavelength meter (HighFinesse Angstrom WS/6). Again the laser power was measured parallel to the FLE measurement with the power meter. Again, optical short pass filters ($\lambda_{SP} = 510$ nm, $\lambda_{SP} = 530$ nm) were used to block fluorescence from the dye jet. Neutral density filters were used to reduce the excitation power on the sample and thereby to minimize the laser induced broadening by a saturation of the optical transition. For the single molecule experiments laser powers between 30 mW/cm^2 and 1500 mW/cm^2 have been used.

For the acquisition of the FL spectra the spectrometer and the CCD-camera were controlled with the commercial software WinSpec32. FLE spectra were recorded with the aid of self-written LabView programs. A detailed description of the used LabView programs can be found in Appendix C.1. FL spectra were typically recorded with exposure times between 0.1 and 10 s and with up to 100 accumulations. For the FLE measurements the FL spectra were not accumulated.

At a CCD temperature of -120 °C thermal noise can be neglected. The signal to noise ratio is limited by the readout noise of the A-D converter. Readout noise was minimized by use of the 'low noise' port, an operation frequency of the A-D-converter of 100 kHz, and the setting 'Gain $= 2$'. This resulted in a background signal of $\approx$ 100 counts per read out operation that was almost constant across all read out pixels.

The spectrometer was always used in the spectroscopy mode, which means that vertical pixels of the CCD-array were hardware binned. For the single molecule FLE measurements additionally each 20 of those pixel rows were binned horizontally in order to increase the signal to (readout) noise ratio at the expense of the spectral information. A further binning of pixels would have made it impossible to exclude remnant excitation light from the spectra and was therefore not applied. In order to get the highest spectral resolution in the FL measurements, the entrance slit of the spectrometer was kept as narrow as possible (0.005 mm). Contrarily, for the single molecule FLE measurements it was opened widely (2 mm) for maximal light collection.

In order to calibrate the wavelength scale of FL and FLE measurements, additional reference spectra of a calibration lamp (Xe-lamp, Hg(Ar)-lamp, Newport) were measured for each experiment. In case of the single molecule FLE measurements the spectral position of the laser according to the wavemeter measurement was used. The measured spectra were not corrected for the sensitivity of the spectrometer. This can largely be neglected, since the combined wavelength dependence of the spectrometer and the CCD is rather flat on the scale of the measured FL spectra. For FL spectra that were plotted against wavenumbers instead of the wavelength, the relative spectral intensity was corrected for the different pixel sizes of the both scales by multiplying the measured intensity by an factor of λ^2.

4.2 Sample preparation

4.2.1 Preparation of the Ag(100) crystal

The experiments of this work were carried out on the (100)-surface of a Ag single crystal. The surface was prepared in three consecutive steps: First the crystal was heated up to 850 K for 3 minutes in order to desorb weakly bound adsorbates, e.g., thin alkali halide films. In the second step the surface was cleaned from remnant strongly bound adsorbates by sputtering with Argon ions at an energy of 1000 eV and at an Argon pressure of $2.5 \cdot 10^{-5}$ mbar. The sample was sputtered for each 10 minutes in $+45\,^{\circ}$ and $-45\,^{\circ}$ tilted positions with respect to the surface normal. Typically a sputtering current of 4-6 μA was measured at the sample. In the last step the crystal was annealed for one hour at 1000 K in order to induce a healing of the sputtered and hence roughened surface.

The microscopic quality of the Ag(100) surface was controlled by measuring the width of the SPA-LEED profiles. At an electron energy of 81 eV, which corresponds to an in-phase condition with respect to monoatomic Ag steps for the (0,0) spot, a FWHM of $\Delta k_{||} = 0.01$ Å^{-1} was obtained for the respective spot. This corresponds to a correlation length of $L = 2\pi/\Delta k_{||} = 600$ Å and can be considered to be very good value for a metal crystal.

With aid of the light microscope the crystal surface was investigated on a scale of several hundreds of micrometers. On this scale the crystal was not ideally flat as suggested by the LEED pattern but showed macroscopic defect structures and a corrugation. These results are presented in Chapter 7 and Appendix A.4.

4.2.2 Epitaxial growth of KCl(100) films

For the growth of thin, high quality KCl films on the former prepared Ag(100) surface the KCl was thermally evaporated from a ceramic crucible at a temperature of $\approx$ 830 K. The KCl flux was monitored with the QMS at $m/z = 74$. The crucible temperature was thermally adjusted to achieve a constant growth rate of 1 atomic layer per 10 minutes in the QMS. This growth rate was initially calibrated by M. Müller with a quartz micro balance. During the evaporation the sample surface faced the evaporator and was held at an elevated temperature of 520 K. This induced a rapid diffusion of KCl molecules on the surface and a let the film growth nucleate particularly at the silver step edges [14]. At these temperatures the grown films have high structural quality and are widely extended. A drawback of the elevated sample temperature is however a partial dewetting of the film from the metal sample that is not present at lower temperatures. Typically 5-10 atomic monolayers (ML) were grown. After deposition the sample was held at the elevated temperature of 520 K for 20 minutes in order to smoothen the film and increase its terrace widths.

At the described conditions highly ordered films with an average terrace width of $L = 350$ Å were obtained. This was determined from the width of the KCl(1,0) LEED profiles at an electron energy of 95.6 eV. This energy corresponds to an anti-phase condition for the KCl(1,0) spots with respect to monoatomic KCl steps. It is estimated that the films are closed after the deposition of $\approx$ 5 ML of

KCl, so that no free Ag regions remain. This can be deduced from the dampening of the intensity of the Ag spots of the LEED pattern (about 2 orders of magnitude) due to the deposition of the KCl layers.

4.2.3 Deposition, growth, and site selection of PTCDA on KCl(100)

The PTCDA molecules were deposited from a glass crucible by thermal evaporation. The molecular flux was monitored with the QMS at $m/z = 392$. The deposition rate was calibrated with respect to thermal desorption experiments of PTCDA multilayers grown on Ag(100) [115]. Dependent on the desired coverage different deposition parameters were used.

Monolayer phase: For the growth of an ordered monolayer of PTCDA on KCl(100) the sample was slightly cooled to 260 K. This temperature was found to be a good compromise between a high mobility of the molecules, which is favorable for the formation of large domains on the one side and the tendency for a dewetting of the molecules from the KCl surface on the other side. The deposition rate of the molecules was chosen very low, about 1 ML per 25 minutes (crucible temperature $\approx$ 810 K). This was done in order to keep the concentration in the mobile PTCDA phase low and generate only few nucleation centers. After deposition the sample temperature was kept at 260 K for 90 minutes to heal domain boundaries between different PTCDA domains and improve the overall order on the sample.

The average lateral size of the grown PTCDA domains was again determined from the LEED profiles. It was found that the described preparation protocol leads to a broad geometric domain size distribution that contains few very large domains and many smaller domains. The average domain size was determined at $L \approx 160$ Å. Details on the obtained distribution and its determination from the LEED profiles can be found in Appendix A.2.

Isolated and single molecules: For the preparation of a (strongly) diluted phase of isolated molecules the sample was cooled to 20 K. At this temperature the molecular diffusion is hampered so that the molecules stick statistically distributed on the KCl terraces [8]. At this temperature the molecules arrange themselves on well defined adsorption sites [8]. An even lower sample temperature during deposition was consciously avoided, since it leads to a mixture of unfavorable meta stable adsorption geometries [46].

Dependent on the desired final coverage of molecules on the sample, the temperature of the PTCDA crucible was varied. For typical coverages between 10^{-4} ML and 10^{-2} ML a crucible temperature of 780 K and a corresponding deposition rate of $5 \cdot 10^{-3}$ ML per minute were used. After deposition, a migration of the molecules to energetically favorable step edge sites could be induced by an annealing the sample for 20-30 minutes at 150 K [17].

For coverages that were sufficiently low for the optical detection and separation of single molecules ($< 2 \cdot 10^{-6}$ ML) much lower deposition rates and therefore also lower crucible temperatures were necessary. This however required a different procedure for the heating of the PTCDA crucible. In a first step the PTCDA crucible was heated to a temperature ($\approx$ 700 K) at which a significant signal was obtained in the QMS. In the second step the temperature was reduced to the

point ($\approx$ 600 K), at which no signal was measurable anymore. Only then the sample was turned towards the evaporator and the molecules were deposited for 1 s. It was not possible to achieve these minimal deposition rates by directly setting the crucible temperature to the final deposition temperature. In this case typically no molecules were deposited on the sample. The minimal detectable signal in the QMS resembled a deposition rate of $1.5 \cdot 10^{-4}$ ML per minute. The true deposition rate for a crucible temperature of 600 K was expected to be lower than this. Due to the limited sensitivity of the QMS, only an upper limit of $< 2 \cdot 10^{-6}$ ML for the coverage on the sample can be given here.

5 Finite size effects in the PTCDA/KCl brickwall phase

This chapter presents optical and structural results obtained for a single PTCDA monolayer on the KCl(100) surface. Parts of these results have been published and can be found in Appendix A.1 and A.2. These are especially those results that deal with the finding of an anomalous temperature dependence of the superradiant enhancement in the FL spectrum that was obtained for samples prepared according to an optimized preparation protocol. In the following these results and the theory that was applied for their understanding will be briefly summarized and supplemented by further unpublished results obtained from FLE measurements. Ahead, a short overview on the optical spectra and the sizes of the grown structures will be given. The obtained results will be compared to the results described precedingly by M. Müller et al. [14, 16].

5.1 Spectral and structural overview

The brickwall structure of PTCDA on KCl(100) has already been investigated by several previous studies, so that both the structural and optical properties are well documented [13, 14, 16]. In the present work, these properties have been re-investigated using an optimized preparation procedure (cf. Chapter 4.2.3) and at lower experimental temperatures. Fig. 5.1 gives an overview on the FL and FLE spectra that were measured in the present work. A real space model of the commensurate brickwall superstructure is given in the inset. As known from the literature [13, 16], the FL spectrum shows a strong superradiant pure electronic transition, which can be seen from a single intense peak at 19600 cm^{-1} and widely suppressed but persistent vibrational modes (< 18750 cm^{-1}). The electronic transition in the FLE spectrum is asymmetrically broadened [16] and has the identical transition energy as the electronic peak in the emission spectrum. Compared to the spectra of isolated molecules the spectra of the brickwall phase are red-shifted by 400 cm^{-1}.

These observations are qualitatively identical to those of the preceding studies and correspond to the typical properties of J-aggregates. Important for the present work were however especially the quantitative properties, i.e. the superradiant enhancement factor η_{SR} of the pure electronic transition in the emission spectrum and the shape and width of the asymmetric broadening of the electronic transition in the absorption spectrum. These properties are related to the finite sizes of the investigated aggregates and are thus strongly affected by the preparation conditions.

The results of a detailed investigation of these properties will be discussed in the following chapters on the basis of two different samples. While sample A was prepared according to the new

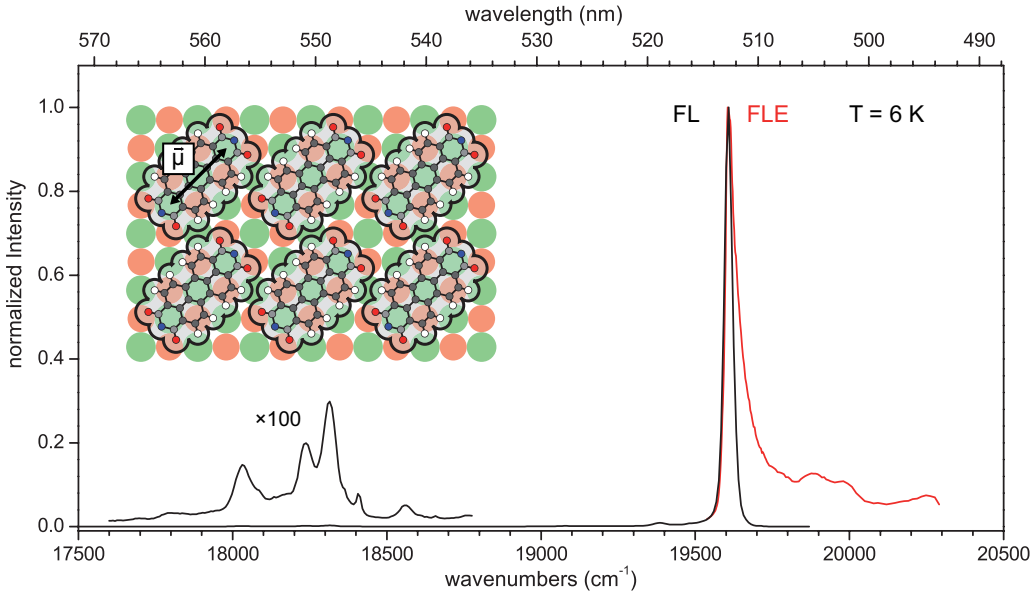

Figure 5.1: *Fluorescence and fluorescence excitation spectra of the PTCDA/KCl brickwall phase. Both spectra were acquired at a sample temperature of* 6 K*. For the FL spectrum the sample was excited by laser beam (*30 mW*) at* $\lambda_{\text{exc}} = 476$ nm*. For visibility, the fluorescence signal of the suppressed vibrational modes was magnified by a factor of* 100*. For the FLE spectrum the sample was excited by a tunable dye laser (*$\approx$ 50 mW*), the induced fluorescence signal was detected in the range between* 17856 cm^{-1} *and* 18542 cm^{-1}*. Inset: Real space model of the commensurate PTCDA/KCl(100) brickwall structure the transition dipole moment* $\vec{\mu}$ *of PTCDA is oriented along the long molecular axis. For further details see text.*

optimized preparation protocol, the data of sample B was taken from the work of M. Müller, who used the same experimental setup but different preparation conditions [14, 16].

For the theoretical description of the aggregates of both samples, rectangular aggregates of the size $N_x \times N_y$ molecules with unpolar aggregate boundaries were used, just like the aggregate depicted in the inset of Fig. 5.1. Such unpolar aggregate boundaries are energetically favorable compared to polar boundaries and therefore presumably favored during the growth [14]. Hints for the presence of aggregates on the sample that are terminated in this way can be deduced also from the profile form of the LEED spots (cf. Appendix A.2).

Differences between the investigated samples are particularly the average aggregate size and aggregate size distribution. These were in both cases determined by SPA-LEED. While for sample B a narrow Poissonian aggregate size distribution with an average size of 7×7 molecules was found to explain the data [16], for the present sample A, a much broader geometric aggregate size distribution with an average size of 12.4×12.4 molecules was found. This distribution contains many small and few large aggregates. For information on the detailed two dimensional SPA-LEED analysis and the obtained geometric size distribution it is referred to Appendix A.2.

5.2 Temperature dependence of the superradiant enhancement

5.2.1 Experimental results

The superradiant enhancement factor η_{SR} (in the literature typically called N_{coh}) was determined for a series of FL spectra as a function of the sample temperature in the range between 6 K and 220 K. This was done by the method described by Spano [84] via the intensity ratio of the enhanced 0-0 transition with respect to an effective 0-1 transition. Details on this procedure can be found in Appendix A.2.

The temperature dependence of η_{SR} of the two samples A and B is depicted in Fig. 5.2. Particularly two observations can be made: First, the maximal achieved value of η_{SR} of sample A is more than twice as large (≈ 50) than the one of sample B (≈ 20). This can be explained to be an effect of both the reduced minimal achieved temperature (6 K vs. 20 K) and the larger average aggregate size on the sample.

The second observation is a slight rise of the $\eta_{SR}(T)$ curve of sample A at the lowest temperatures, which leads to a maximum of η_{SR} at the finite temperature of $T_{max} = 10$ K. This observation is remarkable since such a temperature behavior has never been experimentally observed before for J-aggregates and cannot be explained in the established theoretical picture of a temperature induced localization of the exciton [78, 80, 89, 145].

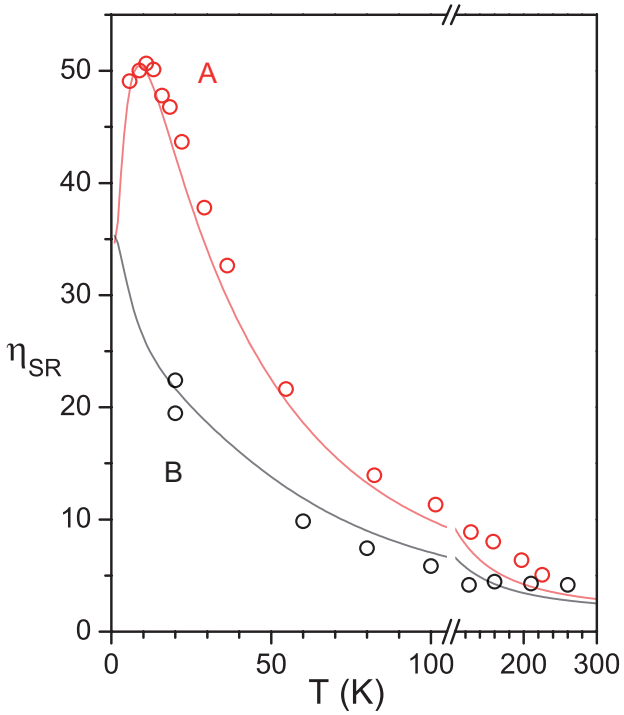

Figure 5.2: *Temperature dependence of the superradiant enhancement factor η_{SR}. The open circles show experimental data for two different samples A and B. While sample A corresponds to an optimized preparation condition, the data of sample B was taken from an earlier work [16]. The solid lines are theoretical simulations based on model aggregate size distributions determined from SPA-LEED. For further details see text.*

5.2.2 Theoretical explanation by aggregates with unpolar boundaries

In the present work the initial rise of the $\eta_{SR}(T)$ curve was described by a theory based on finite size effects that was provided by A. Eisfeld. This theory had been already successfully applied for the description of the asymmetric line broadening of the FLE of sample B in a work by M. Müller et al. [16] and was slightly extended in the present work to describe also the temperature dependence of the superradiant enhancement factor η_{SR} (cf. Chapter 3.2.3). The applied theory distinguishes from the more usual theories used for the explanation of superradiance. In contrast to these theories the exciton does not localize due to temperature but remains always extended over the entire aggregate. The temperature dependence of the superradiance is then explained by the thermal population of excited excitonic states with higher or lower transition strength (TS). Within this theory a rise in the $\eta_{SR}(T)$ curve can be explained very intuitively by the thermal depopulation of a dark or weakly radiant ground state and the thermal population of a superradiant excited state.

The presence of a dark ground state in a J-aggregate is however far from typical. Therefore the conditions for its occurrence have been theoretically investigated and will be explained in the following. The reason for the occurrence of dark states at the bottom of an exciton band can be found in the extended coupling between the molecules in a brickwall aggregate. An overview on the respective dipole-dipole couplings in the brickwall structure is given in Fig. 5.3. It can be seen that all nearest neighbor couplings in the brickwall structure are attractive, which leads in general to the typical J-aggregate behavior. Decisive for the occurrence of a dark state at the bottom of the exciton band is however the coupling between next nearest neighbors perpendicular to the orientation of the transition dipoles. This dipole-dipole interaction is repulsive and H-aggregate like. Therefore it can be energetically stabilized by the formation of (few) node planes in the excitonic wavefunction perpendicular to the repulsive interaction. These convert the repulsive interactions into attractive ones but reduce the transition strength of the respective excitonic states.

Indeed such node planes have been found in the calculated wavefunctions of the excitonic ground states ($k = 1$) of rectangular aggregates of the size $N_x \times N_y$ with unpolar boundaries. This is illustrated in Fig. 5.4 for a series of aggregate sizes. Due to the node planes the obtained collective transition strengths (TS) of all depicted excitonic ground states are reduced compared to the classical situation in a linear J-aggregate with the same number of coupled molecules N. This can be understood to be an effect of the mutually canceling of the coefficients c_{nk} of molecules on opposite sides of a node plane. For an anti-symmetric wavefunction this directly results in a dark state TS $= 0$ (30×10 aggregate), since all coefficients c_{nk} cancel each other out. For a symmetric wavefunction the transition strength is only partially reduced. This reduction however increases with an increasing number of node planes (40×10 aggregate vs. 20×10 aggregate).

For better comparability the transition strength of the depicted excitonic ground states in Fig. 5.4 are given in units of the transition strength of an individual molecule and normalized to the number of molecules in the aggregate. Values between TS $= 0$ and TS $= 0.4\ N$ were obtained for the depicted states. For comparison TS $= N$ is the theoretic value for a linear aggregate of N

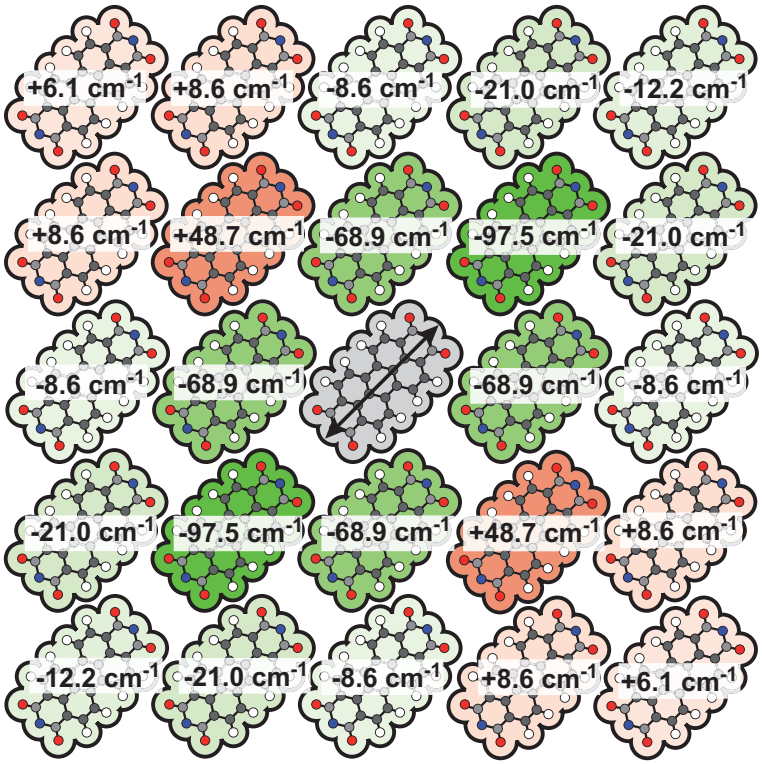

Figure 5.3: *Calculated dipole-dipole interactions in the PTCDA brickwall structure. All nearest neighbor couplings are attractive (negative sign, green). In the direction perpendicular to the transition dipoles also significant repulsive interactions exist (positive sign, red). The given values were calculated in the point-dipole approximation with a molecular transition dipole moment* $\mu = 7.4$ *Debye and a lattice constant of the unit cell* $a = 12.6$ Å.

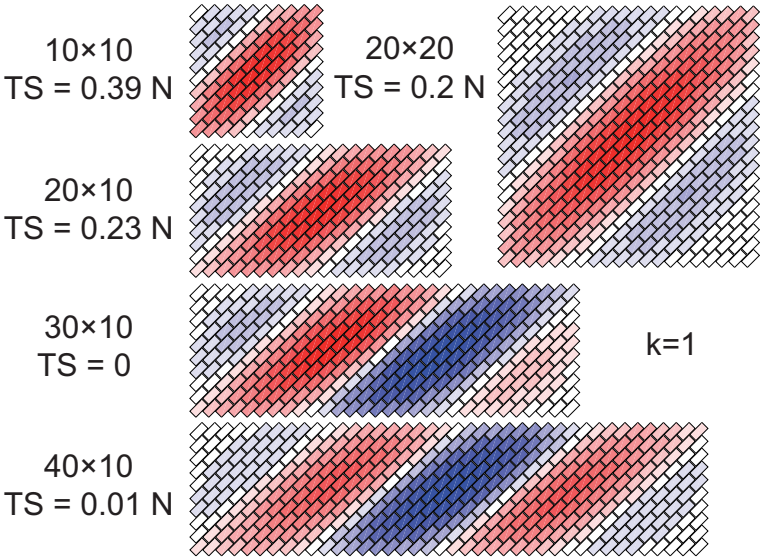

Figure 5.4: *Calculated excitonic wavefunctions of the lowest excitonic state* $k = 1$ *for a series of rectangular brickwall aggregates of the size* $N_x \times N_y$ *molecules. All wavefunctions have node planes perpendicular to the transition dipole axis of the molecules. These reduce the transition strength (*TS*) of the respective state. The TS becomes zero for anti-symmetric wavefunctions and gets smaller with increasing number of node planes. The distance between the node planes of the wavefunctions depends mainly on the shorter of the two lengths of the aggregate in x and y direction.*

molecules with periodical boundary conditions [140, 146]. In the more comparable case of a linear chain with open boundaries still TS $= 0.81\ N$ is obtained [89]. The transition strength of the depicted brickwall aggregates is therefore significantly reduced.

The spacing of node planes in the excitonic wavefunctions depends on the interplay of the cumulative attractive and repulsive couplings along the corresponding directions of the aggregate. In the present aggregate shape these directions are both 45° rotated with respect to its boundaries. Therefore both the cumulative couplings in the direction of attractive coupling and in the direction of repulsive coupling are limited in the same way by the length of the shorter axis of the aggregate. A further elongation of an aggregate thus leads to the formation of further node planes. In contrast to an elongation of the shorter aggregate axis, the distance between the node planes increases. This can be seen by a comparison of the wavefunctions of the 10×10 aggregate and the 20×20 aggregate in Fig 5.4.

In conclusion, dark or weakly radiant excitonic ground states can be explained for the investigated aggregate shapes by the presence of node planes in the excitonic wavefunctions. Quadratic aggregates exhibit a superradiant ground state with a transition strength only partially reduced by the occurence of few node planes. The number of node planes, however, increases with the elongation asymmetry of the aggregates, which leads to dark or weakly radiant excitonic ground states of highly elongated aggregates.

5.2.3 Simulation of the experimental data

Based on this understanding, the next step was to model the experimental $\eta_{\mathrm{SR}}(T)$ curves. For this reason also the transition strengths and energies of all excitonic states ($k > 1$) have been calculated for the respective aggregates. An exemplary absorption spectrum of a 30×10 aggregate and its corresponding $\eta_{\mathrm{SR}}(T)$ curve are depicted in Fig. 5.5. Calculated absorption spectra and $\eta_{\mathrm{SR}}(T)$ curves of further aggregate shapes and sizes are described in Appendix A.1. The depicted absorption spectrum shows that despite the darkness of the ground state, strongly superradiant states are located within the first few excited states ($k \approx$ 2-10) and can be thermally populated already at low temperatures. The $\eta_{\mathrm{SR}}(T)$ curve of this aggregate shows the predicted initial rise and a maximum at a finite temperature. For more quadratic aggregates a maximum at zero temperature and a monotonic decay is obtained instead (cf. Appendix A.1). At higher temperatures, in both cases more and more dark excited states are populated so that η_{SR} decreases monotonically and reaches $\eta_{\mathrm{SR}} = 1$ at infinite temperatures.

Despite the qualitative agreement of the theoretical temperature behavior with the measured one, the quantitative dependence of the temperature dependence fits not to the experimental data (Fig. 5.2). This concerns both the position of the maximum of the curve and its subsequent decay. The maximum occurs at lower temperatures and the decay of the calculated curve is faster than the experimental one. Both deviations are present independent from the size and shape of the calculated aggregates. They can be traced back to the simplicity of the used model that includes only pure excitonic states and neglects the presence and possible inter-mixture with low energetic vibrational states of the molecules and phonons of the aggregate. These would lead to additional

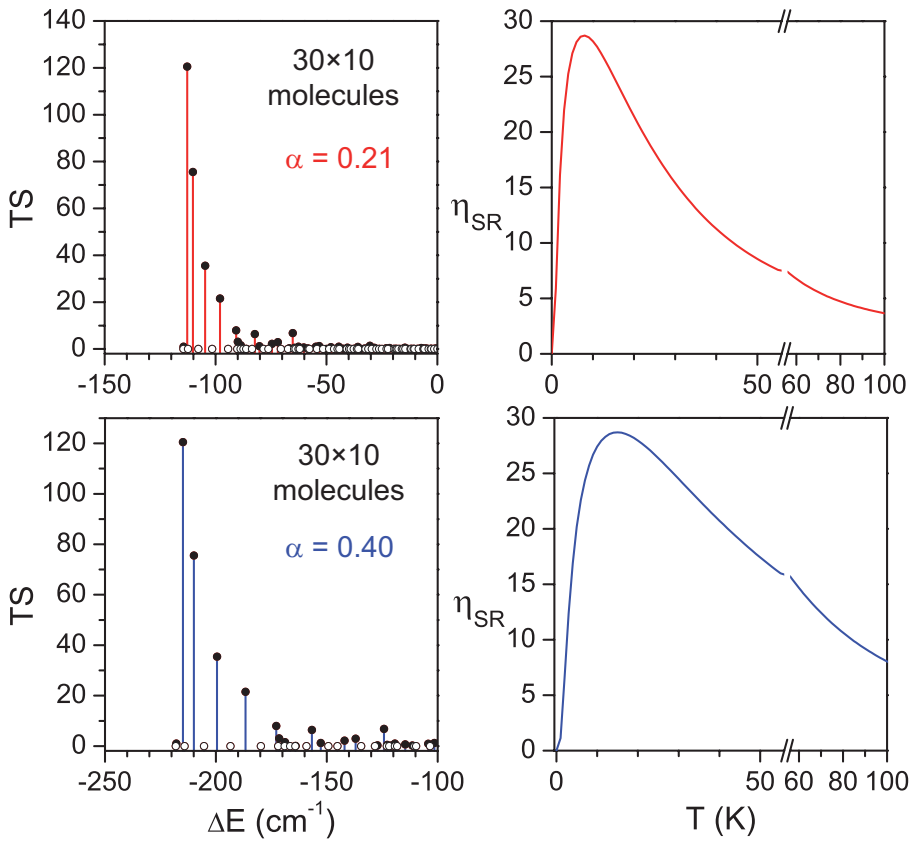

Figure 5.5: *Calculated absorption spectra and $\eta_{SR}(T)$ curves for a 30×10 aggregate. The absorption spectra are depicted on the left side and the corresponding $\eta_{SR}(T)$ curves can be found on the right side. Bright states with* TS > 0 *are marked with filled dots and dark states with $TS = 0$ are marked with open dots. ΔE denotes the calculated stabilization energy of the excitonic state k with respect to an isolated monomer. Please note the different energy axes in the upper and lower panel. The dipole-dipole coupling in the top panels was scaled with $\alpha = f_{00} = 0.21$, which is the oscillator strength of the electronic transition of the individual PTCDA molecule. In the bottom panel a larger value of $\alpha = 0.4$ was used. This spreads the absorption spectrum and thereby effectively shifts the maximum of the $\eta_{SR}(T)$ curve. For further details see text.*

transition strength at higher excitation energies and thus shift the maximum and the subsequent decay of the $\eta_{SR}(T)$ curve to higher temperatures [147].

In the present work these effects have been compensated in an effective manner by scaling the coupling strength J between the molecules by an artificial value $\alpha = 0.4$ that replaced the Franck-Condon factor $f_{0\nu'}$ in Eq. 3.22 and was higher than the typically used oscillator strength of the 0-0 transition of the individual molecule $f_{00} = 0.21$ (cf. Chapter 3.2.3). The resulting spectrum and $\eta_{SR}(T)$ curve is plotted in Fig. 5.5 below the original one. The larger factor spreads the absorption spectrum and thereby shifts the maximum of the $\eta_{SR}(T)$ curve to higher temperatures. The value of $\alpha = 0.4$ was determined empirically and fits the calculated curves to the experiment. For a more detailed description of the calculations and the limitations of the used model it is referred to Appendix A.2.

The experimental temperature dependence of η_{SR} was finally simulated based on the calculated temperature dependence of η_{SR} ($\alpha = 0.4$) for different aggregates. For this purpose the aggregate size distribution determined from SPA-LEED was used. The exact procedure of this simulation

and the used formulas can be found in Appendix A.1. Additionally, also a simulation for the different aggregate size distribution of sample B was performed. Both simulated curves are drawn as solid lines in Fig. 5.2 and fit the experimental data points in good proximity. It can be seen that the curve of sample B in contrast to the one of sample A has no maximum at finite temperatures, which is because of the different underlying size distribution that contains mainly smaller and more quadratic aggregates.

5.2.4 Aggregates with polar boundaries

Up to this point the finding of node planes in the wavefunctions of the excitonic ground state of brickwall aggregates was only demonstrated for the very special case of rectangular aggregates with unpolar boundaries. It is however of interest if equal phenomena can also be observed for other aggregate geometries and boundary conditions. This is especially important since a rise of the superradiant enhancement factor η_{SR} with temperature was observed so far only in the present experimental work but not in former experiments on brickwall aggregates [70, 148] and could thus be a pure effect of the special aggregate geometry.

For this reason also a second type of brickwall aggregates has been theoretically investigated. These are rectangular aggregates with polar boundaries. A real space model of such an aggregate is depicted in Fig. 5.6. Additionally the wavefunctions of the excitonic ground states of different aggregate sizes are shown similar to Fig. 5.4. It can be seen, that also for this geometry node planes can be found in the excitonic ground states of some aggregates (20×10, 20×20). Again these node planes are formed perpendicular to the direction of the repulsive interactions. Different from aggregates with unpolar boundaries however now also ground states without any node planes can be observed (10×10, 10×20). These have the symmetry that is typically expected for the ground state of a classical J-aggregate and also their transition strength (TS $\approx 0.7N$) is comparable to the one obtained for classical linear J-aggregates.

These observations can be explained by the different orientation of the transition dipoles with respect to the main axes of the aggregate. Different from the aggregates with unpolar boundaries, here the main axes of the attractive and repulsive dipole couplings are oriented along the main y and x axes of the aggregate, respectively. Therefore a 10×20 aggregate has comparably more attractive interactions and less repulsive interactions than a 20×10 aggregate. Node planes in the excitonic ground state occur only for those aggregates, in which the cumulative repulsive interactions have a comparably large contribution compared to the attractive ones. A simple prediction of the symmetry of the excitonic ground state wavefunction based on the ratio x/y of the aggregates axes x and y can however not be given. This can be seen from the comparison of a 10×10 and a 20×20 aggregate. Although they both exhibit the same ratio x/y, the symmetries of their excitonic ground state wavefunctions differ. For an accurate prediction presumably further factors like the coupling strengths in the different directions and the decrease of the coupling strength with the distance between the coupled molecules would be needed to be taken into account.

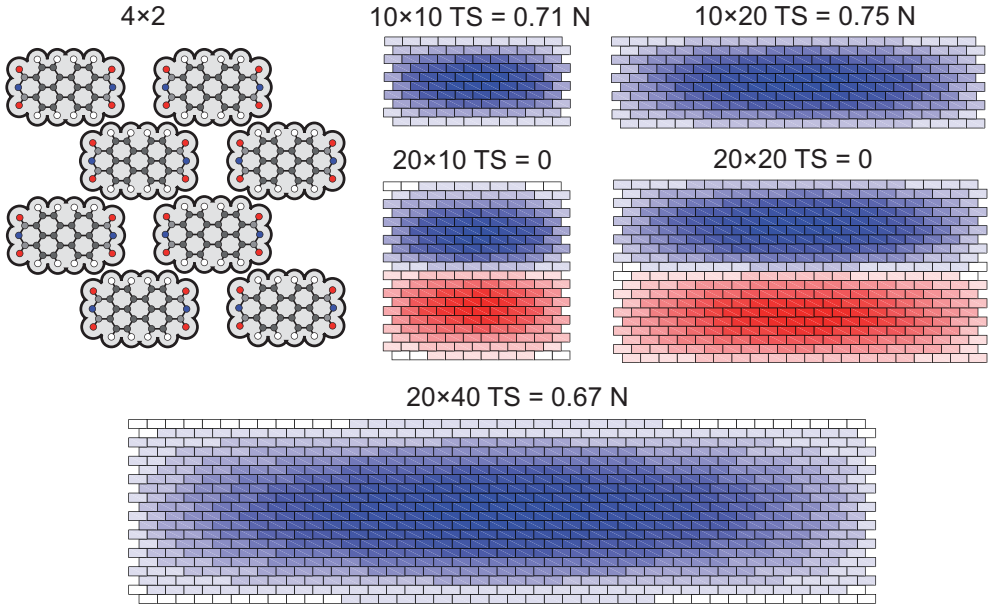

Figure 5.6: *Calculated excitonic wavefunctions of the lowest excitonic state $k = 1$ for a series of rectangular brickwall aggregates with polar boundaries. A real space model of a 4×2 aggregate of this geometry is shown in the top left corner. Some of the wavefunctions show node planes perpendicular to the repulsive dipole-dipole interactions. The ground states of other aggregate shapes show no node planes and high transition strength as it is expected for typical J-aggregates. For further details see text.*

Finally these results show that the occurrence of a dark or weakly radiant ground state in a finite size aggregate is not only possible for a single special boundary condition. It however strongly depends on the exact coupling situation and the interplay of the cumulative attractive and repulsive couplings. This finding may be used in the future to tune the interactions and sizes of aggregates in order to obtain J-aggregates with either stronger superradiance or higher excited state lifetimes. While the first would be favorable as strong and sharp emitters, the second could be beneficial for the decay free transport of excitons, e.g. in a solar cell.

5.3 Evaluation of the asymmetry of the FLE spectra

5.3.1 Comparison of different FLE spectra

Besides the superradiance that was described and explained in the previous chapter also the FLE spectra and especially the asymmetric broadening of the pure electronic transition depends on the finite aggregate sizes on the sample. This had already been demonstrated in detail in the publication of M. Müller et al. [16] for sample B and was here re-investigated for the present sample A. In Fig. 5.7 two excitation spectra A1 and A2 measured for sample A at a temperature of 6 K are depicted together with the FLE spectrum of sample B that had been measured at 20 K. All spectra show the characteristic asymmetric broadening of the 0-0 line on the high energy side, that is both the result of several bright excitonic states present at the lower energies of the excitonic spectrum of finite size J-aggregates, and of the distribution of aggregate sizes [16].

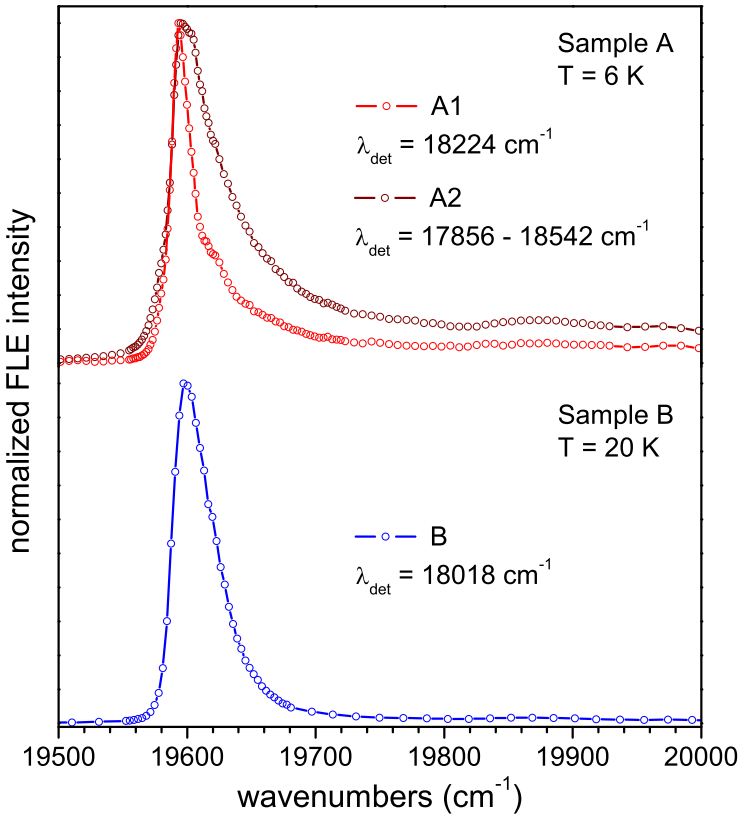

Figure 5.7: *Comparison of the 0-0 line shape in the FLE spectra of the two samples A and B. The spectra were measured for the respective lowest achievable experimental temperatures of* 6 K *for sample A and* 20 K *for sample B. Different from sample B, the spectra of sample A (A1, A2) depend strongly on the choice of the detection wavelength* λ_{det} *and are thereby broader (A2) or sharper (A1) than spectrum B. For further details see text.*

Different from the measurements of M. Müller, the excitation spectrum of sample A depends strongly on the choice of the detection window. For spectrum A1 the intensity variation of a single pixel of the CCD (at a spectral position of 18224 cm^{-1}) is plotted as a function of the excitation wavelength. For spectrum A2 the intensity variation of a much broader detection window (100 pixels, 17856 - 18542 cm^{-1}) of the same measurement is plotted. As can be seen from Fig. 5.7, this influences the width and form of the spectra dramatically. The full width at half maximum (FWHM) of the 0-0 line for the narrow detection window of A1 is considerably smaller (20.2 cm^{-1}) than the one of sample B (40.0 cm^{-1}). Moreover, an additional shoulder can be observed on its high energy side at 19630 cm^{-1}. In contrast, using the broad detection window (A2) results in a 0-0 line that is even broader (47.0 cm^{-1}) than the one of sample B. In both cases the increased or decreased broadening concerns only the high energy side of the spectrum, the low energy side and the position of the peak maximum of the spectra are almost identical to that of sample B .

Important for the understanding of these observations are the differences in the excitonic stabilization energy between aggregates different in size. The excitonic stabilization energy refers to the red-shift of the excitonic ground state of an aggregate with respect to excited state of a monomer

due to the attractive coupling of transition dipoles. It increases with the aggregate size and saturates in the limit of large aggregates. For example, it is only -77 cm^{-1} for an aggregate containing 4×4 molecules and already -123 cm^{-1} for an aggregate containing 20×30 molecules.

The dependence on the detection wavelength can now be understood primary as an effect of the broad (geometric) aggregate size distribution of sample A. For the new preparation conditions, a variety of aggregate sizes is present on the surface, ranging from very small to very large aggregates (cf. Appendix A.2). The difference between the excitonic stabilization between these extrema is considerable so that the absorption energies of their lowest excitonic states differ strongly from each other. As a result the fluorescence signals of the respective aggregates are shifted by these amounts. Therefore, dependent on the position and width of the fluorescence detection window, different fractions of the aggregate size distribution contribute to the FLE spectrum. For the broad detection window (spectrum A2) all aggregate sizes within the distribution contribute to the spectrum leading to the broader peak in the FLE spectrum. For the narrow detection windows (like given by only one a single pixel, Spectrum A1) a smaller fraction of the aggregates contributes to the spectrum. In case of the specific detection wavelength of spectrum A1 (18224 cm^{-1}) mainly the larger aggregates of the distribution contribute to the FLE spectrum. This can be seen from Fig. 5.8. At the detection energy of spectrum A1 mainly the vibrational peak of the orange FL spectrum in the lower left panel of Fig. 5.8 contributes intensity to the FLE spectrum and is responsible for the sharp maximum of spectrum A1. This orange spectrum contains the most red-shifted FL peaks of this vibrational mode during the FLE measurement which resemble the most stabilized and therefore largest aggregates. For further details on Fig. 5.8 it is referred to the following Chapter 5.3.2.

For comparison, the variation of the FLE spectrum with the size and position of the detection window was checked also for the dataset of sample B (not shown). There no dependence on the detection window was observable. This can primarily be explained by the much narrower Poissonian aggregate size distribution [16]. In this distribution, the excitonic stabilization and the position of the FL signals of all aggregate sizes are very similar. Additionally, these measurements were performed at a higher sample temperature of 20 K, which slightly broadens the FL signals and leads to an overlap of the FL signals of the different aggregate sizes. Therefore, at the resolution of the spectrometer the FL signals of the different aggregate sizes of the distribution were indistinguishable and no variation with the choice of the detection window occurred.

5.3.2 Variation of the FL spectrum during the FLE measurements

The different excitonic stabilization of different sized aggregates can be observed in the FL spectra that were measured during an FLE measurement. Fig. 5.8 shows the evolution of the FL signal of sample A during the FLE measurement as a function of the excitation wavelength. The detected fluorescence signal in the regime of the vibronic modes (17800 - 18500 cm^{-1}) is depicted in the lower left panel. The corresponding excitation light of the dye laser scanning through the asymmetrically broadened 0-0 line of the absorption spectrum is shown in the lower right panel. As a reference, the FL spectrum for an excitation wavelength of 476.5 nm (cf. Fig. 5.1) and the FLE spectra for the broad detection window (cf. spectrum A2 in Fig. 5.7) are depicted in the top panel.

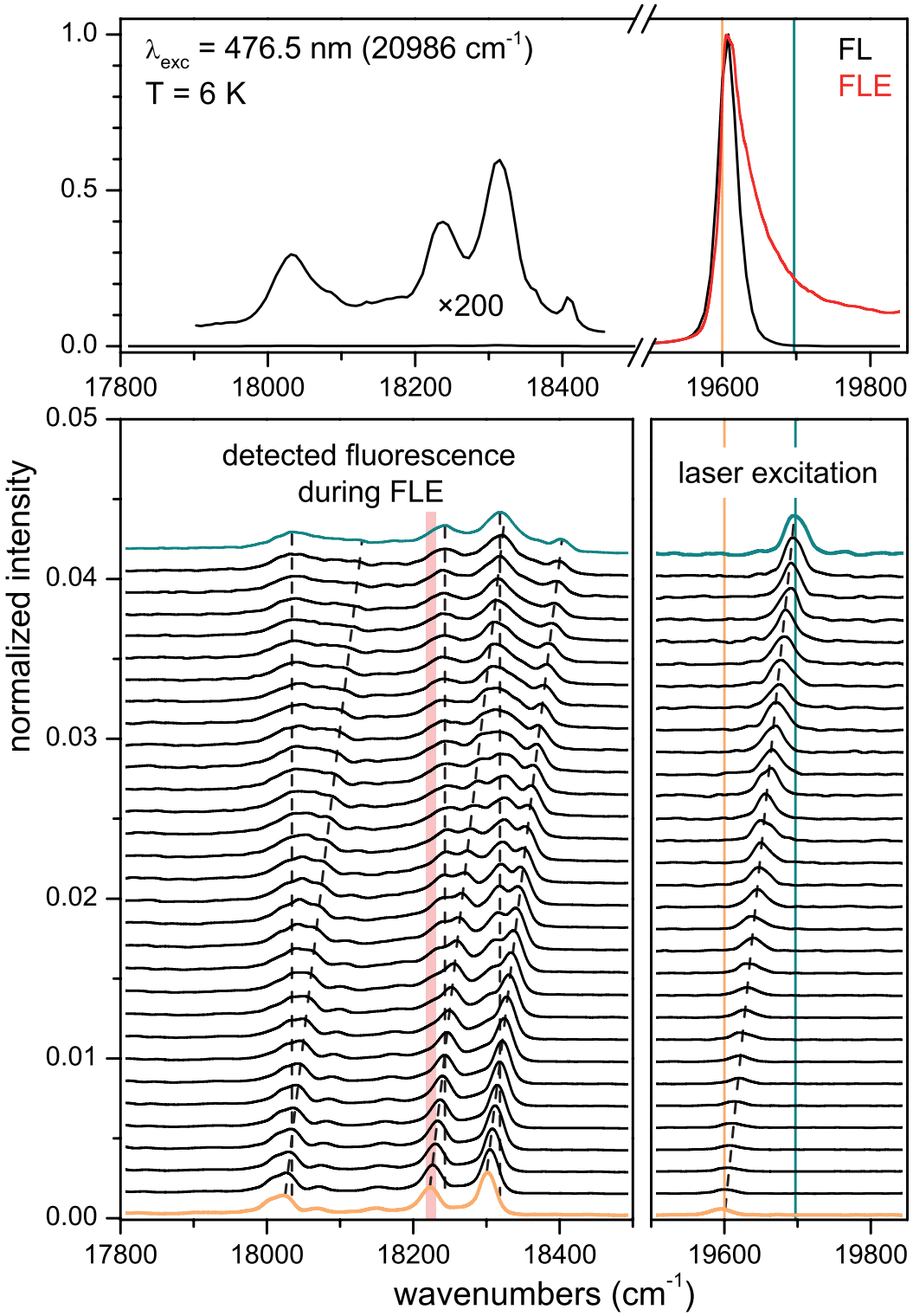

Figure 5.8: *Variation of the FL spectrum during the FLE measurement. In the lower left panel a series of FL spectra that were measured for varying excitation wavelengths λ_{exc} are shown. The spectra are normalizes with respect to the maximum intensity and vertically shifted for clarity. The corresponding signal of the varied excitation laser is plotted in the lower right panel, the laser signal is broadened by the spectrometer. Some of the vibrational peaks in the FL spectra shift Raman-like with the excitation wavelength, while other peaks remain stationary. These are marked with guidelines for the eye, respectively. For a reference of the respective absorption and emission positions the measured FL ($\lambda_{exc} = 476.5$ nm) and FLE spectra (Fig. 5.7 A2) are plotted in the upper panel. The narrow detection window of FLE spectrum A1 (not shown) is highlighted by a light red bar at* 18224 cm^{-1}. *For further details see text.*

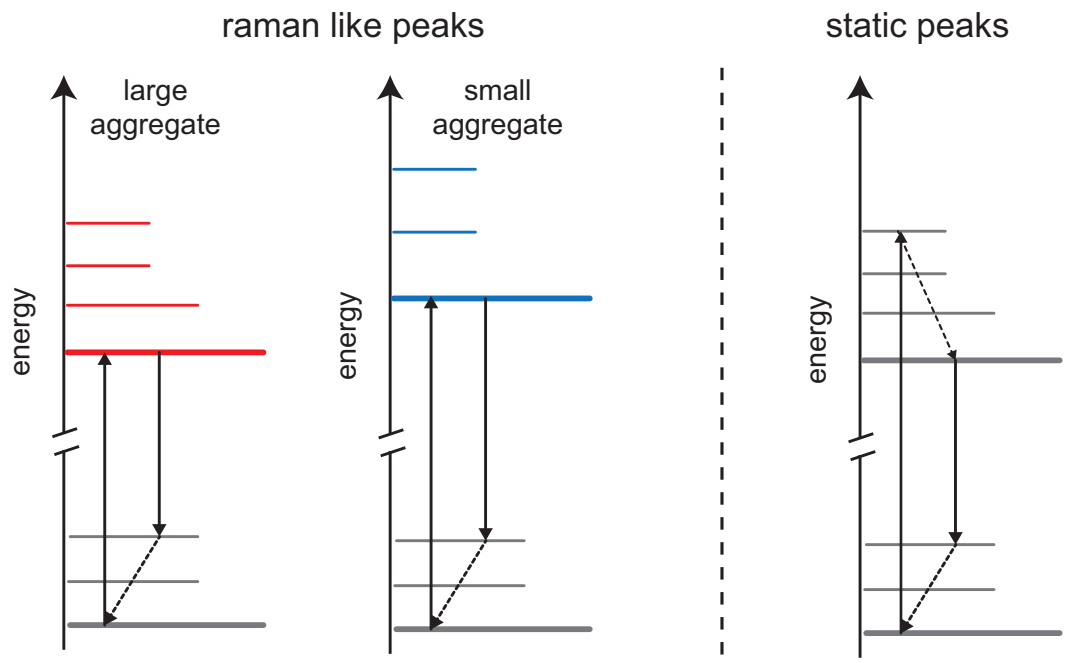

Figure 5.9: *Schematic energy level diagrams illustrating the origin of Raman-like and static fluorescence peaks during the FLE measurement. The Raman-like peaks are explained by a selective excitation of the excitonic ground states of differently sized aggregates dependent on the excitation energy. Larger aggregates can be excited at lower excitation energies and emit fluorescence light of lower energy. For smaller aggregates both the excitation energy and the emission energy are higher, between these extrema there is a continuum of different aggregate sizes. The static peaks are explained by the excitation of higher excitonic excited states and the non-radiant decay in the excitonic ground state before emission. For further details see text.*

The excitation wavelength was varied between 19600 cm^{-1} (at the low energy edge of 0-0 line of the FLE spectrum, orange spectrum) and 19700 cm^{-1} (after the main absorption peak of the FLE, blue spectrum). As can be seen the detected fluorescence signal varies strongly with the excitation wavelength. Two groups of peaks can be identified: The peaks of the first group shift their spectral position parallel to the excitation wavelength (Raman-like). The peaks of the second group appear only for excitation energies higher than $\approx$ 19630 cm^{-1} and do not shift with a variation of the excitation energy (static). Compared to the Raman-like peaks the corresponding static peaks are red shifted. The fraction of the static peaks increases with increasing excitation energy.

The different mechanisms leading to the Raman-like and static peaks are exemplary sketched in Fig. 5.9. The Raman like peaks can easily be explained by the broad continuous distribution of aggregate sizes present on the sample. Dependent on the excitation wavelength aggregates of different sizes absorb the excitation light. The fluorescence signal of the vibrational modes appears then red shifted by the vibrational energy. Since the vibrational energy is independent of the aggregate size, the shift of the respective peaks is directly parallel to the excitation wavelength. At the lowest excitation energies the largest aggregates absorb, at the highest excitation energies the smallest aggregates absorb, and in between these two energies the corresponding aggregate size of the continuum is selected.

The static peaks can be understood by remembering that the excitonic absorption spectrum of a single finite size aggregate consists of more than just a single transition with oscillator strength. Therefore, at higher excitation energies also higher excited excitonic states have some oscillator strength (cf. Fig. 5.5) and can absorb. After absorption, they decay into the ground state of the excitonic states because of the low temperature. Then the radiative decay back into the electronic ground state occurs, which is red shifted with respect to the excitation energy (vibrational energy + relaxation energy). With increasing excitation energies also the fraction of aggregates that absorb via higher excited excitonic states increases. Therefore also the fraction of the static signal increases. The position of the peaks remains mostly static however small deviations due to the varying subset of absorbing aggregates of the aggregate size distribution can be observed. In general, also the static peak would be expected to shift to higher energies with increasing excitation energy, since also the number of excited small and blue shifted aggregates increases. This could however not be observed, presumably due to a very dominant spectral contribution of larger red shifted aggregates to the static peaks.

No further pronounced changes in the FL spectra are observed for excitation energies higher than $\approx$ 19700 cm^{-1} (teal spectrum). Already at this excitation energy the majority of the aggregates contributes to the static peaks. Comparing this teal spectrum with the FL spectrum in the top panel of Fig. 5.8 it can be seen that the spectral shape and positions of the peaks in the two spectra are very similar to each other. From this agreement it is can be deduced that also for the FL experiment with an excitation wavelength of 476.5 nm (20986 cm^{-1}), i.e. far above the energy of the 0-0 transition, the majority of the aggregates of the sample was excited and contributes to the FL spectrum. Thus no undesirable spectral selection of a specific aggregate size/shape takes place and the assumption that all aggregates of the aggregate size distribution contribute to the measured $\eta_{SR}(T)$ dependency discussed in Chapter 5.2 is justified.

It should be mentioned that also an alternative explanation for the static peaks in the FL spectra exists. Generally, it is possible that an exciton migrates between neighboring aggregates. In this case the excitation on a smaller aggregate (less excitonic stabilization) could be transferred to a higher excited state of a larger neighboring aggregate (more excitonic stabilization) of same energy. Then again a non-radiative decay into the thermal ground state of the excitonic states occurs before the red shifted fluorescence occurs from the largest aggregates. This mechanism cannot be excluded. It was however shown by polarization dependent fluorescence spectroscopy that at least no exciton migration between 90° rotated aggregates occurs [16].

5.3.3 Simulation of the FLE spectra

Up to this point, the new findings concerning the FLE spectra of sample A could be explained on a qualitative basis under consideration of the presence of a broad geometric aggregate size distribution. In order to confirm these findings also quantitatively, the experimental FLE spectrum of sample A (spectrum A2) was simulated according to the procedure described for sample B in Ref. [16]. First, the excitonic absorption spectra of all aggregates of the type $N_x \times N_y$ with $1 \leq N_{x,y} \leq 100$ were numerically calculated. Here, for a start the inter-molecular coupling J was scaled with the

correct value of the oscillator strength of the electronic transition $\alpha = f_{00} = 0.21$. This value had been extracted from the monomer FL spectrum [8] and had also been used for the simulation of the asymmetric broadening in Ref. [16]. Likewise as in Ref. [16], site disorder was implemented in the calculation by the varying the individual transition energies of the monomers of the aggregate within a Gaussian distribution (27 cm^{-1}). This induces a broadening of the aggregate stick spectra that is partially reduced with an increasing size of the aggregate due to exchange narrowing [146].

The calculated spectrum for a single aggregate of the size 12×12 molecules, which corresponds to the average aggregate size of sample A, is depicted in the top panel of Fig. 5.10. The spectrum contains several separated absorption lines that have decreasing intensity towards higher energies. This behavior is typical for finite size aggregates and was found to be the main reason for the asymmetric broadening of the FLE spectrum of sample B [16].

By comparison of this single aggregate spectrum with the experimental FLE profile of sample A, it can however be seen that the width and shape of the envelope of the calculated absorption spectrum does not sufficiently describe the experimental profile, especially its high energy wing. This is different from the situation of sample B, but so far in agreement with the above finding of a broad aggregate size distribution. The so far not reproduced regions of the profile should rather be described by very large and very small aggregates of the distribution. These have absorption spectra that are red or blue shifted with respect to that of the 12×12 aggregate and could therefore describe the low energy and high energy wings, of the experimental profile.

In order to test this, the FLE profile was calculated by weighting and summing up the individual aggregate spectra according to the geometric aggregate size distribution with the expectation value $\Gamma_{x,y} = 12.4$ (cf. Appendix A.2). The resulting profile is depicted as a red line in the bottom panel of Fig. 5.10. Surprisingly, it does not fit the experimental profile and is by far too narrow on its high energy wing. This seems to be astonishing on the first sight, since the majority of the aggregates of the distribution is smaller than the 12×12 aggregate and hence exhibits a blue shifted absorption spectrum. On the second sight, these aggregates however contain significantly less molecules and have thus also significantly less transition strength than the less frequent but larger aggregates. In the end, the absorption spectrum is therefore dominated by those larger aggregates with high transition strength.

Nevertheless, the significant discrepancy between the simulated and the experimental FLE profile needs to be explained. One solution for this could be the use of a modified aggregate size distribution that contains a larger quantity of small aggregates. This approach is indeed possible and leads to a good agreement of the simulated and experimental profile (not shown). The modified size distribution however needs to contain several orders of magnitude more small aggregates (4×4 molecules and smaller) and thereby contradicts both the experimental LEED profiles and the observed maximum η_{SR} values.

Therefore, just like in Chapter 5.2.3, rather the simplicity of the applied model is supposed to be the limiting factor. The model is used to calculate pure excitonic states but neglects molecular vibrations. For the most molecular vibrations this simplification is justified, since their vibrational energy is much higher than the energy of the excitonic states with high transition strength. This

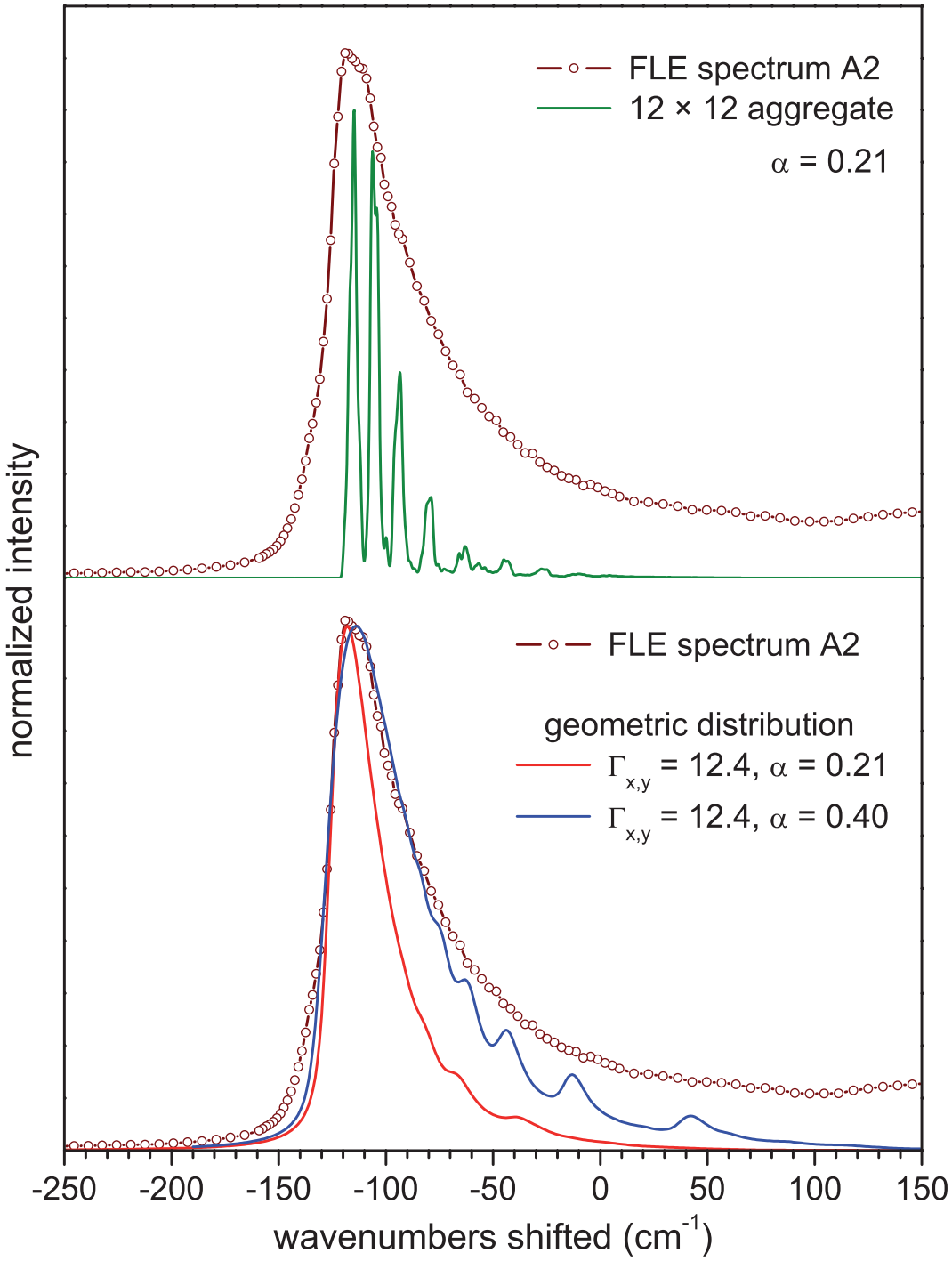

Figure 5.10: *Simulation of the experimental FLE of sample A. In the top panel the FLE spectrum A2 and the simulated absorption spectrum for a single aggregate of the size* 12×12 *molecules are shown. The coupling J between the molecules was scaled by* $\alpha = f_{00} = 0.21$ *and site disorder on the order of* 27 cm^{-1} *was introduced. The experimental FLE spectrum was spectrally shifted to the position of the calculated spectrum by the transition energy of the monomer* (-20000 cm^{-1}) *and the D-term* (≈ 270 cm^{-1}, *arbitrarily chosen). In the bottom panel simulated FLE profiles according to a geometric aggregate size distribution with* $\Gamma_{x,y} = 12.4$ *are shown. Despite the broad size distribution the calculation with* $f_{00} = 0.21$ *results in a much too narrow FLE profile and does not explain the experimental broadening. Again an increase of the scaling factor from* $\alpha = f_{00}$ *to* $\alpha = 0.40$ *compensates the lack of vibration induced transition strength at higher energies by effectively spreading the absorption spectrum. Both the experimental profile and the simulated profile for* $\alpha = 0.40$ *were shifted to the position of the simulated profile with* $\alpha = 0.21$. *For further details see text.*

is however not the case for the low energetic surface induced modes (50-200 cm^{-1}), that have been described by Paulheim et al. [19]. They are on a similar energetic scale as some of the bright excitonic states, which means that they can intermix. This intermixture would lead to a further redistribution of transition strength towards the vibrational modes, which results in additional transition strength at higher energies and is frequently termed 'intensity borrowing' [149]. This transition strength at higher energy induced by low energetic vibrations appears to be necessary to describe also the high energy wing of the experimental FLE profile of sample A.

Effectively the lack of transition strength at higher energies of sample A can again be compensated by scaling the coupling strength J (Eq. 3.22) with a value α larger than the oscillator strength of the electronic transition f_{00} (cf. Chapter 5.2.3). A simulation of the FLE spectrum based on a scaling factor $\alpha = 0.4$ that stretches the individual absorption spectra is depicted as a blue line in the bottom panel of Fig. 5.10, and it describes the width of the experimental spectrum in good proximity. For a more accurate description however more advanced calculations including molecular vibrations should be applied.

In conclusion the detailed evaluation of the FLE spectra has shown several effects that are related to the different aggregate size distribution of sample A compared to sample B. Especially the possibility to excite aggregates different in size selectively by the choice of the excitation wavelength is interesting and may have potential for future experiments on finite size molecular aggregates. From a quantitative comparison, especially the limitations of the used theoretic model became aware. These do not lead to problems in the description of sample B, but are decisive for the description of the present sample A. It became especially evident that besides the pure excitonic peaks also molecular vibrations need to be considered for a more accurate description of the absorption spectrum.

6 Optical single molecule spectroscopy of PTCDA adsorbed at KCl step sites

This chapter presents results on the high resolution spectroscopy of single PTCDA molecules at KCl step sites. A manuscript prepared for publication that concerns these results can be found in Appendix A.3. In the following the experimental approach and the major experimental findings are summarized and interpreted in a molecular picture. At the end of this chapter the limiting experimental factors, open questions, and suggestions for their solution are discussed.

6.1 Experimental approach

The spectroscopy of single PTCDA molecules on defined alkali halide surface sites has been the next step in a series of experiments that were concerned with the optical and structural properties of diluted PTCDA phases on alkali halide surfaces (cf. Chapter 2.4) [8, 14, 15, 17–19]. In the preceding experiments the high spectral resolution in combination with the structural order made it possible to obtain very detailed information on the interaction of molecules with specific surface adsorption sites. In addition also the influence that these interactions have on the molecular optical properties was studied (cf. Chapter 2.4).

Nevertheless, the information that can be extracted from the spectroscopy of an ensemble is limited, the measured spectra always resemble the averaged or superimposed signal of this ensemble of molecules, and the information on the individual molecules gets lost. The aim of the present work was therefore to separate the optical signals of the individual molecules from each other by application of high resolution single molecule fluorescence excitation spectroscopy. This technique facilitates to study the sharp optical absorption lines of single molecules independently from the signals of other similar but not identical molecules of the ensemble. Until now this technique has mainly been used for molecules embedded in solid hosts but never for molecules on a defined surface.

The goal of the present work was therefore to apply this high resolution spectroscopy method to molecules adsorbed at surface sites, measure their individual homogeneous absorption profiles, and test the possibilities of this method in a surface science experiment. Compared to the previous experiments mainly the laser setup for the fluorescence excitation measurements was changed (cf. Chapter 4.1.2). The detection apparatus, on the other hand, was so far only slightly modified by the construction of a black box for the exclusion of background light. As a sample system PTCDA molecules adsorbed at KCl step sites were investigated.

In order to separate the molecular absorption lines from each other, the spectral density inside the inhomogeneous broadening of the absorption spectrum needed to be reduced in several steps. First, the molecule density on the surface and inside the focus of the excitation laser was reduced by modified evaporation parameters (cf. Chapter 4.2.3). These lead to a surface coverage $< 2 \cdot 10^{-6}$ ML and between 400 and 40000 molecules in the focus of the laser (cf. Appendix A.3). In a second step, the spectral areas far off the center of the inhomogeneous broadened line have been measured since there the density of molecules with appropriate transition energies decreases.

Finally, the sample temperature and the excitation power of the laser were reduced as much as applicable. This was done in order to reduce a temperature and laser induced broadening of the single molecule absorption lines (cf. Chapter 3.2.2) that otherwise could result in a spectral overlap of neighboring molecular transitions.

6.2 Inhomogeneous profiles

6.2.1 Substructures of the inhomogeneous profile

Prior to the high resolution measurements of single molecules, the inhomogeneous broadening of PTCDA at KCl step sites has been reinvestigated by 'low resolution' FLE measurements. This was done in order to check for an influence of the reduced surface coverage or the reduced line width of the excitation laser on the spectra. Similar to earlier measurements of Paulheim et al. [18], the width and the shape of the FLE profile changed slightly between different preparations. Additionally, some of the measurements with reduced coverage and laser linewidth revealed a slight splitting of the inhomogeneous profile. This was interpreted to stem from a superposition of signals from molecules at two energetically minimally dissimilar adsorption sites (cf. Appendix A.3). An exemplary FLE profile that shows such a splitting is depicted in Fig. 6.1 and will be compared to an earlier measured profile from Paulheim et al. [18] in the following.

Despite the differences in coverage and the sample temperatures, the widths of both profiles are similar. Therefore it has been assumed that in both cases the same types of adsorption sites are populated and that the populated adsorption sites are independent from the surface coverage. The main difference between the measurements is therefore the above indicated small indentation at the profile of the recent measurement. This profile could be fitted by a sum of two Lorentzian peaks separated by 2 cm^{-1} resembling two different species. Fitting the profile and especially the indentation with a sum of two Gaussian profiles was however not successful.

Based on theoretical calculations and assumptions that have been described in Ref. [18] these contributions could be assigned to the *deep vacancy site* and the *deep vacancy site +1* of PTCDA at KCl steps, respectively. These were calculated to be the energetically most favorable step sites with an energetic difference of the binding energy of only 0.01 eV [18]. Structure models of these adsorption sites are given on the right side of Fig. 6.1.

It turned out, that the profile splitting was only observable due to the significantly reduced instrumental broadening $\Delta\nu_{\text{inst}}$ that was obtained by using the ring laser for excitation ($\Delta\nu_{\text{inst}} =$

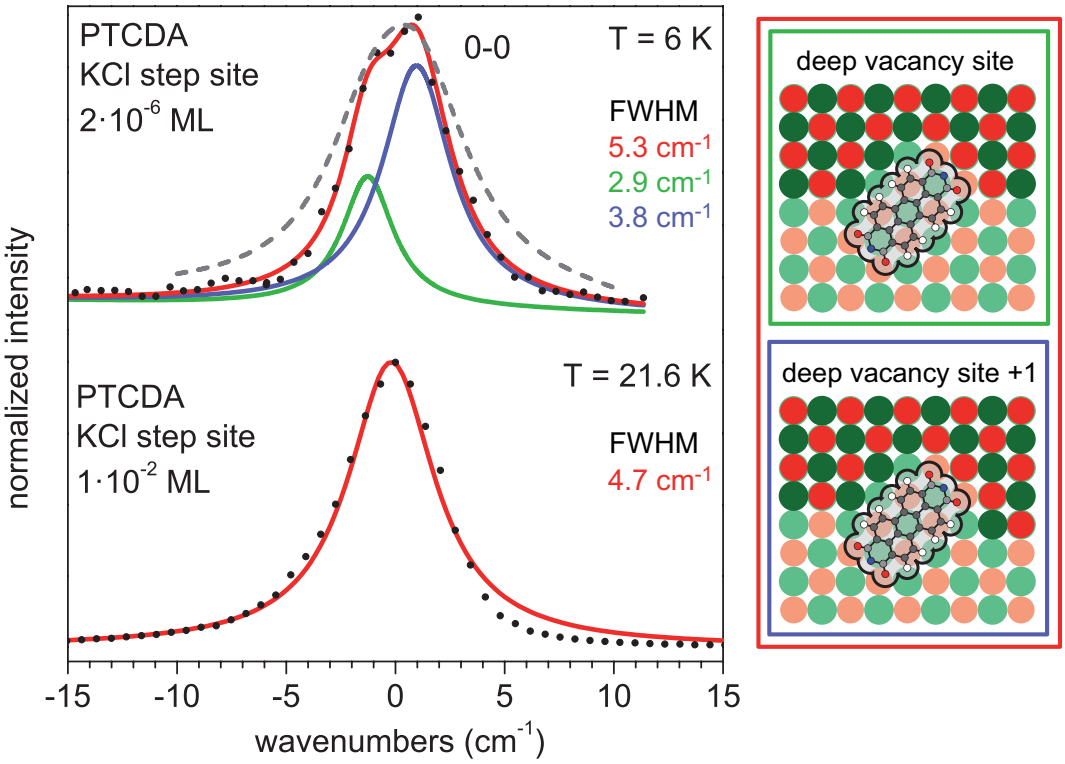

Figure 6.1: *Fluorescence excitation spectra of the 0-0 transition of PTCDA at KCl step sites for different experimental conditions. The upper spectrum was acquired for a highly diluted phase at a coverage of* $2 \cdot 10^{-6}$ ML *and at a sample temperature of* 6 K. *For excitation a narrow line width (*0.0007 cm^{-1}*) ring laser was used. The bottom spectrum was taken from Ref. [18]. Here the surface coverage was* 10^{-2} ML *and the temperature was* 21.6 K. *The spectrum was measured with a broader excitation laser (*1 cm^{-1}*). Due to the higher resolution of the excitation laser in the upper measurement a splitting of the profile into two contributions can be resolved. The profile can be fitted as a sum of two Lorentzian functions resembling two different adsorption sites of PTCDA at KCl steps. Real space models of these adsorption sites are depicted on the right side of the figure and are framed with a color referring to the individual and cumulated fit functions in the upper plot. A convolution of the upper profile with a Lorentzian instrument function (*1 cm^{-1}*) is depicted as a dashed gray line in the upper graph. There no splitting of the profile is observable. A Lorentzian fit of the bottom spectrum is depicted as a red line. For further details see text.*

0.0007 cm^{-1}) and not, as before, a standing wave laser ($\Delta\nu_{\mathrm{inst}} = 1\ \mathrm{cm}^{-1}$) [18] (cf. Chapter 4). To demonstrate the effect of the instrumental broadening, the splitted profile has been convoluted with a Lorentzian instrument function with a width of 1 cm^{-1}. The resulting profile is depicted as a dashed gray line in Fig. 6.1. There, no longer an indentation can be observed and only a minimal asymmetry of the profile shape remains. Keeping this in mind, also the slight asymmetry of the profile measured by Paulheim et al., which can be seen from the deviations of the measured profile from an ideal Lorentzian fit (cf. Fig 6.1), can be interpreted as an indication for the superposition of different species.

By scanning smaller parts of the inhomogeneous profile with high resolution and in small increments, further small intensity variations in the wing of the inhomogeneous profile known as the statistical fine structure [128] could be detected. Consecutive scans of this fine structure are depicted in Appendix A.3 and show that these measured intensity variations are not induced by noise but are an intrinsic property of the sample at the position of the excitation laser. By changing

this position on the sample also different statistical fine structures could be measured in the same spectral range. The average distance between neighboring maxima of this fine structure is smaller than 0.1 cm^{-1} and thereby much smaller than width of the inhomogeneous profile. In conclusion this was a clear evidence that the measured Lorentzian profiles are indeed a superposition of a multitude of homogeneously broadened 0-0 transitions and thus inhomogeneously broadened.

What remains unclear at this point is the reason for the Lorentzian profile form of the individual contributions of the inhomogeneous broadening. Interestingly, this profile form is identical to the one found for PTCDA at NaCl step sites where the (presumably) inhomogeneous profile is expected to stem from just a single type of adsorption site [18]. Possible mechanisms inducing this inhomogeneous broadening will be discussed in the following.

6.2.2 Molecular picture of the inhomogeneous broadening

The inhomogeneous broadening of an ensemble of molecules, i.e. the spread of their transition energies, is typically explained by the presence of a variety of different molecular environments. Each molecule in its unique environment exhibits a slightly different optical transition energy, which leads to a distribution of energies. In the present system these different environments are likely caused by different step surroundings of the KCl at which the PTCDA molecules are partially embedded.

Indeed, in a series of previous studies [15, 17, 18] it has been demonstrated that the binding energy of the molecule at a step adsorption site and the energy of the optical transition at this site vary according to the morphology of the step site. Thereby, the spectral shifts that are induced by small structural changes of the KCl step in direct contact to the molecule were found to be on the order of 1 - 100 cm^{-1} [18]. The smallest of these changes in transition energy is the one that could be observed as the peak splitting in the previous chapter. Here the difference between the *deep vacancy site* and the *deep vacancy site +1* was induced by an additional row of ions at one side of the molecule and caused a splitting of the inhomogeneous broadening into two main contributions separated by 2 cm^{-1}.

At this point it becomes clear that the much smaller differences in transition energies that have been resolved in the statistical fine structure cannot be explained in the simple picture of such archetype adsorption sites that involve changes of the K^+ and Cl^- ions in close vicinity to the molecule. The direct molecular environment influences the transition energy on a larger scale but cannot explain the dense distribution and the small shifts between the different transition energies.

In order to explain these smaller shifts therefore also much smaller interaction strengths have to be considered. One possible explanation could be the influence of weaker long range order Coulombic interactions between the molecule and KCl ions multiple lattice constants away at the step edge. In this model, the center of the inhomogeneous broadening would correspond to the KCl ions in direct contact with the molecule. Smaller shifts based on this center position

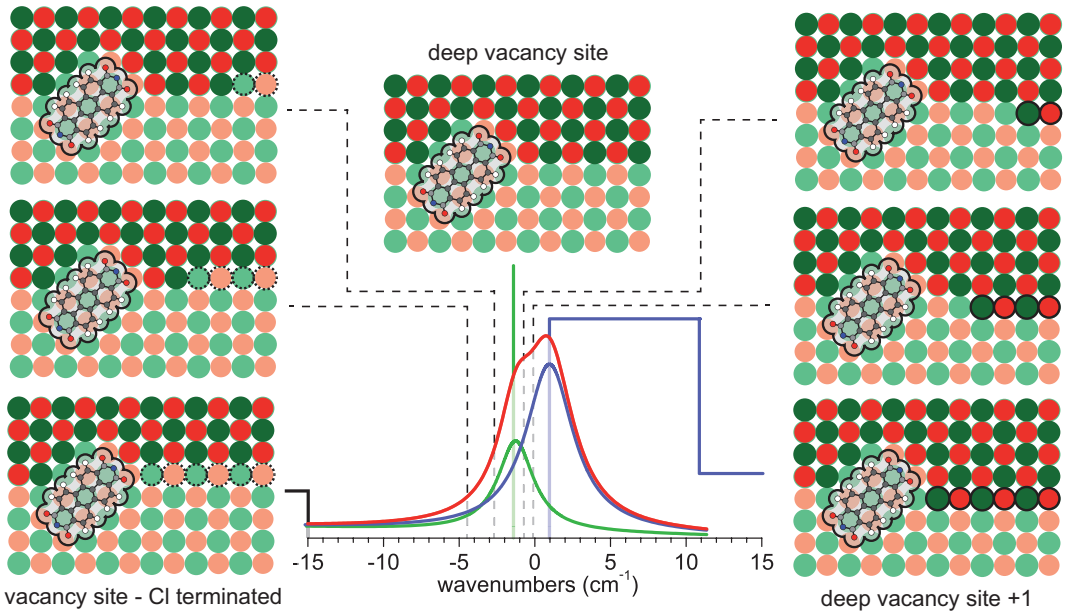

Figure 6.2: *Possible explanation for the inhomogeneous broadening by higher order Coulombic interactions at step sites. The center of the inhomogeneous profile of the deep vacancy site is given by molecules embedded in a flat KCl step (central model). Additional (right) or missing (left) KCl atoms along the step edge induce smaller spectral shifts. The closer the position of the additional or missing atoms is to the molecule, the larger is the spectral shift. As a reference also the structures and the spectral positions of the deep vacancy site +1 and the Cl terminated vacancy site taken from Ref. [18] are shown (bold lines). The spectral positions of the intermediate sites (dashed lines) have been set in rough estimation of an $1/d^3$ distance dependence of the Coulombic interactions. For further details see text.*

would be induced by KCl ions with a larger distance to the molecule. This principle is sketched schematically in Fig. 6.2 for the *deep vacancy site* and will be outlined in the following.

The center position of the inhomogeneous broadening of the *deep vacancy site* supposedly corresponds to a KCl step edge that is linear except for the (deep) vacancy formed at the molecule. Deviations from this linear step edge cause a small blue or red shift dependent on the type of step defect. The size of this shift would then be related to the distance d between the defect and the molecule. It will scale with $1/d^3$ according to the Coulombic dipole-dipole interaction between the transition dipole of the molecular transition and the dipole induced by the missing or additional ions on the surface. For the case of several deviations from a linear step edge in vicinity to a molecule, the respective shifts having impact on this molecule are expected to sum up. Possible step defects are neighboring additional or missing atomic rows (cf. Fig. 6.2), kinks, vacancies, corners or single ad-atoms. The profile form of the inhomogeneous broadening is then the result of many small shifts due to defects at the step edge that are comparably far away from the molecule (peak of the inhomogeneous profile) and few larger shifts that are induced by variations in the step morphology closer to the molecule (wings of the inhomogeneous profile).

Apart from this explanation also inter-molecular interactions via resonant or off-resonant coupling of transition dipoles similar to the situation inside the monolayer of PTCDA on KCl (cf. Chapter 5) could explain the inhomogeneous broadening. Here again the spectral shift scales with the distance d between the molecules $1/d^3$ (cf. Figure 5.3). Therefore the splitting of transition energies

is far too large for molecules in direct contact but becomes reasonable for molecules separated by few molecular distances. Regarding the low surface density of molecules in the present experiments, about one molecule per μm^2, this type of interaction can definitely not explain the entire inhomogeneous broadening, since at such distances no significant intermolecular interactions are present. It is however imaginable that some molecules are located close together by chance and are therefore also affected by intermolecular interactions. For higher surface coverages, e.g. 1% of a monolayer, these intermolecular interactions should become more important.

Finally, as a third possibility also slight conformational differences between different molecules at identical step sites could induce small energetic shifts. A necessary condition for the occurrence of such conformers is however the presence of local minima of the potential energy surface of the molecule at the adsorption site. In addition the energetic barriers between these minima need to be sufficient in order to freeze the molecule in its respective conformation at the experimental temperatures. Regarding the stability of the statistical fine structure upon optical excitation it appears however unlikely that the molecules are optically excited, relax into vibrational states of the ground state (vibration energy: 50 - 1500 cm^{-1}, 0.01 - 0.20 eV [8]), but obtain not enough energy to overcome such barriers. This would result in small conformational changes and hence small optical jumps that were at least not regularly observed for the statistical fine structure.

6.3 Single molecule measurements

6.3.1 Single molecule detection

By a further spatial and spectral dilution the individual homogeneously broadened single molecule profiles have been separated from each other. Fig. 6.3 shows two different scans far off the center of the inhomogeneous broadening ($\approx$ 1.9 - 2.3 $\times$ $FWHM_{inhom}$) that demonstrate the spectral dilution. While the scan in Fig. 6.3a shows several single molecule profiles that are still energetically close together and partially superimposed, the scan in Fig. 6.3b at a higher energetic distance with respect to the inhomogeneous center shows fewer and more separated single molecule peaks.

All measured profiles show a Lorentzian profile shape, but vary somewhat in absolute size and width. In general these variations can be explained by differences in the absorption of the excitation light of different molecules. On the one side, these differences can be caused by different positions of the molecules inside the focus of the excitation laser and thereby by different power densities of the excitation light at the position of the molecule. On the other side, different orientations of the molecule and its optical transition dipole with respect to the polarization of the excitation laser can reduce the molecular absorption. Especially the latter aspect has been investigated in several single molecule studies in cold matrices [102, 103] since here the molecular orientation was variable in all three dimensions. For the sample system investigated in this work the variety of molecular orientations is however reduced to only two possible molecular orientations rotated by 90° with respect to each other due to the defined binding to the two dimensional substrate (cf. Ref. [8]). By additionally aligning the polarization of the excitation light to only

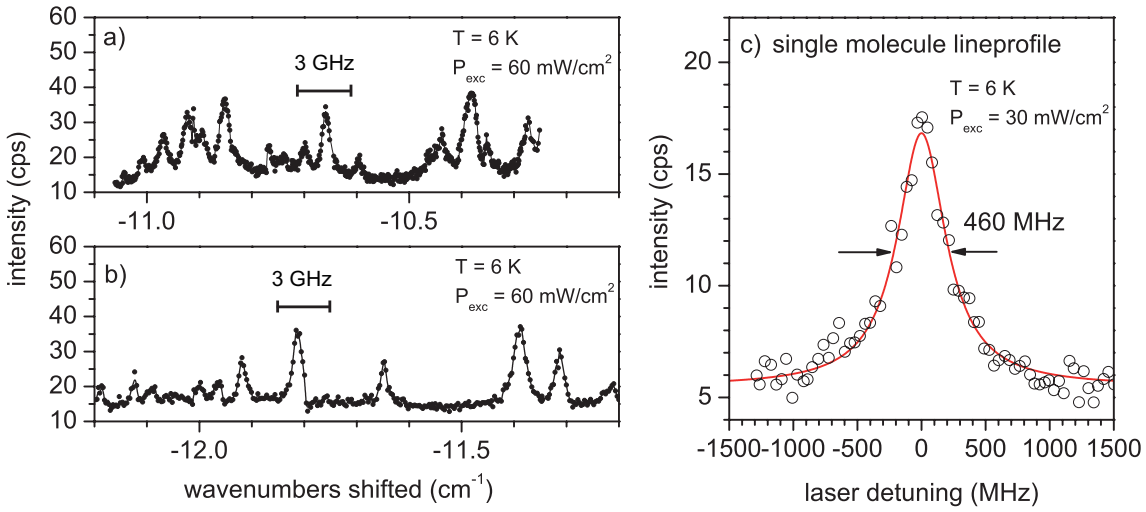

Figure 6.3: *Spectral dilution and single molecule absorption profile. (a) and (b) show FLE scans with several separated single molecule absorption profiles. With increasing energetic distance to the center of the inhomogeneous broadening also the distance between the individual peaks increases. Intensity variations can be explained by different positions of the molecules inside the focus of the laser and hence by a different power density of the excitation light. (c) shows a single lineprofile of a preparation with a lower molecule density on the sample. The profile was measured only* 5 cm^{-1} *separated from the center of the inhomogeneous profile. The single molecule profile was measured at the minimal power density and is fitted by a Lorentzian peak function. The integration time for every measuring point was* 2 s. *For further details see text.*

one of these molecular orientations, also the last difference in the molecular orientation has been experimentally excluded. Therefore the observed intensity variations of the single molecule profiles could be explained entirely by different positions inside the focus of the laser and hence by a different local power density of the excitation light (cf. Appendix A.3).

Fig. 6.3c finally shows a single molecule line profile that was obtained at minimal experimental temperature (6 K) and a power density of the excitation light (30 mW/cm^2). The depicted profile has a linewidth of 463.8 ± 24.5 MHz (1.9 μeV), which is a typical value and was found to be the experimental limit to small values independent from the spectral position and the KCl film thicknesses between 5 and 10 ML (1.6-3.2 nm).

Compared to the minimal line widths that were obtained in optical single molecule studies of molecules in solid hosts (8-180 MHz) the obtained line width in the present experiment is considerably broader [97, 103, 106]. This broadening is presumably an effect of the comparably "high" sample temperature of 6 K. In typical optical single molecule experiments minimal sample temperatures of $\approx$ 1.5 K have been achieved, so that a temperature induced broadening could be excluded [97, 98]. Comparing the obtained width with other profiles measured at 6 K showed that the obtained width perfectly fits into the broad range of previously reported single molecule line widths at this temperature (60-1000 MHz) [98, 100, 101]. This broad range of profile widths at this elevated temperature is the result of different host materials and hence a different coupling of the optical transition to phonons and local librations of the molecule inside these hosts.

Due to the temperature induced broadening only a lower limiting value of the radiative lifetime of 0.34 ns could be determined from the obtained profile width (cf. Appendix A.3). As a reference

the free molecule inside a liquid helium droplet at 380 mK has a radiative lifetime of 5.5 ns [150], which would result in a natural linewidth of only $\approx$ 30 MHz.

It shall be noted that a straight forward explanation of the determined profile width in accordance with the model [131] that was applied in Ref. [18] to describe the temperature dependent linebroadening of the ensemble spectrum between 6 K and 110 K was not possible. This model describes the broadening of the profile induced by the coupling of the optical transition to acoustical phonons, which is well suited for temperatures > 10 K, but results in a broadening much too small at the lowest temperatures ($\Delta\nu(6\text{ K}) \approx 0.3$ MHz). In the lowest temperature regime other mechanism are thus responsible for the temperature induced broadening. These can be for example the tunneling between 'two level systems' (TLS) or the coupling to low frequency pseudolocal modes (LFM) [151].

6.3.2 Single molecule characteristics

After the successful detection of single molecule profiles the next step was to study the influence of external parameters like the laser intensity or the sample temperature on the behavior of the single molecule absorption profiles and extract molecular parameters like fluorescence rates or the interaction of the molecule with phonons of the substrate.

A series of profiles measured for variable power density of the excitation laser is depicted in Fig. 6.4a. This series was measured in order to study the saturation behavior of the optical transition. The corresponding profile widths and detected fluorescence rates are depicted in Fig. 6.4b. Different from earlier single molecule studies [102, 103], here not the saturation behavior of one single molecule, but from several different molecules have been plotted in the same curve. This was necessary due to frequent spectral jumps and the laser induced vanishing of molecular transitions at higher power densities (cf. Chapter 6.3.3). In order to reduce the uncertainty of the laser intensity at the position of the molecule, always the largest profile within the scan range has been chosen for the evaluation assuming that it belongs to a molecule close to the intensity maximum of the focused laser.

Nevertheless, the obtained spectra show the expected saturation of the fluorescence rate and broadening with increasing power. The saturation and the broadening behavior could be fitted according to Eq. 3.13 and Eq. 3.15 and yielded a saturation intensity of $I_S \approx 270 \pm 100$ mW/cm^2 and a maximum emission rate of $R_\infty \approx 11500$ photons per second (for details see Appendix A.3). The obtained values were found to be in the typical range of other single molecule experiments, e.g., of terrylene in hexadecane [102, 106]. For the line width at vanishing laser intensity ν_0 a value of $\nu_0 = 443 \pm 33$ MHz was obtained, which shows that the minimal achieved profile widths, i.e. 463 MHz, were not significantly power broadened. The maximum emission rate of R_∞ is significantly reduced compared to the value that would be expected for an undisturbed two level system ($\approx 10^9$ photons per second at a radiative lifetime of 1 ns), which implies the presence of additional non-radiative decay channels, e.g via non-radiative triplet states. Nevertheless the temporarily intermittency of fluorescence known as blinking could not be observed, possibly due to the long exposure time of 2 s per data point used for the present experiments.

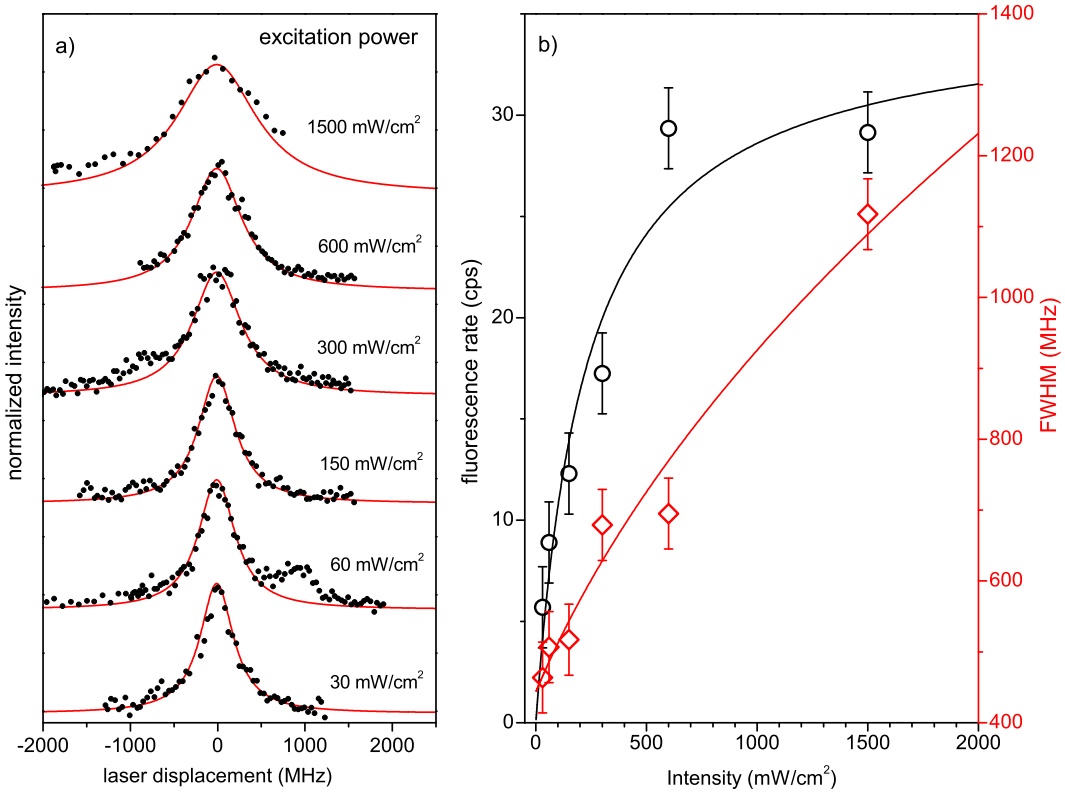

Figure 6.4: *Saturation effects and power broadening of single molecule profiles. (a) Series of single molecule profiles for different power densities in the range between* 30 mW/cm^2 *and* 1500 mW/cm^2. *The profiles are fitted by Lorentzian peak functions and show a power induced broadening. The profiles of different molecules have been plotted. The profile shown at the lowest power density is identical with the profile shown in Fig. 6.3c. (b) Dependence of the fluorescence rate and the profile width on the power density. The open symbols have been extracted from the Lorentzian fits of (a), the solid lines are fits to the data points according to Eq. 3.13 and Eq. 3.15. For further details see text.*

An attempt to measure the temperature dependence of the single molecule profiles is illustrated in Fig. 6.5. Here three neighboring profiles were continuously scanned while slightly reducing the liquid helium flow and thus warming the sample. During the first scan, the sample temperature was stable at the lowest possible temperature of 6.1 K. Then the temperature was slowly increased, which resulted in a continuous broadening of the profiles and a loss of the signal to noise ratio. Already at 6.6 K the broadening becomes very pronounced and at 6.8 K additional spectral changes in the form of additional appearing or shifted peaks can be observed. Above 7.0 K the profiles almost vanished completely into the background signal. Finally, by re-cooling the sample the molecular signals partially reappeared. The molecular peak on the right side of the plot however vanished completely, and the central peak shows a shoulder that was not present in the first scan.

In contrast to the saturation behavior, a quantitative evaluation of the temperature behavior was hardly possible. This was on the one hand due to the limited temperature range and the irreversible temperature induced changes of the investigated profiles. On the other hand, also the

measured sample temperature needs to be treated with caution. Since the position of the temperature measurement is located relatively far away from the sample at the sample mounting (cf. Chapter 4.1.1, Appendix A.4), the temperature measurement under non-static conditions could lead to an underestimation of the real sample temperature.

From a qualitative point of view it can however be stated that already a small increase of the sample temperature leads to a very pronounced broadening and a vanishing of signal. In addition, presumably the thermal energy of the system is sufficient to induce a partial reorganization on the sample, which results in the vanishing and shifting of molecular transitions. Similar effects upon short heating have also been observed for the statistical fine structure (cf. Appendix A.3). It should however be noted that such temperature induced spectral changes could also be the result of the more trivial effect of thermal expansion of the manipulator and the sample mounting. This

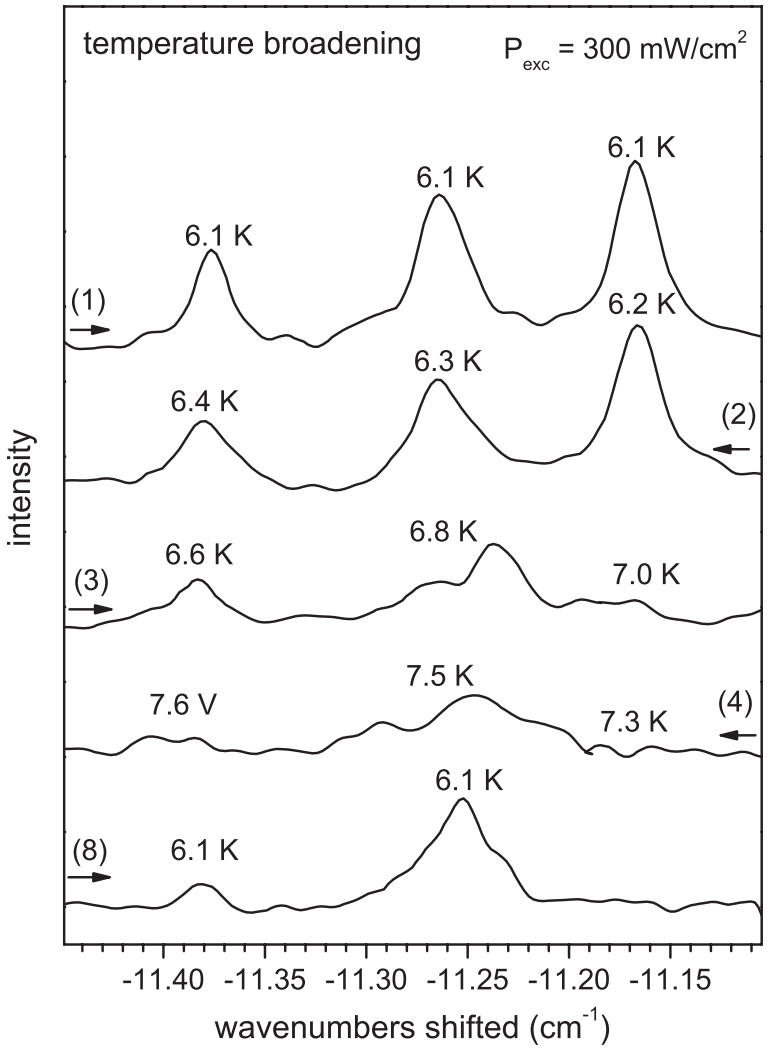

Figure 6.5: *Temperature dependent measurement of single molecule profiles. The temperature was continuously varied during the measurement and the temperatures at the profile positions are given. Small numbers and arrows at the sides mark the number of the respective scan and the scan direction, respectively. All measurements have been considerably smoothened for better visibility. For further details see text.*

would change the position of the probing laser on the sample and let the molecules migrate out of the excitation focus of the laser. For the assumption that the temperature T of the manipulator, which has a length of $l \approx 1000$ mm, increases by $\Delta T = 5$ K during the reduced liquid helium flow, an increase of the manipulator length by $\Delta l = 0.05$ mm, would be obtained for a thermal expansion coefficient $\alpha \approx 10^{-6}$ K^{-1}. This is on the order of magnitude of the diameter of the laser on the sample. Therefore, unfortunately, such thermal expansion effects cannot be fully excluded in the current experimental setup.

6.3.3 Spectral jumps

As noted in the last chapter, occasionally the complete vanishing of single profiles or their small spectral jumps between or during consecutive scans have been observed. The probability for such a spectral change was found to increase with the power density of the excitation laser (cf. Appendix A.3). At constant power density differences in the stability of the molecules could be identified. Here three types of molecular transitions could be distinguished. The stable type did not change its spectral position independent on how often it was scanned at a given power density. In contrast, the instable type vanished directly upon excitation and probably jumped to a spectral position outside the scan range (> 60 GHz). Finally the meta-stable type was found to undergo small and reversible jumps on the length scale of the width of the profile (< 1000 MHz). These occurred mainly upon excitation, but also independent from being in resonance with the laser. While the stable and instable type have been observed rather frequently, the meta-stable type was observed very infrequently and is therefore considered to be related to special conditions. Exemplary scans that show the behavior of the instable and meta-stable type are depicted in Appendix A.3.

Under the assumption that the irreversible vanishing of the instable molecular transitions is connected to a large spectral jump and not to a chemical bleach (cf. Appendix A.3), this type of jump is presumably related to a structural change of the KCl step in vicinity to the excited molecule, e.g., the hopping of a single ion pair towards or away from the molecule (cf. Chapter 6.2.2). This is schematically depicted in Fig. 6.6a. Regarding the dependency of these jumps on the power density of the excitation laser the structural change at the step edge is presumably activated by molecular vibrations or the dissipation of the vibrational energy on the surface. The differences in stability upon excitation could be explained by different initial step geometries and hence different activation barriers for the hopping process of a pair of KCl ions. After the hopping process also the absorption wavelength of the molecule has changed. Therefore a further excitation of the molecule at the probed wavelength, which could supply the energy for a reversible back-hopping, is not possible and the spectral jump is irreversible.

The smaller jumps that were observed for the meta-stable profiles can presumably not be explained by this simple model. To induce a spectral jump on this much smaller energy scale the structural change at the step edge supposedly needs to occur in much larger distances with respect to the molecule. At this point it becomes however unclear why the local excitation on the molecule

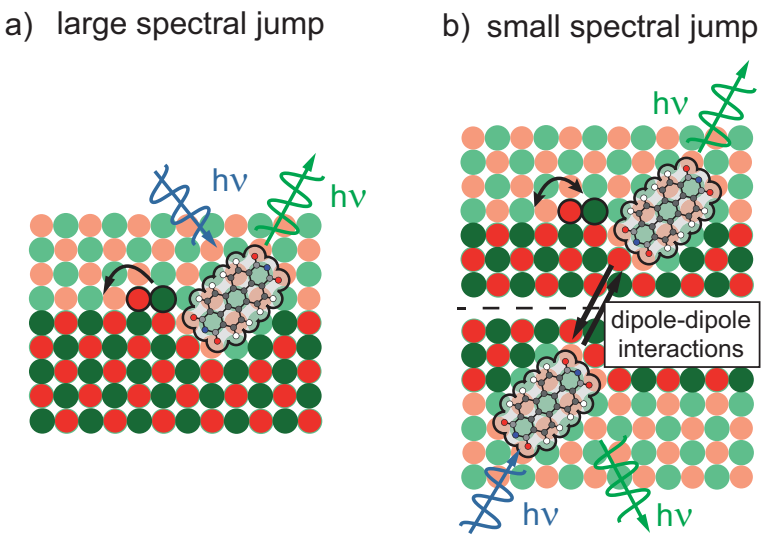

Figure 6.6: *Possible mechanisms that are responsible for the occurrence of large (a) and small (b) laser induced spectral shifts. In (a) the vibrational energy that remains after excitation and fluorescence on the molecule induces a structural change at the step edge, which induces a large spectral shift. In (b) this process takes place on a second molecule that is coupled with the initially excited molecule via dipole-dipole interactions. The large spectral shift of the second molecule affects the intermolecular interaction with the first molecule and leads to a very small shift. The dashed line between the molecules indicates an arbitrary distance of several lattice constants between the coupled molecules. For further details see text.*

should induce such structural changes far apart from the molecule itself. Therefore presumably a different mechanism needs to be found.

Small spectral jumps on a similar energy scale were also reported for the absorption lines of single molecules in solid hosts and have been frequently described under the term *spectral diffusion* [100, 102, 134]. Here the jumps were commonly explained by the tunneling of the molecule or the surrounding matrix atoms between different confirmations, so called two level systems. The presence of metastable confirmations of the molecules and their environment were already briefly discussed as a reason for the inhomogeneous broadening in Chapter 6.2.2. For the case of strongly bound PTCDA molecules at ionic KCl step edges this mechanism was however expected to be rather unlikely.

Finally a possibility based on inter-molecular dipole-dipole interactions can be imagined. On the one hand these interactions are expected to be very rare in the present experiment because of the extremely low molecule density on the surface. On the other hand the molecules investigated in a single molecule experiment are located energetically far away from the center of the inhomogeneous broadening and thus represent especially those molecules that have different local surroundings than the average molecule. Therefore such interactions could explain the comparably rare phenomenon of small spectral jumps.

A possible mechanism based on intermolecular interactions is schematically shown in Fig. 6.6b. It concerns two molecules on different sites with unequal transition energies that are off-resonantly coupled via transition dipole-dipole interactions. Due to the coupling both transition energies are affecting each other, which already initially leads to a small splitting. After excitation of one of the

molecules the excitation can be transferred to the second molecule, where it decays. This energy transfer is not resolvable in FL measurement due to the small energetic difference in transition energies and the limited resolution of the spectrometer. If the decay on the indirectly excited molecule induces the hopping of an ion pair close to it, the transition energy of this molecule undergoes a large jump spectral. On the initially excited molecule this larger jump translates into a much smaller spectral jump due to the change of the intermolecular coupling. Since the interaction between the two molecules persists also after the spectral jump, the excitation can still be transferred and may lead to reversal or additional structural changes in the vicinity of the second molecule.

In the end none of these possible interpretations could yet be experimentally proven or falsified. Nevertheless these experimental findings and their possible interpretations give an insight on what kind of processes may be further investigated in future experiments. Here especially the combination of optical spectroscopy and spatial imaging may lead to new insights in these dynamic interactions.

6.3.4 Co-adsorption of Argon

In order to check for the influence of long range order van-der-Waals interactions on the molecular transition energy a co-adsorption experiment with argon atoms was carried out. Here the profiles of single molecules were continuously scanned, while small amounts of argon were dosed into the UHV-chamber and sticked on the cold sample surface. The idea of this experiment was to induce small spectral shifts of the transition energy of single molecules, that could be related to the distance between the molecule at its step site and argon atoms on the surface. With increasing doses also the average distance between a molecule and an argon atoms should decrease and thus there should be an increasing likelyhood for a larger shift with increasing doses.

A typical experimental sequence is depicted in Fig. 6.7 for a single isolated absorption profile. First, a molecular transition was scanned as a reference. Then the ionization gauge was switched on in order to measure the argon pressure. Already this induces a short increase of pressure, that could possibly induce an adsorption of gas atoms on the sample. A spectral shift of a profile was however not observed. Instead a small rise of the background level due to the detection of the glowing filaments of the ionization gauge was detected. In the next step, argon was incrementally dosed into the UHV chamber starting at a pressure of $5 \cdot 10^{-10}$ mbar and ending at a pressure of $3 \cdot 10^{-7}$ mbar. Although the argon valve was each time opened for only few seconds, the pressure of the UHV chamber needed more than a minute of pumping at pressures above $1 \cdot 10^{-8}$ mbar to reach the base pressure level. Therefore the doses of argon that have been applied to the UHV chamber have only been roughly estimated to be in the range between $2 \cdot 10^{-9}$ mbar $\cdot$ s and $5 \cdot 10^{-6}$ mbar $\cdot$ s. Assuming that all argon atoms that hit the surface at a sample temperature of 6 K stick on the surface a complete argon monolayer is expected at a dose of $3.8 \cdot 10^{-6}$ mbar $\cdot$ s.

Surprisingly, not even an argon dose of $5 \cdot 10^{-7}$ mbar $\cdot$ s (cf. Fig. 6.7), which resembles about 15% of a full argon monolayer, induced any observable shift in one of the detected molecular absorption profiles, although at this coverage, statistically at least one argon atom should be close

to the investigated molecule. Only when increasing the dose to $5 \cdot 10^{-6}$ mbar $\cdot$ s (more than a monolayer), a spectral change could be observed. This was however not a small shift as initially intended, but the complete vanishing of all single molecule profiles in the complete scan range. Finally, by shortly heating the sample to 60 K and desorbing the argon from the sample, the single molecule profiles reappeared. They appeared, however, on different spectral positions, possibly due to small structural reorganizations on the sample or the irreversible thermal expansion of the sample mounting (cf. Chapter 6.3.2).

Up to now it is not clear, why no small spectral shifts could be observed in these experiments. The simplest explanation is that the molecular transition energy is only affected, if the argon atom is in direct contact with the molecule. The adsorption on a site near the molecule would then have a negligible effect on the transition energy. By taking in mind that the argon atoms carry no charge and can thus interact only by weak van-der-Waals interactions with the molecule this appears at least imaginable. These interactions scale with $1/r^6$ compared to $1/r^3$ for the Coulombic interactions of the KCl ions and have thus a much lower range.

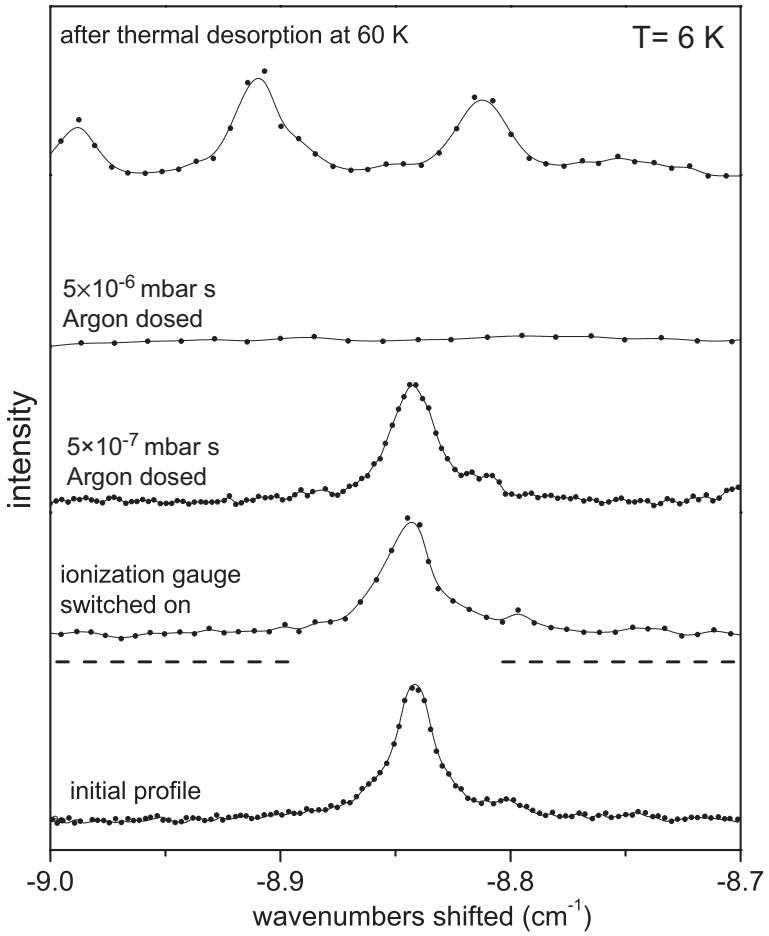

Figure 6.7: *Influence of the co-adsorption of argon on the spectral position of a single molecule profile. The offset of the baseline of the second scan with respect to the first scan due to the switched on ionization gauge is marked by a dashed line. All scans have been performed at* $T = 6$ K. *For further details see text.*

6.4 Classification of results and future experimental improvements

Concluding these first high resolution optical single molecule spectroscopy experiments on a defined surface, it can be stated that the optical properties of a single molecule adsorbed on a thin insulating film are qualitatively similar to those reported for molecules inside a solid host. This includes the width and shape of their absorption profiles at a given sample temperature, the saturation behavior with increasing excitation density, and the observation of temperature and laser induced processes.

Comparing the minimal achieved linewidth (463.8 ± 24.5 MHz) and thus the obtained energy resolution of the current experiment (1.9 μeV) with more typical surface science techniques, like, e.g. photo electron spectroscopy (UPS: $>$ 20 meV [152], XPS: $>$ 100 meV [153]), the obtained energy resolution of a single molecule experiment is extraordinarily high. This shows the large potential of this technique for the studying of so far not resolvable minimal interactions at surfaces.

Also with respect to recent optical single molecule experiments that induced fluorescence by the tip of an STM [110, 111, 154] (STM-LE, cf. Chapter 2.3), the profiles measured in the present experiments are several orders of magnitude sharper. This demonstrates that the broadening in these STM based experiments has to be either experimentally induced or an effect of the lower thickness of the insulating film, typically only 2-3 atomic layers. In the latter case this broadening could be induced by a partial quenching process due to the close-by metal surface [141]. This would result in a reduction of the radiative lifetime and a broadening of the natural line width (cf. Chapter 3.2.2).

Despite the principle agreement of the present single molecule experiment with earlier experiments on single molecules in solids and the potential of this technique for future highly sensitive surface science experiments, the experimental setup and thus also the quality of the achievable data is limited at the present. Therefore the obtained data sets do so far not allow to extract robust molecular constants or deliver a large statistics for example concerning the length of spectral jumps or the broadening of individual molecules with the laser intensity or the temperature. This has several experimental reasons that will be discussed in the following including possible steps for a future optimization.

Temperature: At the present the experimental setup is limited with respect to the minimal achievable temperature, the detection efficiency of photons, and the spatial resolution. The most obvious limitation is the minimum temperature of 6 K, since it broadens the homogeneous profiles. This results in a lower resolution and hence in a smaller sensitivity for energetic shifts or broadenings. Moreover, the signal-to-background ratio decreases significantly with the temperature [101, 129], which results in less clear profiles. This is also an effect of the spectral broadening, but results from the overlapping wings of broadened molecules energetically close to the investigated molecule. Finally, the limited minimal temperature prevents to measure larger temperature ranges and thus to study the temperature dependence of the induced broadening.

A further improvement of the minimal experimental temperature would therefore definitely enable a larger number of experiments. However, at the moment the sample temperature is limited

mainly by the used cryostat so that additional improvement demands for a complete change of the present continuous flow cryostat (5 K) to a multistage cryostat (1.5 K). This would include also the change of the sample manipulator and the sample mounting, which would in sum be a very costly modification in many aspects.

Collection efficiency: The second experimental limitation concerns the collection efficiency of the emitted photons: Here so far the nearly unmodified detection apparatus of the previous works with a detection efficiency of only 0.3% of the emitted photons has been used. As a reference, highly optimized experiments can reach overall collection efficiencies of $\approx$ 10% [130]. The comparably low collection efficiency in combination with the increased background signal due to the higher temperature demands for rather long exposure times (2 s per data point). Therefore, the high resolution measurement of a single line profile takes several minutes, which aside of the pure temporal costs leads to additional problems: The experiment is slow with respect to fast changes, for example of the laser position on the sample or a change of temperature. Furthermore, the molecules stay in resonance with the laser for long time, which increases the probability for unintended laser induced spectral jumps. And finally temporal effects on a shorter time scale than the exposure time, e.g., the blinking of molecules, may not be observable due to the temporal averaging.

In the present setup the highest loss of photons occurs at the collection lens (NA 0.22) in front of the sample that collects only 2.5% of the emitted photons. Highly optimized setups that use for example a parabolic mirror detector (NA 1.0) can collect up to 50% of the emitted photons at this stage [97]. In the present setup the use of a high NA collection optics is however not straight forward. The use of an parabolic mirror detector requires a transparent sample and is therefore not possible with a non-transparent Ag crystal. Other optics with high collection efficiency, for instance microscope objectives, need to get very close to the sample. This is difficult because the sample is under vacuum and thus separated from the outside by at least the thickness of the wall of the glass head. Fortunately, this problem has already been tackled for the construction of the UHV-light microscope that will be discussed in detail in the following Chapter 7 and which enables at least the use of a microscope objective with NA 0.5. This results in a collection efficiency of about 10% at this stage. Much higher NA values above 0.6 can however only be obtained with custom bake-able microscope objectives inside the vacuum.

Further significant efficiency losses are due to the quantum efficiency of the CCD detector (65%) the gratings inside the spectrograph (65% transmission) and the parts of the molecular fluorescence spectrum that are blocked together with the light of the excitation laser by optical filters (35% of the spectral intensity are transmitted) (cf. Appendix A.3). While the last point is unavoidable, the detection losses in the spectrometer and the CCD could be partially reduced by use of sensitive and fast point detector like a single photon avalanche diode. This would also further enhance the acquisition rate during the measurements, since the current setup has an internal delay time of $\approx$ 0.2 s between the acquisition of two data points (cf. Appendix C.1).

Spatial resolution: The last significant limitation of the present setup is the spatial resolution. At present, this is given by the size of the laser spot on the sample, i.e. $\approx$ 0.2 mm in diameter. This

spot includes a multitude of molecules even at the lowest obtained surface coverages (400-40.000). This is on the one side problematic, since one needs to significantly dilute the molecule density spectrally in order to separate the individual signals. Therefore the molecular species that can be investigated are rather exotic and do not represent the typical molecules and their surroundings. In addition also the background signal induced by the fluorescence of molecules that are excited via absorption in the wings of their absorption profiles increases. With respect to single molecule spectroscopy in the bulk, this background signal is however not such a large problem due to the reduced dimensionality on a surface. On the other side, at the moment the larger spot diameter is experimentally beneficial since the investigated sample position is less susceptible for thermal drift or vibrations.

Nonetheless, an additional spatial separation of molecular signals would be desirable. This has for instance been demonstrated by Güttler et al. who built a setup for both spatial and energetically resolved single molecule microscopy [155]. In this publication several single molecule spectra have been measured in parallel since they appeared spatially separated in the microscope images. Due to the spatial image also thermal drift should not be a problem anymore.

Since an optical microscope is now available at the UHV-chamber (cf. Chapter 7), the next experimental step should be to combine the single molecule measurements with the microscope and obtain spatially and energetically resolved images. By using the microscope for detection, the so far used spectrometer and its grating would be replaced by the microscope camera. This does not allow for a spectral resolution but should improve the collection efficiency. In combination with the microscope objective that also improves the collection efficiency, this should additionally reduce the measurement times.

7 Optical microscopy of samples under ultra high vacuum conditions

This chapter presents results that were obtained by use of an optical microscope that was mounted to an UHV-chamber and is able to image sample surfaces in brightfield and fluorescence mode directly under UHV-conditions. The detailed design principles of the microscope, its construction, and the first results that have been obtained were published and can be found in Appendix A.4. In the following, these results are briefly summarized and complemented by more recent improvements and applications.

7.1 Field of application and design

The intention for building an optical microscope that is able to image samples directly under ultra high vacuum conditions was to obtain information on the macroscopic sample morphology, the distribution of molecular fluorescence on the sample, and the spatial correlation of these two properties. So far the surface morphology in the present experiment had always been determined from SPA-LEED patterns, i.e. from the width and form of the diffraction profiles. Although this is sensitive for the microscopic morphology, e.g. for the presence of steps and grain boundaries on the surface, it is insensitive for more mesoscopic structures and distances on the order of several micrometers instead of nanometers. Moreover the obtained information is averaged over a large sample area and not locally resolved. On the other side the distribution of fluorescence from molecules on the sample was so far checked by probing different sample positions with a focused excitation laser (diameter 0.2 mm). Although it could be roughly confirmed that the intensity of fluorescence was usually homogeneously distributed across the sample, no information about the mesoscopic fluorescence distribution inside the laser focus was obtainable. An optical microscope should however be capable of imaging such mesoscopic structures and obtain both optical and structural information in parallel. It should therefore supplement the existing techniques in ideal manner.

Surprisingly, it turned out that optical microscopy under UHV conditions had so far attracted hardly any attention among surface scientists, and only a single work by Blumenfeld et al. describing the construction of an UHV optical microscope had been published [112]. There a confocal scanning microscope with a custom bakeable reflective microscope objective inside the UHV had been constructed. In the present work, a different approach has been chosen, which is sketched in Fig. 7.1. A far-field incident light microscope and conventional microscope objectives outside the vacuum have been used. The sample was imaged through a 1.75 mm thick glass window. This

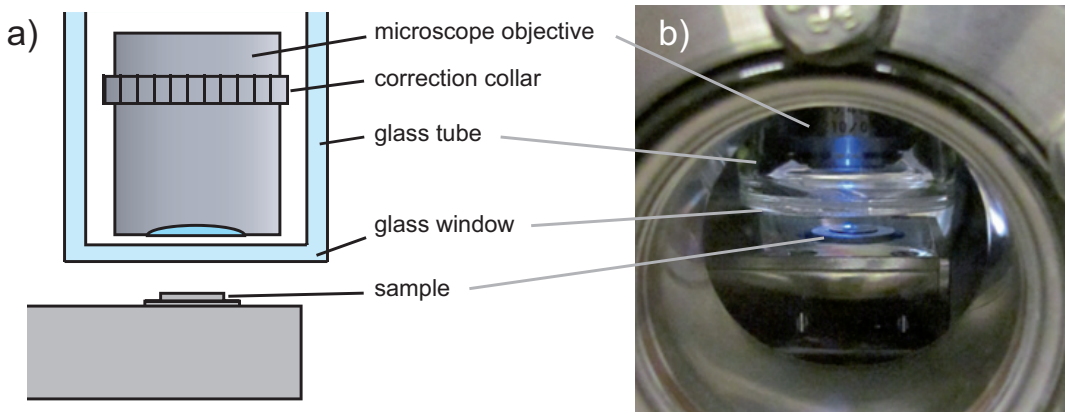

Figure 7.1: *Schematic drawing (left) and photography (right) of the glass window between the sample inside the vacuum and the microscope objective outside the vacuum. In order to compensate for the* 1.75 mm *thickness of the glass window, microscope objectives with large working distances and a correction collar have been used. For ideal imaging conditions the microscope objective needs to be as close as possible to the glass window.*

approach involves some mechanical and optical difficulties related to the glass window, but facilitates more flexibility in the exchanging of parts of the microscope without braking the vacuum, especially in the use of different microscope objectives.

A detailed description of the microscope, its construction, and its imaging probabilities can be found in Appendix A.4. This includes also a detailed overview drawing of the microscope. At this point only the most important points of the design will be briefly summarized: The glass window in front of the sample has been attached at the end of a glass tube that points out of the vacuum and has a U-turn before a metal glass transition. The U-turn accounts for the strain resistance of the metal-glass transition. The microscope objectives were positioned as close as possible to the glass window, nevertheless objectives with extra large working distances needed to be used to overcome the thickness of the window. In case of the $40\times$ objective the objective was additionally equipped with a correction collar that compensates for the thickness of the glass window (cf. Fig. 7.1) and improves the image quality. The microscope objective then was connected with an incident light microscope by a metal tube including a telescope optics. The telescope optics maintains the Köhler illumination of the incident light microscope and compensates for the extended tube length of the microscope. All parts of the microscope, including the glass tube were mounted on a linear transfer and could be retracted from the UHV chamber. The microscope was equipped with blue high power light emitting diodes and optical filters for fluorescence imaging. In the master thesis of N. Rohbohm it was additionally extended by polarization filters in order to measure polarization dependent fluorescence images [156]. The microscope was tested to reach an optimum resolution of 0.7 μm with a $40\times$ microscope objective of an NA $= 0.5$ and by use of a blue light source ($\lambda = 450$ nm). This is about 1.5 times the Abbe limit of the used microscope objective at the given wavelength, but can be considered to be a good value regarding the simplicity of the used microscope optics and the difficulties that are connected with the imaging through a thick glass plate.

7.2 Sample morphology

Bright field images of the Ag(100) surface were taken in order to investigate the surface morphology. The Ag(100) oriented sample itself was well prepared and had been used for several years in the experimental setup. Exemplary images of that sample surface including an overview image can be found in Appendix A.4. Contrary to expectations from an excellent LEED pattern of the sample (cf. Appendix A.4), its mesocopic surface showed several significant defect structures. The most prominent structure was a corrugation that was present on the entire sample surface in different strength. An image showing both a stronger and a weaker corrugated crystal region is depicted in Fig. 7.2a. Both regions show the same structural motives: flat roundish areas that are surrounded by elongated and curved protrusions. At higher magnifications also additional smaller structures on top of these mesoscopic protrusions could be imaged (cf. Appendix A.4). In contrast, no additional structures were found on the flat areas. No drastic changes of the observed surface structures were observable after several cycles of sputtering and annealing with the typical parameters (cf. Chapter 4.2.1). Therefore it has been supposed that the mesoscopic surface morphology had reached a stable equilibrium.

Additional surface defects that were observed are larger point like protrusions, slight scratches, and contaminations of the surface by larger metal splinters. Apart from the corrugation that was ascribed above, especially the larger point like protrusions are of interest. They have been observed randomly distributed all over the surface and seem to be independent from other defects of the surface. In Fig. 7.2a some of them are marked by circles. They occur both on the stronger and weaker corrugated regions of the image. A detailed image of a particularly remarkable protrusion is shown in Fig. 7.2b. This one is surrounded by smaller structures that have the stair step appearance typical for tungsten or bismuth crystals [157]. It is therefore plausible to assume that this defect has a different chemical composition than the average surface and stems from a contamination of the surface or the bulk of the sample. In the case that it stems from the bulk it could have been uncovered during the initial crystal preparation (cutting and polishing). In the case that is stems from a contamination of the surface, e.g., by a particle that has fallen on the surface, this particle could have merged with the surface during multiple cycles of sputtering and annealing.

A further argument for a different chemical composition of the surface in the region near such point like protrusions came from a growth experiment of C. Brülke that failed [158]. Instead of the growth of a single monolayer of hexagonal boron nitride on the Ag(100) crystal, a macroscopic and presumably poly-crystalline film was grown on parts of the surface. This macroscopic film was clearly observable under the microscope but revealed circular open regions where no film growth occurred. An image of this phenomenon is shown in Fig. 7.2c. As can be seen these circular open regions occurred around the central position of some of the point like protrusions, so that it can be deduced that the surface composition in these areas was different and hindered the macroscopic film growth. Although the largest open region occurred around the defect depicted in Fig. 7.2b, also other, but not all, point like protrusion showed a similar pattern. This in turn gave evidence for varying compositions of the different defects.

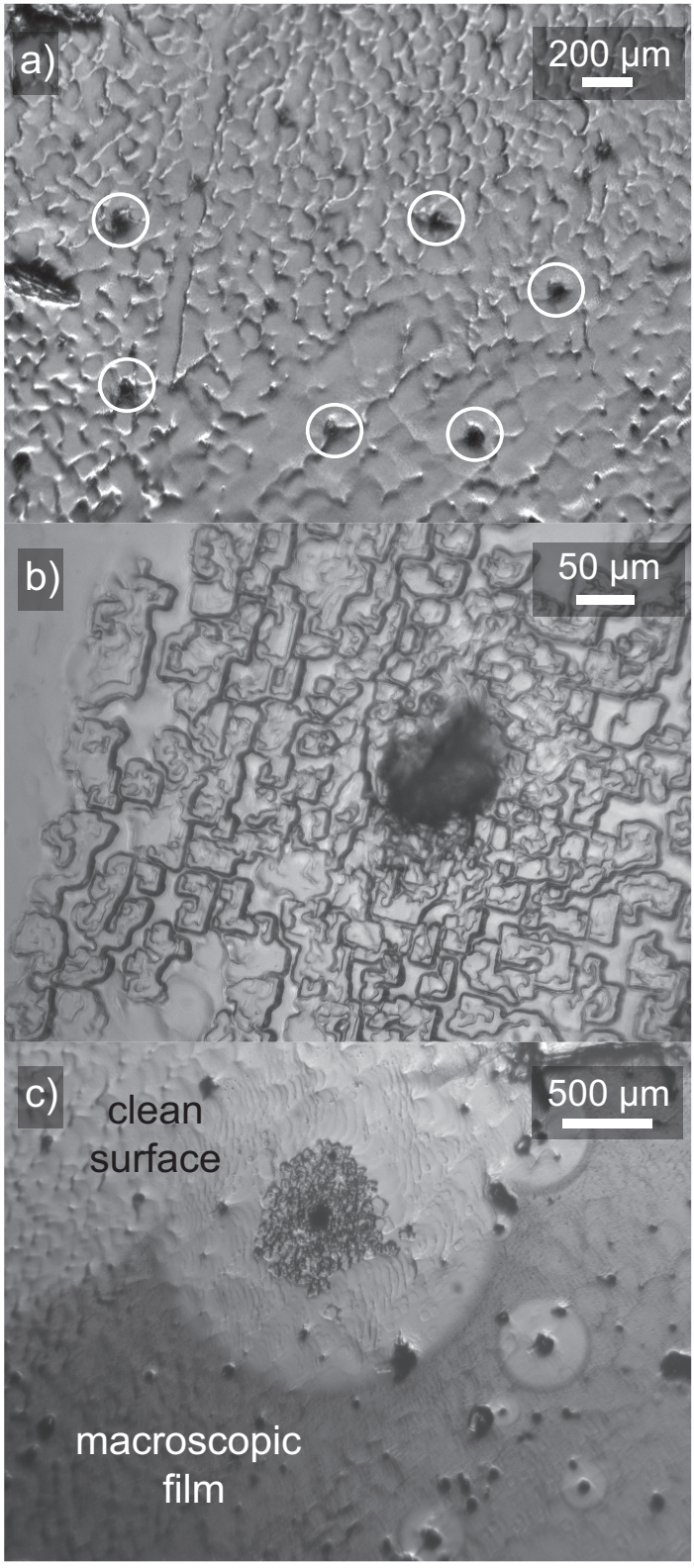

Figure 7.2: *Bright field images of defect structures on a Ag(100) crystal surface. a) Image that shows both a stronger (top) and weaker corrugated surface region (bottom) with roundish flat areas and elongated protrusions. Additional point like protrusions that appear randomly distributed across the surface are marked by white circles. b) Detail image of a prominent point like protrusion that is surrounded by small crystallites that presumably stem from a contamination metal on the sample. c) Overview image after a macroscopic growth of a boron nitride film on the Ag sample. The grown film covers the darker regions. Almost perfect circles of the clean surface remain around some of the point like protrusions indicating differences in the chemical reactivity of these areas. For further details see text.*

Concluding the observations from the bright field images, a variety of different mesoscopic defects have been observed on the surface of a typical metal single crystal. Until now the mechanisms that are responsible for the formation of these different structures have not yet been understood. It has however been checked that similar mesoscopic surface structures, i.e. a corrugation and point like defects, could also be observed on further coinage metal crystals (a further Ag(100) crystal and a Cu(111) crystal) that have been imaged outside the vacuum after use as samples in different UHV experiments. The formed structures therefore seem to be characteristic for such metal crystals.

For a better understanding of the structure formation, the necessary next step would be to investigate the morphology of a freshly polished crystal and monitor its evolution during the initial preparation. It is well known that the surface of Ag crystals that have been stored under ambient conditions typically undergoes a transition from a shiny to milky surface and back to a shiny surface during the first 10-20 preparation cycles. Therefore, it comes naturally to ones mind that such mesoscopic structures will probably evolve during this initial preparation. Otherwise already the initial polishing and etching process could lead to similar corrugations. Finally, also other influences of the sample preparation like the culmination of remaining fragments of adsorbates cannot be fully excluded.

7.3 Fluorescence distribution

With knowledge of the sample morphology, the next step was to check for the distribution of fluorescence from the sample. This could for example be influenced by the homogeneity of the evaporation procedure or by mesoscopic and microscopic defect structures on the surface. As a sample system for the fluorescence microscopy experiments isolated PTCDA molecules ($\leq$ 5% ML) on thin insulating KCl films (5-10 ML) have been investigated. Neither the KCl film nor the PTCDA was observable in the bright field images. As already expected from earlier spectroscopy experiments, the integral fluorescence intensity on a macroscopic scale was found to be uniformly distributed across the crystal surface. This confirmed the general homogeneity of the evaporation procedure.

On a shorter length scale, however, two different types of intensity variations or inhomogeneities have been observed (cf. Appendix A.4). The first inhomogeneity was identified to be a shading effect of the protruding structures, which resulted from an inclined angle of incident of the molecular beam with respect to the surface normal of the sample (45°). A very illustrative example of this effect can be seen in Fig. 7.3a. Here one of the larger point like protrusion that sticks out of the surface induced a large and structured shadow on an otherwise homogeneously fluorescing sample. The evaporated molecules sticked to one side of the defect that appears brighter; the other side cannot be reached by the molecules and remains dark. This kind of shading effect was observed for all kinds of protruding structures of the sample with various degree.

The second effect occurred only occasionally and is depicted and discussed in Appendix A.4. Here presumably an inhomogeneity of the KCl film that followed the corrugation of the surface inside the flat surface areas induced a weak additional fluorescence contrast. Brighter fluorescent

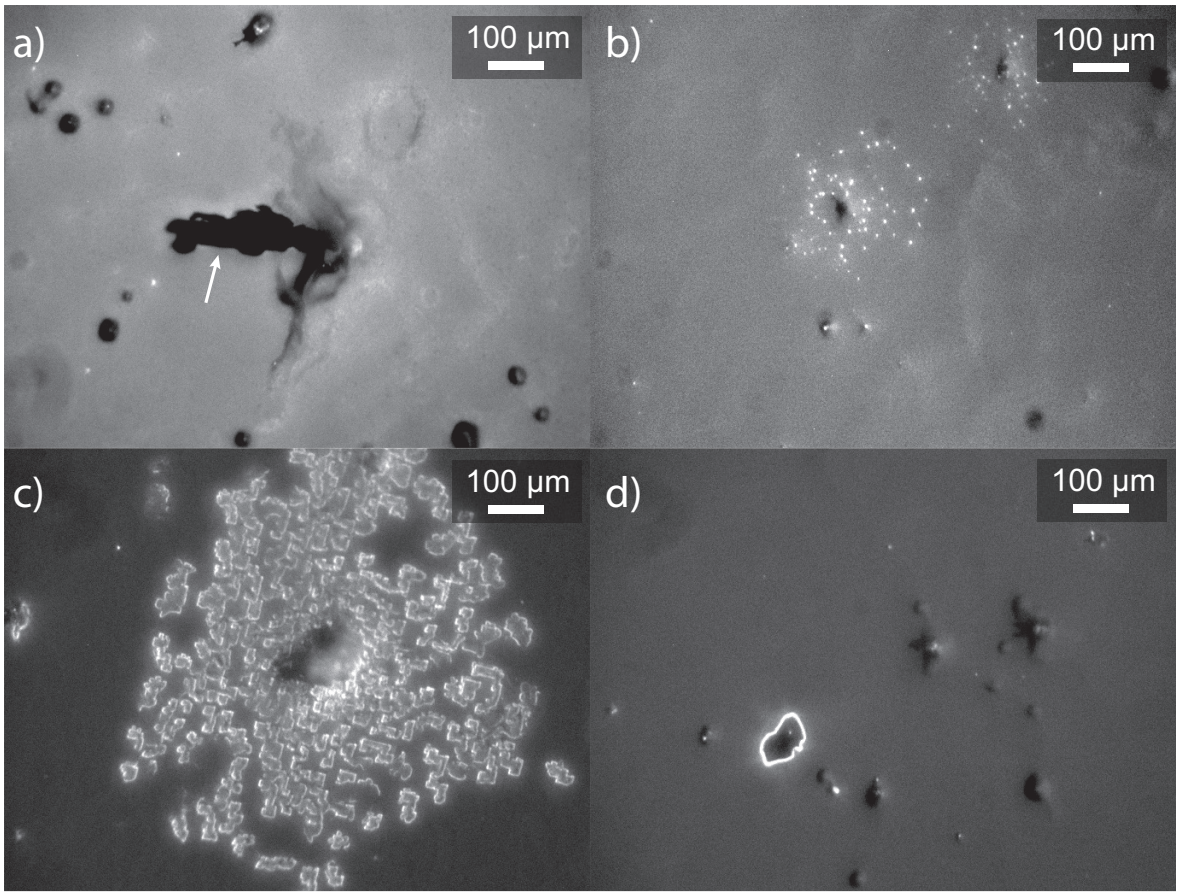

Figure 7.3: *Fluorescence microscope images of mesoscopic surface defects. a) A large point like protrusion casts a shadow (marked by a white arrow) where no molecules adsorbed. b) Small bright fluorescent spots around point like protrusions. c) Bright fluorescent edges of small crystallites around a point like protrusion. d) Bright fluorescent edge of a single point like protrusion. All images have been taken by use of a* $20\times$ *microscope objective at surface coverages between 1% and 5% of a monolayer and a sample temperature of* 6 K*. The sample was illuminated with blue light (*$\lambda_{\mathrm{exc}} = 450$ nm*) and the detection window was set between* $\lambda_{\mathrm{det}} = 485$ nm *and* $\lambda_{\mathrm{det}} = 555$*. For details see text.*

patches surrounded by darker lines were observed (cf. AppendixA.4). The contrast was explained by variations of the KCl film thickness that were induced by the mesoscopic morphology of the sample. Locally thinner regions of the KCl film could possibly lead to a partial quenching of the fluorescence and thereby reduce the fluorescence intensity.

Besides these more general observations also further, more local phenomena that could be related to distinct defects of the sample have been observed. These are exemplary depicted in Fig. 7.3b-d and can be subdivided into two groups: The first group consists of sharp and bright fluorescent spots that appeared inside the otherwise homogeneous fluorescence signal (Fig. 7.3b). These bright spots occurred either very isolated or bunched around some of the point like protrusions. The second group appeared as a brightly fluorescent edge decoration of mesoscopic defect structures of the sample. It was observed both for the smaller crystallites of presumably foreign material around the large point defect (Fig. 7.3c) that was already discussed in the previous chapter (cf. Fig. 7.2b) and around some (but not all) of the other point like protrusions on the surface (Fig. 7.3d).

So far it is not clear what these brighter fluorescent species are. Notably, none of these bright fluorescence spots could be observed without the presence of PTCDA molecules on the sample. Therefore one possible solution would be a photonic antenna effect [159] that massively enhances the absorption rate of PTCDA molecules close to a nearby metallic defect. A different solution could however also be the fluorescence of surface defects like color centers inside the KCl film that do not directly absorb the excitation light but become indirectly excited via close-by excited PTCDA molecules. Such defects could appear preferentially close to a macroscopic sample defect. Possibly the spectral information of these species has been detected during experiments with pentacene on KCl (cf. Appendix B.2). In these experiments spectral features independent from the pentacene molecules could be detected at distinct sample positions. At that time of the experiments, however, a direct correlation to the microscopic position on the sample was impossible.

For a more precise evaluation of such local defects the next experimental step should be the combination of spatial imaging with spectral resolution. This would complement the current measurements with chemical information and could for example be achieved by analyzing the locally detected light by a spectrometer. A different approach would be given by spatially and spectrally resolved FLE measurements similar to the ones proposed for the measurements of single molecules in Chapter 6.4. In case of an indirect absorption of color centers this method would however still measure the absorption lines of the surrounding PTCDA molecules.

Finally, it should be noted that also monolayer phases of organic molecules can be investigated by means of the UHV optical microscope. This has been done in the master thesis of N. Rohbohm with polarization dependent fluorescence microscopy for a monolayer of PTCDA on KCl(100). The structural and optical quality of this monolayer was of comparable quality as the one described in Chapter 5 [156]. Here, in the fluorescence microscope images an additional polarization contrast based on the two types of rotational domains of PTCDA (rotated by 90° with respect to each other) could be observed. Since the size of the individual domains was significantly below the resolution of the microscope, this was only possible due to a slight excess of one type of rotational domain in certain surface regions ($\approx 55 : 45$). It was found that the regions with excess of one type of rotational domain were gigantic with up to 1000 μm^2 in size. Within these regions the excess of one type of rotational domain was almost constant. In addition these regions were found to be related to the mesoscopic morphology of the Ag(100) surface. Therefore, it can be assumed that the morphology of the surface influences the growth probabilities of the otherwise energetically equal domains. Thus a further understanding of this growth processes could possibly help to suppress the rotational domain boundaries and to facilitate the growth of much larger continuous structures with further improved optical properties.

8 Conclusions and outlook

In the present work, condensed and diluted phases of 3,4,9,10-perylenetetracarboxylic dianhydride (PTCDA) have been investigated on thin KCl(100) films on the Ag(100) surface. While the structural properties of the sample system were investigated by spot profile analysis low energy electron diffraction (SPA-LEED), and bright field microscopy, the optical properties were investigated by fluorescence spectroscopy (FL), fluorescence excitation spectroscopy (FLE), and fluorescence microscopy. The work tackled advanced questions of the so far already quite well understood sample system. For this purpose, the experimental setup was improved and completed by additional techniques. A more detailed understanding of the superradiance of the PTCDA on KCl(100) brick wall phase was of interest. Additional topics were the spectroscopy of isolated molecules beyond the inhomogeneous broadening including the detection of single molecules, and the spatial imaging of the fluorescence by use of optical microscopy under ultra high vacuum conditions. In the following the main results of these three topics will be briefly summarized:

I The condensed PTCDA brickwall phase was investigated by SPA-LEED, FL, and FLE with a special focus on the temperature dependence of the superradiance. With respect to the earlier work of M. Müller et al. [16], an improved sample preparation and a redesigned cooling allowed investigating larger aggregates and achieving lower minimum temperatures. A detailed SPA-LEED analysis revealed a broad distribution of the aggregate sizes that included strongly elongated (asymmetric) aggregates.

The temperature dependence of the superradiant enhancement factor showed an atypical initial rise in the low temperature regime that could be explained by a theory based on finite size effects. It was found that besides the strong attractive transition dipole-dipole interactions between nearest-neighbor molecules also the weaker repulsive next-nearest-neighbor interactions are important for the optical properties of brick wall aggregates. It was shown that these interactions induce node planes in the wavefunctions of the excitonic ground state. Thus the transition strengths of these states are reduced or even zero, despite the overall attractive J-aggregate like coupling. It was found that the occurrence of such dark excitonic ground states depends on the size and shape of the aggregates. Especially highly asymmetric aggregates were found to exhibit a larger number of node planes and a dark ground state.

For the simulation of the temperature dependent superradiance of a single aggregate the transition strengths of its dark and bright states were weighted by their thermal population. By averaging over the aggregate size distribution obtained from the SPA-LEED analysis the experimental temperature dependence could be simulated. This broad distribution of aggregate sizes could also be confirmed from an asymmetrically broadened FLE profile and the shifting of the fluorescence signals depending on the wavelength of the excitation laser.

II PTCDA molecules at KCl(100) step sites were investigated by high resolution single molecule spectroscopy. Here first a splitting of the inhomogeneous broadening into two main species that had already been proposed by Paulheim et al. [18] could be proven. In addition, it was shown that the absorption profiles of these main species were inhomogeneously broadened and consist of a superposition of many individual homogeneously broadened single molecule absorption profiles. Here, primarily the statistical fine structure was observed. Far off the center of the inhomogeneous profile, also spectrally isolated single molecule profiles were measured.

   The FLE measurements of these single molecules adsorbed on a surface revealed a molecular behavior qualitatively equivalent to that observed in earlier single molecule studies on molecules in solid hosts. This includes aspects as: the width and the form of the absorption profiles, the saturation behavior with the intensity of the excitation light, an observed broadening with temperature, and a tendency to undergo laser induced and independent spectral jumps. Especially the high energetic resolution and sensitivity should make it possible to measure minimal interactions that had so far not been accessible in typical surface science experiments in future.

III The mesoscopic morphology of the surface of the Ag(100) crystal and the spatial distribution of the fluorescence of isolated PTCDA molecules on thin KCl(100) films on this crystal were investigated by a self-built optical microscope. This was developed for the investigation of samples under ultra high vacuum conditions and images the surface through a glass window.

   Bright field images of the sample revealed a characteristic mesoscopic corrugation and a variety of local defects. In the fluorescence images, a mostly homogeneous coverage of the sample could be proven. However, also exceptions from this homogeneity were observed and could be correlated with the sample morphology. These included shading effects of mesoscopic surface protrusions related to an inclined angle of the molecular beam, occasional intensity variations presumably due to a local inhomogeneity of the KCl film thickness, and very local and bright fluorescence signals at some special surface defects. By polarization dependent fluorescence microscopy at the condensed PTCDA on KCl(100) brickwall phase also local preferences in the growth direction of two different rotational domains could be observed and related to the sample morphology [156].

In conclusion, the results of the present work demonstrated the large variety of interactions, spatially and energetically that can have an influence on the growth and the optical properties of molecules on surfaces. These can be very subtle differences within the local adsorption sites that can induce minimal shifts between two otherwise spectrally equivalent single molecules, the boundary conditions of an molecular aggregate that determine its optical transition strength, or the vicinity to a mesoscopic surface defect that influences the molecular growth and the fluorescence behavior.

Both newly introduced experimental techniques, i.e. the optical single molecule spectroscopy and the optical microscopy inside an UHV experiment, possess large potential for the investigation of surfaces on very different and so far unusual length and energy scales. However, in order to

achieve the full benefits of both techniques, they should be directly combined in future experiments. Then one would be able to spatially distinguish between spectrally superimposed molecular signals in single molecule spectroscopy or to obtain spectral information from specific surface sites. Needless to say, this could also be applied for the spectral and spatial isolation of specific molecular aggregates or the studying of defect sites.

A Publications

A.1 "Superradiance from two dimensional brick-wall aggregates of dye molecules: The role of size and shape for the temperature dependence"

by Alexander Eisfeld, Christian Marquardt, Alexander Paulheim, and Moritz Sokolowski

published in: Physical Review Letters **119**, 097402 (2017).

PRL 119, 097402 (2017) PHYSICAL REVIEW LETTERS week ending 1 SEPTEMBER 2017

Superradiance from Two Dimensional Brick-Wall Aggregates of Dye Molecules: The Role of Size and Shape for the Temperature Dependence

Alexander Eisfeld,[1,*] Christian Marquardt,[2] Alexander Paulheim,[2] and Moritz Sokolowski[2]
[1]*Max-Planck-Institut für Physik komplexer Systeme, Nöthnitzer Str. 38, D-01187 Dresden, Germany*
[2]*Universität Bonn, Institut für Physikalische und Theoretische Chemie, Wegelerstr. 12, 53115 Bonn, Germany*
(Received 10 November 2016; revised manuscript received 10 June 2017; published 31 August 2017)

Aggregates of interacting molecules can exhibit electronically excited states that are coherently delocalized over many molecules. This can lead to a strong enhancement of the fluorescence decay rate which is referred to as superradiance (SR). To date, the temperature dependence of SR is described by a $1/T$ law. Using an epitaxial dye layer and a Frenkel-exciton based model we provide both experimental and theoretical evidence that significant deviations from the $1/T$ behavior can occur for brick-wall-type aggregates of finite size leading even to a maximum of the SR at finite temperature. This is due to the presence of low energy excitations of weak or zero transition strength. These findings are relevant for designing light-emitting molecular materials.

DOI: 10.1103/PhysRevLett.119.097402

Aggregates of fluorescent dye molecules are of great interest not only for various technological applications, e.g., organic light-emitting displays, but also as model systems for studying the delocalization of electronic excitations in many-particle physics. Often in these aggregates the distances between the molecules are so large that there is negligible overlap of electronic wave functions; i.e., there is no exchange of electrons. However, the molecules can exchange electronic excitation via transition dipole-dipole interaction. This can have a strong effect on their optical properties [1–3]. Some aggregates show an enhancement in the fluorescence emission rate of a single electronic excitation compared to that of the individual, noninteracting monomers. This phenomenon is generally referred to as superradiance (SR). (It is related to the general concept of SR introduced by Dicke [4], but in the present case restricted to a single optical excitation [5].) Superradiant molecular aggregates have been extensively investigated experimentally [6–16] and theoretically [17–24].

The SR depends strongly on temperature. In several studies a $1/T$ decay of the SR was observed (see, e.g., Refs. [11,12]). It is explained by an excited lowest energy state of high transition strength (TS) that dominates at low temperature, but is thermally depopulated at the expense of states at higher energies with reduced TS. This "canonical" situation is generally encountered for typical 1D J aggregates of infinite and finite size with parallel arrangement of the transition dipoles [1].

Here we provide experimental and theoretical results demonstrating that strong deviations from this $1/T$ behavior are possible for 2D aggregates with a brick-wall-type arrangement of the transition dipoles and a finite size of $N_x \times N_y$ molecules (cf. inset in Fig. 1). The temperature dependence of the SR yields direct information on the excited states and their energetic spectrum and indirect information on the intermolecular coupling. The 2D brick-wall arrangement bears competing negative interactions (mainly along the direction of the transition dipoles) and positive interactions (mainly in the direction perpendicular to the transition dipoles). As we will demonstrate, this can result in antisymmetric (with respect to the center of the aggregate) excitonic multiparticle wave functions of the lowest excited eigenstate. These wave functions lead to destructive interference of the molecular transition dipoles, causing vanishing TS. As a consequence, for certain aggregate sizes and shapes, at small temperatures an *increase* of the fluorescence with increasing temperature is possible, contrary to the established $1/T$ behavior.

Our experiments were performed on 2D aggregates prepared by epitaxial growth of about one layer of the perylene-type dye PTCDA (see Fig. 1) on the (100) surface of KCl [25,26]. This surface promotes the arrangement of the PTCDA molecules in ordered aggregates of the brick-wall type as illustrated in Fig. 1(a). The transition dipole $\vec{\mu}$ of the PTCDA molecules is parallel to the long molecular axis. The details and the optical spectra of this structure were described in Ref. [27]. One important aspect of our experimental system is that effects such as static disorder or strong exciton-phonon coupling that typically complicate the interpretation of observations are very small, as reviewed in Sec. I of the Supplemental Material [28].

For measuring the SR, the sample was excited by a weak laser beam (476 nm) and fluorescence spectra were recorded systematically under variation of the sample temperature. The SR enhancement η_{SR} is defined via the change in the radiative decay rate, namely, $k_{\mathrm{rad}}^{\mathrm{aggregate}}/k_{\mathrm{rad}}^{\mathrm{monomer}}$. For its experimental determination we use the procedure described by Spano, which exploits the increase of the intensity of the pure electronic transition without excitation of an additional vibron (I_{0-0}) relative to

PRL 119, 097402 (2017) PHYSICAL REVIEW LETTERS week ending 1 SEPTEMBER 2017

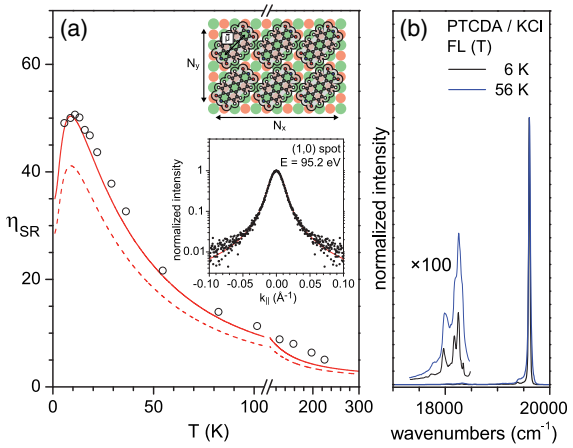

FIG. 1. (a) Enhancement factor η_{SR} of the superradiance as a function of temperature. The open circles show experimental data for a monolayer of PTCDA on the KCl (100) surface. Note the maximum of $\eta_{SR}^{max} = 50$ at $T \approx 16$ K. The dashed line is calculated for a geometric distribution of aggregates sizes with an average size of $\langle N_x \times N_y \rangle = 12.4 \times 12.4$ molecules (cf. Fig. 3) determined from the LEED Profile. The solid line was multiplied by an additional factor of 1.2 adapting the theoretical curve to the experimental situation (for details see the Supplemental Material [28]). Inset top: Hard sphere model of a 3×2 aggregate of PTCDA molecules on the KCl (100) surface. The transition dipole moment $\vec{\mu}$ is depicted for the top left molecule. Inset bottom: Experimental and fitted LEED profile of the PTCDA (1,0) spot using the above mentioned geometric aggregate size distribution. More details are given in the SI. (b) Fluorescence (FL) spectra normalized at the 0-0 transition (19600 cm^{-1}) at 6 and 56 K illustrating the enhancement of the 0-0 transition with respect to the vibronic peaks due to superradiance.

the intensity of transitions to vibrational excited states (I_{0-1}) [24] [cf. Fig. 1(b)]. Our procedure is described in Ref. [27] and additional details on its validity are provided in the Supplemental Material [28]. The obtained SR enhancement η_{SR} versus temperature curve is displayed in Fig. 1(a).

In our experiments, the surface is covered by aggregates separated by structural antiphase boundaries or KCl steps. As a result aggregates with a broad distribution in sizes and shapes are obtained. We determined the aggregate size distribution by a low energy electron diffraction (LEED) profile analysis. We consider aggregates of rectangular shape, with a size of $N_x \times N_y$ molecules with edges as sketched in Fig. 1.

An experimental and a fitted LEED profile are shown in the inset of Fig. 1(a). The details of the analysis are described in the Supplemental Material [28]. We find for the size distribution of the aggregates: $P_{N_x,N_y} \sim \exp(-N_x\Lambda_x^{-1}) \times \exp(-N_y\Lambda_y^{-1})$, $\Lambda_{x,y} = \ln[\Gamma_{x,y}/(\Gamma_{x,y} - 1)]$, with $\Gamma_{x,y}$ denoting the expected values of the underlying one dimensional distributions. Our analysis yields $\langle N_x \times N_y \rangle = 12.4 \times 12.4$ molecules ($\hat{=}156 \times 156$ Å^2). Important, because N_x and N_y are independent, the distribution yields also aggregates of elongated shape with aspect ratios $N_x/N_y \neq 1$. We note that due to an optimized sample preparation the average linear aggregate size was about twice as large as that reported in earlier experiments [27] (see also Supplemental Material [28]). This leads to a larger number of coherently coupled molecules. In combination with an extension of the experimental accessible temperature range to low temperatures we obtain an $\eta_{SR}(T)$ dependence with new interesting features: At high temperatures ($\gtrsim 20$ K) $\eta_{SR}(T)$ is roughly compatible with the noted $1/T$ dependence. However, at low T η_{SR} does not decrease, but slightly increases with T and goes through a maximum at a finite temperature $T_{max} \approx 10$ K. This interesting behavior deserves attention.

To understand these observations we perform numerical simulations based on the Frenkel exciton model [43]. We treat each monomer as a two level system with an electronic ground state $|g\rangle$ and one electronically excited state $|e\rangle$, with energies E_g and E_e, respectively. These two states are coupled by a transition dipole $\vec{\mu}$. The electronic ground state is taken as the state where all monomers are in their ground state, i.e., $|g_{agg}\rangle = |g\rangle \cdots |g\rangle$. Fluorescence originates from states which possess a single excitation. To describe such states of the dipole-dipole interacting monomers we consider a basis of localized excitations $|n\rangle = |g\rangle \cdots |e\rangle \cdots |g\rangle$; i.e., states where one monomer n is excited and all the others are in the ground state. The Hamiltonian (of one domain) is given by

$$H_{ex} = \sum_n \epsilon |n\rangle\langle n| + \sum_{n,m} V_{nm} |n\rangle\langle m|. \quad (1)$$

Here, $\epsilon = E_e - E_g$ is the energy difference between the electronic excited state and the electronic ground state, and V_{nm} is the interaction strength between states $|n\rangle$ and $|m\rangle$, which we take as the point transition dipole-dipole interaction $V_{nm} = (1/4\pi\epsilon_0)(\alpha/R_{nm}^3)[\vec{\mu}_n \cdot \vec{\mu}_m - 3(\vec{\mu}_n \cdot \vec{R}_{nm})(\vec{\mu}_m \cdot \vec{R}_{nm})]$, with $\vec{R}_{nm}$ the direction between monomer n and m and R_{nm} the corresponding distance. The scaling factor α is used to take into account various effects including, in particular, the Franck-Condon factor that is relevant for the interaction, cf. Ref. [27], and the polarization screening by the KCl surface. For $\alpha = 1$ the dominant interactions are presented in Fig. 1 of Ref. [27]. All interactions between nearest neighbors are negative. But there are positive interactions between next nearest neighbors perpendicular to the dipole direction. We note that in general one has to use a more sophisticated method to calculate the interactions and one also has to take internal and external vibrational modes of the molecules into account explicitly [41]. However, for the present purpose, where we aim at a qualitative understanding, we found it sufficient to use the simple form of the above given point dipole-dipole interaction.

Formally the eigenenergies and eigenstates can be written as $H_{\mathrm{ex}}|\psi_k\rangle = E_k|\psi_k\rangle$ with $|\psi_k\rangle = \sum_n c_{nk}|n\rangle$. The radiative lifetime of these states is inversely proportional to their TS [44], which are calculated as $F_k = |\langle g_{\mathrm{agg}}|\sum_n \hat{\vec{\mu}}_n|\psi_k\rangle|^2$, where $\hat{\vec{\mu}}_n$ is the dipole operator of monomer n. For aligned molecules with identical transition dipoles ($\vec{\mu}_n = \vec{\mu}$), as in our case, this yields $F_k = \mu^2 A_k$ with

$$A_k = \left|\sum_n c_{nk}\right|^2. \tag{2}$$

To treat finite temperatures we assume that thermalization in the excited state manifold happens fast on the time scale of radiative decay, so that one has always a Boltzmann distribution, where each excited state is populated according to $p_k(T) = (1/Z)\exp(-E_k/k_B T)$ with $Z = \sum_k \exp(-E_k/k_B T)$ and k_B being the Boltzmann factor. Then the (temperature-dependent) decay rate from the excited state to the ground state is given by $F(T) = \sum_k p_k(T)F_k \equiv \mu^2 \eta_{\mathrm{SR}}(T)$ [44] with the enhancement factor

$$\eta_{\mathrm{SR}}(T) = \sum_k p_k(T)A_k. \tag{3}$$

For our calculations we consider the same type of rectangular aggregates as for the LEED profile analysis. We neglect any interaggregate coupling (from our experiments we have no indication of exciton diffusion between aggregates). As in Ref. [27] we take $|\vec{\mu}| = 7.4$ D. For the calculations we use $\alpha = 0.4$. This is about twice as large as the interaction strength that is obtained when we take only the Franck-Condon factor of the 0-0 transition into account [27] and treats several of the above noted effects in an effective manner. This value of α is motivated because it fits the calculations to the experiment. We note that our principle findings are robust with respect to the value of α. In Sec. II. b of the Supplemental Material [28] we treat the coupling to phonons and discuss our approximations. We note that the used value of α can also fit the $\eta_{\mathrm{SR}}(T)$ curve of Ref. [27].

Figure 2 presents exemplary curves from the calculations, illustrating three cases (A–C) representing different behaviors of $\eta_{\mathrm{SR}}(T)$, which are found for different aspect ratios N_x/N_y of the aggregates. From top to bottom N_y is increased, while $N_x = 10$ is fixed. In case A (10×10), we find a monotonic decay of $\eta_{\mathrm{SR}}(T)$ with increasing temperature. The curve shows a fast initial decay before it decays more slowly (roughly like $1/T$). For case B (10×20), the initial decay is very steep and followed by a slight increase leading to a local maximum and a slow decay again. Finally, in case C (10×30), an initial increase is found followed by a decrease after a maximum. These three cases are a consequence of the different energies and corresponding TS of the lowest excited eigenstates of the different aggregates. These are illustrated together with the wave functions of the lowest states ($k = 1$) in the right column of Fig. 2.

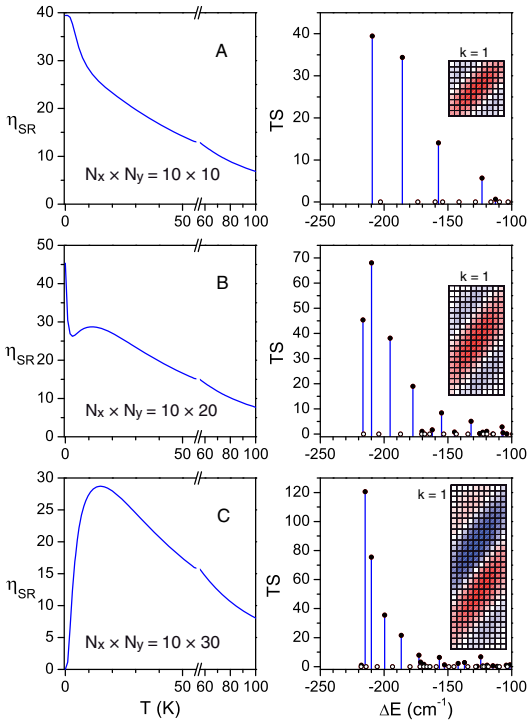

FIG. 2. Left: Temperature dependence of the enhancement factor η_{SR}, according to Eq. (3) for different aggregates of $N_x \times N_y$ molecules. Right: Stick spectra of the transition strengths of the lowest eigenstates corresponding to the respective aggregates. The energies are referenced versus the excitation energy ϵ of the single molecule. The eigenstates are marked by filled (TS > 0) or open circles (TS $= 0$). The inset illustrates the normalized wave function of the lowest state ($k = 1$). The values of the real coefficients c_{nk} are plotted with red and blue color indicating positive and negative values, respectively. Note that the two wave functions at the top are symmetric, while the lower is antisymmetric leading to TS $= 0$ for the $k = 1$ state.

To understand the $\eta_{\mathrm{SR}}(T)$ behavior we consider the energies E_k and the corresponding TS ($\mu^2 A_k$) of the lowest eigenstates. Numerically, we find that if the state with the lowest energy is bright ($A_1 > 0$), then the state with the next higher energy is dark ($A_2 = 0$), and vice versa. Thus it is instructive to discuss the origin of bright and dark states as the lowest energy states. It can be understood from the wave functions illustrated in the right panel of Fig. 2 and it is an effect from the brick-wall arrangement. Important to note are the parallel node lines of the wave functions running along the direction of the transition dipoles which are a consequence of the intermolecular interactions. Because a pair of molecules (n, m) contributes to the eigenenergy by $V_{nm}c_{nk}c_{mk}$ the presence of node lines turns positive interactions V_{nm} between molecules separated by a

PRL 119, 097402 (2017) PHYSICAL REVIEW LETTERS week ending 1 SEPTEMBER 2017

node line into negative contributions by the factor $c_{nk}c_{mk} < 0$. The interplay between negative interactions along the dipole direction (supporting $c_{nk}c_{mk} > 1$) and positive interactions in the perpendicular direction thus leads to the node lines in the wave functions. The number of node lines increases with the elongation of the aggregate. In addition the symmetry of the wave function of the lowest eigenstate can change. This is seen in Fig. 2. While the wave function is symmetric for the quadratic (10×10) and the slightly elongated aggregate (10×20) (2 node lines), an antisymmetric wave function (3 node lines) is formed for the strongly elongated aggregate (10×30). Similar patterns of the wave functions with alternating symmetries are observed for larger aggregates with increasing elongation. Importantly, antisymmetric wave functions lead to zero values of TS, because the positive and negative c_{nk} values cancel each other in Eq. (2). Thus the size- and shape-dependent formation of symmetric and antisymmetric wave functions of the lowest energy state leads to the occurrence of bright or dark eigenstates at the lowest energies.

In case C one will have a rise in $\eta_{SR}(T)$ for increasing temperature, since bright states are thermally occupied. In the opposite case when the lowest state is bright (and the second excited state dark) one has an initial decrease of $\eta_{SR}(T)$ (cases A and B). The details depend on the TS and the energy differences between the lowest states. Numerically, we found that most of the TS is located on the first 5–10 states where the ratio between bright and dark states is roughly equal. As long as the temperature is smaller than the energy difference of these states, details of the TS play a role. When the temperature becomes larger, details of the energy differences and TS of the few lowest energy states are no longer important and for all aggregate sizes one obtains a similar curve, which goes roughly like $1/T$ as expected for a single bright state at $k = 1$ and a linear density of states [24].

In Fig. 3 we present an overview of η_{SR}^{max} and the corresponding temperatures T_{max} for which this maximum occurs for a large number of $N_x \times N_y$ combinations. In the top panel η_{SR}^{max} values are displayed for different $N_x \times N_y$ aggregates. In the bottom panel the corresponding T_{max} values are shown, whereby regions corresponding to the three cases A, B, and C are indicated. Aggregates where η_{SR}^{max} occurs at $T = 0$ (black region) are foremost found for an aspect ratio N_x/N_y close to one (cases A and B), but also for N_x or $N_y \leq 3$ (case A). In the latter case, node planes perpendicular to the direction of the transition dipoles cannot form due to the reduced coupling in that direction. From the top panel one sees that for symmetric aggregates $\eta_{SR}^{max} \sim 2(N_x + N_y)$, which is much smaller than the number of coherently coupled molecules ($N_x \times N_y$). Outside the black area, the maximum occurs at finite temperatures (case C). In the corresponding regions in the top panel one finds a clear decrease in η_{SR}^{max} compared to similar aggregates located in the black region of the bottom panel. One

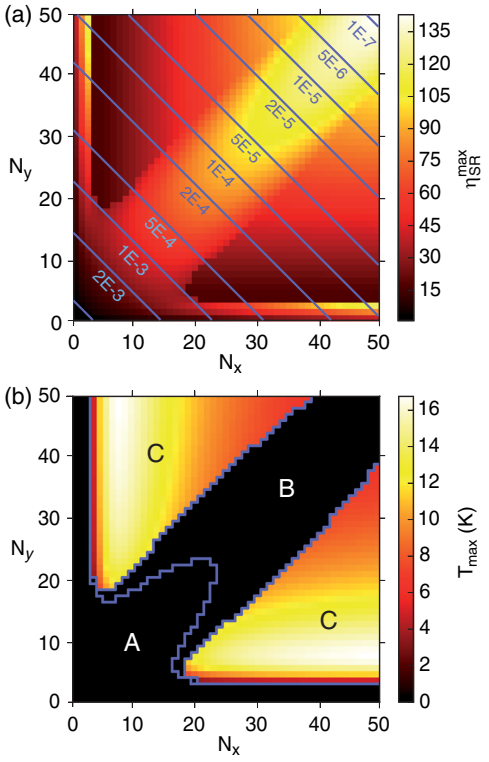

FIG. 3. (a) The maximum of the enhancement factor η_{SR}^{max} for aggregates of different size $N_x \times N_y$. The blue overlayed isolines refer to the geometric aggregate size distribution used for the calculated $\eta_{SR}(T)$ curve presented in Fig. 1(a). (b) The corresponding temperature T_{max}. The regions where the three cases A, B, and C apply are indicated and separated by blue lines. For further details see text.

also sees that in this region the smaller value of N_x and N_y determines η_{SR}^{max} and the temperature T_{max} at which it appears.

We finally compare to our experimental results. In Fig. 1(a), in addition to the experimental data, the calculated $\eta_{SR}(T)$ curves are shown: $\eta_{SR} = \sum \tilde{P}_{N_x,N_y} \cdot \eta_{SR}(N_x, N_y, T)$, whereby $\tilde{P}_{N_x,N_y} = P_{N_x,N_y}(N_x \times N_y) / \sum P_{N_x,N_y}(N_x \times N_y)$. Here, results from Eq. (3) for different $N_x \times N_y$ aggregates are averaged using the probability distribution P_{N_x,N_y} extracted from LEED and a geometric factor $N_x \times N_y$ accounting for the absorption cross section of the respective aggregates. The distribution P_{N_x,N_y} is indicated in Fig. 3(a). We obtain a very good agreement to the shape of the experimental $\eta_{SR}(T)$ curve. We note that the $\eta_{SR}(T)$ curve cannot be explained by quadratic aggregates only, because then the T dependence (in particular the shape) cannot be fitted. This implies that in the experiment a large number of rectangular aggregates with a ratio $N_x/N_y \neq 1$ exists, which is plausible from the two independent growth directions x and

y, and also supported from LEED analysis (see Supplemental Material [28]).

Our theoretical and experimental results show that for 2D brick-wall aggregates the smallest temperature does not necessarily give the largest fluorescence rate. Theoretically, we have found that the temperature dependence of the enhancement can show various different behaviors, which strongly depend on the shape of aggregates. The reason is that elongated aggregates favour antisymmetric wave functions which exhibit small transition strength. Our results can be used for the design of light emitting materials, since they demonstrate that the radiative lifetime can be dramatically effected not only by the size but also by the shape of finite size molecular aggregates.

We acknowledge helpful discussions with J. Wollschläger and support by the Deutsche Forschungsgemeinschaft through the Project No. So407/8-1.

*eisfeld@mpipks-dresden.mpg.de

[1] *J-Aggregates*, edited by T. Kobayashi (World Scientific, Singapore, 1996).
[2] F. Würthner, T. E. Kaiser, and C. R. Saha-Möller, Angew. Chem., Int. Ed. Engl. **50**, 3376 (2011).
[3] S. K. Saikin, A. Eisfeld, S. Valleau, and A. Aspuru-Guzik, Nanophotonics **2**, 21 (2013).
[4] R. H. Dicke, Phys. Rev. **93**, 99 (1954).
[5] M. Gross and S. Haroche, Phys. Rep. **93**, 301 (1982).
[6] F. Meinardi, M. Cerminara, A. Sassella, R. Bonifacio, and R. Tubino, Phys. Rev. Lett. **91**, 247401 (2003).
[7] H. Z. Wang, X. G. Zheng, F. L. Zhao, Z. L. Gao, and Z. X. Yu, Phys. Rev. Lett. **74**, 4079 (1995).
[8] S.-H. Lim, T. G. Bjorklund, F. C. Spano, and C. J. Bardeen, Phys. Rev. Lett. **92**, 107402 (2004).
[9] H. Fidder, J. Knoester, and D. A. Wiersma, Chem. Phys. Lett. **171**, 529 (1990).
[10] H. Fidder, J. Terpstra, and D. A. Wiersma, J. Chem. Phys. **94**, 6895 (1991).
[11] D. H. Arias, K. W. Stone, S. M. Vlaming, B. J. Walker, M. G. Bawendi, R. J. Silbey, V. Bulović, and K. A. Nelson, J. Phys. Chem. B **117**, 4553 (2013).
[12] S. De Boer and D. A. Wiersma, Chem. Phys. Lett. **165**, 45 (1990).
[13] S. Özjcelik and D. L. Akins, J. Phys. Chem. B **103**, 8926 (1999).
[14] D. L. Akins, S. Özçelik, H.-R. Zhu, and C. Guo, J. Phys. Chem. **100**, 14390 (1996).
[15] V. F. Kamalov, I. A. Struganova, and K. Yoshihara, J. Phys. Chem. **100**, 8640 (1996).
[16] M. Müller, S. Izadnia, S. M. Vlaming, A. Eisfeld, A. LaForge, and F. Stienkemeier, Phys. Rev. B **92**, 121408 (2015).
[17] M. Orrit, C. Aslangul, and P. Kottis, Phys. Rev. B **25**, 7263 (1982).
[18] J. Grad, G. Hernandez, and S. Mukamel, Phys. Rev. A **37**, 3835 (1988).
[19] E. O. Potma and D. A. Wiersma, J. Chem. Phys. **108**, 4894 (1998).
[20] F. C. Spano and S. Mukamel, J. Chem. Phys. **91**, 683 (1989).
[21] D. J. Heijs, V. A. Malyshev, and J. Knoester, Phys. Rev. Lett. **95**, 177402 (2005).
[22] F. C. Spano, J. R. Kuklinski, and S. Mukamel, Phys. Rev. Lett. **65**, 211 (1990).
[23] F. C. Spano, Chem. Phys. Lett. **331**, 7 (2000).
[24] F. C. Spano and H. Yamagata, J. Phys. Chem. B **115**, 5133 (2011).
[25] T. Dienel, C. Loppacher, S. Mannsfeld, R. Forker, and T. Fritz, Adv. Mater. **20**, 959 (2008).
[26] M. Müller, J. Ikonomov, and M. Sokolowski, Surf. Sci. **605**, 1090 (2011).
[27] M. Müller, A. Paulheim, A. Eisfeld, and M. Sokolowski, J. Chem. Phys. **139**, 044302 (2013).
[28] See Supplemental Material at http://link.aps.org/supplemental/10.1103/PhysRevLett.119.097402 for detailed properties of the sample, details on the theoretical modeling, aspects of the determination of the superradiant enhancement from the fluorescence spectra, and the LEED profile analysis. The Supplemental Material includes Refs. [29–42].
[29] M. Müller, A. Paulheim, C. Marquardt, and M. Sokolowski, J. Chem. Phys. **138**, 064703 (2013).
[30] A. Paulheim, M. Müller, C. Marquardt, and M. Sokolowski, Phys. Chem. Chem. Phys. **15**, 4906 (2013).
[31] Q. Guo, A. Paulheim, M. Sokolowski, H. Aldahhak, E. Rauls, and W. G. Schmidt, J. Phys. Chem. C **118**, 29911 (2014).
[32] A. Paulheim, C. Marquardt, M. Sokolowski, M. Hochheim, T. Bredow, H. Aldahhak, E. Rauls, and W. G. Schmidt, Phys. Chem. Chem. Phys. **18**, 32891 (2016).
[33] A. Paulheim, C. Marquardt, H. Aldahhak, E. Rauls, W. G. Schmidt, and M. Sokolowski, J. Phys. Chem. C **120**, 11926 (2016).
[34] H. Fidder, J. Knoester, and D. A. Wiersma, J. Chem. Phys. **95**, 7880 (1991).
[35] A. Eisfeld and J. S. Briggs, Chem. Phys. **324**, 376 (2006).
[36] M. Voigt, A. Langner, P. Schouwink, J. M. Lupton, R. F. Mahrt, and M. Sokolowski, J. Chem. Phys. **127**, 114705 (2007).
[37] C. Marquardt, A. Paulheim, and M. Sokolowski, Surf. Sci. **641**, 128 (2015).
[38] J. Libuda, F. Winkelmann, M. Bäumer, H.-J. Freund, Th. Bertrams, H. Neddermeyer, and K. Müller, Surf. Sci. **318**, 61 (1994).
[39] C. S. Lent and P. I. Cohen, Surf. Sci. **139**, 121 (1984).
[40] C. Marquardt, A. Paulheim, N. Rohbohm, R. Merkel, and M. Sokolowski, Rev. Sci. Instrum. **88**, 083702 (2017).
[41] J. Roden, A. Eisfeld, M. Dvořák, O. Bünermann, and F. Stienkemeier, J. Chem. Phys. **134**, 054907 (2011).
[42] M. Henzler, Appl. Phys. A **34**, 205 (1984).
[43] J. Frenkel, Z. Phys. A **59**, 198 (1930).
[44] V. May and O. Kühn, *Charge and Energy Transfer Dynamics in Molecular Systems*, 3rd ed. (Wiley-VCH, Weinheim, 2011).

A.2 "Supplemental Material: Temperature dependence of superradiance in finite brick-wall aggregates"

by Alexander Eisfeld, Christian Marquardt, Alexander Paulheim, and Moritz Sokolowski

published as supplemental material to: Physical Review Letters **119**, 097402 (2017).

SUPPLEMENTAL MATERIAL.
Temperature dependence of superradiance in finite brick-wall aggregates

Alexander Eisfeld,[1,*] Christian Marquardt,[2] Alexander Paulheim,[2] and Moritz Sokolowski[2]

[1] *Max-Planck-Institut für Physik komplexer Systeme, Nöthnitzer Str. 38, D-01187 Dresden, Germany*
[2] *Universität Bonn, Institut für Physikalische und Theoretische Chemie, Wegelerstr. 12, 53115 Bonn, Germany*

In this Supporting Information we provide additional details on the following points:

I. What are the detailed properties of the sample and what do they imply for the theoretical modeling?

II. Details on the theoretical modeling. In particular, we discuss how we handle vibrations.

III. Aspects of the determination of the superradiant enhancement from the fluorescence (FL) spectra.

IV. LEED profile analysis for determination of the aggregate size distribution.

I. DISCUSSION OF VARIOUS ASPECTS REGARDING THE EXPERIMENT AND THEIR CONSEQUENCES FOR THE THEORETICAL MODELING

In several recent publications we have characterized the experimental system [1–7]. In the following we will briefly discuss specific properties that are important in the context of the present work, and which also motivated many aspects of our theoretical modeling.

A. Sample properties

a. The KCl surface as template for aggregate formation: The KCl surface, on which the PTCDA molecules were deposited was prepared as an epitaxial film on a Ag(100) surface. It is not perfectly flat and consists of terraces that are limited by KCl steps remnant from the epitaxial growth process. These steps on the KCl surface limit the maximum achievable size of the PTCDA domains. However, the main limitation of the domain sizes is caused by the incoherent nucleation of two types of PTCDA domains that are rotated by 90° with respect to each other. From electrostatic considerations one expects that the molecules at the edges of a domain are arranged as depicted in Fig. 1 of the Letter.

b. Optimized preperation protocol: The new experiment is based on an optimized preperation protocol of the PTCDA layer, yielding much larger average aggregate sizes ($\langle N_x \times N_y \rangle = 12.4 \times 12.4$ molecules, details see Chapter IV) compared to the protocol used for the sample ($\langle N_x \times N_y \rangle = 7 \times 7$ molecules) described in Ref. [1]. This was achieved by using a kinetically favourable very low deposition rate of the PTCDA (25 min per layer) and a subsequent prolonged annealing procedure of the sample (90 min at 260 K) to induce healing of PTCDA aggregate boundaries. Also the quality of the Ag(100) crystal surface and the KCl film was improved before PTCDA deposition. The Ag(100) crystal was now annealed for 60 min at 1000 K (before 723 K). The KCl film (about 5 KCl monolayers in thickness) was grown at 520 K (before 500 K) and subsequently annealed (520 K, 20 min) to smoothen the film. Now we achieved an average KCl terrace size of $2\pi/\mathrm{FWHM} \sim 350$ Å. This was estimated from the width of the KCl(1,0) profile at anti-phase conditions under consideration of the instrument function of the SPA-LEED apparatus.

c. Static disorder within one domain: Disorder in the positions and orientations of the PTCDA molecules is negligible. The PTCDA brickwall structure is commensurate to the KCl(100) lattice [2] and strong Coulombic interactions exist between the partially negatively charged anhydride groups of the PTCDA and the K^+ ions of the sample. Therefore, the PTCDA molecules are strongly bound on the KCl(100) surface and exhibit well-defined adsorption sites [5]. This is in contrast to typical self-assembled molecular aggregates in solution, where disorder in the transition energies of the monomers is an important issue [8]. We can estimate the amount of this disorder from the width of the absorption spectrum at low coverage, i.e. for isolated molecules ($\lesssim 1\%$ of a monolayer PTCDA). In Ref. [1] we discuss this point in detail and conclude that the random disorder has a distribution with a full width at

*Electronic address: eisfeld@mpipks-dresden.mpg.de

half maximum (FWHM) of the absorption line width ≈ 27 cm^{-1}. Further insight comes from calculated transition energies for PTCDA located at different KCl step sites [7]. One sees in particular that the influence of the step on the transition energy variation of molecules not excactly located at the step is expected to be below 10 cm^{-1}. In Ref. [1] we have performed numerical simulations for the lineshape using Gaussian disorder and found that this disorder strength is also consistent with the experimental result for a monolayer. To estimate how strong the results of the present Letter are affected by static disorder in the transition energies, we have performed such simulations for exemplary aggregates. For disorder which is consistent with the linewidth of isolated PTCDA molecules on KCl (i.e., FWHM ≈ 27 cm^{-1}) we find, as expected, only minor changes in the curves of $\eta_{\mathrm{SR}}(T)$ shown in Fig. 1 of the paper.

d. Vibron (phonon) emission / coupling to molecular vibrations: For our arrangement one can estimate that the dipole-dipole interaction between the monomers is small compared to the energies of the majority of the molecular vibrational modes (> 230 cm^{-1}). Therefore, in contrast to many J-aggregates in solution [9] or PTCDA oligomers in Helium nanodroplets [10] one does not have to take these modes explicitly into account. There are some molecular low energy modes (with energies approximately smaller than 200 cm^{-1}) which will couple to the electronic transition [6]. However, the Huang-Rhys-factors of these modes are very small, so that one does not expect a large influence; in particular for the states at the bottom of the exciton band, which are responsible for the low temperature behaviour of the SR enhancement.

e. Coupling to substrate phonons: From measurements on isolated molecules one sees that at low temperature (up to approximately 20 K) disorder dominates the inhomogeneous molecule linewidth [7]. Since this linewidth is quite small (less then 5 cm^{-1} in FLE) the coupling to low energy phonons is also expected to be quite small.

f. Spatial diffusion: We have no evidence of exciton diffusion between domains (aggregates). For example, from recording the polarization of the emission with respect to the absorption we know that there is no excitation transfer between domains with 90 degree rotation of the molecules (note that this is expected to be the most relevant mechanism for domain formation). Therefore, in the Letter we have focused on individual domains.

g. Multi-exciton effects: We worked at low laser powers (30 mW) with the laser focused to a spot on the sample. The laserspot had a diameter of about 0.3 mm, which resulted in a power density of ≈ 40 W/cm^{-2} on the sample. Therefore there was not more than one excitation in a domain at the same time (we estimate on average less than 0.1 excitations per 1000 molecules). Hence, multi-exciton effects such as exciton-exciton scattering or exciton-exciton annihilation within one domain are negligible. In addition, we have varied the power of the excitation laser and observed a linear dependence of the number of emitted photons with the laser intensity.

h. Re-absorption of emitted photons: Is negligible: Our sample consists of a single monolayer PTCDA. The measurement is performed such that the excitation laser hits the monolayer with at angle of 45°. Emission is detected in normal direction to the monolayer.

i. Emission from trap sites: We have not seen any variations in the fluorescence spectra as a function of temperature which could indicate the emission from different states. Temperature variations of the aggregate spectra (fluorescence and absorption) are discussed in detail in Ref. [1]. No spectral changes other than the noted variation in the enhancement of the 0-0 emission and general broadening of the lines due to thermal dephasing are seen [1]. Under these aspects the spectra of our sample are much clearer than those of common organic films which often show different emissive species at different temperatures (e.g., see [11]).

j. Polarisation of light: The sample was excited by linearly polarized laser light. The polarisation of the laser was chosen in the way that aggregates of both symmetry equivalent growth directions (cf. Ref. [2]) were excited. The fluorescence detection was performed independent of the polarization.

II. DETAILS ON THE THEORETICAL MODELING

The theoretical derivations of the temperature dependence of the fluorescence rate presented in this section are for aggregates with general arrangement of the monomers. Results specific to a parallel arangement of the molecules are indicated; these results are applied to PTCDA domains in the Letter.

A. Electronic Hamiltonian

We treat each molecule (monomer) as a two level system with ground state $|g\rangle$ and one excited state $|e\rangle$, with energies E_g and E_e respectively. This approximation is justified because the next electronic state of PTCDA is

energetically well separated. The two states $|g\rangle$ and $|e\rangle$ are coupled by a transition dipole $\vec{\mu}$, which for PTCDA is aligned along the long molecular axis.

The electronic ground state of the aggregate is taken as the state where all monomers are in their ground state, i.e.,

$$|g_{\rm agg}\rangle = |g,\ldots,g\rangle = |g\rangle\cdots|g\rangle \tag{1}$$

Fluorescence originates from a state which posseses a single excitation. To describe such states of the dipole-dipole interacting monomers we consider a basis of localized excitations

$$|n\rangle = |g\rangle\cdots|e\rangle\cdots|g\rangle \tag{2}$$

i.e., states where one monomer n is excited and all the others are in the ground state. The Hamiltonian in this one-exciton manifold is given by

$$H_{\rm ex} = \sum_n \epsilon_n |n\rangle\langle n| + \sum_{n,m} W_{n,m}|n\rangle\langle m| \tag{3}$$

Here $\epsilon_n = E_e(n) - E_g(n)$ is the energy difference between the electronic excited state and the electronic ground state of monomer n and $W_{n,m}$ is the interaction-strength between a state $|n\rangle$ and $|m\rangle$. For the derivations presented below the exact form of the interaction does not matter. In the numerical calculations of the Letter the point dipole-dipole interaction is used, which is expected to be sufficiently accurate for the distances between the PTCDA molecules on the KCl surface (the center-to-center distances larger than 1 nm).

Formally the eigenenergies and eigenstates can be written as

$$H_{\rm ex}|\psi_k\rangle = E_k|\psi_k\rangle \tag{4}$$

with

$$|\psi_k\rangle = \sum_n c_{nk}|n\rangle \tag{5}$$

Note that in general one has to take internal vibrational modes of the molecules and coupling to the surrounding into account. We will comment on internal vibrations below. However, first we will discuss the radiative decay for this purely electronic Hamiltonian.

1. Radiative decay rates

Let us start by considering the case when the aggregate is prepared in an excited eigenstate $|\psi_k\rangle$. The radiative lifetime of this state is inversely proportional to its transition strength[12] which is calculated via

$$F_k = \left|\langle g\cdots g|\sum_n \hat{\vec{\mu}}_n|\psi_k\rangle\right|^2 \tag{6}$$

(in this work we neglect the overall dependence on the cube of the transition frequency). Using Eq. (5) we can write

$$F_k = \Big|\sum_n c_{nk}\vec{\mu}_n\Big|^2 \tag{7}$$

$$= \mu^2\Big|\sum_n c_{nk}\Big|^2 \quad (\text{for } \vec{\mu}_n = \vec{\mu}) \tag{8}$$

where the second line holds when all molecules are aligned parallel, and have identical transition dipoles, as it is the case for the PTCDA domains considered in the Letter. This leads to Eq. (2) of the Letter.

a. Finite temperature: To treat finite temperature T, in general one has to consider explicitly the relaxation and decoherence dynamics in the excited state manifold. For the sizes of the domains we consider in the Letter (larger than 100 molecules) the corresponding density matrix evoltion becomes quite involved. However, more seriously, for PTCDA molecules on KCl we do not have detailed information on the relaxation dynamics or the underlying processes. From fluorescence measurements of diluted PTCDA on KCl we conclude that relaxation dynamics happens faster than the fluorescence lifetime (which is around 1 ns). Based on this observation we model fluorescence assuming that thermalization happens fast on the timescale of radiative decay, so that one is always in a Boltzmann distribution,

where each state is populated according to $p_k(T) = \frac{1}{Z}\exp\{-E_k/k_\mathrm{B}T\}$ with $Z = \sum_k \exp\{-E_k/k_\mathrm{B}T\}$ and k_B is the Boltzmann factor. Note that for an enhancement of $\eta_\mathrm{SR} = 50$, as deduced for PTCDA in the Letter, this implies that relaxation in the excited state manifold should happen in the order of a few picoseconds.

Then the (temperature-dependent) decay-rate for excitation to the ground state is given by [12]

$$F(T) = \sum_k p_k(T) F_k \tag{9}$$

With Eq. (8) this leads to Eq. (3) of the Letter.

Note that a global scaling of the dipole-dipole interaction, i.e. $W_{nm} \to \alpha W_{nm}$, does not change the coefficients c_{nk} and therefore also F_k is unchanged. However, the eigenenergies scale as $E_k \to \alpha E_k$. Thus one finds that under the above scaling the curve $F(T)$ stays invariant, if one scales the temperature via $T \to \alpha T$.

B. Inclusions of vibrations

So far we have ignored internal vibrations of the molecules. Including vibrations the eigenstates of a monomer (within Born-Oppenheimer approximation) are given by $|g,\nu\rangle$ and $|e,\nu\rangle$, where ν lables the vibrational states in the ground and excited electronic state. To a good approximation the transition dipole operator can be considered to be independent of vibrations so that one obtains $\langle g,\nu|\vec{\boldsymbol{\mu}}|e,\tilde{\nu}\rangle = \vec{\mu} f_{\nu,\tilde{\nu}}$ with the so-called Franck Condon factors.

$$f_{\nu,\tilde{\nu}} = \langle \nu|\tilde{\nu}\rangle \tag{10}$$

1. *Vibrations in the one-exciton manifold*

To describe excited states of the aggregate we will then use as a basis states $|n,\vec{\nu}_n\rangle$ where monomer n is electronically excited while all other monomers are in their electronic ground state. The respective vibrational states are comprised in the vector $\vec{\nu}_n$. The Hamiltonian (3) then becomes

$$\begin{aligned} H_\mathrm{ex} = &\sum_n \sum_{\vec{\nu}_n} \epsilon_{n,\vec{\nu}_n} |n,\vec{\nu}_n\rangle\langle n,\vec{\nu}_n| \\ &+ \sum_n \sum_{\vec{\nu}_n} \sum_m \sum_{\vec{\nu}_m} V_{n,\vec{\nu}_n;m,\vec{\nu}_m} |n,\vec{\nu}_n\rangle\langle m,\vec{\nu}_m| \end{aligned} \tag{11}$$

and $V_{n,\vec{\nu}_n;m,\vec{\nu}_m} = f_{\nu_n,\tilde{\nu}_n} f_{\tilde{\nu}_m,\nu_m} W_{nm}$. The diagonalization of this Hamiltonian is in general limited to rather small aggregates if one has to take many vibrationaly excited states into account.

As mentioned above (point I.c) all dominant vibrational modes have frequencies more then twice as large as the dipole-dipole interaction between the molecules. To a good approximation the vibrationally excited states of these modes do not have to be explicitly considered when calculating the low energy eigenstates of Eq. (11). The most important states to consider are $|n,\vec{0}_n\rangle$, i.e., the states where monomer n is electronically excited and in the vibrational ground state of the excited potential surface and all other monomers are in the ground vibrational state of the lower potential surface. As discussed above (point 1.d) the coupling to low energy phonons is quite weak. To take their effect approximately into account we include their transition strength to that of the 0-0 transition of a individual PTCDA molecule.

Under the above made assumption that the dipole-dipole interaction is much smaller than the vibrational frequencies and the assumption that the temperature is smaller than the vibrational energy, the Hamiltonian relevant for fluorescence is approximately given by

$$H_\mathrm{ex} = \sum_n \epsilon_n |n,\vec{0}_n\rangle\langle n,\vec{0}_n| + \sum_n \sum_m \tilde{\alpha} |f_{00}|^2 W_{n,m} |n,\vec{0}_n\rangle\langle m,\vec{0}_m| \tag{12}$$

where $|f_{00}|^2$ is the Franck-Condon factor of the 0-0 transition of an individual PTCDA molecule, and the factor $\tilde{\alpha}$ accound for the effect of low energy phonons.

The corresponding eigenstates are given by

$$|\psi_k\rangle = \sum_n c_{nk} |n,\vec{0}\rangle \tag{13}$$

where the coefficients c_{nk} are identical to those obtained from Eq. (3) and the corresponding eigenenergies are the ones of Eq. (3), simply scaled by $\tilde{\alpha}|f_{00}|^2$. Here $\tilde{\alpha}$ is a number slightly larger than one.

Denoting $V_{nm} = \tilde{\alpha}|f_{00}|^2 W_{n,m}$ we arrive at Eq. (1) of the Letter.

2. Radiative decay rates

From our assumption that the transition dipole-dipole interaction is much smaller than the vibrational frequencies we could ignore details of the vibrations when forming the exciton band (only the 0-0 Franck-Condon factor enters). However we have to keep in mind, that emission proceeds to all vibronic states of the ground state. Since in the ground state there is no excitonic interaction, the corresponding Hamiltonian is the sum of the ground state Hamiltonians $H_g^{(n)}$ of the monomers, i.e.

$$H_g = \sum_n H_g^{(n)} = \sum_n \sum_{\nu_n} E_{g,\nu_n} |g,\nu_n\rangle\langle g,\nu_n| \tag{14}$$

where E_{g,ν_n} are the vibrational eigenenergies of the groundstate potential of monomer n and $|g,\nu_n\rangle$ the corresponding eigenstates. The eigenenergies $E_{g_{\mathrm{agg}},\vec{\nu}}$ and corresponding eigenstates $|g_{\mathrm{agg}},\vec{\nu}\rangle$ of the Hamiltonian H_g are given by

$$|g_{\mathrm{agg}},\vec{\nu}\rangle = |g\cdots g\rangle|\nu_1\cdots\nu_N\rangle \tag{15}$$

$$E_{g_{\mathrm{agg}},\vec{\nu}} = \sum_{n=1}^{N} E_{g\nu_n}. \tag{16}$$

Then the rate for a transition from the state Eq. (13) to the state Eq. (15) is given by

$$F_k(\nu_1\cdots\nu_N) = \Big|\langle g\cdots g|\langle\nu_1\cdots\nu_N|\sum_{\mathbf{n}}\hat{\vec{\mu}}_{\mathbf{n}}|\psi_k\rangle\Big|^2 \tag{17}$$

$$= \Big|\sum_n c_{nk}\vec{\mu}_n\langle\nu_1\cdots\nu_N|0_1\cdots 0_n^e\cdots 0_N\rangle\Big|^2 \tag{18}$$

$$= \Big|\sum_n c_{nk}\vec{\mu}_n\delta_{\nu_1,0}\cdots f_{0,\nu_n}\cdots\delta_{\nu_N,0}\Big|^2 \tag{19}$$

Here, and in the following, f_{00} should be regarded as the scaled Franck-Condon factor, i.e., $f_{00}\to\sqrt{\bar{\alpha}}f_{00}$.

For emission to the *vibrationless* ground state ($\nu_1=0,\ldots,\nu_N=0$) one finds

$$F_k(0\cdots 0) = |\sum_n c_{nk}\vec{\mu}_n f_{00}|^2 \tag{20}$$

$$= \mu^2|f_{00}|^2|\sum_n c_{nk}|^2 \quad (\text{for } \vec{\mu}_n=\vec{\mu}) \tag{21}$$

and for states with vibrational excitation on *one* monomer one finds

$$F_k(0\cdots\nu_m\cdots 0) = |c_{mk}\vec{\mu}_m f_{0\mu_m}|^2 \tag{22}$$

$$= \mu^2|f_{0m}|^2|c_{mk}|^2 \quad (\text{for } \vec{\mu}_n=\vec{\mu}) \tag{23}$$

Note that in contrast to the vibrationless case now there is no summation over all coefficients involved.

All other final states where more than two vibrations are involved are zero:

$$F_k(\nu_1\cdots\nu_N) = 0; \quad \text{more than one } \nu_j\neq 0 \tag{24}$$

The total rate from the state Eq. (13) to the electronic ground state is

$$F_k = \sum_{\nu_1\cdots\nu_N} F_k(\nu_1\cdots\nu_N) \tag{25}$$

$$= F_k(0\cdots 0) + \sum_m\sum_{\nu_m\neq 0} F_k(0\cdots\nu_m\cdots 0) \tag{26}$$

$$= \mu^2\Big\{|f_{00}|^2|\sum_n c_{nk}\Big|^2 + \sum_m\sum_{\nu_m\neq 0}|f_{0\nu_m}|^2|c_{mk}|^2\Big\} \quad (\text{for } \vec{\mu}_n=\vec{\mu}) \tag{27}$$

$$= \mu^2\Big\{|f_{00}|^2\Big|\sum_n c_{nk}\Big|^2 + (1-|f_{00}|^2)\Big\} \tag{28}$$

In going from the second to the third line we have used that all transition dipoles are parallel and identical in magnitude. In going from the third to the fourth line we used that for identical monomers $f_{0\nu_m}$ is independent of m so that $\sum_m \sum_{\nu_m} |f_{0\nu_m}|^2 |c_{mk}|^2 = \sum_{\nu\neq 0} |f_{0\nu}|^2 \sum_m |c_{mk}|^2 = (1-|f_{00}|^2)\cdot 1$

The total temperature dependent radiative decay rate is with Eq. 9 given by

$$F(T) = \sum_k p_k F_k \tag{29}$$

$$= \mu^2 \Big\{ |f_{00}|^2 \sum_k p_k \Big| \sum_n c_{nk} \Big|^2 + (1-|f_{00}|^2) \Big\} \quad (\text{for } \vec{\mu}_n = \vec{\mu}) \tag{30}$$

$$\equiv \mu^2 \Big\{ |f_{00}|^2 N_{\text{coh}}^{\text{opt}}(T) + (1-|f_{00}|^2) \Big\} \tag{31}$$

$$\approx \mu^2 |f_{00}|^2 N_{\text{coh}}^{\text{opt}}(T) \tag{32}$$

with

$$N_{\text{coh}}^{\text{opt}}(T) = \sum_k p_k \Big| \sum_n c_{nk} \Big|^2 \tag{33}$$

This 'optical coherence size' is what is denoted as $\eta_{\text{SR}}(T)$ in the Letter (see Eq. 3 of the Letter).

III. EXTRACTION OF THE SR ENHANCEMENT FROM THE FL SPECTRUM

A. Theoretical considerations

1. FL spectrum of the aggregate

In this section we will briefly discuss the fluorescence spectra for our finite size aggregates. Note that our derivation does not rely on harmonic modes. The FL spectrum can be written as

$$\text{FL}(\omega) \sim \sum_k \sum_{\vec{\nu}} p_k F_k(\vec{\nu}) \delta(\omega - \omega_{0-0} + \omega_{\vec{\nu}}) \tag{34}$$

where we have ignored dephasing and relaxation in the electronic ground state. Here, ω_{0-0} is the energy of the 0-0 transition and $\omega_{\vec{\nu}} = \sum_n \epsilon_{\nu_n}$, where ϵ_{ν_n} is the energy of the ν_nth vibrational state of monomer n. Inserting the expressions Eq. (20), Eq. (22) and Eq. (24) one finds

$$\text{FL}(\omega) \sim \sum_k p_k F_k(\vec{\nu}=\vec{0}) \delta(\omega - \omega_{0-0}) \tag{35}$$

$$+ \sum_k p_k \sum_n \sum_{\nu_n} F_k(0,\cdots,\nu_n,\cdots,0) \delta(\omega - \omega_{0-0} + \omega_{\nu_n})$$

$$= \mu^2 \sum_k p_k |f_{00}|^2 \Big| \sum_n c_{nk} \Big|^2 \delta(\omega - \omega_{0-0}) \qquad (\text{for } \vec{\mu}_n = \vec{\mu}) \tag{36}$$

$$+ \mu^2 \sum_k p_k \sum_n \sum_{\nu_n} |f_{0\nu_n}|^2 |c_{kn}|^2 \delta(\omega - \omega_{0-0} + \omega_{\nu_n})$$

$$= \mu^2 |f_{00}|^2 N_{\text{coh}}^{\text{opt}} \delta(\omega - \omega_{0-0}) \tag{37}$$

$$+ \mu^2 \sum_\nu |f_{0\nu}|^2 \delta(\omega - \omega_{0-0} + \omega_\nu)$$

In the last step we have used that for identical monomers $f_{0\nu_n}$ is independent of n, which then allows to evaluate summation over n to give $\sum_n |c_{nk}|^2 = 1$. The resulting expression is independent of k so that one can use $\sum_k p_k = 1$.

To account for interaction with an environment and finite temperature the δ function should be replaced by appropriate lineshape functions. One reasonable choice could be Gaussians where the width scales linearly with temperature.

One sees that one can extract $N_{\text{coh}}^{\text{opt}} \equiv \eta_{\text{SR}}$ from Eq. (37) by considering the relative intensities of the 0-0 line and the peaks with vibrational excitation. Note, that in this equation $|f_{00}|^2$ should be regarded as the Franck-Condon factor scaled by $\tilde{\alpha}$.

2. FL spectrum of the monomer

The aggregate emission spectrum Eq. (37) is closely related to that of the monomer: The monomer spectrum is given by

$$\mathrm{FL}_{\mathrm{mon}} = \mu^2 \sum_{\nu=0} |f_{0\nu}|^2 \delta(\omega - \omega_{0-0}^{\mathrm{mon}} + \omega_\nu) \tag{38}$$

From this one sees that (i) all peaks in the emission spectrum are at the same relative positions as in the monomer case. (ii) All peaks have the same relative intensities as in the monomer case, but the 0-0 peak, which is enhanced in the aggregate.

B. Experimental procedure

The vibrational peaks and the 0-0 line of the fluorescence spectra measured at the lowest temperatures are shown in Fig. 1. All spectra were normalized to the maximal intensity of their respective 0-0 lines, as can be seen in the right panel. In the left panel, the corresponding variation of the intensity of the vibronic peaks can be observed. It shows a clear minimum at 10 K. For better visibility of the effect the spectra were shifted horizontally.

We extracted the superradiance enhancement factor $\eta_{\mathrm{SR}}(T)$ from the ratio of the intensity of the 0-0 line to that of the peaks of the vibrational excitations via $\eta_{\mathrm{SR}}(T) = I_{00}/(I_{01}/f_{01})$. The integrated intensity of the superradiant

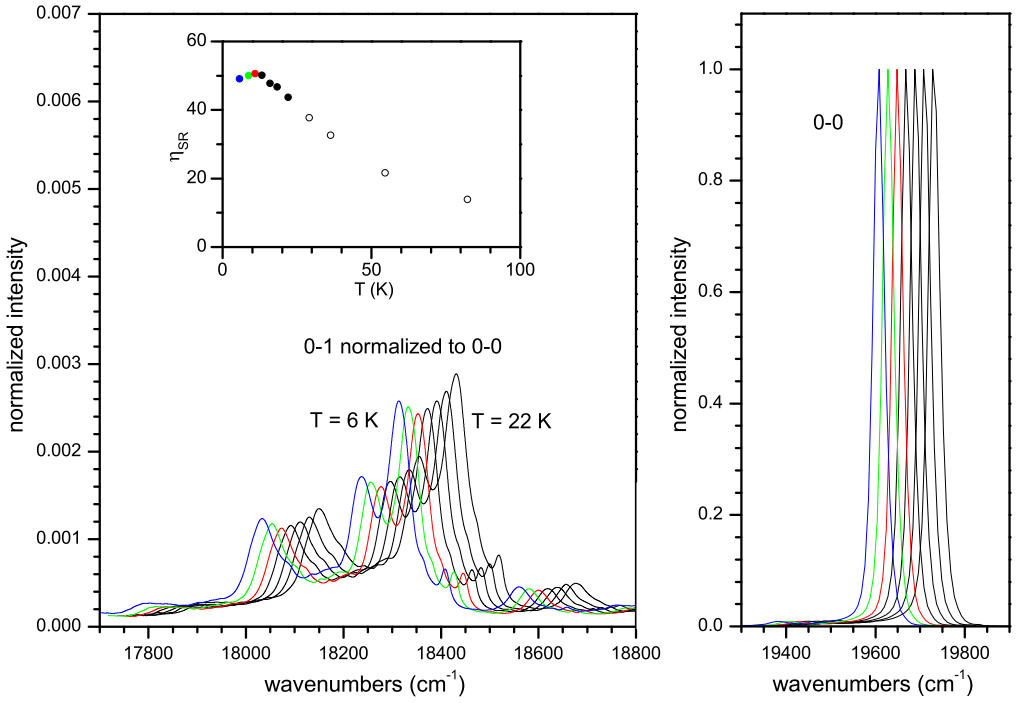

FIG. 1: Temperature dependent fluorescence spectra of the vibronic modes (left) normalized to the integrated intensity of the 0-0 transition (right). For clarity, the spectra were horizontally shifted to the right for increasing temperatures with respect to each other by 12 cm^{-1}. Their colors refer to the data points of the $\eta_{\mathrm{SR}}(T)$ curve shown in the inset. The normalized intensity of the vibronic modes varies with temperature and shows a minimum at 10 K. Please note the very different scaling of the intensity axes on the left and right spectra. The inset shows the low temperature regime of the $\eta_{\mathrm{SR}}(T)$ curve from Fig. 1 of the Letter.

0-0 line (I_{00}) was extracted from the fluorescence spectrum by fitting the high energy side of the peak with a Gaussian profile. This avoids an overestimation of the 0-0 line intensity by a possible overlap with low energetic vibronic modes. The intensity of the peaks with vibrational excitations (named as I_{01}) was determined by a numerical integration over several peaks in the wavenumber interval 17750 cm^{-1} − 18750 cm^{-1}. These integration boundaries were found to be well suited to compile the correct total intensities I_{01} of the chosen peaks at all temperatures. We note that "01" refers to a group of different vibrational peaks. For a detailed assignment of the peaks we refer to Ref. [3]. For calculating η_{SR} an effective Franck-Condon-factor ($f_{01}^{\mathrm{eff}} = 1.06$) describing the intensity ratio of I_{00}/I_{01} determined from a spectrum of diluted molecules (with no SR) was used. Its value differs from the one used in Ref. [1], which is due to the different integration boundaries that were used for the evaluation of I_{01}.

By this procedure the relative T dependence of η_{SR} is determined very reliably. Nevertheless, we cannot fully exclude small systematic errors in the experimental determination of the absolute integrated intensities of I_{00}, I_{01}, and the value of f_{01}. Such errors will result in a scaling of the extracted $\eta_{\mathrm{SR}}(T)$ curve by a proportional factor. This was taken into account when adapting the theoretical (dashed) curve in Fig. 1 of the Letter to the experimental data by an additional scaling factor of 1.2 yielding the solid curve.

IV. LEED PROFILE ANALYSIS FOR DETERMINATION OF THE AGGREGATE SIZE DISTRIBUTION

A. Developement of the functional form of the aggregate size distribution

For the determination of the aggregate size distribution, we analyzed the one- and two-dimensional LEED profiles. Then we used a bottom up simulation to model the profiles and to compare them to the measured ones. All measurements were performed at 260 K sample temperature and at an electron energy of 95.2 eV, which corresponds to an in-phase condition of the (0,0) spot with respect to KCl steps of monoatomic height [13].

A two dimensional LEED pattern of the specular (0,0) spot and the (1,0) spot of the PTCDA superstructure is shown in Fig. 2a. The respective one dimensional LEED scan is given in Fig. 2b. For a complete diffraction pattern see Ref. [2]. As can be seen, the (0,0) spot exhibits a pronounced diamond shaped broadening that is also present for the PTCDA(1,0) spot, although a little less pronounced. This profile shape is an effect of the preferred direction of the nonpolar boundaries of the PTCDA aggregates along the principal surface directions as indicated in Fig. 1 of the Letter. This argument is already valid for quadratic aggregates, but for asymmetric aggregates, e.g. $N_x \ll N_y$, the diamond shape becomes even more pronounced. (This effect can be seen from the simulations for the distributions A and B shown in Fig. 3 below.) According to this observed profile form we used a distribution of rectangular aggregates of the size $N_x \times N_y$ in our model.

In reality not only the size distribution but also the relative arrangement of the aggregates on the surface contributes to the correlation function that determines the LEED profile. However, in our case we can neglect inter-aggregate correlations. We neither observed any additional spots or satellites in the LEED pattern that would imply significant inter-aggregate correlations [14]. Nor did we find any significant variations in the widths and the profile forms of the PTCDA superstructure spots when comparing several diffraction orders (cf. Fig. 2b). This would be otherwise an indication for correlated anti-phase boundaries between the aggregates [15].

The one dimensional profile of the PTCDA(1,0) spot is depicted in the upper left panel of Fig. 3. A background signal (determined at a position in between two neighboring superstructure spots) was substracted and the profile was symmetrized afterwards. The profile form corresponds to a Voigt profile that can be understood as the convolution of a Lorentzian profile, which is related to the size distribution, and a Gaussian profile, which resembles the instrument function. A Lorentzian profile form immediately suggests the presence of a geometric aggregate size distribution, which has an exponentially decaying probability as a function of aggregate sizes N_x and N_y [16]. In one dimension this is given by:

$$P_N = \frac{1}{\Gamma - 1} \cdot \left(\frac{\Gamma - 1}{\Gamma}\right)^N \tag{39}$$

where Γ denots the expectation value.

In order to find the two dimensional form of the aggregate size distribution we analyzed the two dimensional profile of the PTCDA(1,0) spot that is shown in the upper right panel of Fig. 3. Parallel sections along the k_x direction of this profile have only a marginal dependence on k_y and vice versa. Namely, the changes of the full width at half maximum (FWHM) are less than 10%. This indicates that for the aggregate size distribution both directions are widely independent from each other. We can thus use $P_{N_x,N_y} \approx P_{N_x} \cdot P_{N_y}$ with $P_{N_x} = P_{N_y}$ for the two dimensional distribution. $P_{N_x} = P_{N_y}$ is warranted because of the symmetry of the KCl(100) surface.

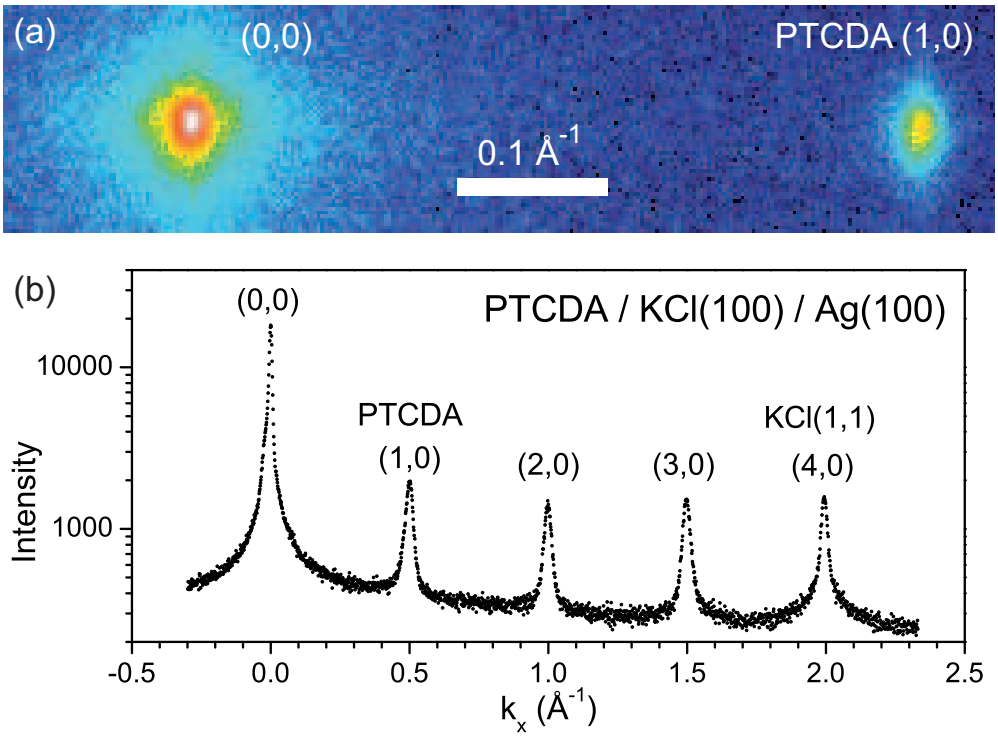

FIG. 2: a) Detailed two dimensional false color LEED pattern of the specular (0,0) spot and the PTCDA(1,0) spot. The (0,0) spot shows a pronounced diamond shaped broadening that is also weakly present for the PTCDA (1,0) spot. Both profiles are elongated in the vertical k_y direction due to a slightly elliptical instrument function. b) Linescan across of the (0,0) spot and the first four PTCDA superstructure spots. The PTCDA(4,0) spot is superimposed with the KCl(1,1) spot due to commensurability. The superstructure spots of the PTCDA show no significant variation of their profile widths. The measurements were performed at a sample temperature of 260 K and at an electron energy of 95.2 eV.

B. Simulation of the experimental profile

We simulated the LEED spot profile in the kinematic approximation [14] as a sum of Laue functions:

$$I(k_x, k_y) = \sum_{N_x} \sum_{N_y} P_{N_x,N_y} \frac{\sin^2(N_x k_x a/2)}{\sin^2(k_x a/2)} \cdot \frac{\sin^2(N_y k_y a/2)}{\sin^2(k_y a/2)}. \tag{40}$$

The two dimensional Laue functions were calculated for each aggregate of size $N_x \times N_y$ and weighted by a probability factor P_{N_x,N_y} according to the aggregate size distribution. Here N_x and N_y denote the number of molecules of a given aggregate in x and y direction, k_x and k_y are the reciprocal lattice vectors, and a is the lattice constant of the aggregates, i.e. 12.6 Å.

The profiles were calculated using Eq. (40) for aggregate sizes between 1×1 and 100×100 molecules. Thereby, the upper limit of $N_x = N_y = 100$ was sufficient to take into account all aggregate sizes with relevant probabilities. The calculated two dimensional spot profile was convoluted with a two dimensional Gaussian function in order to model the instrumental broadening. An asymmetric Gaussian function was used to take into account the elongation of the instrument function in k_y direction (cf. (0,0) spot in Fig. 2a) and additionally the small azimuthal broadening of the PTCDA(1,0) spot in k_y direction. The latter can be traced back to a weak rotational mosaicity of the epitaxial KCl film [2]. Finally we calculated the one dimensional profile in k_x direction from the two dimensional profile. We note that the broadening of the instrument function in k_y direction has only very little impact on the k_x direction.

An independent exact experimental determination of the width of the Gaussian instrument function was not possible. We therefore narrowed this value by an upper and lower limit. The lower limit is given by the maximum theoretical

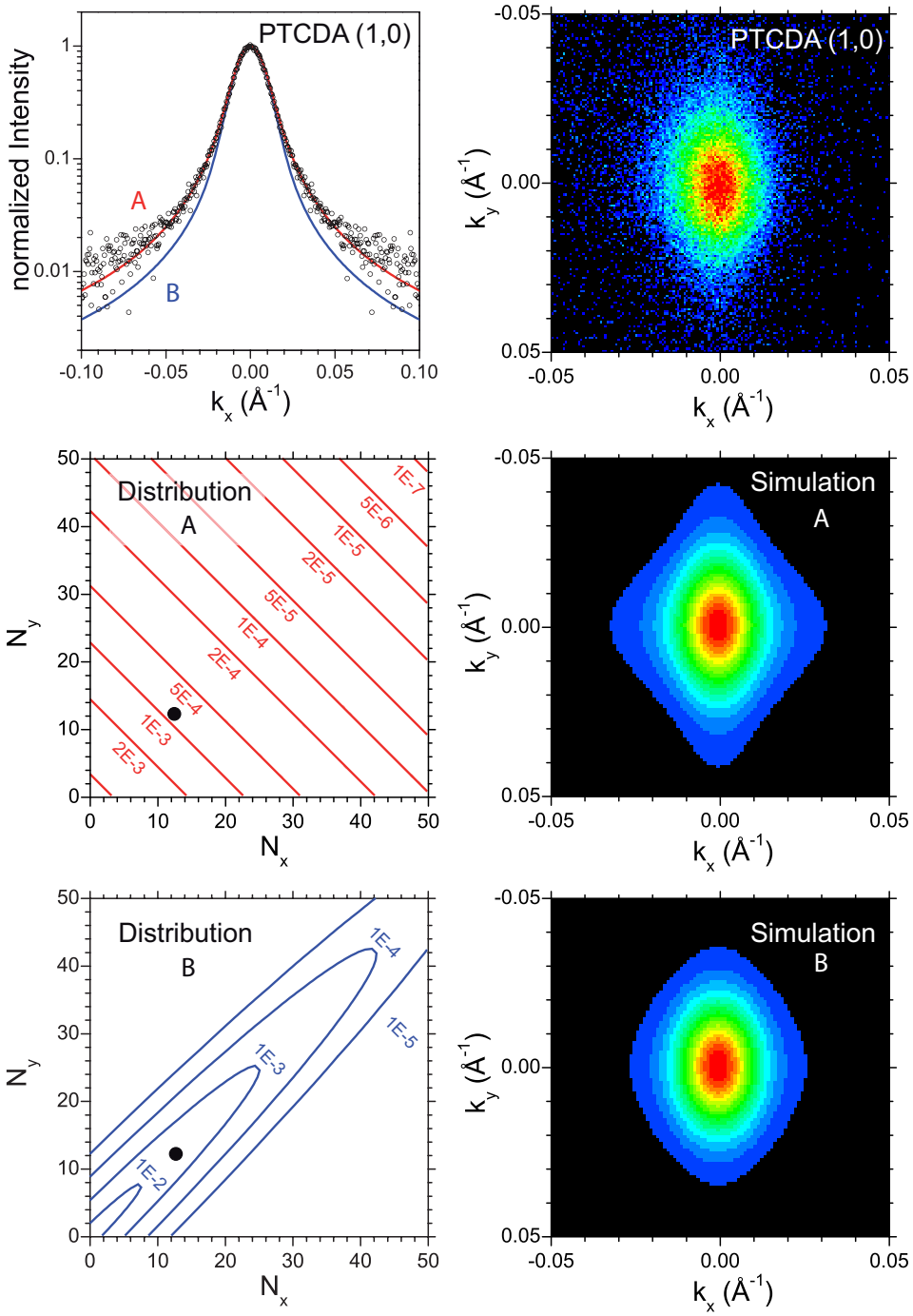

FIG. 3: Experimental and simulated LEED profiles of the PTCDA(1,0) spot. The experimental profiles are depicted in the upper panel (1D left, 2D right). Please note the different k_x scale for the one and two dimensional profile. The middle and lower panel on the left side show two dissimmilar aggregate size distributions (A and B) with an average aggregate size of $\langle N_x \times N_y \rangle = 12.4 \times 12.4$ molecules (marked by a black dot). The probability for the occurence of an aggregate of the dimensions $N_x \times N_y$ molecules is given by the red and blue isolines, respectively. Please note the exponentially decaying probabilites. The corresponding simulated spot profiles are shown on the right side. As can be seen, asymmetric domains (distribution A) lead to a more diamond shaped profile that is necessary to fit the wings of the one dimensional experimental profile.

resolution of our SPA-LEED instrument, namely by a FWHM of 0.005 Å^{-1}. (Please note that, different from the standard setup, we used a 300 μm channeltron aperture for increased counting rates.) The upper limit of 0.01 Å^{-1} was given by the FWHM of the peak of the (0,0) spot. This profile is however slightly broadened by the imperfections of the sample [17], which do not contribute to the PTCDA(1,0) spot.

For our simulation of the experimental data we varied both the width of the instrument function (within the narrow above limits) and the aggregate size distribution to fit the experimental profile. While the overall profile form and especially the wings of the profile ($k_x \geq$ 0.02 Å^{-1}) are mainly determined by the correct form of the aggregate size distribution, the very exact profile shape at the center ($k_x \leq$ 0.02 Å^{-1}) depends on both parameters. We found that for a fully satisfying description of both the center and the wings of the profile it was necessary to use a Gaussian instrument function with a FWHM of 0.0085 Å^{-1} in k_x direction. For the k_y direction a larger width of 0.018 Å^{-1} was used for the Gaussian, as determined from the two dimensional profile.

The aggregate size distribution A ($\Gamma_{x,y} = 12.4$) that fits the data best is depicted in the middle left panel of Fig. 3. It has an average aggregate size of $\langle N_x \times N_y \rangle = 12.4 \times 12.4$ molecules. The averaged aspect ratio of the aggregates seen by a molecule, i.e. $\langle N_x/N_y \times N_x \times N_y \rangle$ for $N_x > N_y$, is about 3. The resulting two dimensional profile is shown in the middle right panel of Fig. 3. A section of this profile fitting the experimental data is displayed as a solid line in the upper left panel. The resulting profile is in very good agreement with the experimental data for two orders of magnitude in the intensity. Merely the wings of the profile are slightly underestimated for larger k_x values ($k_x \geq 0.05$ Å^{-1}).

We further tested the uncertainty in the fitted average aggregate size $\langle N_x \times N_y \rangle$. The fitted value varied between 11.4×11.4 and 13.7×13.7 molecules when the width of the instrument function is varied within its limits of uncertainty (0.005 $\text{Å}^{-1} \leq$ FWHM $\leq 0.010\text{Å}^{-1}$). The range of 11.4 - 13.7 can thus be taken as that of the error bars of $\langle N_x \rangle$ and $\langle N_y \rangle$ of the resulting aggregate size distribution.

For comparison, we also simulated the diffraction profile for a very dissimilar aggregate size distribution B with an identical average aggregate size of 12.4×12.4 molecules, but mainly quadratic, non-asymmetric aggregates. The distribution is depicted in the lower left panel of Fig. 3 and the corresponding simulated spot profile is shown in the lower right panel. A one dimensional section along k_x of this two dimensional profile is also shown in the upper left panel. As can be seen, the center region of the simulated profile ($k_x \leq$ 0.015 Å^{-1}) is very similar to that of the experimental one and that calculated for the distribution A. This is due to the same average aggregate size of both distributions. However, the simulated profile is much too narrow at the wings of the profile ($k_x \geq 0.02$ Å^{-1}) and does not fit the experimental data thus. This discrepancy cannot be lifted by variations of the instrument function. This proves that the presence of many more asymmetric aggregates, as in distribution A, is required to reproduce a more pronounced diamond spot shape and leading to wider wings of the one dimensional profile.

[1] M. Müller, A. Paulheim, A. Eisfeld and M. Sokolowski; J. Chem. Phys. **139** 044302 (2013).
[2] M. Müller, J. Ikonomov and M. Sokolowski; Surf. Sci. **605** 1090–1094 (2011).
[3] M. Müller, A. Paulheim, C. Marquardt and M. Sokolowski; J. Chem. Phys. **138** 064703 (2013).
[4] A. Paulheim, M. Müller, C. Marquardt and M. Sokolowski; Phys. Chem. Chem. Phys. **15** 4906 (2013).
[5] Q. Guo, A. Paulheim, M. Sokolowski, H. Aldahhak, E. Rauls and W. G. Schmidt; J. Phys. Chem. C **118** 29911 (2014).
[6] A. Paulheim, C. Marquardt, M. Sokolowski, M. Hochheim, T. Bredow, H. Aldahhak, E. Rauls and W. G. Schmidt; Phys. Chem. Chem. Phys. **18** 32891 (2016).
[7] A. Paulheim, C. Marquardt, H. Aldahhak, E. Rauls, W. G. Schmidt and M. Sokolowski; J. Phys. Chem. C **120** 11926 (2016).
[8] H. Fidder, J. Knoester and D. A. Wiersma; J. Chem. Phys. **95** 7880 (1991).
[9] A. Eisfeld and J. S. Briggs; Chem. Phys. **324** 376 (2006).
[10] J. Roden, A. Eisfeld, M. Dvořák, O. Bünermann and F. Stienkemeier; J. Chem. Phys. **134** 054907 (2011).
[11] M. Voigt, A. Langner, P. Schouwink, J. M. Lupton, R. F. Mahrt and M. Sokolowski; J. Chem. Phys. **127** 114705 (2007).
[12] V. May and O. Kühn; *Charge and Energy Transfer Dynamics in Molecular Systems*, 3rd ed. (WILEY-VCH, Weinheim, 2011).
[13] C. Marquardt, A. Paulheim and M. Sokolowski; Surf. Sci. **641** 128–134 (2015).
[14] M. Henzler; Appl. Phys. A **34** 205–214 (1984).
[15] J. Libuda, F. Winkelmann, M. Bäumer, H.-J. Freund, Th. Bertrams, H. Neddermeyer and K. Müller; Surf. Sci. **318** 61–73 (1994).
[16] C.S. Lent and P.I. Cohen; Surf. Sci. **139** 121–154 (1984).
[17] C. Marquardt, A. Paulheim, N. Rohbohm, R. Merkel and M. Sokolowski; Rev. Sci. Instr. (2017), submitted.

A.3 "High resolution optical single molecule spectroscopy in a surface science experiment: The homogeneous absorption profile of PTCDA on KCl(100) step edge sites"

by Christian Marquardt, Alexander Paulheim, and Moritz Sokolowski

manuscript prepared for publication.

High resolution optical single molecule spectroscopy in a surface science experiment: The homogeneous absorption profile of PTCDA at KCl(100) step edge sites

Christian Marquardt, Alexander Paulheim, and Moritz Sokolowski *

We perform high resolution fluorescence excitation (FLE) measurements on the single molecule level on PTCDA molecules located at step sites of a KCl(100) surface. The inhomogeneous broadening is overcome by spatial and spectral dilution. At cryogenic temperatures (6 K) we observe narrow peaks (with a FWHM of 460 MHz) that exhibit a Lorentzian shape. They show spectral jumps and a saturation behavior characteristic for single molecules. We determined a saturation intensity between 200 and 300 $\mathrm{mW/cm^2}$, and a maximum emission rate of ≈ 11500 photons per second.

1 Introduction

Probing the properties of single molecules is of great interest for the fundamental understanding of interactions and processes on the microscopic scale. In contrast to properties that are obtained by averaging over an ensemble of molecules, the properties of a single molecule are directly connected to its unique local environment, conformation, and the site specific interactions [1].

Optical single molecule detection was first performed on impurities in solid hosts [1–6]. Here, at high spatial and spectral dilution, the natural linewidth of single molecules became accessible, which is at cryogenic temperatures several orders of magnitude below that of the inhomogeneously broadened ensemble [2]. It can thus be used as a sensitive probe for fundamental interactions [7] or smallest environmental changes. Besides, also photo physical phenomena like blinking [8], spectral diffusion [4,5,9], or the coupling of the optical transition to local two level systems [5,10], were observed and further investigated. One drawback of these experiments inside a solid is however the lack of complementary structural information. This would be beneficial for a further understanding of the interactions but is hardly accessible inside a solid.

Leaving the bulk and going to the surface, especially this local structural information is commonly investigated. Scanning probe methods [11,12] are capable of imaging microscopic structures with up to atomic resolution or manipulate and reassemble the local environment by use of the tip [13,14]. In addition these techniques can be extended or combined with other techniques to obtain further local information. For example by tunneling induced light emission (STM-LE) also local optical and vibrational information can be obtained [15–20]. Single molecules, decoupled from a metallic substrate by a thin insulating film, can be electronically excited by the STM tip and show a fluorescence spectrum with resolved vibronic transitions [15–17].

An aspect that remains discussion worthy in these surface experiments is however the achieved energetic resolution for a low temperature single molecule experiment. Compared to the linewidth of optical transitions obtained by high resolution optical single molecule spectroscopy in solids (between 10 MHz [2] and few 100 MHz [6]), the narrowest line reported recently from STM-LE experiments is 60 GHz [19], which is already small for a typical photoluminescence experiment, but still orders of magnitude broader. Moreover, in typical STM-LE experiments rather linewidths on the order of few THz were achieved [15–17]. Therefore one of the biggest advantages of single molecule spectroscopy, the ultra-narrow linewidth and hence the high sensitivity for minimal perturbations, remains inaccessible in these experiments.

It is up to now not understood, what causes the line broadening in these STM mediated experiments and if the obtained spectral linewidths are an intrinsic property of the molecules on the surfaces or broadened by the experimental technique. Here we provide an experimental approach that combines an optical approach, namely high resolution spectroscopy via fluorescence excitation spectroscopy (FLE), with molecules adsorbed on defined surface adsorption sites. We are particularly interested in the homogeneous linewidth of molecules on an insulating surface. This value is especially interesting for molecules on thin insulating films nearby a metal surface. Here the excitation could possibly be affected by partial quenching by the metal [21], which would lead to a reduction of the radiative lifetime and thus a significantly broadening of the homogeneous lines. Additionally, it is yet unknown whether and which of the typical single molecule related photophysical processes can be observed also on surfaces and under ultra high vacuum conditions. It is for instance possible that the process of bleaching that is often related to interactions with impurities like oxygen is not observable under clean vacuum conditions.

As a sample system we use isolated molecules of 3,4,9,10-perylenetetracarboxylic dianhydride (PTCDA) adsorbed on defined step sites of a thin KCl film. The structural and optical properties of this system were extensively investigated in former experiments and are well understood [22–26]. By annealing after deposition the molecules diffuse to KCl step edges and are partially embedded into the step at highly defined step sites [22,24–26].

Institut für Physikalische und Theoretische Chemie, Universität Bonn, Wegelerstr. 12, 53115 Bonn, Germany. E-mail: sokolowski@pc.uni-bonn.de

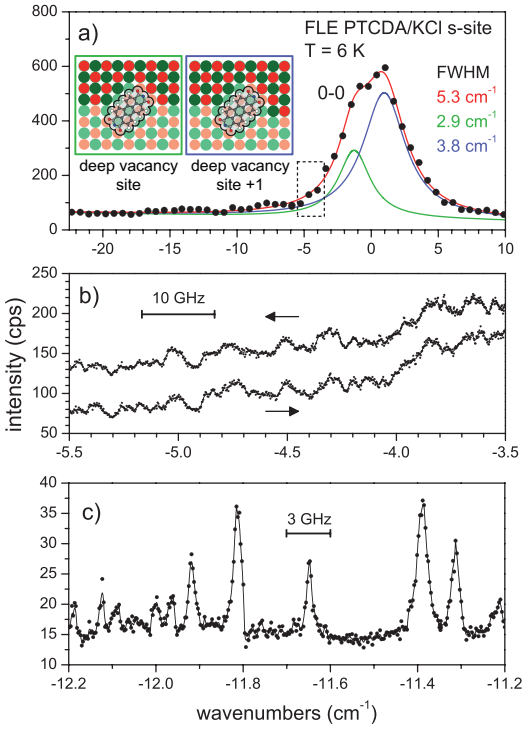

Fig. 1 Excitation spectra of PTCDA at KCl step sites measured at 6 K. a) Low resolution scan of the inhomogeneously broadened 0-0 transition. The origin of wavenumber scale is shifted to the center of the inhomogeneous broadening. The measured profile shows a peak splitting at the top that can be explained by a superposition of the contributions of two different adsorption sites. The profile can be fitted by two Lorentzian contributions. Real space models of the two adsorption sites are given as an inset. b) High resolution scans in the low energy wing of the inhomogeneously broadened profile. The scan range is marked in a) by a dashed box. The scans show the statistical fine structure with distinct maxima and minima at fixed positions. Only minor changes are observed between consecutive scans. The laser intensity was 15 $\mathrm{W/cm^2}$. c) Scan with single adsorption peaks on a flat baseline. The single peaks are the resolved zero phonon lines (ZPL) of single molecules. For this scan the molecule density on the sample was reduced by an additional factor of 10-100. Here the laser intensity was 300 $\mathrm{mW/cm^2}$. For details see text.

Structure models of these step sites are shown in Fig. 1a as an inset. The molecules embedded in these sites are energetically very similar so that the inhomogeneous broadening is already considerably reduced compared to that of the ensemble on the statistically occupied terrace sites[24,25].

2 Experimental

Our experiments were performed under ultra high vacuum (UHV) conditions. The sample could be heated by a tungsten filament and cooled by liquid helium. The lowest achievable sample temperature was 6 K[27].

We worked on high quality epitaxially grown KCl-films on a Ag(100) single crystal surface[28]. The KCl-films had a typical thickness of 10 atomic layers. The PTCDA was sublimed onto the sample from a homemade Knudsen-type evaporator and the PTCDA flux was monitored in the quadrupole mass spectrometer (QMS) at $m/z = 392$ amu.

We specify the surface coverage of PTCDA in monolayers (ML). Hereby, 1 ML refers to a coverage of 7.5×10^{-3} molecules per $\mathrm{Å}^2$. We used deposition rates below the detection limit of the QMS, i.e. below $1.5 \cdot 10^{-4}$ ML/min. This was achieved at temperatures of the PTCDA crucible between 600 K and 630 K. The sample was kept at 20 K during deposition. With a deposition time of ≈ 1 s we can estimate an upper limit for the coverage of $\approx 2.5 \times 10^{-6}$ ML from the detection limit of the QMS. This corresponds to one molecule per $\mu\mathrm{m}^2$. Directly after deposition the molecules were statistically adsorbed on the KCl terraces. After deposition the sample was heated to 150 K for 20 min in order to thermally induce a migration of all PTCDA molecules to step edges[24].

For the optical experiments the sample was cooled to 6 K and transferred into a glass head standing out at the end of the UHV chamber. The glass head and the whole detection apparatus were placed inside a black box for an exclusion of room light. The quality of the sample was then checked by fluorescence spectroscopy (FL). Here, the molecules were excited by an optically pumped semiconductor laser (Coherent Sapphire LP USB CDRH) operated at 458.0 nm (50 mW). For fluorescence excitation (FLE) spectroscopy we used a tunable ring laser (Sirah Matisse II DS) operated with Coumarin 498 as the laser dye. The ring laser was pumped by an optically pumped semiconductor laser (Coherent Genesis CX 480 4000) at 480 nm and 4 W excitation power. With a custom output coupler, stable and tunable single mode operation with laser output > 50 mW was obtained between 495 and 525 nm. The wavelength of the laser was monitored with a wavelength meter (HighFinesse Angstrom WS/6).

The excitation light was filtered by a 510 nm short pass filter in order to block unwanted fluorescence from the laser dye. Then the laser beam was focused onto the sample. We focused the laser under an angle of incidence of 45° to the sample. The directly reflected beam was blocked by a beam dump. The size of the focused spot on the sample was approximately 0.2 mm in diameter. The number of molecules inside the focus was estimated to be 40000 at the maximum coverage. We used different power densities between ≈ 30 and 1500 $\mathrm{mW/cm^2}$ for excitation. To reduce the laser power, neutral density filters were used. The fluorescence from the sample was collected and focused on the entrance slit of a spectrograph by a pair of collecting lenses ($f_1 = 100$ mm, $NA_1 = 0.22$, $f_2 = 200$ mm). The excitation light scattered from the sample was blocked by a 520 nm long pass filter. The spectrograph (Acton 2300i, $f/\# = 4$, $f = 0.3$ m) was equipped with a liquid nitrogen cooled CCD Camera (Spec10:100BR(LN)). We used a wide opened entrance slit (2 mm) for increased detection efficiency and hardware binning of the CCD pixels (binning of each 20 pixel columns) to minimize readout noise.

The FLE spectra were computed from FL spectra recorded for varying excitation wavelength by integration of the fluorescence intensity in the regime between 518 and 602 nm. Each FL spectrum was measured with an exposure time of 2 s, while continuously scanning the cavity of the ring laser with a speed of 30 MHz/s. The instrumental broadening of the FLE spectra is determined by the width of the laser line of the ring laser. We

operated the laser in the non frequency stabilized mode with a linewidth of < 20 MHz rms. For this experimental setup we estimate an overall detection efficiency of 0.3% of the emitted photons. This value is comparably low, which is also the reason for the comparably high but necessary exposure time. The detection efficiency is majorly limited by the NA (0.22) of the collection optics that was taken from the former experimental setup and has not yet been optimized with respect to the more demanding single molecule experiment. Therefore currently only 2.5% of all emitted photons are collected by the collection lens. Further losses are due to the chosen detection window (35% efficiency), the spectrograph ($\approx 65\%$), the CDD ($\approx 65\%$) and partial reflections on the surfaces of lenses and filters ($\approx 80\%$).

3 Results and Discussion

3.1 Inhomogeneously broadened profile

We begin with the measurements of the inhomogeneously broadened 0-0 line profile. The FLE profile depicted in Fig. 1a was measured by scanning the thin etalon of the ring laser. Thereby, the excitation wavelength is varied in steps defined by the free spectral range of the thick etalon, i.e. 0.63 cm^{-1}. The total width of the measured profile can be described by a Gaussian peak shape with a center at 20140.5 cm^{-1} and a full width at half maximum (FWHM) of 5.3 cm^{-1} (≈ 160 GHz).† This is slightly larger than the value obtained in Ref. 24, but within the range of FWHM values obtained for typical preparations.

However additionally, small indentations at the top of the peak are observed that can be interpreted as a splitting into two main contributions separated by ≈ 2 cm^{-1}. In Ref. 25 it was already proposed from theoretical calculations that the measured 0-0 profile could have contributions from both the *deep vacancy site* and the *deep vacancy site +1* (for real space models see the inset of Fig. 1). So far this was however not resolved experimentally due to a limited resolution of the excitation laser.

Generally inhomogeneously broadened profiles are expected to exhibit a Gaussian shape that originates from a Gaussian distribution of the energies of the positions of the homogeneous lines[29]. However, fitting the profile with two Gaussians for the two respective adsorption sites was not successful here. Instead, the measured profile can be well fitted as a sum of two Lorentzian contributions (20139.3 cm^{-1}, FWHM: 2.9 cm^{-1}, 20141.6 cm^{-1}, FWHM: 3.8 cm^{-1}). A similar shape and width was already obtained for the inhomogeneous broadening of PTCDA molecules located at NaCl step sites[25] and seems to be characteristic for this type of adsorption sites.

3.2 Statistical fine structure

Aside from the rough scan of the inhomogeneously broadened profile also high resolution scans on its low energy wing were measured, i.e., on the low energy wing of the deep vacancy site. Such a scan is shown in Fig. 1b. Here the curves show distinct variations with several local maxima and minima. The positions and intensities of these maxima are mostly fixed and barely change within several scans. They belong to the statistical fine structure, that was already observed for molecules in solid hosts[29], and resembles the local energetic distribution of the energy levels of the molecules inside the excitation area of the laser spot. The statistical fine structure is an intrinsic property of the investigated sample and must not be confused with noise[29].

Already from the appearance and the width of the local maxima in the fine structure depicted in Fig. 1b we can derive that the single molecule linewidth in our sample system is orders of magnitude smaller than that of the inhomogeneous broadened line. Though, due to the superposition of the signals of several molecules it remains not possible to investigate the molecules separately or determine the single molecule linewidth.

Despite the mostly fixed positions of the maxima and minima of the statistical fine structure, small local changes can be observed already between consecutive scans (cf. Fig. 1b). Then one or more maxima shift or vanish between consecutive scans. This can be due to a local reorganization on the sample or by a small thermal drift of the sample with respect to the probing laser. Generally, by changing the position of the laser spot on the sample different local distributions can be probed. Therefore also the individual positions and intensities change. At a fixed sample position the probability for a local reorganization can be related to the laser intensity and the sample temperature. For higher laser intensities (> 100 mW/cm^2) also the probability for a local variation increases. Selectively inducing a local variation by long term excitation of a specific maximum is however not possible. The effect of the sample temperature is more dramatical. Flashing the sample to ≈ 15 K for a few seconds leads to a complete reorganization of the local fine structure.

3.3 Single molecule spectroscopy

The next step towards the detection of single molecules was a further decrease of the number of excited molecules. This was done spectrally by scanning the spectral regions far off the center of the inhomogeneous broadening, and also spatially by a further reduction of the total coverage; we estimate by an additional factor of 10 - 100. Fig. 1c finally shows a scan 11.2-12.2 cm^{-1} apart from the center of the inhomogeneous broadening. Here isolated peaks on a smooth baseline with no additional substructure can be observed. As it is expected the peak density decreases with the distance from the inhomogeneous center. The observed peaks are the resolved zero phonon lines (ZPL) of the electronic absorption of single molecules.

By scanning the same spectral area repeatedly, spectral shifts and the vanishing and appearing of some peaks can be observed. Intensity drops after the vanishing of a single peak go always to the background level, which gives evidence for a single molecule behavior. This is also supported by the form and the width of the profiles. A detailed scan of a single ZPL is shown in Fig. 2. Like all of the observed profiles it exhibits a Lorentzian like profile form as it is expected for a homogeneously broadened transition[2].

† The central wavelength of the inhomogeneous broadening is shifted by ≈ 10 cm^{-1} compared to the position reported in our earlier publications[24,25]. This deviation is due to the different method of determination. While the wavelength of the excitation laser in earlier experiments was determined via a manually calibrated spectrometer now a self-calibrated wavelength meter with higher absolute accuracy is used.

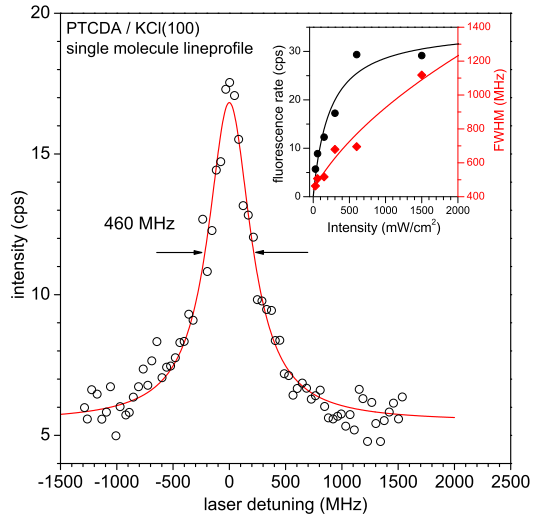

Fig. 2 Absorption peak profile of a single PTCDA molecule at a KCl step site. The profile was measured at the lowest applicable laser intensity of 30 mW/cm^2 and a temperature of 6 K. The profile was fitted by a Lorentzian with a FWHM of 460 MHz. The inset shows the saturation behavior and power broadening of single molecule peaks. The maximum fluorescence rate (black dots) and linewidth (red diamonds) were evaluated for different molecules as a function of the laser intensity. The solid lines are fits to the data points according to the saturation behavior of a molecular three-level system. For further details see text.

The minimal achieved linewidth, at the FWHM, was 463.8 ± 24.5 MHz (1.9 μeV). This was measured at the lowest achievable temperature (6 K) and power density (30 mW/cm^2) in order to reduce a broadening by temperature or saturation effects. Indeed the achieved resolution is remarkably high compared to that of common surface science techniques, e.g. photoelectron spectroscopy (UPS: 20 meV[30], XPS: 100 meV[31]). The obtained minimal linewidth is however still significantly broader than the ones reported in earlier high resolution optical single molecule studies[2,3]. This has been identified to be mainly a temperature effect[3,5,32].

The width of homogeneous profiles $\Delta\nu$ is ultimately limited by the natural linewidth $\Delta\nu_0$ of the transition that is given by the radiative lifetime τ via

$$\Delta\nu_0 = 1/(2\pi\tau).$$

It is however also broadened by the interaction with the environment, i.e. interaction with phonons and local librations, a process that is temperature dependent and commonly referred to as thermal dephasing[32]. Therefore typically high resolution optical single molecule spectroscopy is performed at or below liquid helium temperature (in many cases around 1.5 K[2,3,6]), so that thermal induced dephasing is eliminated. Our experimental setup is limited to a lowest temperature of 6 K. At this temperature the homogeneous profiles are presumably still significantly temperature broadened. Nevertheless, it is possible to state a lower limit of 0.34 ns by $\tau = 1/(2\pi\,\Delta\nu)$. As a reference the free molecule inside a liquid helium droplet at 380 mK has a radiative lifetime of 5.5 ns[33]. This would result in a natural linewidth of only 30 MHz.

We also tried to check for the temperature induced broadening of the investigated system. This however failed due to an extraordinarily limited temperature range for the measurements. We found that by slightly reducing the liquid helium flow and thus warming the sample by only 1 K two effects occur. The first effect is a strong broadening of the molecular transitions combined with an over proportionate increase of the background signal. Thus we can only estimate a linewidth of $\approx$ 1000 MHz at 7 K. The second effect is an instability of the position of the ZPL, which means irreversible shifting within or to the outside of the scan range. In combination an exact and reliable determination of the temperature behavior in this small temperature window was hardly possible.

3.4 Saturation behavior

For studying the saturation behavior of the molecular transitions, i.e. the dependency of the profile height and width on the laser intensity, we varied the laser intensity between 30 mW/cm^2 and 1600 mW/cm^2. The investigated intensity range was limited by the detection efficiency for the lowest intensity and by the signal to background ratio for the highest intensity. The measured peaks were evaluated by subtracting a constant background signal and fitting the profile with a Lorentzian. Then the fluorescence rates at the peak maximum and the FWHM of the Lorentzian fit were extracted. The dependencies of the emission rate and the total linewidth on the laser intensity are plotted in the inset of Fig. 2.

We note that unlike to previous single molecule studies[6,34], the plotted data points correspond to different molecules. This was necessary since we did not succeed in measuring the complete intensity range for just a single molecule, which was mainly due to instabilities upon excitation. Due to the defined adsorption geometry of the molecules on the sample (the molecules adsorb planar with two possible orientations rotated by 90° with respect to each other) an insecurity in the orientation of the molecules can be widely excluded by the selective excitation of a single orientation with polarized light[24]. The polarization of the laser was set to preferably excite molecules with one of the two orientations. Due to the different positions of the molecules inside the focus of the laser, the error bars on the intensity axis are large and prevent an exact determination of the system parameters. Nevertheless the obtained data set allows observing the general trends and giving an estimate on the system parameters.

The fluorescence rate (inset of Fig. 2 black data) shows a monotone rise and a saturation behavior. This behavior is typical for single molecules and can be described by the model of a molecular three level system with a triplet bottleneck[3,35]

$$R = R_\infty \frac{I/I_S}{1+I/I_S},$$

where R is the fluorescence rate obtained at a power density I, with the maximum fluorescence rate R_∞ and the saturation intensity I_S. By fitting the data to the model we determined an experimental maximum fluorescence rate R_∞ of 35 ± 4 cps and a saturation intensity I_S of 230 ± 80 mW/cm^2.

Within the same model also the saturation broadening (inset of Fig. 2 red data) can be described. Here the width of the profile $\Delta\nu$ increases with the root of the laser intensity as can be seen from [3]

$$\Delta\nu = \Delta\nu_0\sqrt{1+I/I_S},$$

where $\Delta\nu_0$ is the width of the profile at vanishing laser intensity, I is the laser intensity, and I_S is again the saturation intensity. Here the saturation intensity I_S obtained from the fit was 300 ± 70 mW/cm^2, which is larger but within the error bar of the value obtained from the saturation of the fluorescence rate. For the minimal linewidth a value of 443 ± 33 MHz is obtained, which means that a significant saturation broadening can be excluded for the profiles measured at the lowest applicable laser intensity ($\Delta\nu = 463.8$ MHz).

For a comparison with other experiments, the experimental maximum fluorescence rate R_∞ has to be corrected for the detection efficiency of the experimental setup, namely by 0.3%. After correction a maximum fluorescence rate $R_\infty \approx 11500$ photons per second is obtained, which is comparable to experiments on terrylene in hexadecane [34]. Also the obtained saturation intensity is in the typical range [35].

3.5 Spectral jumps

As noted above, spectral shifts and the vanishing of some of the peaks can be observed by scanning the same spectral region or the same spectral profile repeatedly. These processes are strongly dependent on the excitation intensity. While for the lowest laser intensities of up to 60 mW/cm^2 barely any spectral shifts are observable, for higher intensities (> 150 mW/cm^2) also the probability for spectral changes increases. This could either be related to a laser induced heating of the sample or to relaxation processes after photo excitation. At fixed excitation intensity, differences in the stability of the ZPLs of individual molecules can be observed. Overall, three principle types of ZPLs can be distinguished: We name them (i) *stable* , (ii) *instable*, and (iii) *meta-stable* ZPLs.

The spectral position of the stable type (i) of ZPLs does not change independent on how often their profile is scanned, at least at a given power density. This is particular interesting concerning photochemical bleaching. It can be widely excluded for these molecular transitions. As noted above this can presumably mainly be traced back to the clean environment inside the UHV and especially to the absence of oxygen that is often responsible for photooxidation reactions.

Also the intermittently vanishing and reappearance of the molecular transition, commonly known as blinking was not observable. However this absence may also be explained by the limited temporal resolution of the experiment in combination with a triplet state lifetime significantly lower than the used exposure time of 2 s.

Exemplary scans of the instable (ii) and meta-stable (iii) types of ZPLs are depicted in Fig. 3a and Fig. 3b, respectively. The ZPL of the instable type (ii) vanishes directly upon excitation. Here an abrupt and irreversible drop in the intensity is observed while scanning into the wing of a profile. This vanishing is most likely connected to a large spectral shift of the line to a position outside

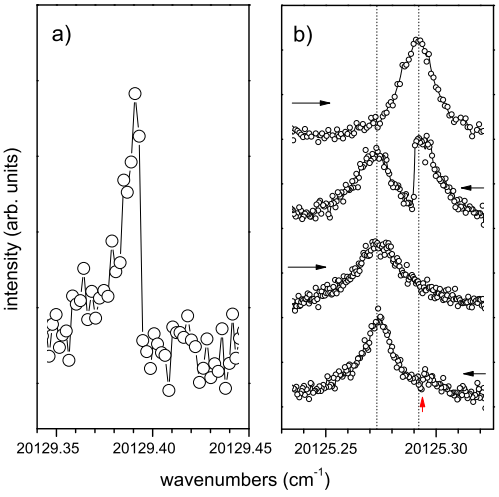

Fig. 3 Vanishing and shifting of peaks due to spectral jumps. a) Laser induced vanishing of an instable ZPL. The intensity drops spontaneously to the baseline intensity while scanning the wing of the profile. The laser intensity was 250 mW/cm^2. b) Sequence of consecutive scans of a metastable ZPL. The scan directions are marked by black arrows. The ZPL is stable during the first scan (top) but undergoes a laser induced shift by ≈ 500 MHz during the second scan. The third scan is again stable and the fourth shows a minimal intensity drop like in the first scan marked by a red arrow. Laser intensity: 300 mW/cm^2. For better visibilities the scans are vertically shifted with respect to each other. The measurement of the 4 consecutive scans took about 30 min. For further details see text.

the scan range, likely due to an environmental change. But also a photochemical bleaching cannot be fully excluded. Regarding the clean environment inside the UHV chamber and also the finding of other molecular transitions that are fully stable this possibility appears however rather unlikely.

The metastable type (iii) (Fig. 3b) is comparably rare. It involves smaller jumps (often < 1 GHz) so that the molecular transition appears at a different position inside the scan range. Again the spectral shift can be induced photophysically by resonance with the laser. However also excitation independent reversible and irreversible shifts or a vanishing of the ZPL can be observed at times. For example the ZPL in Fig. 4b is first shifted ≈ 500 MHz by the laser. However in the last scan again a small intensity drop at the initial position of the ZPL is observed, which can be interpreted by a prior back shifting of the ZPL independent on the resonance with the laser.

The shifting in small steps is commonly reported as spectral diffusion and related to the existence of local two level systems [5]. Such effects were already observed for molecules in solid and particularly amorphous hosts, where they were explained by tunneling of nearby atoms or molecular groups between different confirmations [5,10,34]. For the situation of a rigid PTCDA molecule on a KCl step site such an explanation can however not be used. For example already for the hopping of a single ion pair in the vicinity of the molecule one can estimate an energetic shift on the order

of $\approx 1\ \mathrm{cm}^{-1}$ (30 GHz)[25], which is by far larger than the observed spectral changes. Therefore rather weak long range interactions with other molecules or substrate atoms far away from the detected molecule are conceivable. In this case however the question remains why the excitation of the molecule with the laser should induce small environmental changes relatively far away from the excited center.

4 Summary and conclusion

In this paper we reported on first optical high resolution single molecule investigations in a surface science experiment. Homogeneously broadened single molecule absorption lines of PTCDA molecules on step sites of a thin KCl film on a Ag(100) substrate were measured by high resolution fluorescence excitation spectroscopy. The measured profiles showed properties and behavior comparable to molecules embedded in solid hosts. Namely, a comparable linewidth and profile form, a saturation behavior with laser intensity, and spectral jumps upon excitation were observed. Blinking and photochemical bleaching were however not observed.

Especially the finding of the high energy resolution may be important for the development of future experiments that may combine high resolution optical spectroscopy with local imaging and selective manipulation of the investigated systems for the investigation of smallest interactions. For example investigating the spectral shift of a ZPL as a function of the distance between the molecule and an ad-atom, a second molecule, or even an STM tip could help to understand these minimal interactions.

Acknowledgements

The project was supported by the Deutsche Forschungsgemeinschaft under the project SO407/8-1.

References

1 W. E. Moerner and L. Kador, *Phys. Rev. Lett.*, 1989, **62**, 2535–2538.
2 M. Orrit and J. Bernard, *Phys. Rev. Lett.*, 1990, **65**, 2716–2719.
3 W. P. Ambrose, T. BaschÃĭ and W. E. Moerner, *J. Chem. Phys.*, 1991, **95**, 7150–7163.
4 T. Basché, W. P. Ambrose and W. E. Moerner, *J. Opt. Soc. Am. B*, 1992, **9**, 829–836.
5 L. Fleury, A. Zumbusch, M. Orrit, R. Brown and J. Bernard, *J. Lumin.*, 1993, **56**, 15–28.
6 P. Tchénio, A. B. Myers and W. E. Moerner, *J. Lumin.*, 1993, **56**, 1–14.
7 M. Orrit, J. Bernard, A. Zumbusch and R. I. Personov, *Chem. Phys. Lett.*, 1992, **196**, 595–600.
8 D. A. V. Bout, W.-T. Yip, D. Hu, D.-K. Fu, T. M. Swager and P. F. Barbara, *Science*, 1997, **277**, 1074.
9 W. P. Ambrose and W. E. Moerner, *Nature*, 1991, **349**, 225–227.
10 A. Zumbusch, L. Fleury, R. Brown, J. Bernard and M. Orrit, *Phys. Rev. Lett.*, 1993, **70**, 3584–3587.
11 G. Binnig, H. Rohrer, C. Gerber and E. Weibel, *Phys. Rev. Lett.*, 1982, **49**, 57–61.
12 G. Binnig, C. F. Quate and C. Gerber, *Phys. Rev. Lett.*, 1986, **56**, 930–933.
13 D. M. Eigler and E. K. Schweizer, *Nature*, 1990, **344**, 524–526.
14 T. Kumagai, F. Hanke, S. Gawinkowski, J. Sharp, K. Kotsis, J. Waluk, M. Persson and L. Grill, *Nat. Chem.*, 2014, **6**, 41–46.
15 X. H. Qiu, G. V. Nazin and W. Ho, *Science*, 2003, **299**, 542.
16 B. Doppagne, M. C. Chong, E. Lorchat, S. Berciaud, M. Romeo, H. Bulou, A. Boeglin, F. Scheurer and G. Schull, *Phys. Rev. Lett.*, 2017, **118**, 127401.
17 C. Chen, P. Chu, C. A. Bobisch, D. L. Mills and W. Ho, *Phys. Rev. Lett.*, 2010, **105**, 217402.
18 C. Chen, C. A. Bobisch and W. Ho, *Science*, 2009, **325**, 981.
19 M. C. Chong, G. Reecht, H. Bulou, A. Boeglin, F. Scheurer, F. Mathevet and G. Schull, *Phys. Rev. Lett.*, 2016, **116**, 036802.
20 X. L. Guo, Z. C. Dong, A. S. Trifonov, K. Miki, K. Kimura and S. Mashiko, *Appl. Surf. Sci.*, 2005, **241**, 28–32.
21 W. Gebauer, A. Langner, M. Schneider, M. Sokolowski and E. Umbach, *Phys. Rev. B*, 2004, **69**, 155431.
22 Q. Guo, A. Paulheim, M. Sokolowski, H. Aldahhak, E. Rauls and W. G. Schmidt, *J. Phys. Chem. C*, 2014, **118**, 29911–29918.
23 M. Müller, A. Paulheim, C. Marquardt and M. Sokolowski, *J. Chem. Phys.*, 2013, **138**, 064703.
24 A. Paulheim, M. Müller, C. Marquardt and M. Sokolowski, *Phys. Chem. Chem. Phys.*, 2013, **15**, 4906–4913.
25 A. Paulheim, C. Marquardt, H. Aldahhak, E. Rauls, W. G. Schmidt and M. Sokolowski, *J. Phys. Chem. C*, 2016, **120**, 11926–11937.
26 A. Paulheim, C. Marquardt, M. Sokolowski, M. Hochheim, T. Bredow, H. Aldahhak, E. Rauls and W. G. Schmidt, *Phys. Chem. Chem. Phys.*, 2016, **18**, 32891–32902.
27 C. Marquardt, A. Paulheim, N. Rohbohm, R. Merkel and M. Sokolowski, *Rev. Sci. Instr.*, 2017.
28 M. Müller, J. Ikonomov and M. Sokolowski, *Surf. Sci.*, 2011, **605**, 1090–1094.
29 W. E. Moerner and T. P. Carter, *Phys. Rev. Lett.*, 1987, **59**, 2705–2708.
30 R. Matzdorf, *Surface Science Reports*, 1998, **30**, 153–206.
31 B. Stadtmüller, M. Willenbockel, S. Schröder, C. Kleimann, E. M. Reinisch, T. Ules, S. Soubatch, M. G. Ramsey, F. S. Tautz and C. Kumpf, *Physical Review B*, 2015, **91**, 155433.
32 S. Kummer and T. Basché, *J. Phys. Chem. C*, 1995, **99**, 17078–17081.
33 O. Bünermann, *PhD thesis*, University of Bielefeld, 2006.
34 W. E. Moerner, T. Plakhotnik, T. Irngartinger, M. Croci, V. Palm and U. P. Wild, *J. Phys. Chem.*, 1994, **98**, 7382–7389.
35 T. Plakhotnik, W. E. Moerner, V. Palm and U. P. Wild, *Opt. Commun.*, 1995, **114**, 83–88.

A.4 "A surface science compatible epifluorescence microscope for inspection of samples under ultra high vacuum and cryogenic conditions"

by Christian Marquardt, Alexander Paulheim, Nils Rohbohm, Rudolf Merkel, and Moritz Sokolowski

published in: Review of Scientific Instruments **88**, 083702 (2017).

REVIEW OF SCIENTIFIC INSTRUMENTS **88**, 083702 (2017)

A surface science compatible epifluorescence microscope for inspection of samples under ultra high vacuum and cryogenic conditions

Christian Marquardt,[1] Alexander Paulheim,[1] Nils Rohbohm,[1] Rudolf Merkel,[2] and Moritz Sokolowski[1]
[1]*Institut für Physikalische und Theoretische Chemie der Universität Bonn, Wegelerstrasse 12, 53115 Bonn, Germany*
[2]*Institute of Complex Systems, ICS-7: Biomechanics, Forschungszentrum Jülich GmbH, 52425 Jülich, Germany*

(Received 14 March 2017; accepted 26 July 2017; published online 11 August 2017)

We modified an epi-illumination light microscope and mounted it on an ultra high vacuum chamber for investigating samples used in a surface science experiment. For easy access and bake out, all optical components are placed outside the vacuum and the sample is imaged through a glass window. The microscope can be operated in reflection brightfield or epifluorescence mode to image the sample surface or fluorescent dye molecules adsorbed on it. The homemade sample mounting was made compatible for the use under the microscope; sample temperatures as low as 6 K can be achieved. The performance of the microscope is demonstrated on two model samples: Brightfield-images of a well-prepared Ag(100) surface show a macroscopic corrugation of the surface, although low energy electron diffraction data indicate a highly ordered crystalline surface. The surface shows macroscopic protrusions with flat regions, about 20–200 μm in diameter, in between. Fluorescence images of diluted 3,4,9,10-perylene tetracarboxylicacid dianhydride (PTCDA) molecules adsorbed on an ultrathin epitaxial KCl film on the Ag(100) surface show a shading effect at surface protrusions due to an inclined angle of incidence of the PTCDA beam during deposition. For some preparations, the distribution of the fluorescence intensity is inhomogeneous and shows a dense network of bright patches about 5 μm in diameter related to the macroscopic corrugation of the surface. We propose that such a light microscope can aid many surface science experiments, especially those dealing with epitaxial growth or fluorescent materials. *Published by AIP Publishing.* [http://dx.doi.org/10.1063/1.4997953]

I. INTRODUCTION

When talking about microscopy in the field of surface science, most people think about scanning probe microscopy[1,2] (SPM), low energy electron microscopy[3] (LEEM), or photoemission electron microscopy[4] (PEEM). Whereas SPM techniques are best suited for imaging surface areas in the range between a few nm and several 100 nm on the lateral scale with up to atomic resolution,[5] LEEM and PEEM can be used to image surface areas on a mesoscopic scale between a few μm and several 100 μm with up to a few nm resolution.[6,7] For a larger scale, light microscopy (LM) is the method of choice. However, up to today there are less than a handful of publications describing the use of LM for samples under ultra high vacuum (UHV) conditions.[8,9] This is astonishing since LM can be performed in various modes yielding complementary information: Besides brightfield or darkfield imaging for investigations of the sample morphology, also fluorescence- and polarization microscopy can be applied. With the latter techniques, the positions and orientations of isolated or aggregated dye molecules can be determined,[10] giving one the opportunity to study and control thin film growth, nucleation, and phase transitions of the related materials under surface science conditions. Moreover, LM is capable of detecting single molecules and hence gives one the opportunity to study single molecule dynamics and distributions.[8,9,11] We note that earliest experiments on organic molecular beam deposition on single crystal surfaces were done by LM, although only *ex vacuo*.[12]

Most experimental groups that use both surface science techniques and LM perform the sample preparation and first experimental investigations inside the vacuum. The LM is performed outside the vacuum.[13–15] This is extra time consuming and can lead to contamination, modification, or decomposition of the prepared samples. An *in vacuo* solution would therefore be desirable. However, the design of an UHV compatible light microscope is not trivial: First, it has to fulfill the requirements for UHV operation, which are low outgassing rates and bake out stability so that pressures down to 1×10^{-10} mbar can be achieved. Second, it should have ideal illumination and imaging properties as well as flexibility in the use of different objectives and filters. For the design of such a microscope, the major problem is the short working distance between the front lens of the microscope objective and the sample surface that is usually less than a millimeter already for medium magnification microscope objectives (20×, 40×). Blumfeld *et al.* constructed a confocal laser-scanning microscope.[8] They chose an approach with a custom-made vacuum compatible and bakeable Schwarzschild microscope objective placed *inside* the UHV. They were able to image single molecule fluorescence on various substrates with near-diffraction-limited resolution. However, due to the placement of the microscope objective inside the UHV, they had to accept a maximum bake out temperature of

only 100 °C and the risk of a deterioration of the microscope objective.

In this paper, we report on a different and in some aspects more flexible approach to an UHV microscope. It is based on a standard wide field (non-confocal) microscope, which is able to image large sample areas in brightfield or fluorescence mode. It was adapted to an existing surface science setup. This adaption had to fulfill the following aspects: (a) the sample preparation and observation have to be performed under UHV conditions, (b) for higher flexibility and bake out stability, all optical components (including the microscope objective) have to be mounted outside the vacuum, (c) the sample has to be easily accessible both by the microscope and other surface science techniques, (d) the sample has to be cold for fluorescence imaging, and (e), this is special to our setup, the microscope has to be retractable from the pathway of the sample in order to grant a transition of the sample into a glass head at one end of the UHV chamber (cf. Fig. 1, below).

In Sec. II, the design of the microscope and the sample mounting will be described in detail. In Sec. III, we demonstrate the performance of the microscope on a well-prepared clean Ag(100) surface for brightfield application and on diluted organic dye molecules adsorbed on a thin KCl film on this surface for fluorescence imaging.

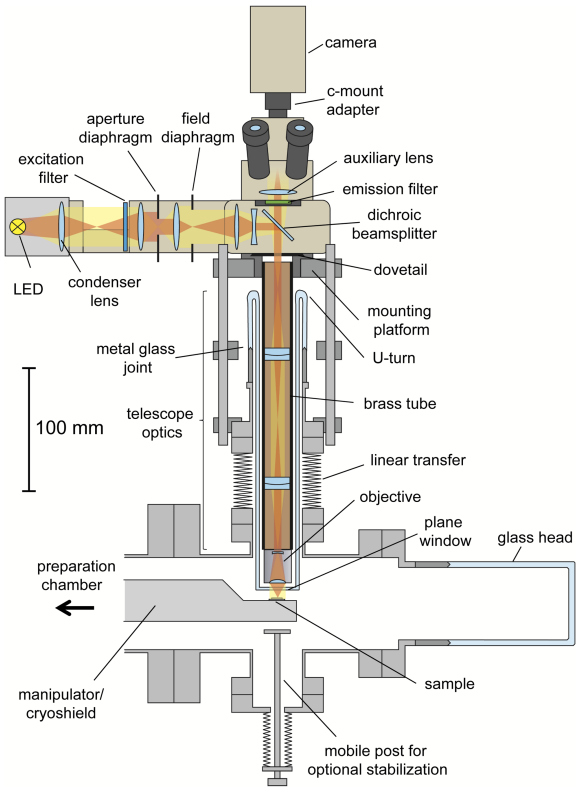

FIG. 1. Overview of the epi-illumination light microscope including the optical components, the sample holder, and the glass head. The optical pathways corresponding to the conjugated field and aperture planes are sketched in red and yellow, respectively. The trinocular head and the camera are not drawn to scale. For further details see the text.

II. SYSTEM DESIGN

A. UHV system

The microscope was implemented onto a horizontal tube attached to a typical stainless steel UHV chamber, which was equipped with an instrument for spot profile analysis low energy electron diffraction (SPA-LEED, Omicron NanoTechnology GmbH) and designed for fluorescence spectroscopy on organic molecules adsorbed on thin films. The chamber contained a sputter gun for surface preparation and homemade Knudsen-type thermal evaporators for the deposition of alkalihalides and organic molecules. For deposition control, a quadrupole mass spectrometer and quartz-microbalances were used. The Ag(100) sample was invariably mounted on a homemade sample mounting on a horizontal long travel manipulator with a liquid helium cryostat (VAb GmbH). Sample temperatures between 6 K and 1000 K were achieved. (We will report the details of the sample mounting in Sec. II D.) Structural characterization of the sample was typically done by the SPA-LEED apparatus. For fluorescence spectroscopy, the sample could be transferred into a glass head at the end of the same horizontal tube to which the microscope was attached. A schematic view of the microscope is shown in Fig. 1.

B. Microscope

The microscope was mounted on a stainless steel UHV 6 way cross (microscope adapter) with a length of 160 mm and an inner diameter of 70 mm. It was inserted between the preparation part of the vacuum chamber and the glass head with two conflat flanges (CF 100 and CF 63) and had four additional CF 40 flanges on diametrically opposed sides of the tube (top, bottom, front, and back). The flanges in front and back were used as viewports. The flange at the bottom was used for a linear motion feedthrough holding a post, which could stabilize the sample against vibrations. The microscope itself was mounted on the top flange.

As mentioned above, the most critical problem concerning the design of an UHV microscope was the required small working distance between the front lens of the microscope objective and the sample. Since the sample was inside the vacuum and in our approach, all optical components were supposed to be outside the vacuum, the sample needed to be imaged through a glass window. For mechanical stability and pressure stability, this window had to exhibit a significant thickness. We used a plane borosilicate window (Borofloat 33, Schott AG) with a diameter of 36 mm and a thickness of 1.75 mm. This thickness was indeed below that of conventional UHV windows of similar size (~3 mm), but it still exceeded the typical working distances of medium magnification microscope objectives (20×, 40×). Therefore, we used microscope objectives with larger working distances (for details see Sec. II C). Optically the window acted as an additional plane parallel plate, i.e., like a thick cover glass slip. We did not use an anti-reflection coating on the glass window so far. This may reduce stray light and increase the detection efficiency. However until now stray light has not been an issue.

To bring the window as close as possible to the sample, it was melted to the foremost end of a glass tube that pointed into the UHV (see Fig. 1). The glass tube had a length of 230 mm,

a wall thickness of 2 mm, and an inner diameter of 32 mm. At its upper end, it turned into a U-turn before it was connected with a metal glass joint on top of a CF40 flange. This construction may appear laborious but had a very simple reason: The metal glass joint can only stand compressive but not tensile forces. This was taken into account by orienting the metal glass joint pointing to the high-pressure side in combination with a U-turn made out of glass. The described construction withstood pumping to vacuum and bake out temperatures of at least 150 °C.

To retract the glass tube out of the pathway of the sample, it was mounted to a 50 mm linear transfer (VG Scienta) on the top flange of the microscope adapter. For microscope operation, the front window of the glass tube can be approached very close to the sample surface while watching this from a horizontal window of the microscope adapter at 90°. A drawback of the linear transfer was the elongation of the length of the glass tube, which added to the optical paths of the microscope. Therefore, this option for retraction may be reconsidered if it is not required.

The optical parts of the microscope were connected to the UHV-part via a mounting platform with a circular dovetail. The microscope objective was mounted at the end of a brass tube (see Fig. 1) that fitted inside the glass tube and positioned the objective close to the window at the front end. To avoid stray light, the brass tube was black oxidized at the in- and outside. It had an outer diameter of 30 mm, a wall thickness of 2 mm, and a length of 230 mm to compensate the length of the glass tube. The mounting platform was moved and fastened on four 200 mm M8 threaded rods that were attached at the top flange of the linear transfer. By moving the platform on the rods, the distance between the microscope objective and the window at the end of the glass tube could be adjusted. For the increase of stiffness and reduction of vibrations, an additional platform was fixed on half way of the rods. The platforms and all optical components could easily be removed for bake out or maintenance. Please note that most conventional microscope objectives typically cannot stand temperatures higher than ~50 °C. Therefore the possibility to remove the objective from the apparatus during bake out was essential.

C. Microscope optical setup

In principle any modular incident light microscope could be used in combination with the above described microscope adapter. We used the *universal epi illuminator* of a Nikon *Optiphot-Pol* microscope and the associated trinocular head for illumination and observation, respectively. The microscope used an incident light Köhler illumination[16] that was designed for a finite tube length of 210 mm. However, due to the elongated glass tube, the nominal standard tube length of 210 mm was exceeded by far (by about 200 mm). To retain ideal Köhler illumination, we thus inserted a telescope optics (elongation length 4f) with two achromatic lenses inside the brass tube. The lenses were arranged in such a way (distance = 2f, f = 50 mm) that the image plane of the aperture diaphragm was projected into the rear focal plane of the objective and the image plane of the field diaphragm was projected onto the sample. The corresponding conjugated image planes are drawn in Fig. 1. For imaging, a series of *Nikon M Plan* microscope objectives (5× NA 0.1, 10× NA 0.25, and 20× NA 0.4) corrected for a finite tube length of 210 mm was used. The 20× microscope objective exhibited an extra long working distance (ELWD) so that the thickness of the glass window could be easily tolerated and the front surface of the window was at a minimum distance of 2-3 mm from the surface of the sample. We note that none of the Nikon objectives was corrected for the 1.75 mm thickness of the glass window, which caused some loss of image quality and fluorescence intensity due to spherical aberrations. These issues became more pronounced with increasing NA of the microscope objectives. Therefore, at higher magnification and NA, an *Olympus CDPlan* 40 *PL* objective (40× NA 0.5) was used. This objective exhibits a larger working distance and is equipped with a correction collar, which we used to compensate the effect of the thickness of the glass window (up to 2 mm). Since this objective was corrected for a finite tube length of only 160 mm, and the trinocular head of the microscope exceeded this distance by 50 mm, it was replaced by a shorter homemade adapter tube for the use of this objective. We note that the maximum diameter of all used microscope objectives was 29 mm so that they all fitted smoothly into the glass tube. For detection we used a monochrome, thermoelectrically cooled 12-bit CCD-camera (PCO *Sensicam*) mounted on commercially available standard 0.4× or 1× c-mount adapters.

The original light source, a halogen lamp, was substituted by a homemade passively cooled illuminator with high power light-emitting diodes of the type Luxeon M LXR7-SW65 (cold white, 6500 K) and LXR0-SR00 (royal blue, 450 nm, Philips Lumileds Lighting Company) for brightfield and fluorescence illumination, respectively. The light was collimated by an aspheric condenser lens (Edmund Optics) with a focal length of 13 mm. For fluorescence application, the royal blue light-emitting diode was used in combination with a bandpass excitation filter (448 nm, 20 nm bandwidth, OD6, Edmund Optics), a dichroic beam splitter (T470lpxr, 470 nm, Chroma), and a bandpass emission filter (520 nm, 70 nm bandwidth, OD6, Edmund Optics). This set of filters was chosen on the basis of the absorption and fluorescence spectra of isolated molecules of PTCDA (3,4,9,10-perylene tetracarboxylicacid dianhydride) adsorbed on KCl(100) terrace sites.[17] In this configuration, we measured a maximum light density of 250 mW/cm^2 at the position of the sample surface with the *Olympus* 40× objective.

D. Sample mounting and cooling

The construction of the sample mounting was optimized for low temperatures, good accessibility by surface science techniques, as, for instance, LEED and photoelectron spectroscopy, and compatibility with the light microscope. Especially the combination of low temperatures and good accessibility was challenging: On the one hand, the sample needed good thermal coupling to the cryostat, which is favored by short distances and large cross-sectional areas; on the other hand, it had to be in an exposed position for the approach of the front window of the microscope, without being hindered by the sample mounting or the cryostat. In addition, reduction of heat impact via cryoshields needed to be considered.

A detailed picture of the sample mounting and the cryoshield is shown in Fig. 2. The sample mounting consisted

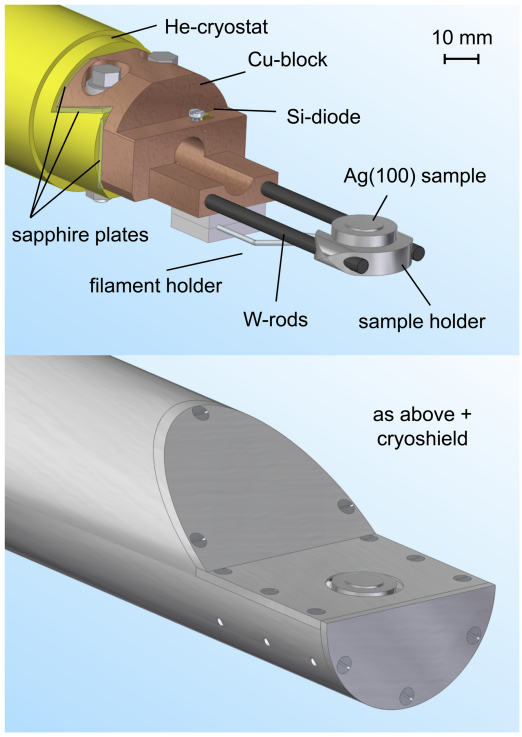

FIG. 2. Schematic drawing of the sample mounting (top) and the cryoshield (bottom). For further details see the text.

of three parts: A block made out of oxygen-free copper, two tungsten rods (3 mm in diameter) pressed into the copper block for optimal thermal contact, and a sample holder made of solid silver pressed onto the tungsten rods. The Ag(100) sample was of the "hat type" and had a diameter of 10 mm. It was fastened on top of the sample holder with a silver ring lid. Silver was used for the sample holder to avoid mechanical strain induced by differences in thermal expansion. As a further benefit, it has a high thermal conductivity. The crystal surface was positioned in the rotational axis of the manipulator, about 4 mm above the tungsten rods. In combination with the length of the rods (80 mm), this brought the sample in an exposed position with ideal accessibility for the microscope.

The copper block was pressed against a liquid helium cryostat by VAb GmbH that reached temperatures down to 5 K. Between the head of the cryostat and the copper block, three 1.5 mm sapphire plates were inserted for electrical isolation. These sapphire plates also granted high heat conductance at low temperatures and thermal isolation at elevated sample temperatures required for annealing of the sample. Annealed 0.1 mm thick gold foil was inserted on both sides of the sapphire plates to compensate small irregularities of the fitted surfaces.

The sample could be heated by radiation from a 100 W tungsten filament at its rear side and by additional electron impact. Sample temperatures above 70 K were measured with a type K thermocouple attached to the sample holder. Cryogenic temperatures ($\leq$70 K) were measured via a silicon diode (DT-670B-SD, Lake Shore Cryotronics Inc.) mounted on the copper block. This location was apart from the sample but is necessary since the Si-diode cannot withstand temperatures higher than 500 K. Despite that, an accurate temperature measurement was possible in the low temperature regime. This was checked by a calibration experiment with a second Si-diode mounted for test purposes directly to the rear side of the sample. We found that the temperature measured directly at the sample was less than 1 K above that measured on the copper block. For a reduced heat impact, Manganin cables were used to connect the Si-diode. All cables that were connected to the sample holder were precooled at the cryostat, as it is common.

We used a cryoshield made of polished aluminum. It was mounted on the second cooling stage of the cryostat, which was cooled by the helium backflow. As can be seen in Fig. 2, the cryoshield was composed of different parts in order to shield the entire sample mounting except the sample surface, which stuck out of the cryoshield and was the topmost surface for unrestricted access. The cryoshield was optimized for allowing inclined incidence or emission of probing beams (or particles) up to an angle of at least 45° with respect to the sample normal in all azimuthal directions.

The cooling was performed by either pumping or pressing liquid helium through the cryostat. Usually the pumping method was used because it was highly reproducible and the flux could easily be controlled especially in the case of small fluxes. However, we found this method to be limited by a minimum sample temperature of 12 K at a flux of 5 dm^3/h of liquid He. By pressing helium through the cryostat, sample temperatures of 6 K at a flux of 8 dm^3/h of liquid He could be achieved. This was done by applying about 400 mbar of extra He pressure to the dewar.

III. RESULTS AND DISCUSSION

A. Brightfield microscopy on a Ag(100) surface

The performance of the microscope is tested on a well-prepared Ag(100) crystal. It represents a typical sample that has been used for surface science experiments for many years. It was extensively prepared by numerous cycles of Ar^+ ion sputtering with 1000 eV and subsequent annealing to 1000 K for 1 h. It exhibits a shiny surface. Originally, the crystal was prepared by chemomechanical polishing. The crystal shows a very good and sharp low energy electron diffraction (LEED) pattern. As a measure for the microscopic crystal quality, the full width at half maximum $\Delta k_{||}$ of the LEED spots is determined at an in-phase condition (81 eV) with respect to monoatomic Ag(100) steps. The corresponding length in real space $L = 2\pi/\Delta k_{||}$[18] has a value of ~600 Å. This can be considered to be a very good value for a metal crystal since in general, the limitations on L by the mosaic spread of metal samples are more pronounced.[19]

In the following, we show brightfield images of the crystal surface that were recorded with the *Nikon* 5× and 20× objectives and with the *Olympus* 40× objective. We estimate that we achieve a resolution of 0.8 μm with the 40× objective, as these are the smallest features visible in our acquired images. Figure 3(a) shows an overview image of the sample that was assembled from individual brightfield images. The contrast

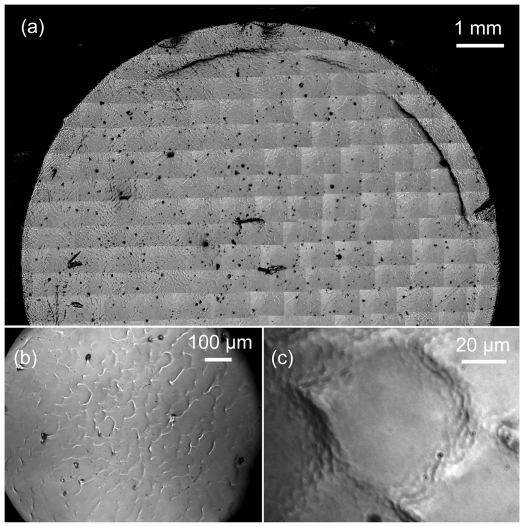

FIG. 3. Brightfield images of the Ag(100) crystal surface. (a) Overview image of the sample. The image was assembled from individual pictures that were taken with a 5× objective and a 1× c-mount adapter. To avoid artifacts from the image plane curvature, the individual images were taken with a reduced field of view. The sample shows macroscopic defects like scratches and splinters and has a macroscopic corrugation. (b) Enlarged brightfield image of the surface corrugation (objective 20×, c-mount 0.4×). The surface shows a dense network of curved linear protrusions with flat areas in between. (c) Detail image of the linear protrusions with additional substructure (objective 40×, c-mount 1×).

present in these images is related to the topology of the surface and originates in either specular or diffuse reflection of light. Unlike the expectations that may have arisen from the diffraction data, the surface shows strong inhomogeneities and a macroscopic height corrugation. In addition, at some positions, the surface is damaged by scratches or contaminated by metal splinters that stick to the surface. On this length scale, no changes are observed after repeated cycles of sputtering and annealing. The corrugation is present on the entire sample surface; however, less and more corrugated regions can be identified. For example, near the edge of the crystal, the surface is slightly elevated with respect to the rest of the crystal and shows a very pronounced corrugation, whereas in the middle of the crystal, smoother regions are more frequent.

A more detailed image of the surface is shown in Fig. 3(b). We find that the surface corrugation corresponds to a framework of flat areas that are surrounded by curved narrow protrusions. These are presumably macroscopic step bunches that locally merge into each other. Additionally, at some positions also larger rather dot shaped protrusions can be observed. The width of the narrow protrusions along their short direction is always about 10 μm, their individual lengths vary and can exceed 200 μm depending on their location on the sample. Also the flat areas between them vary in size. They are 20–30 μm in diameter in the more corrugated and up to ~200 μm in the smoother regions of the surface.

The smallest structures that can be detected in brightfield mode are shown in Fig. 3(c). The image shows a closeup of the above mentioned protrusions. On top and at the sides of the protrusions, a ruffled substructure is observed. The size of the individual ruffles varies between 0.8 and 1.0 μm in diameter. In contrast, in the flat areas between the protrusions, no additional substructure, such as the ruffles, can be detected. Thus, we conclude that the flat areas are the smoothest areas on the surface on this microscopic scale.

On this scale, further cycles of sputtering and annealing have only marginal influence on the images. We therefore assume that the formation or flattening of the corrugation is a rather slow process and the macroscopic morphology of the crystal surface changes rather on the scale of several tens of preparation cycles.

B. Fluorescence microscopy on monomers of PTCDA/KCl/Ag(100)

For the fluorescence imaging of adsorbed molecules, an about 10 atomic monolayer thick KCl film was epitaxially grown on the Ag(100) crystal.[17] This film electronically decouples the dye molecules from the metallic Ag sample and prohibits quenching of the fluorescence.[20] The PTCDA coverage was varied between 1×10^{-5} and 5×10^{-2} of a complete monolayer.[21] Below 20 K sample temperature, the deposited PTCDA molecules are immobile and form a diluted phase. We are able to record fluorescence images for coverages above 1×10^{-3} of a monolayer. Below this concentration, the fluorescence signal is too small and vanishes into a diffuse background signal that originates from residual excitation light surpassing the filters. This light is, different from the situation of fluorescence microscopy in solutions, reflected by the mirror like sample surface. In the brightfield images, neither signatures of the growth of the epitaxial KCl film nor of the deposited PTCDA molecules can be detected.

Before we will consider the details of the fluorescence images, we summarize some facts known about PTCDA on KCl from fluorescence spectroscopy: The molecules adsorb flat lying and azimuthally aligned to the KCl(100) surface on well-defined adsorption sites.[17,22] As said above, the molecular surface diffusion of PTCDA is hampered below 20 K and thus attractive defect sites of the KCl surface, e.g., step edges, are not preferentially populated (different from the situation at higher temperatures). Also no aggregation into compact islands takes place.[23] The fluorescence spectra are dominated by a sharp 0-0 transition and show well-resolved vibrational modes.[17] However, the quality of the fluorescence signal depends to some extend on the exact position of the excitation laser on the surface (diameter 200 μm), i.e., additional diffuse background signal or additional peaks from minor fluorescent species can be observed. Comparing these observations from spectroscopy experiments with the present results from brightfield microscopy, these differences can tentatively be related to the local macroscopic quality of the sample surface. Spectra from generally smoother surface regions [cf. Fig. 3(a)] are proposed to give better quality than spectra taken from stronger corrugated or even defective regions.

In the fluorescence microscopy images, the averaged fluorescence intensity (integration area larger than $100 \times 100\ \mu m^2$) is independent from the sample position, which corresponds to the fact that the deposition procedure leads to a homogeneous coverage. However, on the microscopic scale (see Fig. 4), the fluorescence signal is not constant but shows structures with an additional contrast that increases with dye concentration.

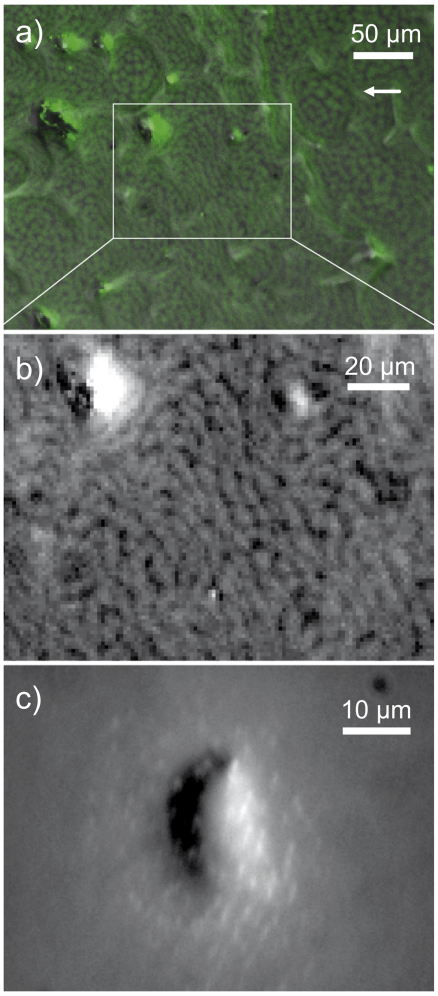

FIG. 4. Fluorescence images of diluted PTCDA molecules (1% of a monolayer) on a 10 monolayer thick KCl film on Ag(100) at T = 6 K. (a) Superposition of a brightfield image and a green colored fluorescence image (objective 20×, c-mount 0.4×, exposure time 0.5 s). The white arrow indicates the azimuthal direction of the molecular deposition, which leads to a shading of the surface protrusions. (b) Magnification of the fluorescence image of the white box in (a). The fluorescence images show an additional structured contrast in the flat surface areas. We attribute this to partial open regions in the KCl film (For better visibility, a background signal was subtracted). (c) Detailed fluorescence image of a single dot shaped protrusion on the surface demonstrating the shading effect and the achieved resolution (objective 40×, c-mount 1×, exposure time 2 s). In contrast to (b), the surface shows no additional structured contrast but small bright spots on top and around the macroscopic defect. For further details see the text.

The image shown in Fig. 4(a) displays an overlay of a green colored fluorescence image with a brightfield image. It allows correlating the fluorescence contrast and the surface morphology. Two observations can be made: The first is a shading effect for the protruding structures. They have a brighter and a darker side. This is due to the inclined angle of incidence of the molecular beam (45° with respect to the surface normal). The protrusions are covered on the sides that face the evaporator; the opposite sides are shadowed and appear darker in fluorescence images. The second aspect is an additional contrast in the flat regions between the macroscopic protrusions [see the closeup in Fig. 4(b)]. This contrast depends on the particular preparation of the sample, presumably on the preparation of the KCl film. We see a dense pattern of brighter oval patches, about 5 μm in average diameter. Near the protrusions and on top of them, they are elongated and their density increases, whereas in the smoother areas, they are more roundish and clearly separated from each other. Between these oval patches, the detected fluorescence intensity is not zero but noticeably smaller.

Up to now it is not fully understood, what causes this additional contrast in the fluorescence images. We can nevertheless exclude a relation to the concentration of PTCDA molecules on the surface since the form and size of the patches do not change for increasing PTCDA concentrations. We estimate that at a coverage of 1×10^{-3} of a monolayer, about 10^4 molecules contribute to a single patch of 20 μm^2. Consequently, a single molecule related contrast or random fluctuations of the molecule density can be excluded. Regarding the fact that the structure of the fluorescence contrast is correlated with the morphology of the surface, it is more likely that additional morphologic effects of the surface or the epitaxial KCl film are decisive here. One explanation is, e.g., based on a further corrugation of the Ag surface that is not seen in brightfield mode due to a lack of contrast. Corrugations on this length scale (5 μm) were reported, for example, by Cheynis *et al.* They observed a morphology of a Au(111) surface with plateau- and canyon-like structures in LEEM images.[24] Possibly the KCl film is also inhomogeneous and surface areas remain unwetted by the KCl, preferentially where canyon-like structures are present. There, the PTCDA molecules are adsorbed to the bare silver surface where their fluorescence is quenched. In conclusion, we propose that in these images the fluorescence contrast is related to the inhomogeneities in the KCl film.

Finally, in Fig. 4(c), we show a fluorescence image of a larger dot shaped protrusion in order to demonstrate the achieved resolution. As can be seen, it is covered and surrounded by small bright spots that have a diameter of about 0.7 μm. The origin of these spots is not clear, yet. They could be related to the cluster formation of molecules or emission from defect sites. A reliable explanation and assignment of these are however out of reach of the present work and ask for a combination of spatial and spectral resolution.

IV. SUMMARY

We demonstrated the operation of an epi-illumination light microscope adapted to an UHV chamber by recording brightfield images of a well-prepared Ag(100) surface used for surface science experiments. We could resolve a surface morphology with regular corrugations in height on a lateral scale of 10–200 μm. Fluorescence images of diluted dye molecules deposited and imaged at 6 K on a thin KCl film show a pattern of structures on the scale of 2–10 μm, which we attribute to inhomogeneous "wetting" of the surface by the KCl film. We propose that this type of UHV light microscope is a helpful tool to identify well-suited surface positions for experiments with other techniques or to study the growth of deposits on the µm scale, e.g., for organic semiconductors. A combination with spectroscopic resolution also appears possible.

ACKNOWLEDGMENTS

We thank Peter Koll for manufacturing the metal glass joint and the associated glass tube. The project was supported by the Deutsche Forschungsgemeinschaft under the Project No. SO407/8-1.

[1] G. Binnig, H. Rohrer, C. Gerber, and E. Weibel, Phys. Rev. Lett. **49**, 57 (1982).
[2] G. Binnig, C. F. Quate, and C. Gerber, Phys. Rev. Lett. **56**, 930 (1986).
[3] E. Bauer, Rep. Prog. Phys. **57**, 895 (1994).
[4] H. H. Rotermund, Surf. Sci. **283**, 87 (1993).
[5] F. J. Giessibl, Science **267**, 68 (1995).
[6] E. Bauer, M. Mundschau, W. Swiech, and W. Telieps, Ultramicroscopy **31**, 49 (1989).
[7] O. H. Griffith and G. F. Rempfer, Ultramicroscopy **24**, 299 (1988).
[8] M. L. Blumenfeld, B. S. Tackett, L. K. Schirra, J. M. Tyler, and O. L. A. Monti, Rev. Sci. Instrum. **80**, 103101 (2009).
[9] L. K. Schirra, B. S. Tackett, M. L. Blumenfeld, and O. L. A. Monti, J. Chem. Phys. **131**, 124702 (2009).
[10] B. Sick, B. Hecht, and L. Novotny, Phys. Rev. Lett. **85**, 4482 (2000).
[11] J. J. Macklin, J. K. Trautman, T. D. Harris, and L. E. Brus, Science **272**, 255 (1996).
[12] D. A. Neuhaus, Angew. Chem. **64**, 158 (1952).
[13] A. H. Schäfer, C. Seidel, and H. Fuchs, Thin Solid Films **379**, 176 (2000).
[14] L. Kankate, F. Balzer, H. Niehus, and H. G. Rubahn, Thin Solid Films **518**, 130 (2009).
[15] F. Balzer and H. G. Rubahn, Adv. Funct. Mater. **15**, 17 (2005).
[16] A. Köhler, J. R. Microsc. Soc. **14**, 261 (1894).
[17] M. Müller, A. Paulheim, C. Marquardt, and M. Sokolowski, J. Chem. Phys. **138**, 064703 (2013).
[18] M. Horn-von Hoegen, Z. Kristallogr. - Cryst. Mater. **214**, 591 (1999).
[19] M. Sokolowski and H. Pfnür, Phys. Rev. B **49**, 7716 (1994).
[20] W. Gebauer, A. Langner, M. Schneider, M. Sokolowski, and E. Umbach, Phys. Rev. B **69**, 155431 (2004).
[21] M. Müller, A. Paulheim, A. Eisfeld, and M. Sokolowski, J. Chem. Phys. **139**, 044302 (2013).
[22] Q. Guo, A. Paulheim, M. Sokolowski, H. Aldahhak, E. Rauls, and W. G. Schmidt, J. Phys. Chem. C **118**, 29911 (2014).
[23] A. Paulheim, M. Müller, C. Marquardt, and M. Sokolowski, Phys. Chem. Chem. Phys. **15**, 4906 (2013).
[24] F. Cheynis, F. Leroy, A. Ranguis, B. Detailleur, P. Bindzi, C. Veit, W. Bon, and P. Müller, Rev. Sci. Instrum. **85**, 043705 (2014).

B Spectroscopic results on further types of molecules

Besides the PTCDA molecules that have been investigated on thin epitaxial KCl(100) films in the main part of this work, also two different types of molecules have been investigated on KCl(100) films by fluorescence spectroscopy. On the one hand this has been the molecule MePTCDI (N,N'-dimethylperylene-3,4,9,10-bis(dicarboximide)), which is a perylene derivative like PTCDA but has imide groups instead of anhydride groups at its ends. On the other hand this has been the molecule pentacene, which is a pure hydrocarbon without any functional groups. For comparison ball and stick models of all three molecules are depicted in Fig. B.1.

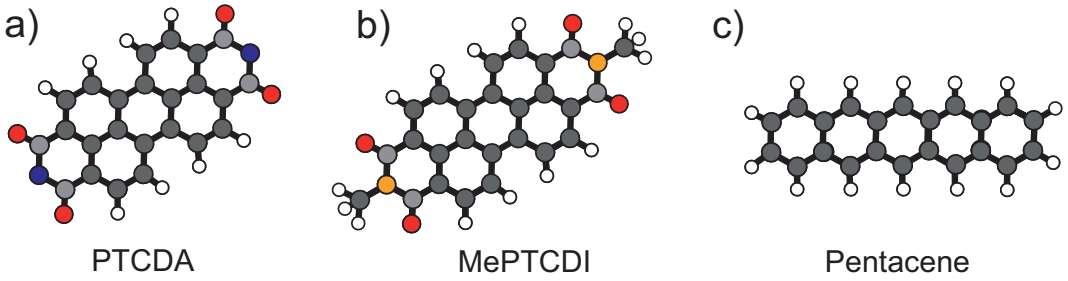

Figure B.1: *Ball and stick models of the molecules (a) PTCDA, (b) MePTCDI, and (c) pentacene.*

B.1 MePTCDI on KCl(100)

The system MePTCDI/KCl(100) has been studied analogue to the system PTCDA/KCl(100) both in a diluted phase and in a condensed monolayer phase.

Diluted phase: Fig. B.2a shows the FL spectrum of the diluted phase of MePTCDI on KCl(100). About 1% of a monolayer has been adsorbed on the KCl(100) surface at a sample temperature of $T = 20$ K. At this sample temperature the molecules are supposedly immobile and thus located at KCl terrace sites. Due to the similarities between the MePTCDI and PTCDA molecules also their adsorption sites on the KCl are probably similar. A structure model of the MePTCDI adsorption site on KCl terraces is depicted as an inset in Fig. B.2a. The terrace site FL spectrum is dominated by the 0-0 transition at 19780 cm^{-1} and shows partially resolved vibrational modes. Compared to the FL spectrum of PTCDA on KCl(100) the 0-0 transition is red shifted by 220 cm^{-1} and significantly broadened ($FWHM_{MePTCDI}(20\ K) = 82\ cm^{-1}$, $FWHM_{PTCDA}(20\ K) = 20\ cm^{-1}$). The broadening is presumably inhomogeneous and caused by a less defined adsorption geometry of the MePTCDI molecule on the KCl(100) terrace sites compared to the PTCDA molecule.

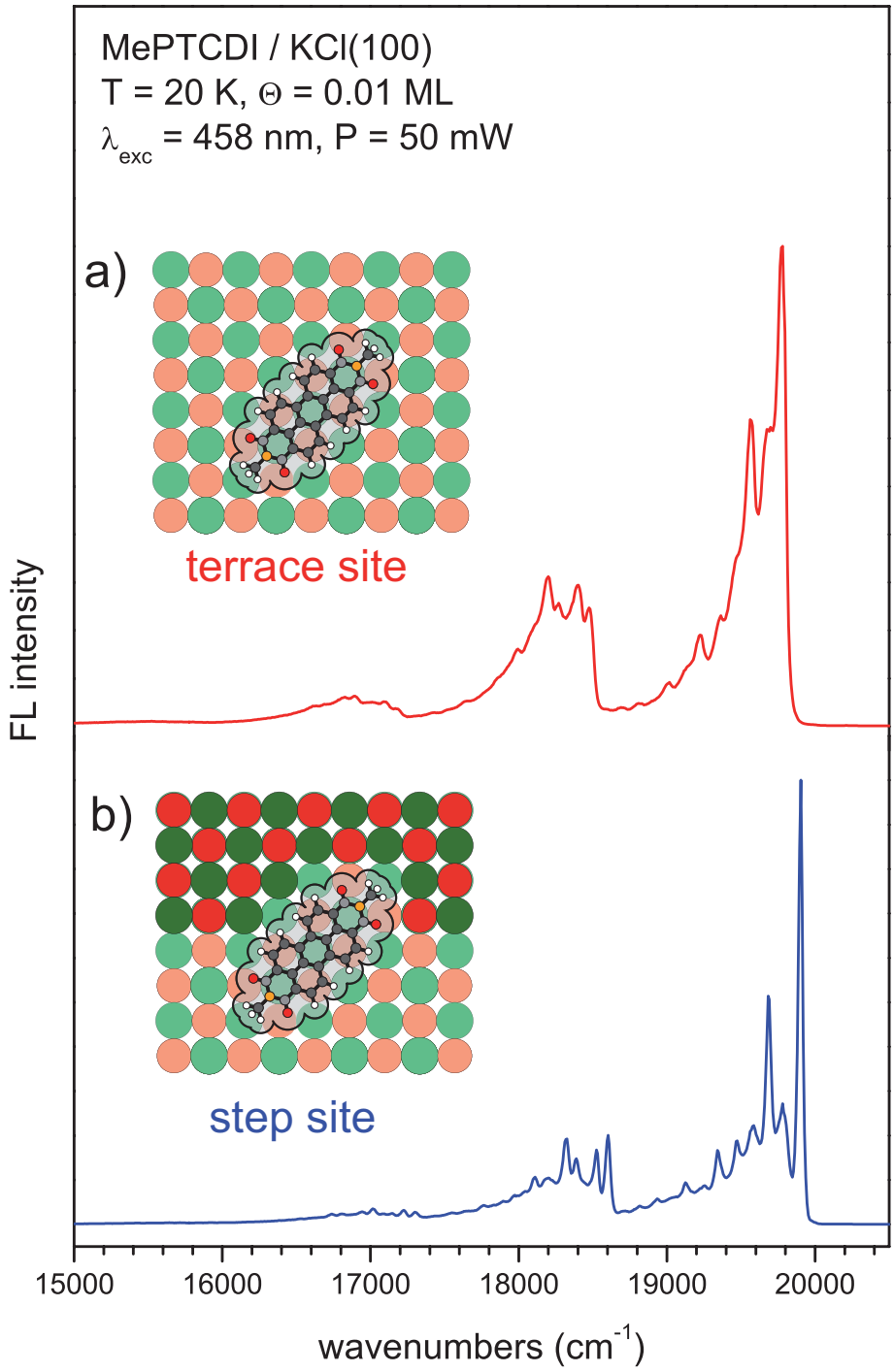

Figure B.2: *Fluorescence spectra of isolated MePTCDI molecules on KCl(100) terrace (a) and step sites (b). Both spectra were measured at a sample temperature of* $T = 20$ K *with an excitation wavelength of* $\lambda_{exc} = 458$ nm. *The surface coverage was* $\approx 1\%$ *of a monolayer. While the terrace site spectrum (a) shows the 0-0 transition at* $19780\ \mathrm{cm}^{-1}$, *the spectrum of the step site shows a blue shifted 0-0 transition at* $19904\ \mathrm{cm}^{-1}$. *The width of the 0-0 transition is reduced from* $\mathrm{FWHM} = 82\ \mathrm{cm}^{-1}$ *for the terrace site spectrum to* $\mathrm{FWHM} = 30\ \mathrm{cm}^{-1}$ *for the step site spectrum. Real space models of the molecules at terrace and step sites are given as insets, respectively. For details see text.*

Differences in the bonding to the KCl substrate between PTCDA and MePTCDI can also be deduced from the optical transition energies of the two molecules in the gas phase compared to the KCl terraces. The 0-0 transition of PTCDA in He-nanodroplets (comparable to the gas phase) is located at 20980 cm^{-1} [114]. On the KCl terrace site it is located at 20000 cm^{-1} [8]. Thus the transition energy of PTCDA molecules is reduced by 980 cm^{-1} due to the bonding to the KCl substrate. For MePTCDI the 0-0 transition in He-nanodroplets is located at 20570 cm^{-1} [160] and on the KCl surface it is located at 19780 cm^{-1}. Here the reduction of the transition energy due to the binding to the KCl is only 790 cm^{-1} and thus 190 cm^{-1} smaller than the one of the PTCDA. This shows that the spectral shift induced by the binding to the substrate is not a material constant of the substrate but dependent on the distinct binding situation.

Analogue to PTCDA on KCl(100) a migration of the molecules can be induced by a heating of the sample to 150 K for 10 minutes. The FL spectrum after annealing is shown in Fig. B.2b. Similar to the system PTCDA/KCl(100) the heating of the sample induces a spectral blue shift and a reduction of the inhomogeneous broadening of the FL spectrum. It can therefore be assumed that also the MePTCDI migrates to defined KCl step sites. The 0-0 transition of MePTCDI molecules at KCl(100) step sites has an energy of 19904 cm^{-1} and a width of FWHM = 30 cm^{-1}. It is shifted by 124 cm^{-1} with respect to the 0-0 transition of MePTCDI molecules on KCl terrace site, which is comparable to the situation for PTCDA. Although the inhomogeneous broadening of MePTCDI at the KCl step site is significantly reduced with respect to the terrace site, it is still broader than the one of PTCDA molecules at KCl steps (FWHM(20 K) $\approx$ 11 cm^{-1}) [18]. This could possibly be an effect of the methyl group at the end of the imide groups that sterically hinders the MePTCDI molecule from getting as close to the step edge as the PTCDA molecule. A possible step geometry based on the *deep vacancy site* of PTCDA on KCl is shown in the inset of Fig. B.2b. As can be seen a further K^+ ion is needed to be removed from the step in order to avoid the overlap with the methyl group.

Monolayer phase: The SPA-LEED pattern of the monolayer structure of MePTCI on KCl(100) is shown together with a structure model in Fig. B.3. Identical to PTCDA, the MePTCDI molecules grow in a brickwall structure commensurate to the KCl(100) lattice ($2\sqrt{2} \times 2\sqrt{2}$ R45°).

The monolayer phase of MePTCDI on KCl(100) has been grown at similar conditions as the PTCDA monolayers investigated by M. Müller et al. [14] at a sample temperature of $T = 260$ K with a growth rate of 1 monolayer per 10 minutes (crucible temperature $\approx$ 760 K). After deposition the sample temperature was kept at $T = 260$ K for 5 minutes in order to heal domain boundaries between MePTCDI domains and improve the overall order on the sample. Different from the situation of PTCDA on KCl (cf. Chapter 4.2.3), slower deposition rates and longer annealing times after deposition did not lead to an improvement in the size of domains but to smaller, more disordered structures.

The average size of MePTCDI domains was estimated from the width of the MePTCDI(1,0) spots (not shown). A full width at half maximum (FWHM) of $\Delta k_{||} = 0.06$ $Å^{-1}$ was determined at an electron energy of $E = 95.6$ eV. By the simple estimation that the average domain size corresponds to $L = 2\pi/\text{FWHM}$ this gives a size of $\approx 100 \times 100$ $Å^2$ or 7×7 molecules. However the spot profile

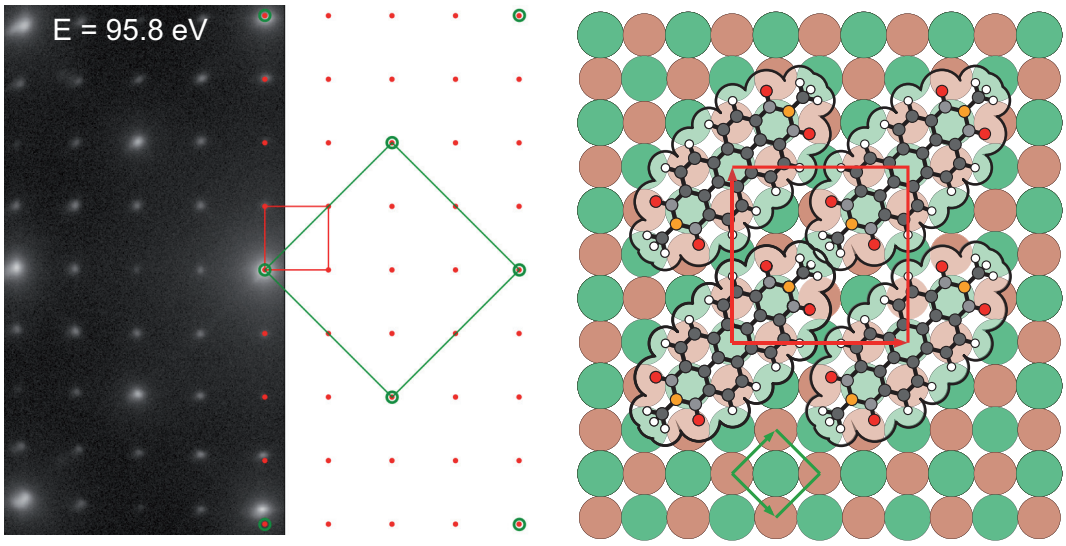

Figure B.3: *SPA-LEED pattern with simulation and structure model of the commensurate MePTCDI/KCl(100) brickwall phase. The LEED pattern was taken at an electron energy of $E = 95.6$ eV and a sample temperature of $T = 100$ K. The simulation shows the LEED spots and the unit cells of the KCl(100) substrate (green) and the MePTCDI superstructure (red). The structure model shows the unit cell of the MePTCDI molecules in the brickwall phase. The adsorption sites are identical to the PTCDA/KCl(100) brickwall phase. Please note the overlap of the van-der-Waals radii of the methyl groups of neighboring molecules in a row. For details see text.*

was found to be also compatible with a geometric domain size distribution as it was found for the optimized preparation conditions of PTCDA on KCl(100). Assuming this type of domain size distribution the average domain size would be determined to be only 3.2×3.2 molecules.

The FL and FLE spectra of the MePTCDI brickwall phase are shown in Fig. B.4. Due to the brickwall arrangement of the molecules in the superstructure also the MePTCDI domains form two-dimensional J-aggregates, which results in a spectral red-shift and a superradiant enhancement of the 0-0 transition with respect to the vibrational modes. The 0-0 transition has an transition energy of 19360 cm^{-1}, which is 420 cm^{-1} red-shifted with respect to the MePTCDI terrace site on KCl(100). This shift is slightly larger than the one for PTCDA on KCl (400 cm^{-1}) and will be partially explained by a different excitonic stabilization of the MePTCDI domains in the following.

The optical transition dipole moment of the MePTCDI molecule $|\vec{\mu}| = 6.8$ Debye [68] is smaller than the one of the PTCDA molecule $|\vec{\mu}| = 7.4$ Debye [68]. According to Eq. 3.22 this will decrease the coupling strength and thereby also the excitonic stabilization of the MePTCDI aggregates with respect to the PTCDA aggregates. However additionally, the Franck-Condon factor of the electronic transition contributes to the coupling strength. This is larger for the MePTCDI molecule $f_{00} = 0.33$ [161] (PTCDA: $f_{00} = 0.21$) and overcompensates the smaller transition dipole moment. Therefore, by calculating the energetic stabilization of the excitonic ground state ($k = 1$), in the limit of an infinite MePTCDI brickwall aggregate, an excitonic stabilzation energy of 173 cm^{-1} is obtained. This is larger than the excitonic stabilzation energy obtained for infinite PTCDA aggregates (130 cm^{-1}). Since the calculated increase of the excitonic stabilization of the MePTCDI is

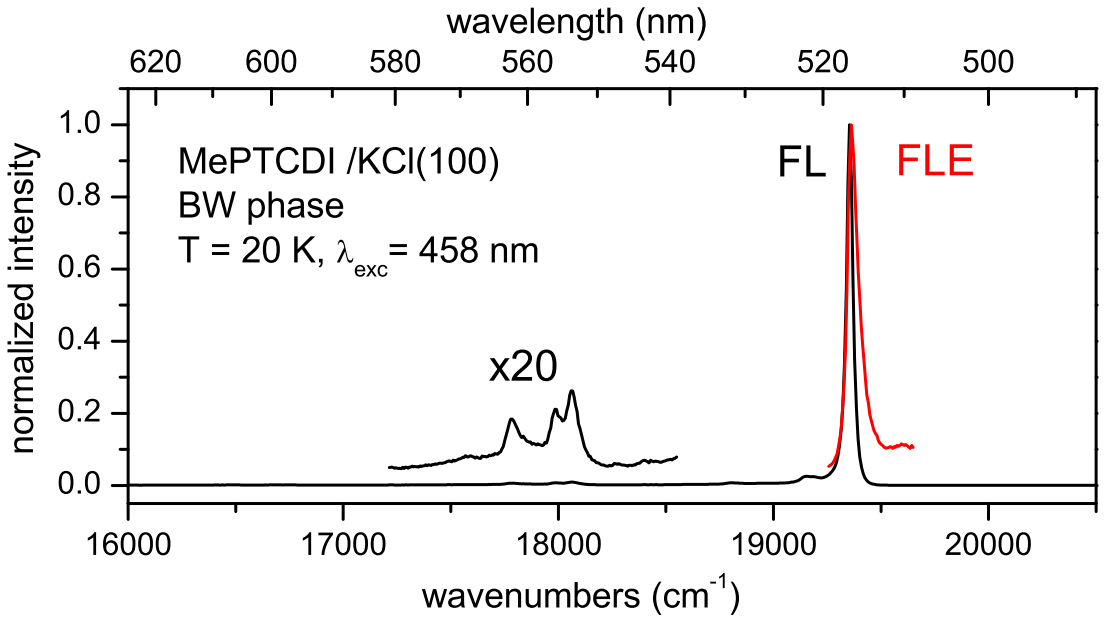

Figure B.4: *FL and FLE spectra of the MePTCDI/KCl(100) brickwall phase. The FL spectrum has been measured for at a temperature of $T = 20$ K and at an excitation energy of $\lambda_{exc} = 458$ nm. The 0-0 transition is superradiantly enhanced with respect to the vibrational modes. It has an energy of 19360 cm^{-1}. A magnification of the suppressed but resolved vibrational modes is shown as an inset. The FLE spectrum of the 0-0 transition was measured at $T = 20$ K, it shows an asymmetric broadening at the high energy side. For details see text.*

even larger than the increased red-shift of the spectrum due to aggregation, it can be assumed that the non-resonant D-term that also contributes to the red-shift is smaller for MePTCDI aggregates.

The superradiant enhancement factor has been determined to be $\eta_{SR} = 17$ at a sample temperature of $T = 20$ K. This value has been extracted from the MePTCDI bw-phase spectrum analogue to the procedure described in Appendix A.2. The extracted value is comparable to the one determined by M. Müller et al. ($\eta_{SR} = 20$) at the same temperature and at similar aggregate sizes of PTCDA on KCl(100) [16].

In summary, the system MePTCDI on KCl(100) showed large structural and therefore also spectral similarities with the system PTCDA on KCl(100). On the one hand these similarities showed that phenomena like the spectral blue-shift due to migration of the molecules to step-edges, or superradiance in a two dimensional brickwall structure are not restricted to the PTCDA molecule alone, but can at least also occur for similar molecules in a similar environment. On the other hand in particular the large similarities between PTCDA and MePTCDI allowed to compare and discuss the small spectral differences and learn about how small differences in the molecule-substrate or molecule-molecule interactions influence the optical properties.

B.2 Pentacene on KCl(100)

The system pentacene/KCl(100) was investigated together with Peter Zeppenfeld during a short term visit of him at the university of Bonn in May 2016. The aim of this investigation was to test

whether the high spectral resolution with clearly resolved vibrational modes that had been obtained in the FL and FLE spectra of isolated PTCDA molecules on alkali halide surfaces [8, 9, 17] could be also obtained for a large organic molecule without functional groups that anchor the molecule on defined adsorption sites. Since the pentacene molecule does not exhibit any functional groups, its binding to the KCl will be limited to van der-Waals interactions.

Fig. B.5 shows a series of FL spectra that were taken for increasing coverages of pentacene on KCl(100). The pentacene molecules have been evaporated onto a 5 ML thick KCl film at a sample temperature of $T = 12$ K and at a crucible temperature of 445 K. The deposition was controlled by monitoring the mass signal of $m/z = 278$ amu in the QMS. A calibration of the coverage has not been performed, therefore the coverages are quantified relative to the maximum coverage in this series (100%). It has been assumed that this coverage is still on the order of a first molecular monolayer. The molecules have been optically excited by use of the ring dye-laser adjusted to a wavelength of $\lambda_{exc} = 519.2$ nm. This wavelength was chosen since it lead to a high absorption at the lowest coverage, it was determined by maximizing the FL signal, while tuning the excitation wavelength.

At the lowest coverage (1%) the spectrum shows a 0-0 transition at 18169.8 cm^{-1} and further weak but narrow vibrational modes on top of two red-shifted broad features. With increasing coverage (2%, 5%, 10%) both the intensity of the narrow and the broad features increases, while especially the narrow features including the 0-0 transition become more clearly distinguishable. At even higher coverages (20%, 50%, 100%) the intensity of the narrow features saturates (or even decreases) and only the broad features increase in intensity. This increase in intensity occurs together with a spectral red-shift of the broader features. Finally, annealing the sample at the maximum coverage to 150 K leads to the complete vanishing of the narrow features and a further red-shift of the broad features.

The narrow features at low coverages and medium coverages stem supposedly from isolated molecules at distinct adsorption sites. These could be special defect sites, e.g. step edges, or simply isolated molecules on defined terrace sites [27]. The broad spectral features, especially at higher coverages, can supposedly be assigned to a condensed phase of pentacene molecules. This may consist of small aggregates of upright standing and π-stacked molecules like they were observed on the quartz(0001) surface [162]. Here also a spectral red-shift was observed during the formation of the first monolayer [162]. A further red-shifting was observed for coverages higher than a monolayer and the formation of multilayers [162]. Similar to condensed phases of tetracene molecules [49, 72], the π-stacking of pentacene molecules presumably leads to a J-aggregates behavior, which induces a spectral red-shift with increasing aggregate size.

In the end many more experiments and further experimental methods would be necessary to obtain a clear picture on the growth situation and the spectral evolution of pentacene molecules on KCl(100). Regarding the initial question, it could however be shown that it is possible to obtain spectra with resolved vibrational modes even for molecules without functional groups on KCl(100).

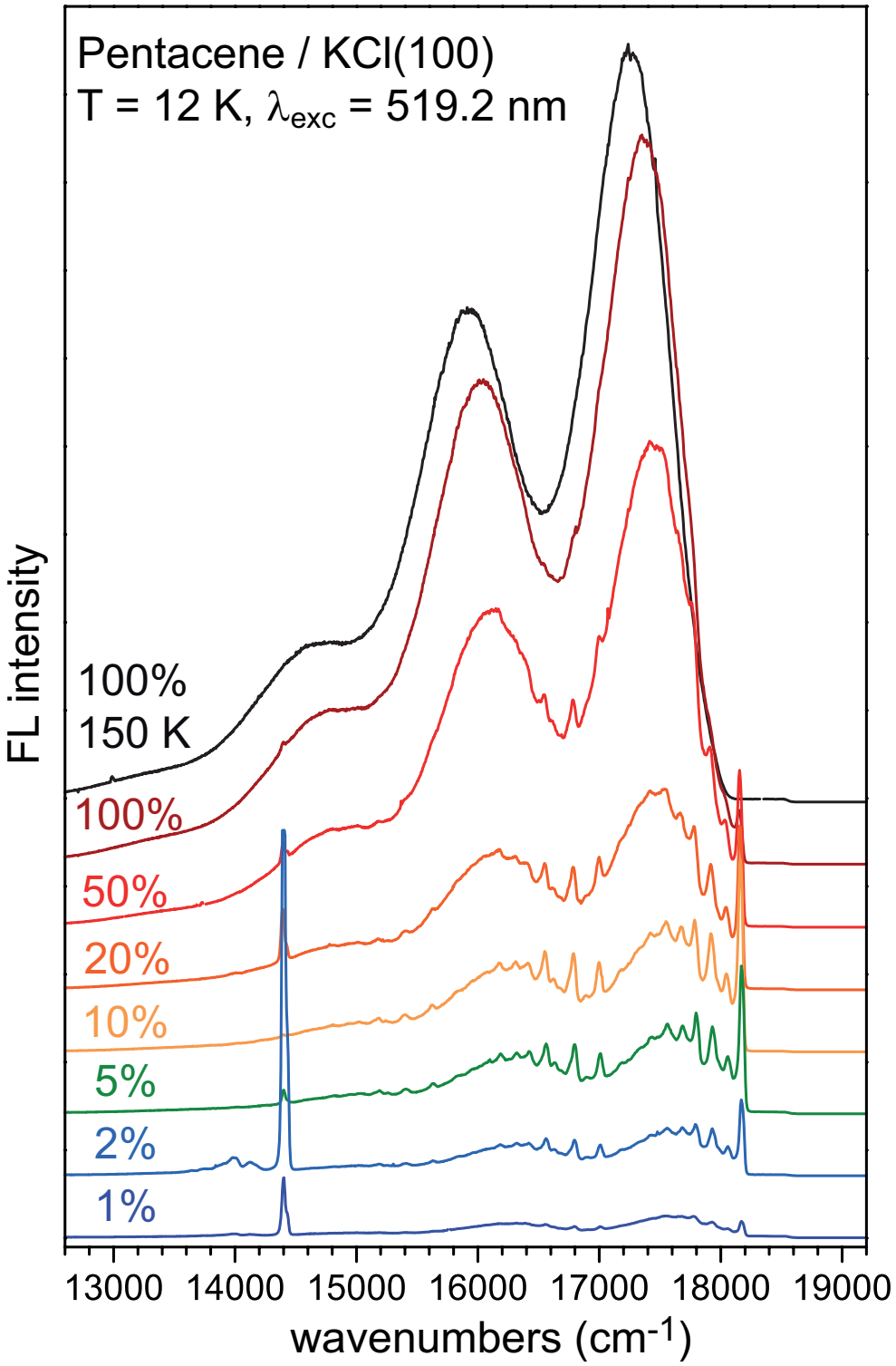

Figure B.5: *FL spectra for different coverages of pentacene on KCl(100). The spectra were measured at a sample temperature of $T = 12$ K with an excitation wavelength $\lambda_{exc} = 519.2$ nm. The sample coverages are given relative to the maximum coverage. At lower coverages the spectrum consists of broad and narrow features. The 0-0 transition of the narrow spectral features is located at 18169.8 cm^{-1}. With increasing coverage first both the narrow and broad features, at higher coverages only the broad features increase in intensity. The maxima of the broad features are slighty red shifted with increasing coverage. Annealing of the sample at the maximum coverage to $T = 150$ K for 5 min results in a further red-shift and the vanishing of the narrow features. The narrow spectral line around at 14480 cm^{-1} is independent from the coverage of pentacene and corresponds to localized defects on the sample. For better visibility the spectra are vertically shifted with respect to each other. For details see text.*

Local defect peaks: Besides the spectral signals of pentacene on KCl(100) also further superimposed signals have been detected around 14480 cm^{-1} (cf.Fig. B.5, 2%). A high resolution spectrum of these signals is shown in Fig. B.6. The spectrum shows two sharp signals at 14481 cm^{-1} and 14514 cm^{-1}, and two broad signals at 14030 cm^{-1} and 14180 cm^{-1}. The signals occurred highly dependent on the position of the excitation laser on the sample but were independent on the coverage of pentacene on the sample.

The same type of signal could also be detected for PTCDA on KCl(100) but was usually not measured due to a different spectral range. For a bare KCl(100) film or the clean Ag(100) surface this type of fluorescence signals could not be detected. In combination this leads to the assumption that the emitting species are local defects in the KCl film or on the Ag crystal that are indirectly excited by an energy transfer from an excited molecule. The type and origin of these defect could however not be solved. Possibly they are however related to the bright point like emitters that have been observed with the UHV-light microscope (cf. Chapter 7.3). These did also occur only for the presence of molecules on the KCl film but were very localized close to mesoscopic defect structures of the Ag surface.

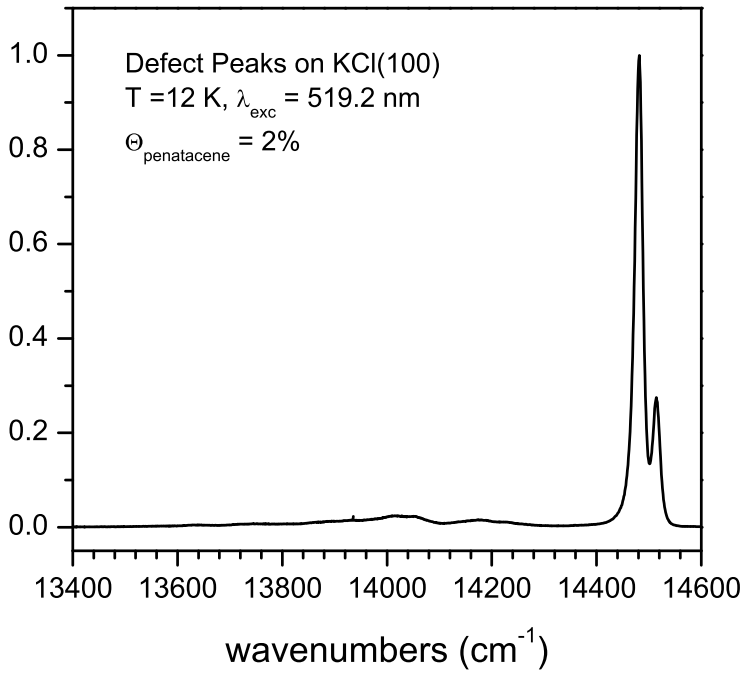

Figure B.6: *Magnified FL spectrum of defect emission detected together with pentacene on KCl(100). The spectrum shows two sharp signals at* 14481 cm^{-1} *and* 14514 cm^{-1}*, and two broad signals at* 14030 cm^{-1} *and* 14180 cm^{-1}*. The occurrence and intensity of the signals was highly dependent on the position of the excitation laser on the sample. The spectrum was taken with the high resolution grating (1200 groves/mm) at a sample temperature of* 12 K *with an exciation wavelength* $\lambda_{exc} = 519.2$ nm*. For details see text.*

C Programs for FLE data acquisition and processing

C.1 LabView program for single molecule FLE experiments

The *LabView* program initially written by M. Müller (and extended by A. Paulheim) for FLE measurements was not designed to meet the requirements of single molecule FLE experiments. Therefore a new LabView program ("FLE kontinuierlich.vi") based on these older programs was written and optimized with respect to the speed of the data acquisition, the implementation of the wavemeter measurement, and the online evaluation and visualization of the FLE measurement.

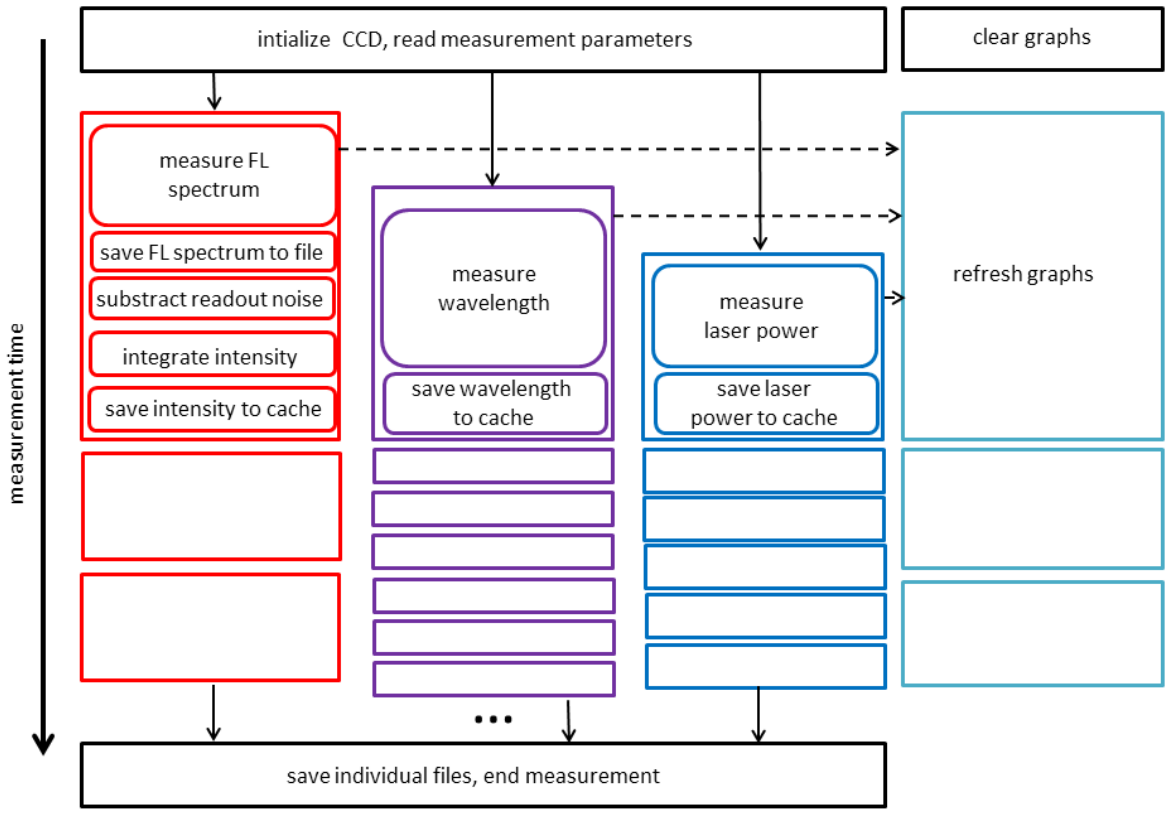

Figure C.1: *Schematic illustration of the LabView program ("FLE kontinuierlich.vi") for single molecule FLE measurements. Different parallel work packages for the collection, evaluation, and visualization of data are drawn in rectangular boxes. The empty boxes illustrate the repetitive execution of the above drawn filled boxes. The different vertical sizes of the empty boxes account for the different time scales that are necessary for their execution. For details see text.*

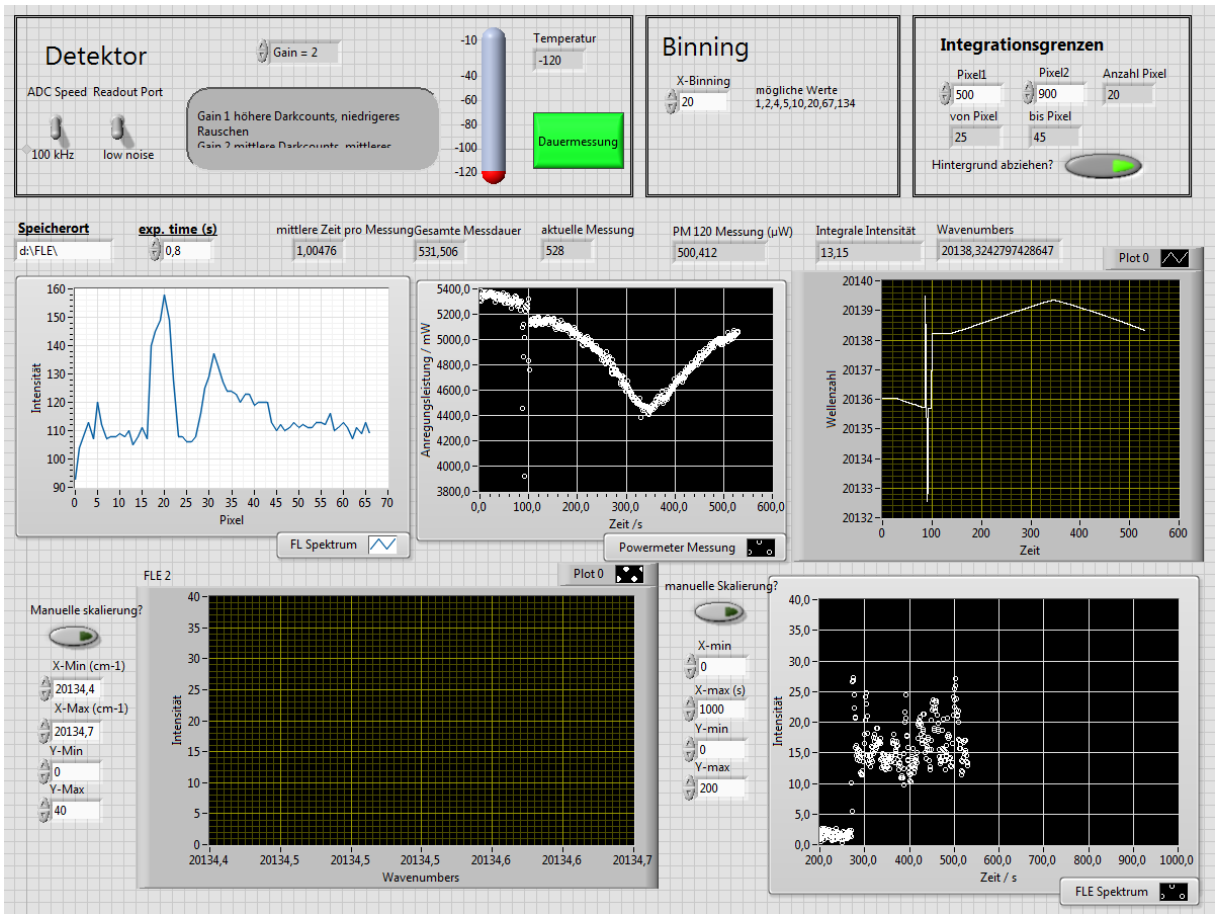

Figure C.2: *Screenshot of the user interface for the measurement of single molecule FLE spectra.*

A schematic overview of the program is depicted in Fig. C.1. In the first step all measurement parameters are read and the measurement is initialized. Then all necessary parameters of the experiment (excitation wavelength, excitation power and FL intensity) are measured in parallel. In combination with some improvements of the LabView code this parallel measurement results in a significant reduction of the interval between two measurement points from initially 6 s + exposure time to 0.3 s + exposure time. The respective values of the excitation wavelength, excitation power, and FL intensity are collected together with individual time stamps in a cache. The use of a shared time grid was avoided, since this was identified to cause additional temporal delay between measurement points. While the measured data of the wavemeter and powermeter are only collected, the FL intensity is extracted from the FL spectrum by integration of a spectral area after an optional substraction of a constant readout noise. For later inspection each FL spectrum is saved. During the measurement all parameters are visualized in graphs. At the end of the measurement the data collection is stopped and the data are saved to individual files.

During the measurement all parameters and their temporal evolution can be monitored on the user interface. A screenshot showing the user interface during a measurement is depicted in Fig. C.2. The first row contains the setting options for the measurement parameters: the file path, the exposure time for each FL spectrum, the binning factor of the CCD, the integration limits for the intensity extraction from the FL spectrum, and the possibility to subtract a constant readout

noise before integration. The second row contains the graphs of the most recent FL spectrum, the powermeter signal vs. time, and the wavemeter signal vs. time. In the last row the integral FL intensity is plotted against the wavemeter signal and the measurement time, respectively. The graphs in the last row can be automatically or manually scaled during the measurement.

The measurement is started by clicking the arrow button in the upper left corner of the LabView program (not shown). It can be stopped by clicking the green "Dauermessung"-button in the first row of the user interface. After stopping the program four files are saved to the file path. They contain: (i) *intensity vs. time*, (ii) *wavenumber vs. time*, (iii) *laser power vs. time*, and (iv) *intensity vs. wavenumber*. Please note that the files (i), (ii), and (iii) have different lengths and time values, whereas file (iv) is not corrected for the intensity of the excitation laser. In order to obtain a corrected version of file (iv) the files (i), (ii), and (iii) can be processed by a script written in *GNU Octave* that is described in Appendix C.2.

Tuning the wavelength of the ring-dye laser is not possible within the LabView program. It must be independently controlled with the "Matisse Commander" software. For FLE measurements with the standing wave dye-laser however a modification of the current program can be used ("FLE 599.vi"). This program has additional controls for the Lyot-filter of the dye-laser but works similar concerning the data collection and monitoring.

C.2 Octave script for FLE data processing

The LabView program described in the previous chapter Appendix C.1 produces output files of the FL intensity (i), the wavemeter signal (ii), and the powermeter signal (iii), each listed with individual time axes. In order to match the time axes of the three files and correct the FL intensity by the powermeter measurement a small script written in *GNU Octave* can be used. The source code of this script is depicted in Fig. C.3.

For the use of the script all three files have to be in a dedicated folder that needs to be specified in the input parameters of the script. When executed, the script reads the files and matches the time axes of the wavemeter signal (ii) and the powermeter signal (iii) to that of the intensity signal by linear interpolating the measured values of (ii) and (iii) at the times of (i). Then the FL intensity is normalized by the powermeter signal. This again is normalized by its mean value so that the mean FL intensity is not affected by the normalization and only variations of the laser power are compensated. Finally, a file is created that contains the normalized FL intensity values against the interpolated wavemeter signal.

```
%Processing of the file-output of the "FLE_kontinuierlich" LabView program
clear
%%%%%%%%%%%%%%%%%%%%%%%%%%%%%%%%%%%%%%%%%%%%%%%%%%%%%%%%%%%%%%%%%%%%%%%%%%%%%%%
%Input Parameters
%%%%%%%%%%%%%%%%%%%%%%%%%%%%%%%%%%%%%%%%%%%%%%%%%%%%%%%%%%%%%%%%%%%%%%%%%%%%%%%
dirname=strcat(["D:/Users/marquardt/Desktop/FLE Temp/"]);%file path
%file names: data vs. time
savename_intensity=strcat([dirname,"FLEMessung.txt"]);%intensity
savename_powermeter=strcat([dirname,"PowermeterMessung.txt"]);%powermeter
savename_wavenumbers=strcat([dirname,"WavemeterMessungInCM-1.txt"]);%wavenumbers
x=1; %correction factor to avoid NA values after interpolation: >=1
%%%%%%%%%%%%%%%%%%%%%%%%%%%%%%%%%%%%%%%%%%%%%%%%%%%%%%%%%%%%%%%%%%%%%%%%%%%%%%%

%read 'intensity vs. time'
I_t=dlmread(savename_intensity);
time=I_t(:,1);
I=I_t(:,2);

%read 'powermeter vs. time' and interpolate (linear)
P_t1=dlmread(savename_powermeter);
t1=P_t1(:,1);
P=P_t1(:,2);
%interpolate powermeter signal to the time stamps of the intensity values
P_int=interp1(t1,P,time);

%read 'wavenumber vs. time'
W_t2=dlmread(savename_wavenumbers);
t2=W_t2(:,1);
W=W_t2(:,2);
%interpolate wavemeter signal to the time stamps of the intensity values
W_int=interp1(t2,W,time);

%correct for NA values
I=I(1:(length(I)-x));
P_int=P_int(1:(length(P_int)-x));
W_int=W_int(1:(length(W_int)-x));
time=time(1:(length(time)-x));

%normalization of intensity signal by powermeter signal
P_mean=mean(P_int); %gives mean value of the powermeter signal
I_corr=I./(P_int./P_mean); %normalize the intensity by a norm. powermeter signal

%create and save corrected intensity vs. wavenumber file
plot(W_int,I_corr) %plot corrected intensity vs. wavenumber
Wint_t=[W_int,I_corr];
savename_output=strcat([dirname,"FLE_korr.txt"]);
dlmwrite(savename_output,Wint_t); %saves corrected intensity file to file path
```

Figure C.3: *GNU Octave script for the processing of the output files of the FLE LabView program.*

Bibliography

[1] N. T. Kalyani and S. Dhoble, "Organic light emitting diodes: energy saving lighting technology – a review", Renewable and Sustainable Energy Reviews **16**, 2696 (2012).

[2] Y.-W. Su, S.-C. Lan, and K.-H. Wei, "Organic photovoltaics", Materials Today **15**, 554 (2012).

[3] M. J. Kamlet, J. L. Abboud, and R. W. Taft, "The solvatochromic comparison method. 6. The π^*-scale of solvent polarities", Journal of the American Chemical Society **99**, 6027 (1977).

[4] E. E. Jelley, "Spectral absorption and fluorescence of dyes in the molecular state", Nature **138**, 1009 (1936).

[5] G. Scheibe, L. Kandler, and H. Ecker, "Polymerisation und polymere adsorption als ursache neuartiger absorptionsbanden von organischen farbstoffen", Naturwissenschaften **25**, 75 (1937).

[6] G. Rouillé, T. Kirchhuebel, M. Rink, M. Gruenewald, J. Kröger, R. Forker, and T. Fritz, "Identification of vibrational excitations and optical transitions of the organic electron donor tetraphenyldibenzoperiflanthene (DBP)", Physical Chemistry Chemical Physics **17**, 30404 (2015).

[7] R. W. Olson and M. D. Fayer, "Site-dependent vibronic line widths and relaxation in the mixed molecular crystal pentacene in p-terphenyl", The Journal of Physical Chemistry **84**, 2001 (1980).

[8] M. Müller, A. Paulheim, C. Marquardt, and M. Sokolowski, "Spectroscopy of isolated PTCDA molecules on the KCl(100) surface: Vibrational spectra and azimuthal orientation", Journal of Chemical Physics **138**, 064703 (2013).

[9] M. Müller, A. Langner, O. Krylova, E. Le Moal, and M. Sokolowski, "Fluorescence spectroscopy of ultrathin molecular organic films on surfaces", Applied Physics B **105**, 67 (2011).

[10] M. Alonso, M. Garriga, N. Karl, J. Ossó, and F. Schreiber, "Anisotropic optical properties of single crystalline PTCDA studied by spectroscopic ellipsometry", Organic Electronics **3**, 23 (2002).

[11] D. Faltermeier, B. Gompf, M. Dressel, A. K. Tripathi, and J. Pflaum, "Optical properties of pentacene thin films and single crystals", Physical Review B **74**, 125416 (2006).

[12] M. Schneider, E. Umbach, and M. Sokolowski, "Growth-dependent optical properties of 3,4,9,10-perylenetetracarboxylicacid-dianhydride (PTCDA) films on Ag(111)", Chemical Physics **325**, 185 (2006).

[13] T. Dienel, C. Loppacher, S. C. B. Mannsfeld, R. Forker, and T. Fritz, "Growth-mode-induced narrowing of optical spectra of an organic adlayer", Advanced Materials **20**, 959 (2008).

[14] M. Müller, J. Ikonomov, and M. Sokolowski, "Structure of epitaxial layers of KCl on Ag(100)", Surface Science **605**, 1090 (2011).

[15] Q. Guo, A. Paulheim, M. Sokolowski, H. Aldahhak, E. Rauls, and W. G. Schmidt, "Adsorption of PTCDA on terraces and at steps sites of the KCl(100) surface", Journal of Physical Chemistry C **118**, 29911 (2014).

[16] M. Müller, A. Paulheim, A. Eisfeld, and M. Sokolowski, "Finite size line broadening and superradiance of optical transitions in two dimensional long-range ordered molecular aggregates", Journal of Chemical Physics **139**, 044302 (2013).

[17] A. Paulheim, M. Müller, C. Marquardt, and M. Sokolowski, "Fluorescence spectroscopy of PTCDA molecules on the KCl(100) surface in the limit of low coverages: site selection and diffusion", Physical Chemistry Chemical Physics **15**, 4906 (2013).

[18] A. Paulheim, C. Marquardt, H. Aldahhak, E. Rauls, W. G. Schmidt, and M. Sokolowski, "Inhomogeneous and homogeneous line broadening of optical spectra of PTCDA molecules adsorbed at step edges of alkali halide surfaces", Journal of Physical Chemistry C **120**, 11926 (2016).

[19] A. Paulheim, C. Marquardt, M. Sokolowski, M. Hochheim, T. Bredow, H. Aldahhak, E. Rauls, and W. G. Schmidt, "Surface induced vibrational modes in the fluorescence spectra of PTCDA adsorbed on the KCl(100) and NaCl(100) surfaces", Physical Chemistry Chemical Physics **18**, 32891 (2016).

[20] S. Barlow and R. Raval, "Complex organic molecules at metal surfaces: bonding, organisation and chirality", Surface Science Reports **50**, 201 (2003).

[21] F. Rosei, M. Schunack, Y. Naitoh, P. Jiang, A. Gourdon, E. Laegsgaard, I. Stensgaard, C. Joachim, and F. Besenbacher, "Properties of large organic molecules on metal surfaces", Progress in Surface Science **71**, 95 (2003).

[22] A. Kühnle, "Self-assembly of organic molecules at metal surfaces", Current Opinion in Colloid & Interface Science **14**, 157 (2009).

[23] C. Ahrens, J. I. Flege, C. Jaye, D. A. Fischer, T. Schmidt, and J. Falta, "Isotropic thin PTCDA films on GaN(0001)", Journal of Physics: Condensed Matter **28**, 475003 (2016).

[24] A. J. Martínez-Galera, Z. Wei, N. Nicoara, I. Brihuega, and J. M. Gómez-Rodríguez, "PTCDA growth on Ge(111)- $c(2 \times 8)$ surfaces: a scanning tunneling microscopy study", Nanotechnology **28**, 095703 (2017).

[25] R. Bennewitz, "Structured surfaces of wide band gap insulators as templates for overgrowth of adsorbates", Journal of Physics: Condensed Matter **18**, R417 (2006).

[26] R. Hoffmann-Vogel, "Imaging prototypical aromatic molecules on insulating surfaces: a review", Reports on Progress in Physics **81**, 016501 (2017).

[27] J. Repp, G. Meyer, S. M. Stojković, A. Gourdon, and C. Joachim, "Molecules on insulating films: scanning-tunneling microscopy imaging of individual molecular orbitals", Physical Review Letters **94**, 026803 (2005).

[28] O. H. Pakarinen, J. M. Mativetsky, A. Gulans, M. J. Puska, A. S. Foster, and P. Grutter, "Role of van der Waals forces in the adsorption and diffusion of organic molecules on an insulating surface", Physical Review B **80**, 085401 (2009).

[29] S. A. Burke, J. M. Topple, and P. Grütter, "Molecular dewetting on insulators", Journal of Physics: Condensed Matter **21**, 423101 (2009).

[30] S. Mohr, T. Xu, T. Döpper, M. Laurin, A. Görling, and J. Libuda, "Molecular orientation and structural transformations in phthalic anhydride thin films on MgO(100)/Ag(100)", Langmuir **31**, 7806 (2015).

[31] P. R. Ribič and G. Bratina, "Initial stages of growth of organic semiconductors on vicinal (0001) sapphire surfaces", Surface Science **602**, 1368 (2008).

[32] J. Schütte, R. Bechstein, P. Rahe, M. Rohlfing, A. Kühnle, and H. Langhals, "Imaging perylene derivatives on rutile $TiO_2(110)$ by noncontact atomic force microscopy", Physical Review B **79**, 045428 (2009).

[33] L. Zhang, X. Fu, M. Hohage, P. Zeppenfeld, and L. D. Sun, "Growth of pentacene on $\alpha - Al_2O_3(0001)$ studied by in situ optical spectroscopy", Physical Review Materials **1**, 043401 (2017).

[34] F. Schulz, R. Drost, S. K. Hämäläinen, and P. Liljeroth, "Templated self-assembly and local doping of molecules on epitaxial hexagonal boron nitride", ACS Nano **7**, 11121 (2013).

[35] L. Liu, T. Dienel, R. Widmer, and O. Gröning, "Interplay between energy-level position and charging effect of manganese phthalocyanines on an atomically thin insulator", ACS Nano **9**, 10125 (2015).

[36] R. Forker, T. Dienel, A. Krause, M. Gruenewald, M. Meissner, T. Kirchhuebel, O. Gröning, and T. Fritz, "Optical transition energies of isolated molecular monomers and weakly interacting two-dimensional aggregates", Physical Review B **93**, 165426 (2016).

[37] H. Proehl, T. Dienel, R. Nitsche, and T. Fritz, "Formation of solid-state excitons in ultrathin crystalline films of PTCDA: from single molecules to molecular stacks", Physical Review Letters **93**, 097403 (2004).

[38] M. Schiek, A. Lützen, K. Al-Shamery, F. Balzer, and H.-G. Rubahn, "Organic nanofibers from chloride-functionalized p-quaterphenylenes", Crystal Growth & Design **7**, 229 (2007).

[39] M. Kittelmann, P. Rahe, M. Nimmrich, C. M. Hauke, A. Gourdon, and A. Kühnle, "On-surface covalent linking of organic building blocks on a bulk insulator", ACS Nano **5**, 8420 (2011).

[40] R. Lindner, P. Rahe, M. Kittelmann, A. Gourdon, R. Bechstein, and A. Kühnle, "Substrate templating guides the photoinduced reaction of C_{60} on calcite", Angewandte Chemie International Edition **53**, 7952 (2014).

[41] M. Pivetta, F. Patthey, M. Stengel, A. Baldereschi, and W.-D. Schneider, "Local work function moiré pattern on ultrathin ionic films: NaCl on Ag(100)", Physical Review B **72**, 115404 (2005).

[42] J. Kramer, C. Tegenkamp, and H. Pfnür, "The growth of NaCl on flat and stepped silver surfaces", Journal of Physics: Condensed Matter **15**, 6473 (2003).

[43] S. Fölsch, A. Stock, and M. Henzler, "Two-dimensional water condensation on the NaCl(100) surface", Surface Science **264**, 65 (1992).

[44] O. Bauer, G. Mercurio, M. Willenbockel, W. Reckien, C. Heinrich Schmitz, B. Fiedler, S. Soubatch, T. Bredow, F. S. Tautz, and M. Sokolowski, "Role of functional groups in surface bonding of planar π-conjugated molecules", Physical Review B **86**, 235431 (2012).

[45] J. Repp, G. Meyer, S. Paavilainen, F. E. Olsson, and M. Persson, "Imaging bond formation between a gold atom and pentacene on an insulating surface", Science **312**, 1196 (2006).

[46] A. Paulheim, "Fluoreszenzspektroskopie an PTCDA-Molekülen auf Alkalihalogenidoberflächen: Die Rolle von Oberflächenstufen", PhD thesis (University Bonn, 2017).

[47] E. Ćavar, M.-C. Blüm, M. Pivetta, F. Patthey, M. Chergui, and W.-D. Schneider, "Fluorescence and phosphorescence from individual C_{60} molecules excited by local electron tunneling", Physical Review Letters **95**, 196102 (2005).

[48] J. L. Neff, J. Götzen, E. Li, M. Marz, and R. Hoffmann-Vogel, "Molecular-resolution imaging of pentacene on KCl(001)", Beilstein Journal of Nanotechnology **3**, 186 (2012).

[49] A. Langner, Y. Su, and M. Sokolowski, "Luminescence quenching of tetracene films adsorbed on an ultrathin alumina AlO_x layer on $Ni_3Al(111)$", Physical Review B **74**, 045428 (2006).

[50] A. C. Dürr, F. Schreiber, K. A. Ritley, V. Kruppa, J. Krug, H. Dosch, and B. Struth, "Rapid roughening in thin film growth of an organic semiconductor (diindenoperylene)", Physical Review Letters **90**, 016104 (2003).

[51] X. Zhang, E. Barrena, D. de Oteyza, and H. Dosch, "Transition from layer-by-layer to rapid roughening in the growth of DIP on SiO_2", Surface Science **601**, 2420 (2007).

[52] M. Müller, "Optische Spektroskopie dünner und ultradünner Rubren-Filme auf epitaktisch gewachsenen Aluminiumoxid", Diploma Thesis (University Bonn, 2007).

[53] J. L. Neff, P. Milde, C. Pérez León, M. D. Kundrat, L. M. Eng, C. R. Jacob, and R. Hoffmann-Vogel, "Epitaxial growth of pentacene on alkali halide surfaces studied by Kelvin probe force microscopy", ACS Nano **8**, 3294 (2014).

[54] L. Gross, F. Mohn, N. Moll, P. Liljeroth, and G. Meyer, "The chemical structure of a molecule resolved by atomic force microscopy", Science **325**, 1110 (2009).

[55] T. Kunstmann, A. Schlarb, M. Fendrich, T. Wagner, R. Möller, and R. Hoffmann, "Dynamic force microscopy study of 3,4,9,10-perylenetetracarboxylic dianhydride on KBr(001)", Physical Review B **71**, 121403 (2005).

[56] M. Fendrich and T. Kunstmann, "Organic molecular nanowires: N,N'-dimethylperyl-ene-3,4,9,10-bis(dicarboximide) on KBr(001)", Applied Physics Letters **91**, 023101 (2007).

[57] P. Liljeroth, J. Repp, and G. Meyer, "Current-induced hydrogen tautomerization and conductance switching of naphthalocyanine molecules", Science **317**, 1203 (2007).

[58] L. Zimmerli, S. Maier, T. Glatzel, E. Gnecco, O. Pfeiffer, F. Diederich, L. Fendt, and E. Meyer, "Formation of molecular wires on nanostructured KBr", Journal of Physics: Conference Series **61**, 1357 (2007).

[59] S. Maier, L.-A. Fendt, L. Zimmerli, T. Glatzel, O. Pfeiffer, F. Diederich, and E. Meyer, "Nanoscale engineering of molecular porphyrin wires on insulating surfaces", Small **4**, 1115 (2008).

[60] P. Rahe, M. Nimmrich, A. Nefedov, M. Naboka, C. Wöll, and A. Kühnle, "Transition of molecule orientation during adsorption of terephthalic acid on rutile $TiO_2(110)$", The Journal of Physical Chemistry C **113**, 17471 (2009).

[61] P. Rahe, M. Kittelmann, J. L. Neff, M. Nimmrich, M. Reichling, P. Maass, and A. Kühnle, "Tuning molecular self-assembly on bulk insulator surfaces by anchoring of the organic building blocks", Advanced Materials **25**, 3948 (2013).

[62] S. A. Burke, W. Ji, J. M. Mativetsky, J. M. Topple, S. Fostner, H.-J. Gao, H. Guo, and P. Grütter, "Strain induced dewetting of a molecular system: bimodal growth of PTCDA on NaCl", Physical Review Letters **100**, 186104 (2008).

[63] E. Le Moal, M. Müller, O. Bauer, and M. Sokolowski, "Stable and metastable phases of PTCDA on epitaxial NaCl films on Ag(100)", Physical Review B **82**, 045301 (2010).

[64] M. Hochheim and T. Bredow, "Adsorption-induced changes of intramolecular optical transitions: PTCDA/NaCl and PTCDA/KCl", Journal of Computational Chemistry **36**, 1805 (2015).

[65] H. Aldahhak, W. Schmidt, and E. Rauls, "Adsorption of PTCDA on NaCl(100) and KCl(100)", Surface Science **617**, 242 (2013).

[66] H. Aldahhak, W. Schmidt, and E. Rauls, "Single PTCDA molecules on planar and stepped KCl and NaCl(100) surfaces", Surface Science **641**, 278 (2015).

[67] F. Würthner, T. E. Kaiser, and C. R. Saha-Möller, "J-aggregates: from serendipitous discovery to supramolecular engineering of functional dye materials", Angewandte Chemie International Edition **50**, 3376 (2011).

[68] M. Hoffmann, K. Schmidt, T. Fritz, T. Hasche, V. Agranovich, and K. Leo, "The lowest energy Frenkel and charge-transfer excitons in quasi-one-dimensional structures: application to MePTCDI and PTCDA crystals", Chemical Physics **258**, 73 (2000).

[69] R. Schuster, M. Knupfer, and H. Berger, "Exciton band structure of pentacene molecular solids: Breakdown of the Frenkel exciton model", Physical Review Letters **98**, 037402 (2007).

[70] D. H. Arias, K. W. Stone, S. M. Vlaming, B. J. Walker, M. G. Bawendi, R. J. Silbey, V. Bulović, and K. A. Nelson, "Thermally-limited exciton delocalization in superradiant molecular aggregates", Journal of Physical Chemistry B **117**, 4553 (2013).

[71] S.-H. Lim, T. G. Bjorklund, F. C. Spano, and C. J. Bardeen, "Exciton delocalization and superradiance in tetracene thin films and nanoaggregates", Physical Review Letters **92**, 107402, 107402 (2004).

[72] M. Voigt, A. Langner, P. Schouwink, J. M. Lupton, R. F. Mahrt, and M. Sokolowski, "Picosecond time resolved photoluminescence spectroscopy of a tetracene film on highly oriented pyrolytic graphite: dynamical relaxation, trap emission, and superradiance", The Journal of Chemical Physics **127**, 114705 (2007).

[73] E. T. Niles, J. D. Roehling, H. Yamagata, A. J. Wise, F. C. Spano, A. J. Moulé, and J. K. Grey, "J-aggregate behavior in poly-3-hexylthiophene nanofibers", The Journal of Physical Chemistry Letters **3**, 259 (2012).

[74] F. C. Spano and C. Silva, "H- and J-aggregate behavior in polymeric semiconductors", Annual Review of Physical Chemistry **65**, PMID: 24423378, 477 (2014).

[75] S. Izadnia, D. W. Schönleber, A. Eisfeld, A. Ruf, A. C. LaForge, and F. Stienkemeier, "Singlet fission in weakly interacting acene molecules", The Journal of Physical Chemistry Letters **8**, PMID: 28421765, 2068 (2017).

[76] T. Kobayashi, ed., *J-Aggregates* (World Scientific, Singapore, 1996).

[77] F. C. Spano and S. Mukamel, "Superradiance in molecular aggregates", Journal of Chemical Physics **91**, 683 (1989).

[78] E. O. Potma and D. A. Wiersma, "Exciton superradiance in aggregates: the effect of disorder, higher order exciton-phonon coupling and dimensionality", Journal of Chemical Physics **108**, 4894 (1998).

[79] H. Fidder, J. Knoester, and D. A. Wiersma, "Superradiant emission and optical dephasing in j-aggregates", Chemical Physics Letters **171**, 529 (1990).

[80] J. Grad, G. Hernandez, and S. Mukamel, "Radiative decay and energy transfer in molecular aggregates: The role of intermolecular dephasing", Physical Review A **37**, 3835 (1988).

[81] H. Fidder, J. Terpstra, and D. A. Wiersma, "Dynamics of Frenkel excitons in disordered molecular aggregates", Journal of Chemical Physics **94**, 6895 (1991).

[82] D. J. Heijs, V. A. Malyshev, and J. Knoester, "Decoherence of excitons in multichromophore systems: thermal line broadening and destruction of superradiant emission", Physical Review Letters **95**, 177402 (2005).

[83] S. Özçelik and D. L. Akins, "Superradiance Of Aggregated Thiacarbocyanine Molecules", Journal of Physical Chemistry B **103**, 8926 (1999).

[84] F. C. Spano and H. Yamagata, "Vibronic coupling in J-Aggregates and beyond: a direct means of determining the exciton coherence length from the photoluminescence spectrum", Journal of Physical Chemistry B **115**, 5133 (2011).

[85] F. Meinardi, M. Cerminara, A. Sassella, R. Bonifacio, and R. Tubino, "Superradiance in molecular H aggregates", Physical Review Letters **91**, 247401 (2003).

[86] V. F. Kamalov, I. A. Struganova, and K. Yoshihara, "Temperature Dependent Radiative Lifetime of J-Aggregates", Journal of Physical Chemistry **100**, 8640 (1996).

[87] F. C. Spano, "Temperature dependent exciton emission from herringbone aggregates of conjugated oligomers", Journal of Chemical Physics **120**, 7643 (2004).

[88] S. Tanaka, K. Miyata, T. Sugimoto, K. Watanabe, T. Uemura, J. Takeya, and Y. Matsumoto, "Enhancement of the exciton coherence size in organic semiconductor by alkyl chain substitution", The Journal of Physical Chemistry C **120**, 7941 (2016).

[89] S. De Boer and D. A. Wiersma, "Dephasing-induced damping of superradiant emission in J-aggregates", Chemical Physics Letters **165**, 45 (1990).

[90] Y. Zhang, Y. Luo, Y. Zhang, Y.-J. Yu, Y.-M. Kuang, L. Zhang, Q.-S. Meng, Y. Luo, J.-L. Yang, Z.-C. Dong, and J. G. Hou, "Visualizing coherent intermolecular dipole-dipole coupling in real space", Nature **531**, 623 (2016).

[91] F. C. Spano, "Emission from aggregates of oligo-phenylene vinylenes: a recipe for superradiant H-aggregates", Chemical Physics Letters **331**, 7 (2000).

[92] H. Yamagata and F. C. Spano, "Interplay between intrachain and interchain interactions in semiconducting polymer assemblies: the HJ-aggregate model", The Journal of Chemical Physics **136**, 184901 (2012).

[93] H. Yamagata, N. J. Hestand, F. C. Spano, A. Köhler, C. Scharsich, S. T. Hoffmann, and H. Bässler, "The red-phase of poly[2-methoxy-5-(2-ethylhexyloxy)-1,4-phenylenevinylene] (MEH-PPV): A disordered HJ-aggregate", The Journal of Chemical Physics **139**, 114903 (2013).

[94] S. W. Hell and J. Wichmann, "Breaking the diffraction resolution limit by stimulated emission: stimulated-emission-depletion fluorescence microscopy", Optics Letters **19**, 780 (1994).

[95] E. Betzig, G. H. Patterson, R. Sougrat, O. W. Lindwasser, S. Olenych, J. S. Bonifacino, M. W. Davidson, J. Lippincott-Schwartz, and H. F. Hess, "Imaging intracellular fluorescent proteins at nanometer resolution", Science **313**, 1642 (2006).

[96] W. E. Moerner and L. Kador, "Optical detection and spectroscopy of single molecules in a solid", Physical Review Letters **62**, 2535 (1989).

[97] M. Orrit and J. Bernard, "Single pentacene molecules detected by fluorescence excitation in a p-terphenyl crystal", Physical Review Letters **65**, 2716 (1990).

[98] W. P. Ambrose, T. Basché, and W. E. Moerner, "Fluorescence spectroscopy and spectral diffusion of single impurity molecules in a crystal", Journal of Chemical Physics **95**, 7150 (1991).

[99] T. Basché, W. P. Ambrose, and W. E. Moerner, "Optical spectra and kinetics of single impurity molecules in a polymer: spectral diffusion and persistent spectral hole burning", Journal of the Optical Society of America B **9**, 829 (1992).

[100] L. Fleury, A. Zumbusch, M. Orrit, R. Brown, and J. Bernard, "Spectral diffusion and individual two-level systems probed by fluorescence of single terrylene molecules in a polyethylene matrix", Journal of Luminescence **56**, 15 (1993).

[101] S. Kummer and T. Basche, "Measurement of optical dephasing of a single terrylene molecule with nanosecond time resolution", Journal of Physical Chemistry C **99**, 17078 (1995).

[102] W. E. Moerner, T. Plakhotnik, T. Irngartinger, M. Croci, V. Palm, and U. P. Wild, "Optical probing of single molecules of terrylene in a Shpol'kii matrix: a two-state single-molecule switch", Journal of Physical Chemistry **98**, 7382 (1994).

[103] P. Tchénio, A. B. Myers, and W. E. Moerner, "Optical studies of single terrylene molecules in polyethylene", Journal of Luminescence **56**, 1 (1993).

[104] S. Mais, J. Tittel, T. Basché, C. Bräuchle, W. Göhde, H. Fuchs, G. Müller, and K. Müllen, "Terrylenediimide: A novel fluorophore for single-molecule spectroscopy and microscopy from 1.4 K to room temperature", The Journal of Physical Chemistry A **101**, 8435 (1997).

[105] M. Orrit, J. Bernard, A. Zumbusch, and R. I. Personov, "Stark effect on single molecules in a polymer matrix", Chemical Physics Letters **196**, 595 (1992).

[106] T. Plakhotnik, W. E. Moerner, V. Palm, and U. P. Wild, "Single molecule spectroscopy: maximum emission rate and saturation intensity", Optics Communications **114**, 83 (1995).

[107] M. Croci, H.-J. Müschenborn, F. Güttler, A. Renn, and U. P. Wild, "Single molecule spectroscopy: pressure effect on pentacene in p-terphenyl", Chemical Physics Letters **212**, 71 (1993).

[108] J. Bernard, L. Fleury, H. Talon, and M. Orrit, "Photon bunching in the fluorescence from single molecules: a probe for intersystem crossing", The Journal of Chemical Physics **98**, 850 (1993).

[109] T. Basché, W. E. Moerner, M. Orrit, and H. Talon, "Photon antibunching in the fluorescence of a single dye molecule trapped in a solid", Physical Review Letters **69**, 1516 (1992).

[110] X. H. Qiu, G. V. Nazin, and W. Ho, "Vibrationally resolved fluorescence excited with submolecular precision", Science **299**, 542 (2003).

[111] B. Doppagne, M. C. Chong, E. Lorchat, S. Berciaud, M. Romeo, H. Bulou, A. Boeglin, F. Scheurer, and G. Schull, "Vibronic spectroscopy with submolecular resolution from STM-induced electroluminescence", Physical Review Letters **118**, 127401 (2017).

[112] M. L. Blumenfeld, B. S. Tackett, L. K. Schirra, J. M. Tyler, and O. L. A. Monti, "Confocal single molecule fluorescence spectroscopy in ultrahigh vacuum", Review of Scientific Instruments **80**, 103101 (2009).

[113] L. K. Schirra, B. S. Tackett, M. L. Blumenfeld, and O. L. A. Monti, "Single molecule power-law behavior on a crystalline surface", Journal of Chemical Physics **131**, 124702 (2009).

[114] M. Wewer and F. Stienkemeier, "Laser-induced fluorescence spectroscopy of 3,4,9,10-perylene-tetracarboxylicdianhydrid in helium nanodroplets", The Journal of Chemical Physics **120**, 1239 (2004).

[115] M. Müller, "Optische Spektroskopie von PTCDA auf Alkalihalogenidoberflächen: vereinzelte Moleküle und Monolagen", PhD thesis (Universität Bonn, 2011).

[116] G. Attard and C. Barnes, *Surfaces*, Vol. 59 of Oxford Chemistry primers (Oxford University Press, Oxford, 1998).

[117] M. Henzler and W. Göpel, *Oberflächenphysik des Festkörpers*, 2nd ed. (Teubner Studienbücher Physik, Stuttgart, 1994).

[118] M. Horn-von Hoegen, "Growth of semiconductor layers studied by spot profile analysing low energy electron diffraction", Zeitschrift für Kristallographie **214**, 591 and 684 (1999).

[119] J. Pendry, *Low Energy Electron Diffraction: The Theory and Its Application to Determination of Surface Structure* (Academic Press, London, 1974).

[120] M. A. V. Hove, W. H. Weinberg, and C.-M. Chan, *Low-Energy Electron Diffraction* (Springer-Verlag, Berlin Heidelberg, 1986).

[121] L. de Broglie, "Recherches sur la théorie des quanta", PhD thesis (1924).

[122] C. Davisson and L. H. Germer, "Diffraction of electrons by a crystal of nickel", Physical Review **30**, 705 (1927).

[123] J. Lapujoulade, "A statistical model for the scattering of atoms from randomly stepped surfaces", Surface Science **108**, 526 (1981).

[124] C. Kittel, *Einführung in die Festkörperphysik*, 12th ed. (R. Oldenbourg Verlag, München Wien, 1999).

[125] W. Schmidt, *Optische Spektroskopie*, 2nd ed. (Wiley-VCH, Weinheim, 2000).

[126] B. Valeur, *Molecular fluorescence - principles and applications* (Wiley-VCH, Weinheim, 2002).

[127] J. M. Hollas, *Modern spectroscopy* (Wiley-VCH, Weinheim, 2008).

[128] W. E. Moerner and T. P. Carter, "Statistical fine structure of inhomogeneously broadened absorption lines", Physical Review Letters **59**, 2705 (1987).

[129] W. E. Moerner and M. Orrit, "Illuminating single molecules in condensed matter", Science **283**, 1670 (1999).

[130] S. Mais, "Spektroskopie und Mikroskopie einzelner Farbstoffmoleküle im Festkörper zwischen 1,4 Kelvin und Raumtemperatur", PhD thesis (Ludwig-Maximilians-Universität München, 2000).

[131] D. Hsu and J. L. Skinner, "Nonperturbative theory of temperature-dependent optical dephasing in crystals. I. Acoustic or optical phonons", The Journal of Chemical Physics **81**, 5471 (1984).

[132] D. Hsu and J. L. Skinner, "Nonperturbative theory of temperature-dependent optical dephasing in crystals. II. Pseudolocal phonons", The Journal of Chemical Physics **83**, 2097 (1985).

[133] K. K. Rebane, "Purely electronic zero-phonon line as the foundation stone for high-resolution matrix spectroscopy, single-impurity-molecule spectroscopy, and persistent spectral hole burning. Recent developments", Low Temperature Physics **29**, 838 (2003).

[134] A. Zumbusch, L. Fleury, R. Brown, J. Bernard, and M. Orrit, "Probing individual two-level systems in a polymer by correlation of single molecule fluorescence", Physical Review Letters **70**, 3584 (1993).

[135] D. P. Craig and S. H. Walmsley, *Excitons in molecular crystals* (Benjamin, New York, 1968).

[136] A. S. Davydov, *Theory of molecular excitons* (Plenum Press, New York, 1971).

[137] J. Frenkel, "On the transformation of light into heat in solids. I", Physical Review **37**, 17 (1931).

[138] J. Frenkel, "On the transformation of light into heat in solids. II", Physical Review **37**, 1276 (1931).

[139] F. C. Spano, J. Clark, C. Silva, and R. H. Friend, "Determining exciton coherence from the photoluminescence spectral line shape in poly(3-hexylthiophene) thin films", The Journal of Chemical Physics **130**, 074904 (2009).

[140] S. de Boer, K. J. Vink, and D. A. Wiersma, "Optical dynamics of condensed molecular aggregates: an accumulated photon-echo and hole-burning study of the J-aggregate", Chemical Physics Letters **137**, 99 (1987).

[141] W. Gebauer, A. Langner, M. Schneider, M. Sokolowski, and E. Umbach, "Luminescence quenching of ordered p-conjugated molecules near a metal surface: Quaterthiophene and PTCDA on Ag(111)", Physical Review B **69**, 155431 (2004).

[142] E. Hecht, *Optik*, 4th ed. (Oldenbourg, München, 2005).

[143] Bergmann-Schaefer, *Lehrbuch der Experimentalphysik Band III Optik*, 7th ed. (de Gruyter, Berlin, 1978).

[144] M. Pluta, *Advanced light microscopy: principles and basic properties.* (Polish Scientific Publishers, Warszawa, 1988).

[145] F. C. Spano, J. R. Kuklinski, and S. Mukamel, "Temperature-dependent superradiant decay of excitons in small aggregates", Physical Review Letters **65**, 211 (1990).

[146] E. Knapp, "Lineshapes of molecular aggregates, exchange narrowing and intersite correlation", Chemical Physics **85**, 73 (1984).

[147] A. Eisfeld, *personal communication*, 2017.

[148] A. G. Dijkstra, H.-G. Duan, J. Knoester, K. A. Nelson, and J. Cao, "How two-dimensional brick layer J-aggregates differ from linear ones: excitonic properties and line broadening mechanisms", The Journal of Chemical Physics **144**, 134310 (2016).

[149] H. Kano, T. Saito, and T. Kobayashi, "Dynamic intensity borrowing in porphyrin j-aggregates revealed by sub-5-fs spectroscopy", The Journal of Physical Chemistry B **105**, 413 (2001).

[150] O. Bünermann, "Spektroskopie von Alkali- und Erdalkaliatomen, -molekülen, Alkaliclustern und Komplexen organischer Moleküle auf Helium-Nanotröpfchen", PhD thesis (Universität Bielefeld, 2006).

[151] K. K. Rebane and L. A. Rebane, *Persistent spectral hole burning: science and applications*, edited by W. E. Moerner (Springer, Berlin, 1988).

[152] R. Matzdorf, "Investigation of line shapes and line intensities by high-resolution UV-photoemission spectroscopy – Some case studies on noble-metal surfaces", Surface Science Reports **30**, 153 (1998).

[153] B. Stadtmüller, M. Willenbockel, S. Schröder, C. Kleimann, E. M. Reinisch, T. Ules, S. Soubatch, M. G. Ramsey, F. S. Tautz, and C. Kumpf, "Modification of the PTCDA-Ag bond by forming a heteromolecular bilayer film", Physical Review B **91**, 155433 (2015).

[154] M. C. Chong, G. Reecht, H. Bulou, A. Boeglin, F. Scheurer, F. Mathevet, and G. Schull, "Narrow-line single-molecule transducer between electronic circuits and surface plasmons", Physical Review Letters **116**, 036802 (2016).

[155] F. Güttler, T. Irngartinger, T. Plakhotnik, A. Renn, and U. P. Wild, "Fluorescence microscopy of single molecules", Chemical Physics Letters **217**, 393 (1994).

[156] N. Rohbohm, "Fluorescence microscopic analysis on the orientation of PTCDA domains on KCl(100) in ultrahigh vacuum", Master's thesis (University Bonn, 2018).

[157] (July 7, 2018) `https://commons.wikimedia.org/wiki/User:Alchemist-hp#/media/File:Bismuth_crystals_and_1cm3_cube.jpg`.

[158] C. Brülke, PhD thesis (University Bonn, in preparation).

[159] L. Novotny and N. van Hulst, "Antennas for light", Nature Photonics **5**, 83 (2011).

[160] M. Wewer and F. Stienkemeier, "Laser-induced fluorescence spectroscopy of N,N'-dimethyl 3,4,9,10-perylene tetracarboxylic diimide monomers and oligomers attached to helium nanodroplets", Physical Chemistry Chemical Physics **7**, 1171 (2005).

[161] L. Gisslén, "Influence of Frenkel excitons and charge transfer states on the spectroscopic properties of organic molecular crystals", PhD thesis (Technische Universität München, 2010).

[162] L. Zhang, X. Fu, C. G. Hu, Y. Yao, Z. Y. Xu, X. T. Hu, M. Hohage, P. Zeppenfeld, and L. D. Sun, "Optical and structural properties of the pentacene/quartz (0001) interface", Physical Review B **93**, 075443 (2016).

Acknowledgements

At this point, I would like to thank all those people who have supported me during the work behind this thesis:

- First of all, I would like to thank my supervisor and mentor, Professor Dr. Moritz Sokolowski, for giving me the opportunity to work in his group. I am deeply grateful for his support during the last years, especially for many motivating and stimulating discussions, and his never ending optimism that encouraged me to explore the exciting fields of surface science and optical spectroscopy.
- I would like to thank Professor Dr. Peter Zeppenfeld (Johannes Kepler Universität Linz, Linz, Austria) for accepting to act as the co-referee for my PhD thesis, and for the short but very stimulating time at the optics laboratory working together on pentacene on KCl(100). Furthermore, I am grateful to Professor Dr. Arne Lützen (Rheinische Friedrich-Wilhelms-Universität Bonn, Bonn, Germany), and Professor Dr. Stefan Linden (Rheinische Friedrich-Wilhelms-Universität Bonn, Bonn, Germany) who also agreed to be on the board of examiners.
- My special thanks go to Dr. Alexander Eisfeld (Max Planck Institut für Physik komplexer Systeme, Dresden, Germany) who supported this work not only by theoretical calculations for the understanding of the superradiance of the PTCDA/KCl(100) brickwall phase, but also with countless fruitful discussions related to all kinds of molecular interactions.
- I would like to thank Professor Dr. Rudolf Merkel (Forschungszentrum Jülich, Jülich, Germany) for many helpful discussions and advices regarding the construction of the UHV optical microscope.
- My thanks also go to Professor Dr. Joachim Wollschläger (Universität Osnabrück, Osnabrück, Germany) who supported this work by discussions on the interpretation and analysis of two dimensional SPA-LEED profiles.
- I would like to thank all my dear colleagues from the Organic Films group for the friendly atmosphere and the enjoyable collaboration over the last years. In particular, I acknowledge the fruitful and exciting collaboration with my colleagues Alexander Paulheim, Christine Brülke, Nils Rohbohm, and Beatrice Wolff at the optics laboratory as well as many technical discussions with Martin Specht.
- My thanks also go to Manuel Hochheim and Professor Dr. Thomas Bredow (Rheinische Friedrich-Wilhelms-Universität Bonn, Bonn, Germany) for many discussions regarding the adsorption sites of PTCDA on alkali-halide surfaces and how the bonding to the substrate influences the optical properties.

- I highly acknowledge the technical support from all staff members of the mechanics and electronics workshops of the Institut für Physikalische und Theoretische Chemie (Rheinische Friedrich-Wilhelms-Universität Bonn, Bonn, Germany). In particular, I would like to thank Heinz-Peter Königshoven for his support during the design and construction of many new components for the optics experiment, Rolf Paulig for fast and competent help with defect electronic devices, and Peter Koll for the construction of the glass-tube of the microscope. Also, technical support by Knut Hintzen from the IT-staff of the institute is highly acknowledged.
- My special thanks go to Toni Hanfland for his efforts to supply liquid helium, also at rather unusual times of the day.
- Financial support by the Deutsche Forschungsgemeinschaft under the project SO 407/8-1 (Fluoreszenz-Spektroskopie an Molekülen auf Oberflächen im Grenzfall kleiner Bedeckungen) is acknowledged.
- Last but not the least, I would like to thank my family for supporting me throughout the years of working on this thesis.